

**A dissertation submitted in partial fulfillment of the requirements for the  
degree of Doctor of Philosophy at Dublin City University**

**ACCELERATED ITERATIVE SOLVERS FOR THE SOLUTION OF  
ELECTROMAGNETIC SCATTERING AND WAVE PROPAGATION PROBLEMS**

**Vinh Pham-Xuan**

*Supervisors: Dr. Conor Brennan and Dr. Marissa Condon*




School of Electronic Engineering

Dublin City University

October 2015

# Declaration

I hereby certify that this material, which I now submit for assessment on the programme of study leading to the award of Doctor of Philosophy, is entirely my own work, and that I have exercised reasonable care to ensure that the work is original, and does not to the best of my knowledge breach any law of copyright, and has not been taken from the work of others save and to the extent that such work has been cited and acknowledged within the text of my work.

Signed: 

ID No: 11211980

Date: 27/10/2015

# Contents

<b>Declaration</b>	<b>i</b>
<b>Acronyms</b>	<b>v</b>
<b>Abstract</b>	<b>xiii</b>
<b>1 Introduction</b>	<b>1</b>
1.1 Contribution . . . . .	7
1.2 Notation . . . . .	7
<b>2 Method of moments for numerical solution of Maxwell equations</b>	<b>8</b>
2.1 Differential form of Maxwell equations . . . . .	8
2.2 Time-harmonic form of Maxwell equations . . . . .	9
2.3 Auxiliary vector potentials . . . . .	10
2.3.1 Magnetic vector potential . . . . .	11
2.3.2 Electric vector potential . . . . .	12
2.4 Volume electric field integral equation . . . . .	14
2.4.1 Volume equivalence principle . . . . .	14
2.4.2 Volume integral equations . . . . .	15
2.5 Surface integral equations . . . . .	18
2.5.1 Boundary conditions . . . . .	18
2.5.2 Surface equivalence principle . . . . .	19
2.5.3 Surface integral equations . . . . .	21
2.6 Method of moments . . . . .	25
2.7 Conclusion . . . . .	27
<b>3 Iterative methods for the solution of linear systems</b>	<b>28</b>
3.1 Introduction . . . . .	28
3.2 Krylov subspace iterative methods . . . . .	29
3.2.1 Arnoldi iteration . . . . .	30
3.2.2 Conjugate gradient method . . . . .	33
3.2.3 Biconjugate gradient method . . . . .	36
3.2.4 Biconjugate gradient stabilised method . . . . .	38
3.2.5 Generalised minimal residual method . . . . .	41
3.3 Stationary iterative methods . . . . .	42
3.3.1 Jacobi method . . . . .	46
3.3.2 Gauss-Seidel method . . . . .	48
3.3.3 Successive overrelaxation method . . . . .	48
3.3.4 Forward backward method . . . . .	50

3.3.5	Block forward backward method . . . . .	53
3.3.6	Buffered block forward backward method . . . . .	56
3.3.7	Overlapping domain decomposition method . . . . .	62
3.4	Preconditioning techniques . . . . .	62
3.4.1	Block Jacobi preconditioner . . . . .	66
3.4.2	Incomplete LU preconditioner . . . . .	67
3.4.3	Sparse approximate inverse preconditioner . . . . .	67
3.5	Conclusion . . . . .	68
<b>4</b>	<b>Modified multilevel fast multipole algorithm for stationary iterative methods</b>	<b>69</b>
4.1	Introduction . . . . .	69
4.2	Combined field integral equation for 3D perfectly conducting problems . . .	70
4.3	Multilevel fast multipole algorithm . . . . .	71
4.4	Modified MLFMA for buffered block forward backward method . . . . .	78
4.4.1	Modified MLFMA . . . . .	83
4.4.2	Computational complexity . . . . .	90
4.5	Numerical results and validations . . . . .	98
4.5.1	Verification of the complexity estimation . . . . .	98
4.5.2	Efficiency and accuracy of the modified MLFMA applied to the BBFB104	
4.5.3	Combination with the interpolative decomposition for an efficient computation of radar cross section . . . . .	109
4.6	Conclusion . . . . .	113
<b>5</b>	<b>Modified improvement step for stationary iterative methods</b>	<b>114</b>
5.1	Introduction . . . . .	114
5.2	Improvement step . . . . .	114
5.3	Modified improvement step . . . . .	118
5.3.1	Formulation . . . . .	118
5.3.2	Computational complexity . . . . .	120
5.4	Numerical results and validations . . . . .	121
5.4.1	Application to the solution of scattering from one dimensional ran- domly rough surface . . . . .	121
5.4.2	Application to the solution of scattering from two dimensional ran- domly rough surface . . . . .	126
5.5	Conclusion . . . . .	127
<b>6</b>	<b>Integral equation approaches for indoor wave propagation</b>	<b>129</b>
6.1	Introduction . . . . .	129
6.2	Volume integral equation accelerated by the fast Fourier transform . . . . .	130
6.2.1	Volume electric field integral equation for two dimensional TM <sup>z</sup> po- larisation problem . . . . .	130
6.2.2	Fast Fourier transform applied to the discretised volume integral equation . . . . .	132
6.2.3	Reduced operator for the enhancement of convergence rate . . . . .	134

6.3	Surface integral equation accelerated by the fast far field approximation . . .	135
6.3.1	Surface electric field integral equation for two dimensional $TM^z$ polarisation problem . . . . .	135
6.3.2	Fast far field approximation applied to the surface integral equation	137
6.4	Numerical results and validations . . . . .	138
6.4.1	Efficiency of the reduced operator . . . . .	138
6.4.2	Efficiency of the adaptive FAFFA . . . . .	139
6.4.3	Comparison between the VEFIE and the SEFIE . . . . .	139
6.5	Conclusion . . . . .	140
<b>7</b>	<b>Wideband solution for three dimensional forward scattering problems</b>	<b>145</b>
7.1	Introduction . . . . .	145
7.2	Volume integral equation . . . . .	146
7.2.1	Volume electric field integral equation . . . . .	146
7.2.2	The weak-form discretisation . . . . .	147
7.3	Asymptotic waveform evaluation . . . . .	149
7.4	Numerical results and validations . . . . .	150
7.5	Conclusion . . . . .	152
<b>8</b>	<b>Conclusions</b>	<b>156</b>
8.1	Future study . . . . .	157
	<b>Bibliography</b>	<b>159</b>
	<b>Publications</b>	<b>171</b>
	<b>Acknowledgments</b>	<b>173</b>

# Acronyms

ACA	Adaptive Cross Approximation
AIM	Adaptive Integral Method
AWE	Asymptotic Waveform Evaluation
BBFB	Buffered Block Forward Backward Method
BFBM	Block Forward Backward Method
BiCG	Biconjugate Gradient Method
BiCGSTAB	Biconjugate Gradient Stabilised Method
CBFM	Characteristic Basis Function Method
CEM	Computational Electromagnetic
CFIE	Combined Field Integral Equation
CG	Conjugate Gradient Method
EFIE	Electric Field Integral Equation
EM	Electromagnetic
FAFFA	Fast Far Field Approximation
FBM	Forward Backward Method
FDTD	Finite Difference Time Domain
FEM	Finite Element Method
FFT	Fast Fourier Transform
FMM	Fast Multipole Method
GMRES	Generalised Minimal Residual Method
GMRES-FFT	Generalised Minimal Residual - Fast Fourier Transform
GPU	Graphic Processing Unit
GTD	Geometrical Theory of Diffraction

---

ID	Interpolative Decomposition
IE	Integral Equation
ISB	Incident Shadow Boundary
MDA	Matrix Decomposition Algorithm
MFIE	Magnetic Field Integral Equation
MLFMA	Multilevel Fast Multipole Algorithm
MoM	Method of Moments
MOMI	Method of Ordered Multiple Interactions
MOR	Model Order Reduction
MS-CBD	Multiscale Compressed Block Decomposition
MVP	Matrix-Vector Product
O-DDM	Overlapping Domain Decomposition Method
PEC	Perfect Electric Conducting
PO	Physical Optics
PTD	Physical Theory of Diffraction
RCS	Radar Cross Section
RSB	Reflection Shadow Boundary
RWG	Rao-Wilton-Glisson
SA	Spectral Acceleration
SEFIE	Surface Electric Field Integral Equation
SMFIE	Surface Magnetic Field Integral Equation
SOR	Successive Overrelaxation Method
SPAI	Sparse Approximate Inverse
SSOR	Symmetric Successive Overrelaxation Method
SVD	Singular Value Decomposition
UTD	Uniform Theory of Diffraction
VEFIE	Volume Electric Field Integral Equation
VMFIE	Volume Magnetic Field Integral Equation

# List of Tables

1.1	Comparison of FDTD, FEM and MoM for the application to open region problems. . . . .	3
4.1	Numbers of updates of the upward and downward processes for a single sweep of the BBFB using the modified MLFMA. . . . .	100
4.2	Numbers of process updates for a rectangular PEC plate with a size of $1.5\lambda \times 40\lambda$ using the BBFB accelerated by the modified MLFMA. . . . .	100
4.3	Numbers of process updates for a rectangular PEC plate with a size of $0.5\lambda \times 20\lambda$ using the BBFB accelerated by the modified MLFMA. . . . .	102
4.4	Comparison of runtime of a BBFB iteration and that of a full matrix-vector product for rectangular PEC plates size of $1.5\lambda \times 40\lambda$ and $0.5\lambda \times 20\lambda$ . . . . .	102
4.5	List of scenarios performed in test case 4. . . . .	103
4.6	Size of local problems of scenarios in test case 4. . . . .	103
4.7	Size of local problems in test case 6. . . . .	103
4.8	Runtime in seconds for each O-DDM iteration when using the modified MLFMA and the original MLFMA for the NASA almond and the NASA double-ogive. . . . .	110
4.9	Runtime for the computation of mono RCS using the ID-ODDM and the ODDM with a phase correction for the NASA almond and the NASA double-ogive. . . . .	112
5.1	Runtime (outside parenthesis) in seconds and number of iterations (inside parenthesis) required to achieve a residual norm of $10^{-4}$ . Exponential surface. Horizontal polarisation. . . . .	125
5.2	Runtime (outside parenthesis) in seconds and number of iterations (inside parenthesis) required to achieve a residual norm of $10^{-4}$ . Exponential surface. Vertical polarisation. . . . .	125
5.3	Runtime (outside parenthesis) in seconds and number of iterations (inside parenthesis) required to achieve a residual norm of $10^{-4}$ . Gaussian surface. Horizontal polarisation. . . . .	125
5.4	Runtime (outside parenthesis) in seconds and number of iterations (inside parenthesis) required to achieve a residual norm of $10^{-4}$ . Gaussian surface. Vertical polarisation. . . . .	125
5.5	Comparison of the brightness temperature between simulation and measurement. $h_{\text{rms}} = 0.88\text{cm}$ . $\epsilon_r = 19.2 + j2.41$ . . . . .	126
5.6	Runtime (outside parenthesis) in seconds and number of iterations (inside parenthesis) required to achieve a residual norm of $10^{-4}$ . Gaussian surface. Horizontal polarisation. . . . .	128



---

5.7	Runtime (outside parenthesis) in seconds and number of iterations (inside parenthesis) required to achieve a residual norm of $10^{-4}$ . Exponential surface. Horizontal polarisation. . . . .	128
6.1	Comparison of the two approaches for the scenario in Figure 6.9. . . . .	140
7.1	Comparison of runtime using the conventional MoM and the AWE for the dielectric sphere. . . . .	151

# List of Figures

1.1	Classification of the main contributions. . . . .	7
2.1	Block diagram for the computation of radiated fields using the vector potentials. . . . .	10
2.2	Volumetric equivalence problem. . . . .	17
2.3	Geometry for boundary conditions at the interface between two homogeneous media. . . . .	20
2.4	Geometry for boundary conditions at the interface between a perfect conductor and a dielectric medium. . . . .	20
2.5	Surface equivalence problem. . . . .	22
2.6	Application of the surface equivalence theorem to a homogeneous problem. . . . .	24
3.1	Forward and backward scattering in the forward backward method. Coloured segments refer to pulse basis function domains which are locally flat segments. Red segment is a segment under consideration. Blue segments refer to segments nearer to the source than the segment under consideration, causing forward scattering. Black segments refer to basis functions further away from the source, generating backward scattering. . . . .	52
3.2	Block forward backward method for problems with abrupt changes in height. . . . .	55
3.3	Group-by-group scheme of the block forward backward method. . . . .	55
3.4	Buffer regions in the buffered block forward backward method. . . . .	58
3.5	Eigenvalue distributions for a square plate. . . . .	63
3.6	Comparison between the BBFB and the BFBM for a PEC square plate. . . . .	63
3.7	Spurious edge effects in the case of a NASA almond. . . . .	64
3.8	Sub-region and buffer region in the overlapping domain decomposition method. . . . .	65
4.1	Illustration of the fast multipole method. . . . .	74
4.2	Translations in the fast multipole method. . . . .	74
4.3	Parent cubes of source and testing groups. . . . .	75
4.4	Shifting and interpolation/antepolation in the multilevel fast multipole algorithm. . . . .	75
4.5	Recursive division of a cube into smaller cubes in the multilevel fast multipole algorithm. . . . .	76
4.6	Octtree structure of the multilevel fast multipole algorithm. . . . .	76
4.7	Illustration of the translation and disaggregation steps of the multilevel fast multipole method. . . . .	79
4.8	Translation and disaggregation at level 2 of an example in Figure 4.7. . . . .	79
4.9	Translation and disaggregation at level 3 of an example in Figure 4.7. . . . .	80

4.10	Near-zone contribution of an example in Figure 4.7. . . . .	80
4.11	Illustration of the scattered fields at step $m$ of the forward sweep of the BBFB. . . . .	81
4.12	Illustration of the scattered fields at step $(m + 1)$ of the forward sweep of the BBFB. . . . .	81
4.13	Near-zone computation in the modified MLFMA. . . . .	85
4.14	Illustration of the recomputation of the upward and downward processes in the modified MLFMA. . . . .	85
4.15	Illustration of a sub-region size ( $GS$ ) and a buffer region size ( $BS$ ). . . . .	91
4.16	Illustration of the complexity of the upward process - $c_1^u$ . . . . .	91
4.17	Illustration of the complexity of the upward process - $c_2^u$ . . . . .	93
4.18	Illustration of the complexity of the upward process - $c_4^u$ . . . . .	94
4.19	Illustration of the complexity of the downward process - $c_2^d$ . . . . .	97
4.20	Illustration of the complexity of the downward process - $c_3^d$ . . . . .	99
4.21	Comparison of the runtime (divided by runtime of one full MVP) between the standard MLFMA and the modified MLFMA for the NASA ogive. . . . .	102
4.22	Comparison between the BBFB and the Krylov iterations for the NASA almond. . . . .	106
4.23	Comparison between the BBFB and the Krylov iterations for the wind turbine blade. . . . .	107
4.24	Comparison between the RCS results computed using the BBFB and the measurement data in [1]. . . . .	108
4.25	Illustration of multiple excitation angles in a mono RCS computation of a PEC problem. . . . .	110
4.26	Partition of the NASA almond and the NASA double-ogive in the overlapping domain decomposition method. . . . .	110
4.27	Comparison between the RCS computed using ID-ODDM and that computed using the ODDM for the NASA almond. . . . .	112
4.28	Comparison between the RCS computed using ID-ODDM and that computed using the ODDM for the NASA double-ogive. . . . .	112
5.1	Illustration of the improvement step. . . . .	115
5.2	Illustration of the modified improvement step. . . . .	115
5.3	Bistatic scattering coefficients of an exponential surface: root mean square height of $0.88\lambda$ ; correlation length of $2.8\lambda$ ; incident angle of $50^\circ$ . . . . .	122
5.4	Comparison of the performance of the modified improvement step using different numbers of correction vectors. . . . .	123
5.5	Two dimensional dielectric random rough surface profile. . . . .	128
6.1	Discretisation of the volume integral equation using pulse basis functions. . . . .	133
6.2	Illustration of the MVP in Equation 6.15. . . . .	133
6.3	Illustration of a homogeneous cylinder illuminated by a $TM^z$ incidence. . . . .	136
6.4	Illustration of the FAFFA. . . . .	136
6.5	Two dimensional indoor environment with a size of $10m \times 10m$ . . . . .	141

6.6	Comparison between the BiCGSTAB with and without the reduced operator for scenario in Figure 6.5. . . . .	141
6.7	Comparison between the BiCGSTAB with the FAFFA and with the adaptive FAFFA for scenario in Figure 6.5. . . . .	142
6.8	Total field throughout the room computed using the SEFIE. . . . .	142
6.9	Two dimensional indoor environment with a size of $15\text{m} \times 15\text{m}$ . . . . .	143
6.10	Total fields throughout the room using the VEFIE and the SEFIE approaches. . . . .	143
6.11	Total fields along the line $y = -1.2437\text{m}$ in the scenario shown in Figure 6.9. . . . .	144
6.12	Total fields along the line $x = -1.2437\text{m}$ in the scenario shown in Figure 6.9. . . . .	144
7.1	Discretisation of the dielectric sphere. . . . .	153
7.2	Value of the relative permittivity of the dielectric sphere with respect to frequency. . . . .	153
7.3	Radar cross section results of the dielectric sphere with the radius of $0.09\text{m}$ . . . . .	154
7.4	Total field along $x$ direction with $y = -0.0874\text{m}$ and $z = -0.1208\text{m}$ at $f = 1.3\text{GHz}$ . . . . .	154
7.5	Total field along $y$ direction with $x = -0.1124\text{m}$ and $z = -0.1124\text{m}$ at $f = 1.3\text{GHz}$ . . . . .	155
7.6	Total field along $z$ direction with $x = -0.1041\text{m}$ and $y = -0.1041\text{m}$ at $f = 1.3\text{GHz}$ . . . . .	155

# List of Algorithms

3.1	The classical Gram-Schmidt process. . . . .	32
3.2	The Arnoldi - modified Gram-Schmidt iteration. . . . .	32
3.3	Algorithm for the minimisation of Equation 3.22 using general direction vectors. . . . .	34
3.4	The conjugate gradient method. . . . .	34
3.5	The biconjugate gradient method. . . . .	37
3.6	The biconjugate gradient stabilised method. . . . .	39
3.7	The generalised minimal residual method. . . . .	43
3.8	The Jacobi method. . . . .	47
3.9	The Gauss-Seidel method. . . . .	47
3.10	The successive overrelaxation method. . . . .	49
4.1	Indication of flags of leaf cubes in the modified MLFMA. . . . .	86
4.2	Indication of flags of cubes at the higher levels in the modified MLFMA. . .	87

# Abstract

The aim of this work is to contribute to the development of accelerated iterative methods for the solution of electromagnetic scattering and wave propagation problems. In spite of recent advances in computer science, there are great demands for efficient and accurate techniques for the analysis of electromagnetic problems. This is due to the increase of the electrical size of electromagnetic problems and a large amount of design and analytical work dependent on simulation tools. This dissertation concentrates on the use of iterative techniques, which are expedited by appropriate acceleration methods, to accurately solve electromagnetic problems. There are four main contributions attributed to this dissertation. The first two contributions focus on the development of stationary iterative methods while the other two focus on the use of Krylov iterative methods. The contributions are summarised as follows:

- The modified multilevel fast multipole method is proposed to accelerate the performance of stationary iterative solvers. The proposed method is combined with the buffered block forward backward method and the overlapping domain decomposition method for the solution of perfectly conducting three dimensional scattering problems. The proposed method is more efficient than the standard multilevel fast multipole method when applied to stationary iterative solvers.
- The modified improvement step is proposed to improve the convergence rate of stationary iterative solvers. The proposed method is applied for the solution of random rough surface scattering problems. Simulation results suggest that the proposed algorithm requires significantly fewer iterations to achieve a desired accuracy as compared to the conventional improvement step.
- The comparison between the volume integral equation and the surface integral equation is presented for the solution of two dimensional indoor wave propagation problems. The linear systems resulting from the discretisation of the integral equations are solved using Krylov iterative solvers. Both approaches are expedited by appropriate acceleration techniques, the fast Fourier transform for the volumetric approach and the fast far field approximation for the surface approach. The volumetric approach demonstrates a better convergence rate than the surface approach.
- A novel algorithm is proposed to compute wideband results of three dimensional forward scattering problems. The proposed algorithm is a combination of Krylov iterative solvers, the fast Fourier transform and the asymptotic waveform evaluation technique. The proposed method is more efficient to compute the wideband results than the conventional method which separately computes the results at individual frequency points.

# 1 Introduction

The development of Maxwell's equations in the 19<sup>th</sup> century, which are named after the Scottish physicist James Clerk Maxwell, marked a crucial turning point in modern science and technology as Albert Einstein once acclaimed that "*The work of James Clerk Maxwell changed the world forever.*" The equations describe the relation of magnetism and electricity, leading to the discovery of many theoretical innovations such as the theory of relativity and the field equations of quantum mechanics. They are essential for advances in diverse areas such as communications (radio, television, radar, microwave, etc.) or medical imaging in biomedical systems, which greatly impact human life. Therefore, much effort has been devoted to the development of powerful electromagnetic (EM) simulation tools which efficiently approximate the equations and are essential for electrical engineers in the design of electrical and electronic equipments.

The EM modelling tools simulate the interaction of EM fields with physical objects and support engineers in the prediction of EM behaviour during the design process such as the design of antennas or the optimisation of base-station location in mobile communication planning. The important role of computational electromagnetic (CEM) applications is also acknowledged in particular research areas. For example, the computation of radar cross section (RCS) is applied to estimate the effects of large bodies on communication systems [2], to detect unknown objects at a long distance [3] or to aid the design of stealth aircraft [4] which can avoid the detection by radar systems by the reduction of reflection of radio-frequency spectrum. The reconstruction of an image of the human body [5, 6, 7] based on the measurement of scattered fields is central to MRI and X-ray tomography in the biomedical area and allow the detection of imminent diseases. As much work relies on the simulation tools, the demand for efficient and accurate electromagnetic analysis tools has increased dramatically, resulting in much research work concentrating on improving and developing CEM tools.

The CEM solvers can be categorised into asymptotic techniques, full-wave techniques and hybrid techniques which are a combination of the two former. In asymptotic techniques, Maxwell equations are approximated by simpler forms, enabling the efficient computation of the electromagnetic characteristics of the problem which is the main advantage of these methods. However, the validation of asymptotic techniques depends on the operating frequency range of the problem where the accuracy of the techniques increases with respect to the frequency. The high-frequency asymptotic techniques can be classified into two families. The first family begins with geometrical optics [8] which considers the propagation of electromagnetic waves as optical rays at a high frequency. Thus, the electromagnetic problem can be analysed using ray tracing techniques which determine the amplitude of the EM fields by the shape of the illuminated surface. The lack of evaluation of fields

diffracted by wedges and edges results in non-physical continuities of the total field at the incident shadow boundary (ISB) and reflection shadow boundary (RSB) in geometrical optics. The accuracy of geometrical optics is improved by including the effects of diffracted fields in the geometrical theory of diffraction (GTD) [9, 10] and later in the uniform theory of diffraction (UTD) [11, 12, 13]. Another family of asymptotic techniques begins with physical optics (PO) which focuses on the primary characteristics of a wave to approximate the induced current density on the surfaces instead of concentrating on the shape of the wavefront surface in geometrical optics. Using the relations of free-space field-source, the radiated fields can be obtained by taking an integral over the induced currents. However, the lack of evaluation of geometrical effects such as edges on the induced currents results in a discontinuity of the induced currents at the boundary between the illuminated and shadow surfaces. The accuracy of PO is improved in the physical theory of diffraction (PTD) [14, 15] by the addition of non-uniform fringe currents to evaluate the geometrical effects. The application of asymptotic techniques to appropriate problems such as large and smooth problems is highly beneficial because their complexity is considerably smaller than that of the full-wave techniques to generate an acceptably accurate solution. However, when the complexity of the electromagnetic problems increases or the desired accuracy is beyond the capability of asymptotic techniques, full-wave techniques are the only choice for the solution of Maxwell equations.

The operation of full-wave techniques is fundamentally based on the idea of discretisation of some unknown electromagnetic quantities such as the electric or magnetic field by the finite element method (FEM) [16, 17] and the finite difference time domain (FDTD) [18, 19], and the surface current by the method of moments (MoM) [20, 21, 22]. The full-wave techniques are further classified in terms of the operating domain (time or frequency) and the form of Maxwell equations (integral or partial differential). The operation of the FDTD method originates from the differential form of Maxwell equations. The approximation of these differential operators is obtained by applying Maxwell's curl equations to time-space grid in the Yee's FDTD scheme [23]. The value of the fields at the next-time step are completely given in terms of the field at the present and the previous time-step. Therefore, the implementation of the FDTD is considerably more straightforward than that of the FEM and MoM which require an evaluation of a matrix equation for the value of the fields. The FDTD method is extensively used for the analysis of wideband problems because the method operates in the time domain. As a consequence, the wideband response is obtained within one FDTD run while the problem has to be recomputed at discrete frequencies for the MoM and the FEM. In addition, the treatment of inhomogeneous problems in the FDTD is straightforward because it is not affected by the composition of the structure. Similar to the FDTD, the FEM starts from the partial differential form of Maxwell equations which is then applied in the frequency domain. The FEM is suitable for the analysis of complicated geometries and inhomogeneous material whose properties might be frequency-dependent, and has a better scaling with frequency as compared to the MoM. However, the meshing for large three dimensional structures in the FEM is more complicated than that in the FDTD. The MoM is derived from the integral form of Maxwell equations and is mainly applied in the frequency domain. Instead of using the direct computation of fields as in the FEM and the FDTD, the MoM initially replaces the



scattering problem by equivalent currents and derives a relationship between these currents in the form of a dense matrix equation which is later solved for the unknown equivalent currents. Then, the fields external to the structure can be computed from these currents. The MoM is more advantageous than the FDTD and the FEM for the analysis of highly conducting problems and homogeneous problems because only the discretisation of the surface of the problems is required instead of the entire space containing the problem as in the FDTD and the FEM. In contrast, for electromagnetically penetrable materials, the complexity of the MoM becomes prohibitively expensive due to the meshing of the entire volumetric structure resulting in a large number of unknowns. A comparison of the three most popular full-wave techniques (FDTD, FEM and MoM) for the application to open region problems is presented in Table 1.1.

Techniques	Equation Type	Domain	WB	PEC	HP	IHP
MoM	Integral	Frequency	~	+	+	~
FEM	Differential	Frequency	~	-	+	+
FDTD	Differential	Time	+	-	+	+

WB: wideband      PEC: perfect electric conductor

HP: homogeneous problem      IHP: inhomogeneous problem

+: good      -: not optimal      ~: satisfactory, but not necessarily the best

**Table 1.1:** Comparison of FDTD, FEM and MoM for the application to open region problems.

The application of the MoM for the solution of electromagnetic problems is the focus of this thesis. In the MoM, the surface of the electromagnetic problems is discretised using appropriate basis functions such as Rao-Wilton-Glisson (RWG) basis functions [24] which represent the discrete current density, leading to the discrete integral form of Maxwell equations for the fields on the surface. The approximate current density on the surface of the problem is a linear combination of the basis functions. Applying a testing procedure [22] to the discrete integral form results in a linear matrix equation  $\mathbf{Z}\mathbf{x} = \mathbf{b}$  where  $\mathbf{x}$  denotes the unknown amplitudes of the corresponding basis functions.  $\mathbf{Z}$  is a  $N \times N$  impedance matrix containing information about the mutual interactions between the basis functions where  $N$  is the number of basis functions used to discretise the surface of the geometries.  $\mathbf{b}$  denotes a vector containing information about the incident field impinging on each basis function. Different approaches depending on the characteristics of the problems have been proposed for the solution of the matrix equations.

The first approach is to compute the product of the inverse of the impedance matrix  $\mathbf{Z}$  and the incident vector  $\mathbf{b}$ , requiring a storage and computational cost of  $\mathcal{O}(N^2)$  and  $\mathcal{O}(N^3)$  for performing a direct matrix inverse, respectively. However, this approach is restricted for the solution of small problems involving a small number of unknowns. There are several techniques proposed to alleviate the expensive cost of the direct matrix inverse such as the multiscale compressed block decomposition (MS-CBD) method [25, 26, 27]. The operation of the MS-CBD method is based on the use of impedance matrix compression techniques such as the adaptive cross approximation (ACA) [28, 29, 30, 31] and the matrix decomposition algorithm (MDA) [32, 33, 34] methods. The block-wise compressed impedance matrices allow an efficient computation of an inverse operator of the MS-CBD method

with the cost of  $\mathcal{O}(N^2 \log^2 N)$  and  $\mathcal{O}(N^{3/2} \log N)$  for the computation and storage requirement, respectively. Another free-iteration method which received much attention recently is the characteristic basis function method (CBFM) [35, 36, 37]. The CBFM proceeds by first dividing the electromagnetic problem into blocks which are manageable in terms of size and then defining a set of macro basis functions including primary and secondary basis functions for each block. These basis functions are then used to generate a reduced matrix which is significantly smaller than the original impedance matrix, allowing an efficient gain in terms of computational and storage cost. The main advantage of the direct inverse approach is that most computations are in the matrix compression process and the inverse operator decomposition process which are independent of the excitation vector  $\mathbf{b}$ . Once these operations have been completed, the solution for each excitation can be quickly obtained, leading to an efficient computation of mono RCS applications. However, the storage requirement and the need to invert the resultant matrix becomes impractical for dense linear systems involving a large number of unknowns.

The second approach using iterative solvers for MoM dense linear systems has been considered as an appropriate solution to overcome the limitations as it requires little or no explicit storage and significantly reduce the number of computations when compared to making a direct inverse of a dense matrix. Approximate solutions are sequentially generated and improved at the end of each iteration until the convergence criteria is met. The requirement of matrix-vector products (MVP) in each iteration of iterative methods results in the cost of  $\mathcal{O}(N^2)$  for both storage and computational expense. There are two main classes of iterative solvers: the non-stationary solvers and the stationary solvers. The non-stationary solvers are typically based on the creation of Krylov subspaces. The conjugate gradient (CG) method [38], biconjugated gradient stabilised (BiCGSTAB) method [39] and the generalised minimal residual (GMRES) method [40, 41] are popular among Krylov methods for their robust convergence. The Krylov methods are reliable in terms of convergence because it is evident that they are convergent to an exact solution within a finite number of iterations in exact arithmetic [42]. In contrast, the stationary methods are more unpredictable in terms of convergence rate. The advantages of the stationary methods over the Krylov methods are that they require a smaller number of iterations to achieve the same accuracy when applied to simple structures and they are more simple for implementation and derivation. Some popular stationary solvers are the Gauss-Seidel method, the Jacobi method and the successive-over-relaxation method [38].

Another key research topic is the development of computationally efficient acceleration techniques to reduce the cost of a MVP performed within each iteration. The operation of most acceleration techniques depends on the idea of the division of the electromagnetic field into the near-zone region and the far-zone [43]. The field strength of the far-zone decreases with distance while that of the near-zone decreases rapidly with distance, resulting in the domination of the far-zone strength in the far-zone region. This phenomenon is exploited in acceleration techniques to optimise the cost of computation where the contribution of the near-zone is exactly computed while that of the far-zone is efficiently approximated by different methods. The approximation of the far-zone can be achieved by the application of low-rank approximation or matrix compression techniques [44, 45], which are purely algebraic, to reduce the size of impedance matrices accounting for far-zone interactions,

leading to a reduction in the cost of a MVP. The approximation can also be achieved by taking advantage of the physical properties of the EM problems. The adaptive integral method (AIM) [46, 47, 48, 49] replaces original basis functions by auxiliary basis functions positioned at the nodes of a Cartesian grid. The auxiliary basis functions are required to produce the same far-zone as the original basis functions, allowing an application of the fast Fourier transform (FFT) for the computation of far-zone interaction which is of  $\mathcal{O}(N^{3/2} \log N)$  and  $\mathcal{O}(N \log N)$  operations for surface and volumetric problems, respectively. The fast-far-field-approximation (FAFFA) [50, 51, 52, 53] efficiently approximates the far-zone interactions using an interpolation/extrapolation scheme. The main drawback of the FAFFA is the large size of the near-zone region, causing a considerable computation of near-zone interaction; otherwise, the accuracy of the FAFFA can significantly worsen when the size of the near-zone region is reduced. The fast multipole method (FMM) [54, 55] improves the accuracy of the far-zone computation by a more careful investigation using the interpolation/extrapolation scheme or expanding the fields using multiple plane waves. The improvement of the FMM to the multilevel fast multipole method (MLFMA) [56, 57, 58], which is extensively applied for the solution of EM problems, increases the efficiency of the MVP by reducing the cost of computation to  $\mathcal{O}(N \log N)$ . Besides acceleration techniques, the total cost of computation can be considerably decreased by improving the convergence rate of iterative solvers. The improvement of the convergence rate is accomplished by the use of a wide range of preconditioners such as the diagonal preconditioner [59], the incomplete LU factorization [60] or the sparse approximate inverse (SPAI) preconditioner [61]. The main idea of the application of preconditioner techniques is that the original ill-conditioned system is replaced by an equivalent better-conditioned system. Consequently, a smaller number of iterations is required to achieve a desired accuracy.

The principal contributions of this work are the proposal of novel algorithms integrating iterative solvers and appropriate acceleration techniques for efficient solutions of three dimensional (3D) scattering and two dimensional (2D) indoor propagation problems. Much research effort has concentrated on Krylov solvers [62, 63] for the solution of arbitrarily 3D perfectly conducting or homogeneous problems. Recently, some attention has been focused on some particular stationary solvers which mimic the physical processes of propagation by using *current marching* techniques. The stationary solver forward backward method (FBM) [64, 65] was first successfully applied to one dimensional (1D) random rough surface problems. The capture of the physical phenomenon in the FBM leads to a high convergence rate, approaching an accurate solution with fewer iterations when compared to the Krylov solvers for the random rough surface problems. The buffered block forward backward (BBFB) method [66, 67], an extension of the FBM for 3D scattering problems, introduces buffered regions to eliminate spurious edge effects which worsen the performance of the FBM for 3D problems. In addition, the convergence rate of the stationary method can be further improved by an application of a special improvement step [68, 69] at the end of each iteration. In the case that the electromagnetic responses over a wide range of frequencies is of interest, it can be efficiently obtained by the integration of model-order-reduction (MOR) techniques and the MoM. For the indoor propagation problems, empirical models, for example, the Motley Keenan model [70] and the COST 231

Multi-Wall model, are popular techniques for the prediction of indoor wave propagation because of their simplicity and speed. The main drawback of these models is the lack of accuracy and reliability which can be achieved using the MoM with a suitable combination of iterative solvers and acceleration methods.

The remainder of this section is for a summary of the material in each of the remaining chapters.

Chapter 2 begins with a review of Maxwell equations to derive integral equations (IEs) comprising of the electric field integral equation (EFIE), the magnetic field integral equation (MFIE) and the combined field integral equation (CFIE) for 2D and 3D electromagnetic problems. These integral equations are extensively used for the analysis of EM problems throughout this dissertation. The application of the MoM to discretise the integral equations is also discussed in this chapter.

Chapter 3 focuses on iterative approaches for the solution of the MoM. The Krylov solvers including the CG, the BiCGSTAB and the GMRES are briefly reviewed. The stationary class of iterative solvers is carefully discussed. The popular stationary solvers such as the Jacobi, the Gauss-Seidel and the successive-over-relaxation method are first mentioned before the introduction of the FBM, the BBFB and the overlapping domain decomposition method (O-DDM) which are the centre of one contribution of this work. The application of preconditioning techniques to iterative solvers is briefly presented.

Chapter 4 is dedicated to the flexible combination of the MLFMA and the BBFB for 3D perfectly conducting scattering problems. The modified MLFMA is proposed to efficiently perform partial MVPs required often within each iteration of the BBFB. The efficiency and the complexity of the modified MLFMA are analysed. Some numerical examples are presented to demonstrate the accuracy and the efficiency of the proposed algorithm.

Chapter 5 extends the improvement step at the end of each iteration of the FBM or the BBFB. Instead of the improvement of the approximate solution using a single correction vector, the extension of the improvement step exploits the information of multiple correction vectors to further correct the approximate solution. The application of the extended improvement step to the computation of scattering from one and two dimensional random rough surfaces is demonstrated through several numerical results.

Chapter 6 concentrates on the application of the volume integral equation and the surface integral equation for the solution of the 2D indoor wave propagation. The FFT and the FAFFA are the accelerators for the discretised volume and surface integral equations, respectively. The reduced-operator [71] and the block diagonal preconditioner are applied to enhance the convergence rate of the iterative solvers. Some numerical results are shown to compare the performance of the approaches.

The use of the wideband technique asymptotic waveform evaluation (AWE) [72, 73, 74] for the analysis of 3D inhomogeneous scatterers over a wide range of frequency is the focus of chapter 7. The GMRES-FFT is applied to iteratively solve for AWE moments which is later used for the generation of discrete frequency responses. A numerical example for scattering from a homogeneous dielectric sphere with frequency-dependent electrical parameters is presented to validate the accuracy of the proposed method.

The summary of this thesis and possible future work are discussed in the final chapter 8.

## 1.1 Contribution

This work comprises the study of efficient numerical methods using iterative solvers and appropriate acceleration techniques for the analysis of 2D and 3D electromagnetic problems. The main contributions of the dissertation described in chapter 4, 5, 6 and 7 are summarised as follows:

- The proposal of the modified MLFMA applicable to the BBFB for the solution of 3D perfectly conducting scatterers to speed up the partial MVPs performed constantly within each iteration.
- The proposal of the extended improvement step for the stationary iterative methods, the FBM and the BFBM methods, leading to a better approximate solution at the end of each iteration.
- The application and the comparison of the FFT and the FAFFA as accelerators for the volumetric and the surface integral equations in the 2D indoor wave propagation, respectively.
- The application of the AWE allowing a fast analysis of 3D inhomogeneous scattering problems over a wide range of frequencies. Each moment of the AWE is efficiently computed using the GMRES-FFT iterative method.

The main contributions can be classified into three groups including the reduction of the cost of each iteration, the reduction of the number of iterations and wideband as shown in Figure 1.1.

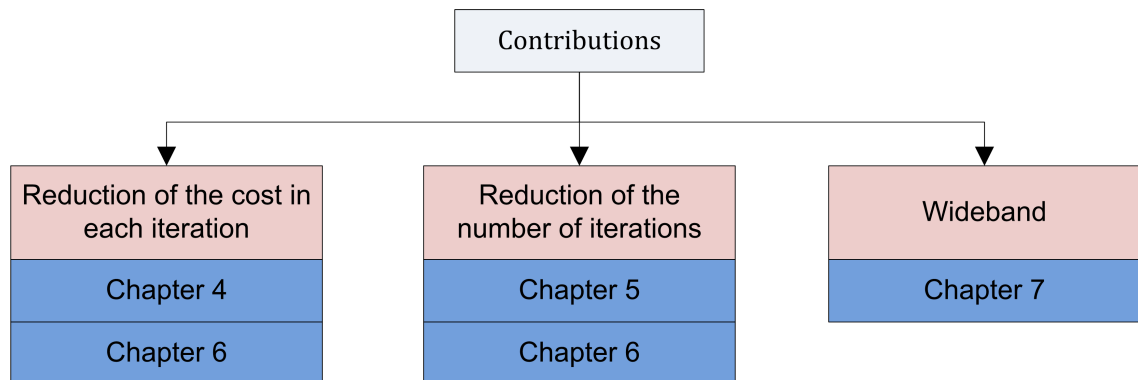


**Figure 1.1:** Classification of the main contributions.

## 1.2 Notation

Matrices, vectors and scalars are denoted by bold capital, bold lower-case and italic lower-case letters, respectively. The transpose and the conjugate transpose of a matrix  $\mathbf{A}$  is denoted by  $\mathbf{A}^T$  and  $\mathbf{A}^H$ , respectively.  $\|\cdot\|_2$  denotes the Euclidean norm.

## 2 Method of moments for numerical solution of Maxwell equations

This chapter introduces the fundamental electromagnetic theory required for an understanding of the following chapters. We start with a review of the differential form and the time-harmonic form of Maxwell equations and then derive the auxiliary vector potentials which aid the solution of electromagnetic scattering problems, described in Section 2.3. Section 2.4 and Section 2.5 introduce equivalence principles which are used to derive the volume and surface integral equations, which are extensively used in the following chapters. Section 2.6 reviews the method of moments (MoM) as a numerical solution for Maxwell equations.

### 2.1 Differential form of Maxwell equations

The differential form of Maxwell equations describes the relationship between the charge densities, current densities and field vectors for *any given space-time point*. For the differential form to be valid, the field vectors are assumed to be *single-valued, continuous* functions of space and time, except for being at the interface between different media. The discontinuity of the field vectors results in sudden changes in current and charge densities at the interfaces. The discontinuity at such interfaces is expressed by *the boundary conditions* which are also derived from Maxwell equations. Therefore, Maxwell equations can completely characterise the field vectors at any given space-time point. Maxwell equations in differential form are given by

$$\nabla \times \mathcal{H}(\mathbf{r}, t) = \mathcal{J}(\mathbf{r}, t) + \frac{\partial \mathcal{D}(\mathbf{r}, t)}{\partial t} \quad (2.1)$$

$$\nabla \times \mathcal{E}(\mathbf{r}, t) = -\mathcal{M}(\mathbf{r}, t) - \frac{\partial \mathcal{B}(\mathbf{r}, t)}{\partial t} \quad (2.2)$$

$$\nabla \cdot \mathcal{B}(\mathbf{r}, t) = \varrho_m(\mathbf{r}, t) \quad (2.3)$$

$$\nabla \cdot \mathcal{D}(\mathbf{r}, t) = \varrho_e(\mathbf{r}, t). \quad (2.4)$$

The definitions of the field quantities are

$\mathcal{E}$  is the electric field intensity (volt/meter)

$\mathcal{H}$  is the magnetic field intensity (ampere/meter)

$\mathcal{D}$  is the electric flux density (coulomb/square meter)

$\mathcal{B}$  is the magnetic flux density (weber/square meter)

$\mathcal{J}$  is the source electric current density (ampere/square meter)

$\mathcal{M}$  is the source magnetic current density (volt/square meter)

$\varrho_m$  is the magnetic charge density (weber/cubic meter)

$\varrho_e$  is the electric charge density (coulomb/cubic meter).

Equation 2.1 is an extension of Ampère's law often called the Maxwell-Ampère equation. The equation states that the generation of a magnetic field can be caused by an electric current or by time-varying electric fields. The Maxwell-Faraday equation derived from Faraday's law is described by Equation 2.2, stating that a magnetic current and time-varying magnetic fields generate a spatially-varying, non conservative electric field with rotation. Although physically non-existent, source magnetic current density is introduced due to the symmetry of Maxwell equations. The last two equations are the consequences of the Gauss flux theorem usually called the law of the conservation of charge. Equation 2.3 relates the behaviour of magnetic flux density to magnetic charge density, which is naturally unphysical but aids the mathematical treatment of electromagnetic scattering problems and allows for the symmetric form of Maxwell equations. Equation 2.4 defines the variation of electric flux density due to electric charge density.

## 2.2 Time-harmonic form of Maxwell equations

In many electromagnetic scattering problems, it is practical to express the time-harmonic fields in the complex form. These are presented by the relation

$$\mathcal{A}(\mathbf{r}, t) = \Re \left( \mathbf{A}(\mathbf{r}) e^{j\omega t} \right), \quad (2.5)$$

where  $\omega = 2\pi f$  is an angular frequency of interest.  $\mathbf{A}$  is a complex-valued vector which depends only on position. The application of Equation 2.5 to the instantaneous field quantities  $\mathcal{E}$ ,  $\mathcal{H}$ ,  $\mathcal{D}$ ,  $\mathcal{B}$ ,  $\mathcal{J}$ ,  $\mathcal{M}$ ,  $\varrho_m$  and  $\varrho_e$  results in the corresponding complex form of  $\mathbf{E}$ ,  $\mathbf{H}$ ,  $\mathbf{D}$ ,  $\mathbf{J}$ ,  $\mathbf{M}$ ,  $\rho_m$  and  $\rho_e$ . Consequently, the differential form of Maxwell equations 2.1-2.4 can be written in the time-harmonic form as

$$\nabla \times \mathbf{H}(\mathbf{r}) = \mathbf{J}(\mathbf{r}) + j\omega \mathbf{D}(\mathbf{r}) \quad (2.6)$$

$$\nabla \times \mathbf{E}(\mathbf{r}) = -\mathbf{M}(\mathbf{r}) - j\omega \mathbf{B}(\mathbf{r}) \quad (2.7)$$

$$\nabla \cdot \mathbf{B}(\mathbf{r}) = \rho_m(\mathbf{r}) \quad (2.8)$$

$$\nabla \cdot \mathbf{D}(\mathbf{r}) = \rho_e(\mathbf{r}). \quad (2.9)$$

At this point, we note that  $\mathbf{B}$  can be related to  $\mathbf{H}$  and  $\mathbf{D}$  to  $\mathbf{E}$  as

$$\mathbf{B}(\mathbf{r}) = \mu_0 \mu_r(\mathbf{r}) \mathbf{H}(\mathbf{r}) \quad , \quad \mathbf{D}(\mathbf{r}) = \epsilon_0 \epsilon_r(\mathbf{r}) \mathbf{E}(\mathbf{r}) \quad (2.10)$$

in the case of linear and isotropic media.  $\epsilon_r$  and  $\mu_r$  denote the relative permittivity and the relative permeability which characterise the electrical properties of a material, respectively. For inhomogeneous problems, these quantities are functions of position. The permittivity and permeability in free-space are represented by  $\epsilon_0$  and  $\mu_0$ , respectively. Their values are given by

$$\epsilon_0 = 8.854 \times 10^{-12} \text{ (farad/meter)} \quad \mu_0 = 4\pi \times 10^{-7} \text{ (henry/meter)}. \quad (2.11)$$

The permittivity and permeability of a specific medium are expressed in relation with free-space by

$$\epsilon(\mathbf{r}) = \epsilon_0 \epsilon_r(\mathbf{r}) \quad \mu(\mathbf{r}) = \mu_0 \mu_r(\mathbf{r}). \quad (2.12)$$

## 2.3 Auxiliary vector potentials

One approach for the solution of Maxwell equations is to take advantage of the auxiliary vector potentials including the magnetic vector potential  $\mathbf{A}$  and the electric vector potential  $\mathbf{F}$  [20, 75]. The illustration of the approach for the computation of radiated fields is shown in Figure 2.1. Although these quantities are physically non-existent, their presence aids the simplification of the solution.

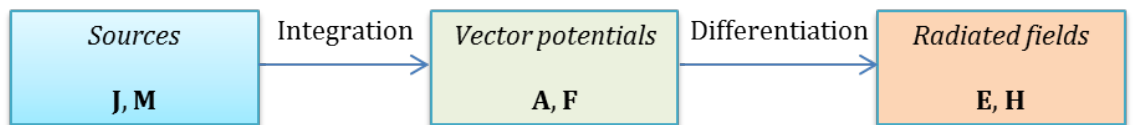


**Figure 2.1:** Block diagram for the computation of radiated fields using the vector potentials.

In the following equations, the  $\mathbf{r}$  dependence is sometimes dropped for simplicity. Taking the curl of Equations 2.6 and 2.7 and applying the vector identity  $\nabla \times \nabla \times \mathbf{A} = \nabla \nabla \cdot \mathbf{A} - \nabla^2 \mathbf{A}$  leads to

$$\nabla^2 \mathbf{E} - j\omega \nabla \times \mathbf{B} = \nabla \times \mathbf{M} + \nabla \nabla \cdot \mathbf{E} \quad (2.13)$$

$$\nabla^2 \mathbf{H} + j\omega \nabla \times \mathbf{D} = -\nabla \times \mathbf{J} + \nabla \nabla \cdot \mathbf{H}. \quad (2.14)$$



Substituting Equations 2.6 and 2.9 into Equation 2.13, and Equations 2.7 and 2.8 into Equation 2.14 results in the Helmholtz equations for a homogeneous medium

$$\nabla^2 \mathbf{E} + k^2 \mathbf{E} = \nabla \times \mathbf{M} + j\omega\mu\mathbf{J} + \frac{1}{\epsilon}\nabla\rho_e \quad (2.15)$$

$$\nabla^2 \mathbf{H} + k^2 \mathbf{H} = -\nabla \times \mathbf{J} + j\omega\epsilon\mathbf{M} + \frac{1}{\mu}\nabla\rho_m \quad (2.16)$$

where  $k = \omega\sqrt{\mu\epsilon}$  is the wavenumber of the homogeneous medium.

### 2.3.1 Magnetic vector potential

In homogeneous space in the absence of source magnetic current and magnetic charge, Equation 2.7 and 2.8 can be rewritten

$$\nabla \times \mathbf{E} = -j\omega\mu\mathbf{H}, \quad (2.17)$$

$$\nabla \cdot \mathbf{B} = 0. \quad (2.18)$$

Applying the vector identity  $\nabla \cdot (\nabla \times \mathbf{A}) = 0$  to Equation 2.18 leads to

$$\boxed{\mathbf{B}_A = \mu\mathbf{H}_A = \nabla \times \mathbf{A}} \quad (2.19)$$

where  $\mathbf{A}$  is a non-unique vector called the magnetic vector potential. Subscript A determines the fields due to the vector potential  $\mathbf{A}$ . The substitution of Equation 2.19 into 2.17 results in

$$\nabla \times (\mathbf{E}_A + j\omega\mathbf{A}) = 0. \quad (2.20)$$

We define an arbitrary electric scalar potential  $\phi_e$  which is a function of position and satisfies the following

$$\nabla \times (-\nabla\phi_e) = 0. \quad (2.21)$$

The combination of Equation 2.20 and 2.21 allows the definition of  $\mathbf{E}_A$  in terms of the electric scalar and the magnetic vector potential

$$\mathbf{E}_A = -\nabla\phi_e - j\omega\mathbf{A}. \quad (2.22)$$

Applying the vector identity  $\nabla \times \nabla \times \mathbf{A} = \nabla(\nabla \cdot \mathbf{A}) - \nabla^2 \mathbf{A}$  to the curl of Equation 2.19 leads to

$$\mu\nabla \times \mathbf{H}_A = \nabla(\nabla \cdot \mathbf{A}) - \nabla^2 \mathbf{A} \quad (2.23)$$

for a homogeneous medium. Applying the Maxwell-Ampère equation

$$\nabla \times \mathbf{H}_A = \mathbf{J} + j\omega\epsilon\mathbf{E}_A \quad (2.24)$$

to Equation 2.23 and then substituting Equation 2.22 into the resultant equation leads to

$$\nabla^2 \mathbf{A} + k^2 \mathbf{A} = -\mu\mathbf{J} + \nabla (\nabla \cdot \mathbf{A} + j\omega\mu\epsilon\phi_e). \quad (2.25)$$

To simplify Equation 2.25, the definition of the divergence of  $\mathbf{A}$  is deliberately determined using the Lorenz gauge

$$\nabla \cdot \mathbf{A} = -j\omega\mu\epsilon\phi_e. \quad (2.26)$$

Equation 2.26 allows the representation of  $\mathbf{E}_A$  in terms of a single quantity  $\mathbf{A}$

$$\boxed{\mathbf{E}_A = -j\omega\mathbf{A} - j\frac{1}{\omega\mu\epsilon}\nabla(\nabla \cdot \mathbf{A})} \quad (2.27)$$

and the simplification of Equation 2.25

$$\boxed{\nabla^2 \mathbf{A} + k^2 \mathbf{A} = -\mu\mathbf{J}}. \quad (2.28)$$

Therefore, once the magnetic vector potential  $\mathbf{A}$  is known, the corresponding electric field  $\mathbf{E}_A$  and magnetic field  $\mathbf{H}_A$  can be computed from Equation 2.27 and 2.19, respectively.

### 2.3.2 Electric vector potential

The absence of source electric current and electric charge allows the rewriting of Equation 2.6 and 2.9 for a homogeneous medium

$$\nabla \times \mathbf{H} = j\omega\epsilon\mathbf{E} \quad (2.29)$$

$$\nabla \cdot \mathbf{D} = 0. \quad (2.30)$$

Applying the vector identity  $\nabla \cdot (-\nabla \times \mathbf{F}) = 0$  to Equation 2.30 results in

$$\boxed{\mathbf{D}_F = \epsilon\mathbf{E}_F = -\nabla \times \mathbf{F}} \quad (2.31)$$

where the magnetic vector potential  $\mathbf{F}$  is non-unique. Again, we refer to associated fields by using a subscript F. Substituting Equation 2.31 into 2.29 leads to

$$\nabla \times (\mathbf{H}_F + j\omega\mathbf{F}) = 0. \quad (2.32)$$

The definition of an arbitrary magnetic scalar potential  $\phi_m$  is similar to that of the electric scalar potential in Equation 2.21, allowing the representation of  $\mathbf{H}_F$  in terms of the magnetic scalar and the electric vector potential

$$\mathbf{H}_F = -\nabla\phi_m - j\omega\mathbf{F}. \quad (2.33)$$

The application of the vector identity  $\nabla \times \nabla \times \mathbf{F} = \nabla(\nabla \cdot \mathbf{F}) - \nabla^2 \mathbf{F}$  to the curl of Equation 2.31 produces

$$\epsilon\nabla \times \mathbf{E}_F = -\left(\nabla(\nabla \cdot \mathbf{F}) - \nabla^2 \mathbf{F}\right) \quad (2.34)$$

for a homogeneous medium. Equating the Maxwell-Faraday formulation

$$\nabla \times \mathbf{E}_F = -\mathbf{M} - j\omega\mu\mathbf{H}_F \quad (2.35)$$

to Equation 2.34 and then substituting Equation 2.33 to the resultant equation leads to

$$\nabla^2 \mathbf{F} + k^2 \mathbf{F} = -\epsilon\mathbf{M} + \nabla(\nabla \cdot \mathbf{F} + j\omega\mu\epsilon\phi_m). \quad (2.36)$$

Equation 2.36 is further simplified by defining the divergence of  $\mathbf{F}$

$$\nabla \cdot \mathbf{F} = -j\omega\mu\epsilon\phi_m. \quad (2.37)$$

Equation 2.37 allows the representation of  $\mathbf{H}_F$  in terms of a single quantity  $\mathbf{F}$

$$\boxed{\mathbf{H}_F = -j\omega\mathbf{F} - j\frac{1}{\omega\mu\epsilon}\nabla(\nabla \cdot \mathbf{F})} \quad (2.38)$$

and the simplification of Equation 2.36

$$\boxed{\nabla^2 \mathbf{F} + k^2 \mathbf{F} = -\epsilon\mathbf{M}}. \quad (2.39)$$

Therefore, once the electric vector potential  $\mathbf{F}$  is known, the corresponding electric field  $\mathbf{E}_F$  and magnetic field  $\mathbf{H}_F$  can be computed from Equation 2.31 and 2.38, respectively. As the consequence, the total fields  $\mathbf{E}$  and  $\mathbf{H}$  in a homogeneous space with the presence of sources can be obtained by means of superposition of individual components

$$\mathbf{E} = \mathbf{E}_A + \mathbf{E}_F \quad , \quad \mathbf{H} = \mathbf{H}_A + \mathbf{H}_F \quad . \quad (2.40)$$

Therefore, the radiated fields are expressed in terms of the vector potentials as follows

$$\boxed{\mathbf{E} = -j\omega\mathbf{A} - j\frac{1}{\omega\mu\epsilon}\nabla(\nabla \cdot \mathbf{A}) - \frac{1}{\epsilon}\nabla \times \mathbf{F}} \quad (2.41)$$

$$\mathbf{H} = -j\omega\mathbf{F} - j\frac{1}{\omega\mu\epsilon}\nabla(\nabla\cdot\mathbf{F}) + \frac{1}{\mu}\nabla\times\mathbf{A}. \quad (2.42)$$

Relations between fields and vector potentials in Equations 2.41-2.42 are used to derive the volume electric field integral equation in the following section.

## 2.4 Volume electric field integral equation

The volumetric approach can be applied for the solution of inhomogeneous problems where the constitutive parameters  $\epsilon$  and  $\mu$  are functions of position. The approach is to replace the inhomogeneity by equivalent induced currents and charges which are assumed to generate the same fields as the original problem. The volumetric equivalence principle is introduced in Section 2.4.1 and then the derivation of integral equations for volumetric problems is presented in Section 2.4.2.

### 2.4.1 Volume equivalence principle

We assume that an inhomogeneous scatterer is embedded in free-space as in Figure 2.2a. The volume equivalence principle simplifies the original problem by replacing the inhomogeneous scatterer with equivalent sources radiating in free-space as in Figure 2.2b. To derive the volume equivalence principle, we first consider that the source electric current  $\mathbf{J}^i$  and the source magnetic current  $\mathbf{M}^i$  are placed in infinite free-space and generate the incident electric and magnetic fields  $\mathbf{E}^i$  and  $\mathbf{H}^i$ , which satisfy Maxwell equations

$$\nabla\times\mathbf{E}^i = -\mathbf{M}^i - j\omega\mu_0\mathbf{H}^i \quad (2.43)$$

$$\nabla\times\mathbf{H}^i = \mathbf{J}^i + j\omega\epsilon_0\mathbf{E}^i. \quad (2.44)$$

If instead the sources radiate inside a different medium characterised by  $\epsilon$  and  $\mu$ , they produce the fields  $\mathbf{E}$  and  $\mathbf{H}$  which also satisfy Maxwell equations

$$\nabla\times\mathbf{E} = -\mathbf{M}^i - j\omega\mu\mathbf{H} \quad (2.45)$$

$$\nabla\times\mathbf{H} = \mathbf{J}^i + j\omega\epsilon\mathbf{E}. \quad (2.46)$$

The difference between the two pairs of fields  $(\mathbf{E}^i, \mathbf{H}^i)$  and  $(\mathbf{E}, \mathbf{H})$  is due to the difference between the constitutive parameters of the free-space and those of the medium. The subtraction of Equations 2.43-2.44 from Equations 2.45-2.46 results in the following equations

$$\nabla\times\mathbf{E}^s = -j\omega(\mu\mathbf{H} - \mu_0\mathbf{H}^i) \quad (2.47)$$

$$\nabla \times \mathbf{H}^s = j\omega (\epsilon \mathbf{E} - \epsilon_0 \mathbf{E}^i) \quad (2.48)$$

where  $\mathbf{E}^s$  and  $\mathbf{H}^s$  denote the scattered electric and magnetic fields caused by the medium, respectively. The scattered fields are defined as

$$\mathbf{E}^s = \mathbf{E} - \mathbf{E}^i \quad (2.49)$$

$$\mathbf{H}^s = \mathbf{H} - \mathbf{H}^i. \quad (2.50)$$

The manipulation of the right hand side of Equations 2.47-2.48 by the addition and subtraction of the terms  $j\omega\mu_0\mathbf{H}$  and  $j\omega\epsilon_0\mathbf{E}$ , respectively yields

$$\nabla \times \mathbf{E}^s = -\mathbf{M}_{\text{eq}} - j\omega\mu_0\mathbf{H}^s \quad (2.51)$$

$$\nabla \times \mathbf{H}^s = \mathbf{J}_{\text{eq}} + j\omega\epsilon_0\mathbf{E}^s \quad (2.52)$$

where the equivalent induced sources responsible for the scattered fields in Figure 2.2b are defined as

$$\mathbf{J}_{\text{eq}} = j\omega (\epsilon - \epsilon_0) \mathbf{E} \quad (2.53)$$

$$\mathbf{M}_{\text{eq}} = j\omega (\mu - \mu_0) \mathbf{H}. \quad (2.54)$$

Therefore, the fields produced by equivalent volumetric electric current  $\mathbf{J}_{\text{eq}}$  and magnetic current  $\mathbf{M}_{\text{eq}}$  radiating in free-space are the same as those produced by the scatterer.

## 2.4.2 Volume integral equations

The application of the same procedure presented in Section 2.3 to Equations 2.51-2.52 allows the representation of the scattered fields in terms of the vector potentials as in Equations 2.41-2.42

$$\mathbf{E}^s = -j\omega\mathbf{A} - j\frac{1}{\omega\mu_b\epsilon_b}\nabla(\nabla \cdot \mathbf{A}) - \frac{1}{\epsilon_b}\nabla \times \mathbf{F} \quad (2.55)$$

$$\mathbf{H}^s = -j\omega\mathbf{F} - j\frac{1}{\omega\mu_b\epsilon_b}\nabla(\nabla \cdot \mathbf{F}) + \frac{1}{\mu_b}\nabla \times \mathbf{A} \quad (2.56)$$

where the vector potentials satisfy

$$\nabla^2\mathbf{A} + k_b^2\mathbf{A} = -\mu_b\mathbf{J}_{\text{eq}} \quad (2.57)$$

$$\nabla^2 \mathbf{F} + k_b^2 \mathbf{F} = -\epsilon_b \mathbf{M}_{\text{eq}} \quad (2.58)$$

where  $\epsilon_b$ ,  $\mu_b$  and  $k_b$  denote the permittivity, permeability and wavenumber of the homogeneous background medium, respectively. For example, the background medium in Figure 2.2 is free-space. The solution of the Helmholtz equations 2.57-2.58 can be expressed as a convolution between the right hand side and the Green's function

$$\mathbf{A} = (\mu_b \mathbf{J}_{\text{eq}}) * \mathbf{G} \quad (2.59)$$

$$\mathbf{F} = (\epsilon_b \mathbf{M}_{\text{eq}}) * \mathbf{G} \quad (2.60)$$

where  $\mathbf{G}$  is the Green's function which is defined for three-dimensions and two-dimensions in Equations 2.61-2.62, respectively.

$$\mathbf{G}(\mathbf{r}) = \frac{e^{-jk_b|\mathbf{r}|}}{4\pi|\mathbf{r}|} \quad (2.61)$$

$$\mathbf{G}(\mathbf{r}) = \frac{1}{4j} H_0^{(2)}(k_b|\mathbf{r}|) \quad (2.62)$$

Equations 2.59-2.60 for three dimensional problems can be written in a form of an integral

$$\mathbf{A}(\mathbf{r}) = \mu_b \iiint_v \mathbf{J}_{\text{eq}}(\mathbf{r}') \frac{e^{-jk_b|\mathbf{r}-\mathbf{r}'|}}{4\pi|\mathbf{r}-\mathbf{r}'|} dv' \quad (2.63)$$

$$\mathbf{F}(\mathbf{r}) = \epsilon_b \iiint_v \mathbf{M}_{\text{eq}}(\mathbf{r}') \frac{e^{-jk_b|\mathbf{r}-\mathbf{r}'|}}{4\pi|\mathbf{r}-\mathbf{r}'|} dv'. \quad (2.64)$$

Substituting Equations 2.63-2.64, 2.26 and 2.37 into Equations 2.55-2.56 yields

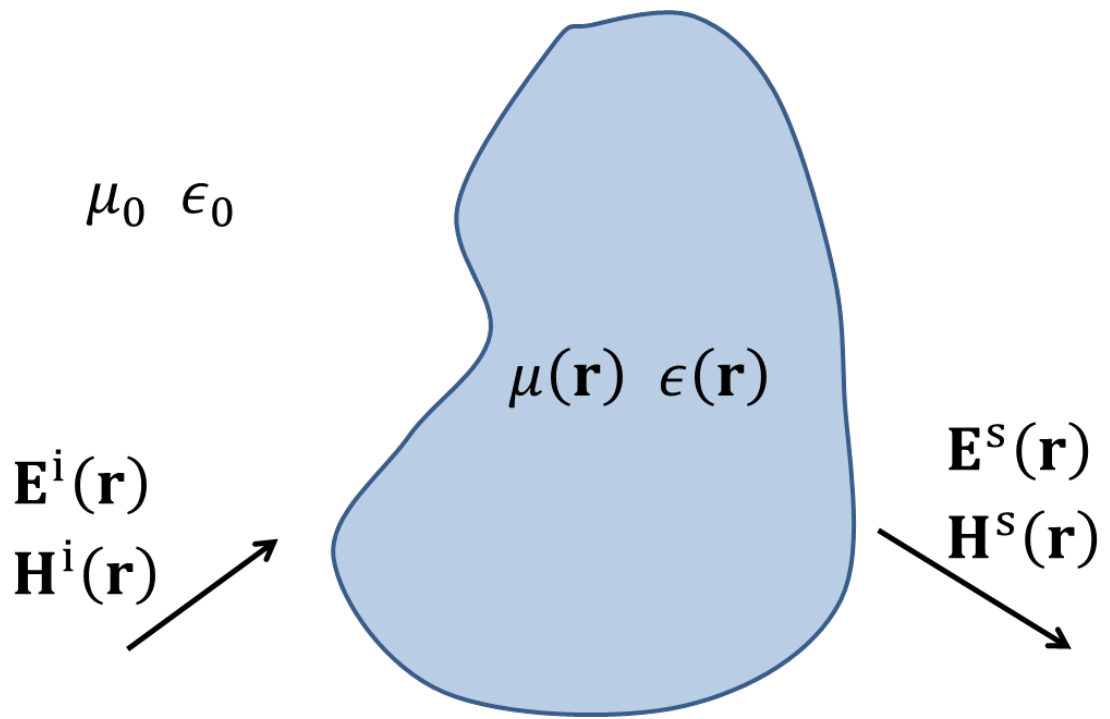
$$\mathbf{E}^s(\mathbf{r}) = -j\omega\mu_b \iiint_v \left( \mathbf{J}_{\text{eq}}(\mathbf{r}') + \frac{1}{k_b^2} \nabla' \nabla' \cdot \mathbf{J}_{\text{eq}}(\mathbf{r}') \right) \frac{e^{-jk_b|\mathbf{r}-\mathbf{r}'|}}{4\pi|\mathbf{r}-\mathbf{r}'|} dv' - \quad (2.65)$$

$$\nabla \times \iiint_v \mathbf{M}_{\text{eq}}(\mathbf{r}') \frac{e^{-jk_b|\mathbf{r}-\mathbf{r}'|}}{4\pi|\mathbf{r}-\mathbf{r}'|} dv'$$

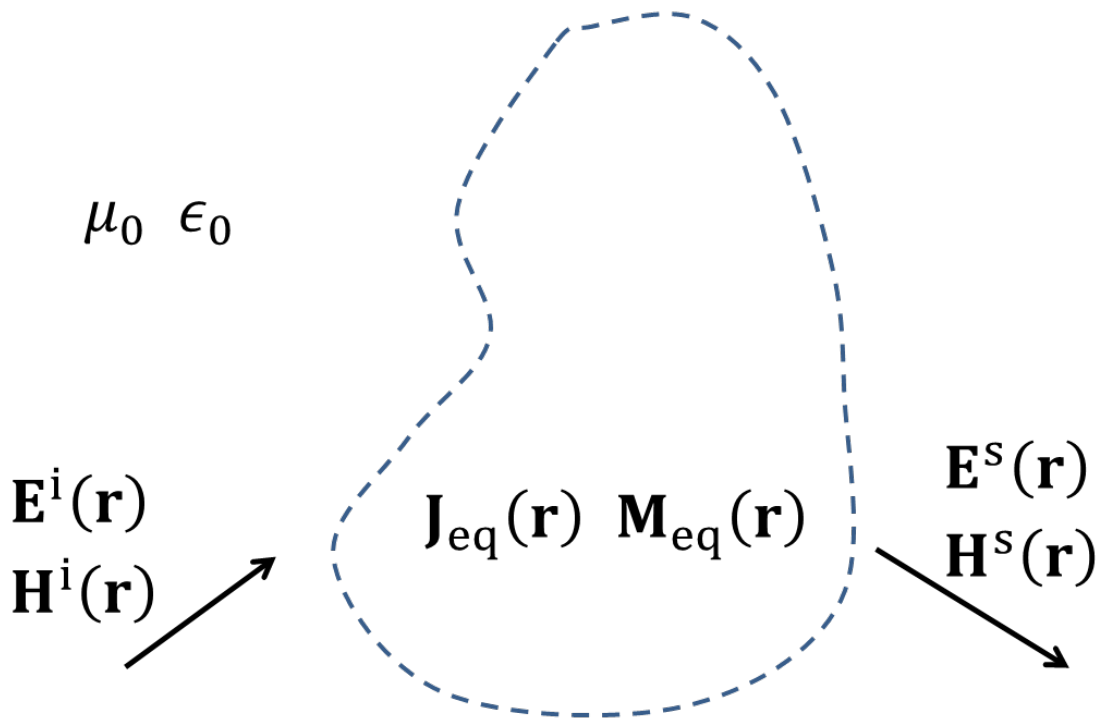
$$\mathbf{H}^s(\mathbf{r}) = -j\omega\epsilon_b \iiint_v \left( \mathbf{M}_{\text{eq}}(\mathbf{r}') + \frac{1}{k_b^2} \nabla' \nabla' \cdot \mathbf{M}_{\text{eq}}(\mathbf{r}') \right) \frac{e^{-jk_b|\mathbf{r}-\mathbf{r}'|}}{4\pi|\mathbf{r}-\mathbf{r}'|} dv' + \quad (2.66)$$

$$\nabla \times \iiint_v \mathbf{J}_{\text{eq}}(\mathbf{r}') \frac{e^{-jk_b|\mathbf{r}-\mathbf{r}'|}}{4\pi|\mathbf{r}-\mathbf{r}'|} dv'$$

Substituting Equations 2.65-2.66 into Equations 2.49-2.50 leads to the volume electric field integral equation (VEFIE) and the volume magnetic field integral equation (VMFIE) in Equations 2.67-2.68, respectively.



a. The inhomogeneous problem



b. The volumetric equivalence problem

Figure 2.2: Volumetric equivalence problem.

$$\begin{aligned} \mathbf{E}^i(\mathbf{r}) &= \frac{\mathbf{J}_{\text{eq}}(\mathbf{r})}{j\omega(\epsilon - \epsilon_b)} + j\omega\mu_b \iiint_v \left( \mathbf{J}_{\text{eq}}(\mathbf{r}') + \frac{1}{k_b^2} \nabla' \nabla' \cdot \mathbf{J}_{\text{eq}}(\mathbf{r}') \right) \frac{e^{-jk_b|\mathbf{r}-\mathbf{r}'|}}{4\pi|\mathbf{r}-\mathbf{r}'|} dv' + \\ &\quad \nabla \times \iiint_v \mathbf{M}_{\text{eq}}(\mathbf{r}') \frac{e^{-jk_b|\mathbf{r}-\mathbf{r}'|}}{4\pi|\mathbf{r}-\mathbf{r}'|} dv' \end{aligned} \quad (2.67)$$

$$\begin{aligned} \mathbf{H}^i(\mathbf{r}) &= \frac{\mathbf{M}_{\text{eq}}(\mathbf{r})}{j\omega(\mu - \mu_b)} + j\omega\epsilon_b \iiint_v \left( \mathbf{M}_{\text{eq}}(\mathbf{r}') + \frac{1}{k_b^2} \nabla' \nabla' \cdot \mathbf{M}_{\text{eq}}(\mathbf{r}') \right) \frac{e^{-jk_b|\mathbf{r}-\mathbf{r}'|}}{4\pi|\mathbf{r}-\mathbf{r}'|} dv' - \\ &\quad \nabla \times \iiint_v \mathbf{J}_{\text{eq}}(\mathbf{r}') \frac{e^{-jk_b|\mathbf{r}-\mathbf{r}'|}}{4\pi|\mathbf{r}-\mathbf{r}'|} dv' \end{aligned} \quad (2.68)$$

The VEFIE and the VMFIE can be applied for the analysis of scattering from inhomogeneous bodies. However, for the solution of a homogeneous problem where the constitutive parameters  $\epsilon$  and  $\mu$  are constant, the use of surface integral equations is more favourable due to the smaller size of the equivalent problem.

## 2.5 Surface integral equations

In contrast to the volume integral equations where the entire volumetric scatterer is replaced by equivalent volumetric sources, the surface integral equations exploit the boundary conditions to substitute a homogeneous original problem by equivalent surface sources located on the interface between the media. The boundary conditions are briefly reviewed in Section 2.5.1 before the introduction of the surface equivalence principle in Section 2.5.2. The surface integral equations are derived in Section 2.5.3.

### 2.5.1 Boundary conditions

The differential form of Maxwell equations is only applicable to regions where the constitutive parameters are unchanged or vary continuously. However, this form is invalid at the boundary of media where the constitutive parameters change abruptly. For these situations, the boundary conditions derived from the integral form of Maxwell equations are applied to investigate the behaviour of the electromagnetic fields across the interface. The boundary conditions define the continuity requirements of the tangential and the normal components of fields at the interface between two media. We examine the interface of two media with constitutive parameters  $(\epsilon_1, \mu_1)$  and  $(\epsilon_2, \mu_2)$  where  $(\mathbf{E}_1, \mathbf{H}_1, \mathbf{D}_1, \mathbf{B}_1)$  and  $(\mathbf{E}_2, \mathbf{H}_2, \mathbf{D}_2, \mathbf{B}_2)$  are their corresponding fields in each region as in Figure 2.3. The normal vector  $\hat{\mathbf{n}}$  to the interface points from region 1 to region 2. The boundary conditions for such an interface are expressed as

$$\hat{\mathbf{n}} \times (\mathbf{E}_2 - \mathbf{E}_1) = -\mathbf{M}_s \quad (2.69)$$



$$\hat{\mathbf{n}} \times (\mathbf{H}_2 - \mathbf{H}_1) = \mathbf{J}_s \quad (2.70)$$

$$\hat{\mathbf{n}} \cdot (\mathbf{D}_2 - \mathbf{D}_1) = \rho_{es} \quad (2.71)$$

$$\hat{\mathbf{n}} \cdot (\mathbf{B}_2 - \mathbf{B}_1) = \rho_{ms} \quad (2.72)$$

where  $\mathbf{M}_s$  and  $\mathbf{J}_s$  are the surface magnetic current density and the surface electric current density, respectively.  $\rho_{es}$  and  $\rho_{ms}$  are the electric and magnetic charge densities on the surface, respectively. Equations 2.69-2.70 imply that the tangential component of  $\mathbf{E}$  and  $\mathbf{H}$  is continuous across the interface without the presence of the surface currents. Equations 2.71-2.72 state that the differences between the normal components of  $\mathbf{D}$  and  $\mathbf{B}$  are equal to the surface electric and magnetic charges on the surface, respectively.

For the interface between a perfect conductor having an infinite electric conductivity  $\sigma$  and a dielectric medium in Figure 2.4, the boundary conditions become

$$\hat{\mathbf{n}} \times \mathbf{E} = 0 \quad (2.73)$$

$$\hat{\mathbf{n}} \times \mathbf{H} = \mathbf{J}_s \quad (2.74)$$

$$\hat{\mathbf{n}} \cdot \mathbf{D} = \rho_{es} \quad (2.75)$$

$$\hat{\mathbf{n}} \cdot \mathbf{B} = 0. \quad (2.76)$$

Details about derivation of the boundary conditions are presented in [75].

### 2.5.2 Surface equivalence principle

The fundamental idea of the *surface equivalence principle* is to replace the actual sources by a different set of fictitious sources which are considered to be equivalent due to their production of the same fields within a region as the original sources. These equivalent sources are located on an imaginary closed surface enclosing the actual sources. The radiated fields of the equivalent electric and magnetic current densities satisfying the boundary conditions on the imaginary surface are zero inside the surface and equal to the fields generated by the actual sources outside the surface.

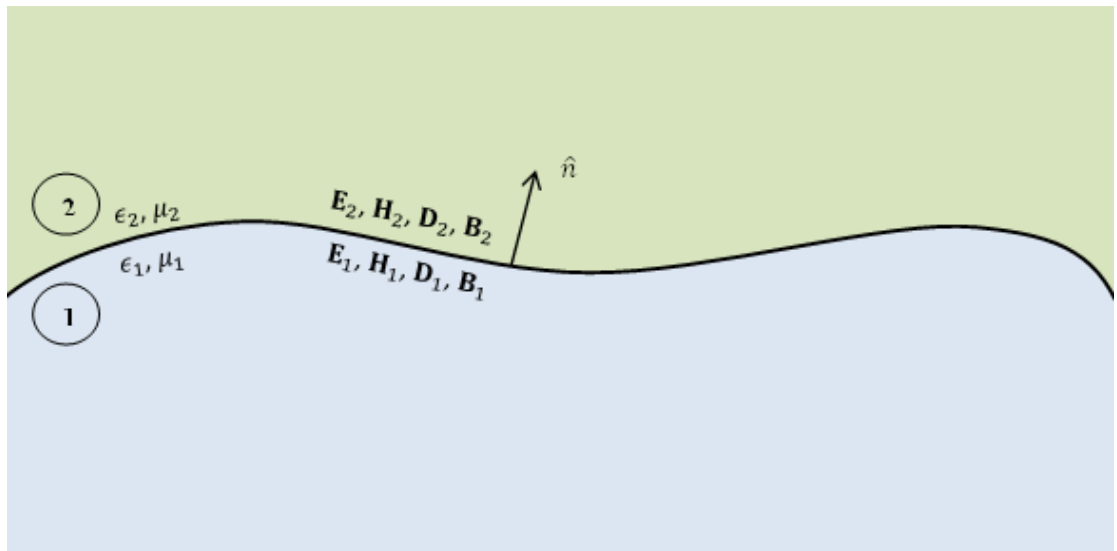


**Figure 2.3:** Geometry for boundary conditions at the interface between two homogeneous media.

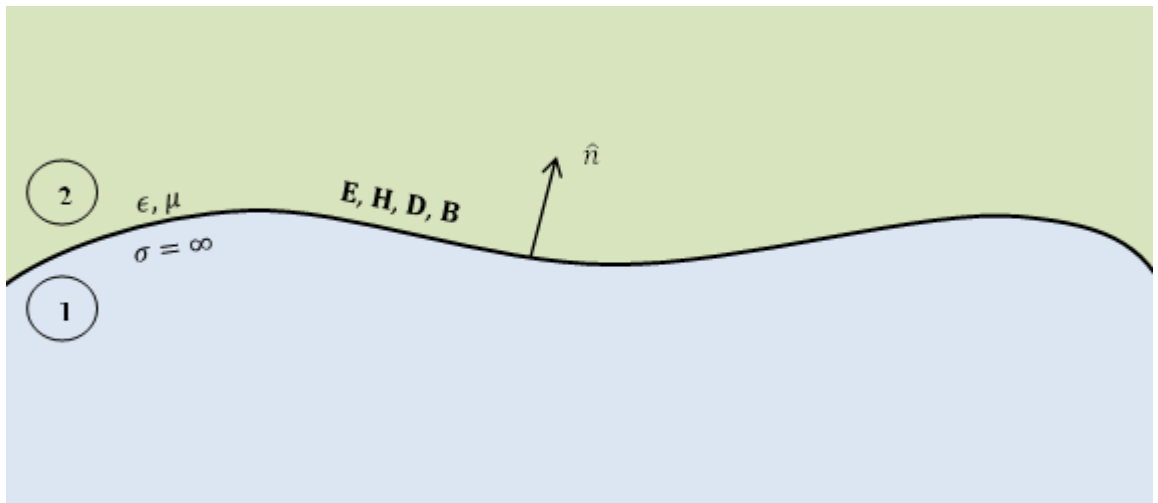


**Figure 2.4:** Geometry for boundary conditions at the interface between a perfect conductor and a dielectric medium.

The derivation of the surface equivalence theorem starts by considering an actual source which is electrically described by the electric and magnetic current densities  $\mathbf{J}_1$  and  $\mathbf{M}_1$ , radiating the fields  $\mathbf{E}_1$  and  $\mathbf{H}_1$  in a homogeneous region with constitutive parameters  $\epsilon_1$  and  $\mu_1$  as shown in Figure 2.5a. To produce a set of fictitiously equivalent sources, the entire homogeneous space is separated by a closed surface  $S$  presented as a dashed line in Figure 2.5a, leading to an introduction of a volume  $V_1$  within  $S$  and a volume  $V_2$  outside  $S$ . The original problem in Figure 2.5a is replaced by an equivalent problem shown in Figure 2.5b where the removal of the physical currents and the introduction of the equivalent currents  $\mathbf{J}_s$  and  $\mathbf{M}_s$  produce the fields  $(\mathbf{E}, \mathbf{H})$  inside  $V_1$  and the original fields  $(\mathbf{E}_1, \mathbf{H}_1)$  inside  $V_2$ . The equivalent surface currents radiating into the unbounded space  $V_2$  are required to fulfil the boundary conditions

$$\mathbf{J}_s = \hat{\mathbf{n}} \times (\mathbf{H}_1 - \mathbf{H}) \quad (2.77)$$

$$\mathbf{M}_s = -\hat{\mathbf{n}} \times (\mathbf{E}_1 - \mathbf{E}). \quad (2.78)$$

The surface currents in Equations 2.77-2.78 are considered to be equivalent to the original currents only for the external region  $V_2$  because they only generate the same fields  $(\mathbf{E}_1, \mathbf{H}_1)$  outside the closed surface  $S$ .

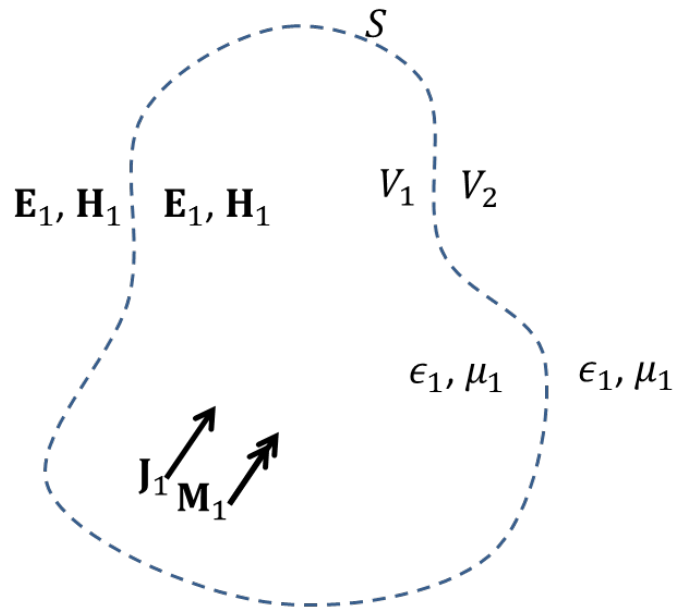
### 2.5.3 Surface integral equations

We examine a scattering problem where an electromagnetic source located in a homogeneous region 1 characterised by  $(\epsilon_1, \mu_1)$  illuminates a homogeneous scatterer 2 characterised by  $(\epsilon_2, \mu_2)$  in Figure 2.6a. The total fields in region 1 and 2 are denoted by  $(\mathbf{E}_1, \mathbf{H}_1)$  and  $(\mathbf{E}_2, \mathbf{H}_2)$ , respectively. The application of the surface equivalent theorem allows the replication of the original fields in both media using equivalent sources on the scatterer surface.

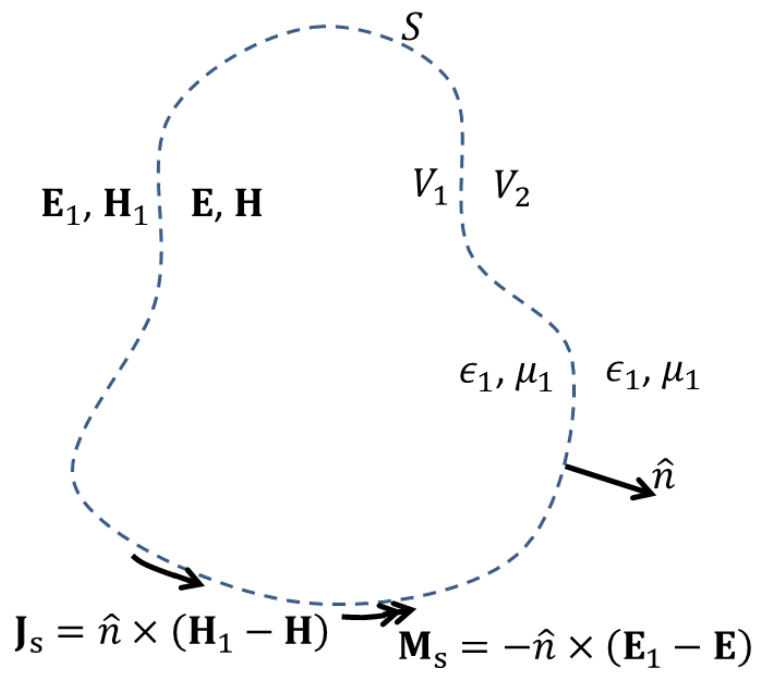
Applying the surface equivalent principle to the exterior problem introduces the equivalent currents  $(\mathbf{J}_{s1}, \mathbf{M}_{s1})$  as illustrated in Figure 2.6b. These surface currents replicate effects of the scatterer and are responsible for the scattered fields. The combination of the replicated fields  $(\mathbf{E}^s, \mathbf{H}^s)$  and the incident fields  $(\mathbf{E}^i, \mathbf{H}^i)$  produced by the electromagnetic source ensures that the original fields are produced in region 1. Because the fields inside the scatterer are not of interest for the exterior problem, we can assume they are zero. Thus, the boundary conditions for the exterior problem can be interpreted as

$$\mathbf{J}_{s1} = \hat{\mathbf{n}} \times \mathbf{H}_1 \quad (2.79)$$

$$\mathbf{M}_{s1} = (-\hat{\mathbf{n}}) \times \mathbf{E}_1 = \mathbf{E}_1 \times \hat{\mathbf{n}}. \quad (2.80)$$



a. The actual problem



b. The surface equivalence problem

**Figure 2.5:** Surface equivalence problem.

A similar procedure is applied for the interior region, resulting in an interior equivalent problem in Figure 2.6c. In the absence of the original source, the equivalent currents  $(\mathbf{J}_{s2}, \mathbf{M}_{s2})$  produce the same scattered fields  $(\mathbf{E}_2, \mathbf{H}_2)$  inside the scatterer. With the same normal vector  $\hat{\mathbf{n}}$  pointing from region 2 to 1 as in Figure 2.6b, the boundary conditions for the interior problem are stated as

$$\mathbf{J}_{s2} = (-\hat{\mathbf{n}}) \times \mathbf{H}_2 \quad (2.81)$$

$$\mathbf{M}_{s2} = \hat{\mathbf{n}} \times \mathbf{E}_2. \quad (2.82)$$

Applying the boundary conditions for the tangential components of  $\mathbf{E}$  and  $\mathbf{H}$  on the dielectric interface gives the relationship between two pairs of the equivalent currents

$$\mathbf{J}_{s1} = -\mathbf{J}_{s2} \quad (2.83)$$

$$\mathbf{M}_{s1} = -\mathbf{M}_{s2}. \quad (2.84)$$

Using the source-field relationship in Equation 2.41 for region 1 and 2 allows us to rewrite Equation 2.80 and 2.82 as

$$\hat{\mathbf{n}} \times \mathbf{E}^i = -\mathbf{M}_{s1} - \hat{\mathbf{n}} \times \mathbf{E}^s \quad (2.85)$$

$$= -\mathbf{M}_{s1} - \hat{\mathbf{n}} \times \left\{ \frac{\eta_1}{jk_1} (k_1^2 \mathbf{J}_{s1} + \nabla (\nabla \cdot \mathbf{J}_{s1})) - \nabla \times \mathbf{M}_{s1} \right\}_{S^+} * \mathbf{G}$$

$$0 = -\mathbf{M}_{s2} + \hat{\mathbf{n}} \times \mathbf{E}_2 \quad (2.86)$$

$$= -\mathbf{M}_{s2} + \hat{\mathbf{n}} \times \left\{ \frac{\eta_2}{jk_2} (k_2^2 \mathbf{J}_{s2} + \nabla (\nabla \cdot \mathbf{J}_{s2})) - \nabla \times \mathbf{M}_{s2} \right\}_{S^+} * \mathbf{G}$$

Equation 2.85 together with Equation 2.86 after the substitution of Equations 2.83-2.84 form the coupled surface electric field integral equations (SEFIE)

$$\hat{\mathbf{n}} \times \mathbf{E}^i = -\mathbf{M}_{s1} - \hat{\mathbf{n}} \times \left\{ \frac{\eta_1}{jk_1} (k_1^2 \mathbf{J}_{s1} + \nabla (\nabla \cdot \mathbf{J}_{s1})) - \nabla \times \mathbf{M}_{s1} \right\}_{S^+} * \mathbf{G}_1 \quad (2.87)$$

$$0 = \mathbf{M}_{s1} - \hat{\mathbf{n}} \times \left\{ \frac{\eta_2}{jk_2} (k_2^2 \mathbf{J}_{s1} + \nabla (\nabla \cdot \mathbf{J}_{s1})) - \nabla \times \mathbf{M}_{s1} \right\}_{S^-} * \mathbf{G}_2$$

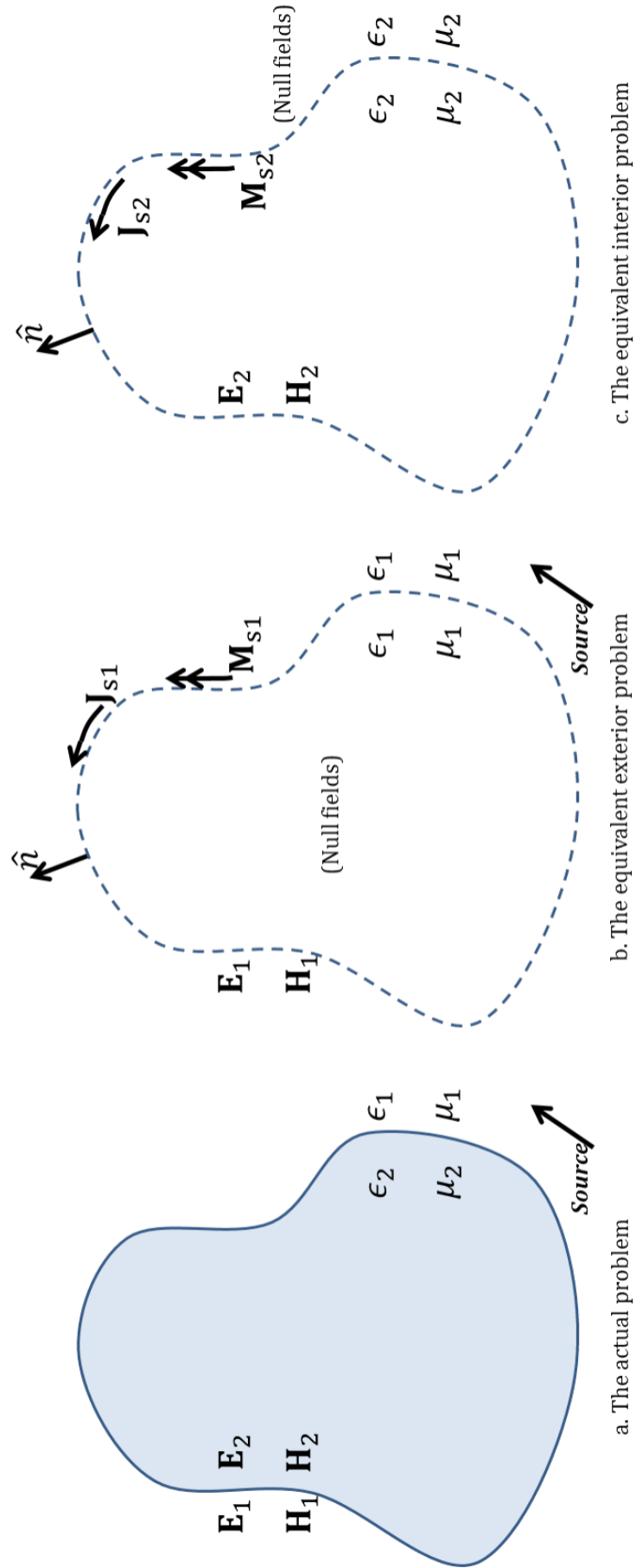


**Figure 2.6:** Application of the surface equivalence theorem to a homogeneous problem.

where  $k_a$ ,  $\eta_a$  and  $\mathbf{G}_a$  are wavenumber, wave impedance and Green's function in region  $a$ , respectively. The subscripts  $S^+$  and  $S^-$  indicate that the function within the bracket is evaluated an infinitesimal distance outside and inside the scatterer surface, respectively. Similarly, the coupled magnetic field integral equations (SMFIE) are obtained using Equations 2.79, 2.81 and 2.42

$$\begin{aligned}\hat{\mathbf{n}} \times \mathbf{H}^i &= \mathbf{J}_{s1} - \hat{\mathbf{n}} \times \left\{ \frac{1}{jk_1\eta_1} (k_1^2 \mathbf{M}_{s1} + \nabla(\nabla \cdot \mathbf{M}_{s1})) + \nabla \times \mathbf{J}_{s1} \right\}_{S^+} * \mathbf{G}_1 \\ 0 &= -\mathbf{J}_{s1} - \hat{\mathbf{n}} \times \left\{ \frac{1}{jk_2\eta_2} (k_2^2 \mathbf{M}_{s1} + \nabla(\nabla \cdot \mathbf{M}_{s1})) + \nabla \times \mathbf{J}_{s1} \right\}_{S^-} * \mathbf{G}_2\end{aligned}\quad (2.88)$$

These equations are later specialised for the particular case of perfect electric conductor (PEC) in chapter 4.

## 2.6 Method of moments

In this section, we review a numerical procedure called the method of moments for the solution of linear equations. The continuous integral equations in the previous sections are converted into a discrete matrix equations. By this process, the form of an integral equation to be solved is

$$Lf = g \quad (2.89)$$

where  $L$  is a continuous linear operator,  $g$  is the known excitation and  $f$  is the unknown function to be determined. The solution of the equation is given by

$$f = L^{-1}g \quad (2.90)$$

where  $L^{-1}$  is the inverse operator of  $L$ . However, the determination of the continuous inverse operator is usually impossible in practice. To numerically solve Equation 2.89, the method of moments is applied to transform the linear operator into a dense matrix from which the inverse operator in a discretised form can be computed. Let  $f$  be expanded in the domain  $L$  into a finite series of the form

$$f \approx \sum_{n=1}^N \alpha_n f_n \quad (2.91)$$

where  $\alpha_n$  are constant and unknown coefficients to be determined and  $f_n$  are expansion functions or basis functions. For an exact solution, the summation should be taken to infinity but has to be truncated in practice. The substitution of Equation 2.91 into Equation 2.89 together with the linearity of  $L$  yields

$$L \sum_{n=1}^N \alpha_n f_n \approx g. \quad (2.92)$$

We define a set of weighting functions or testing functions in the range of  $L$  as

$$w = \{w_1, w_2, \dots, w_N\}. \quad (2.93)$$

Assuming the availability of an appropriate inner product  $\langle f, g \rangle$  for the problem and taking the inner product of Equation 2.92 results in

$$\sum_n^N \alpha_n \langle w_m, Lf_n \rangle = \langle w_m, g \rangle \quad m = 1 \dots N. \quad (2.94)$$

This set of equations can be represented in a matrix form as

$$\mathbf{Z}\mathbf{x} = \mathbf{b} \quad (2.95)$$

where

$$\mathbf{Z} = \begin{pmatrix} \langle w_1, Lf_1 \rangle & \langle w_1, Lf_2 \rangle & \cdots & \langle w_1, Lf_N \rangle \\ \langle w_2, Lf_1 \rangle & \langle w_2, Lf_2 \rangle & \cdots & \langle w_2, Lf_N \rangle \\ \vdots & \vdots & \ddots & \vdots \\ \langle w_N, Lf_1 \rangle & \langle w_N, Lf_2 \rangle & \cdots & \langle w_N, Lf_N \rangle \end{pmatrix} \quad (2.96)$$

$$\mathbf{x} = \begin{pmatrix} \alpha_1 \\ \alpha_2 \\ \vdots \\ \alpha_N \end{pmatrix} \quad (2.97)$$

$$\mathbf{b} = \begin{pmatrix} \langle w_1, g \rangle \\ \langle w_2, g \rangle \\ \vdots \\ \langle w_N, g \rangle \end{pmatrix}. \quad (2.98)$$

The solution of Equation 2.95 can be obtained by means of a direct inversion or iterative methods. The choice of the basis functions and testing functions is important within the implementation of MoM.  $f_n$  should be linearly independent and carefully selected to well



approximate  $f$  by means of the superposition in Equation 2.91. The selection of the testing functions similarly should ensure linear independence. The choice of basis functions depends on many practical features such as the desired accuracy of the approximate solution, the ease of the evaluation of the matrix entries, the computational constraints or the nature of the particular operator  $L$ .

The simplest and most popular basis function for two dimensional problems is the pulse basis function [22]. For three dimensional problems, more complicated basis functions are applied including the rooftop and the RWG functions [24]. As the size of the problem increases in terms of wavelength, the number of basis functions used for the approximation of the problem must also increase in order to accurately capture the behaviour of the system.

## 2.7 Conclusion

Fundamental electromagnetic theory has been reviewed in this chapter. Integral equations, the volume integral equations and the surface integral equations, are derived from the differential form and the time-harmonic form of Maxwell equations. The surface integral equations are used to formulate electromagnetic scattering problems in chapter 4 and chapter 5 while the volume integral equations are applied to analyse electromagnetic propagation and scattering problems in chapter 6 and chapter 7. The method of moments is introduced for the discretisation of the integral equations, resulting in dense linear matrix systems. The prohibitively large size of the matrix systems, resulted from the application of the method of moments to the discretisation of large-scale electromagnetic scattering problems, leads the use of iterative methods for the solution of such matrix equations. Iterative methods are introduced in chapter 3.

## 3 Iterative methods for the solution of linear systems

This chapter reviews iterative methods for the solution of linear systems. Such methods successively approximate the solution over a number of steps. The two main classes of iterative methods, the non-stationary and stationary, are presented in Section 3.2 and Section 3.3, respectively. Some preconditioning techniques which are applied for the improvement of the convergence rate of iterative methods are discussed in Section 3.4.

### 3.1 Introduction

The application of the MoM to the integral equations (IEs) for the solution of Maxwell equations produces a dense linear system

$$\mathbf{Z}\mathbf{x} = \mathbf{v} \tag{3.1}$$

where  $\mathbf{Z}$  is a  $N \times N$  impedance matrix containing information about mutual interactions between basis functions.  $N$  is the number of basis functions used to discretise the problem.  $\mathbf{v}$  is a  $N \times 1$  vector containing information about incident fields impinging on each basis function and  $\mathbf{x}$  is a  $N \times 1$  unknown vector containing information about amplitudes of equivalent currents. There are two main approaches for the solution of the system.  $\mathbf{x}$  can be directly computed by the product of the inverse of the matrix  $\mathbf{Z}$  and the vector  $\mathbf{v}$ . However, this solution is restricted to small systems where the storage and computational complexity of making the inverse scale with  $\mathcal{O}(N^2)$  and  $\mathcal{O}(N^3)$  respectively which become prohibitively expensive for large problems. Due to the computational constraint, the use of iterative methods has been considered as a suitable solution for large systems because of the significant reduction in computational complexity and the requirement of no explicit storage. Iterative solvers apply successive corrections to attain more accurate solutions at each step which requires a computation of  $\mathcal{O}(N^2)$ . The termination of the iterative process is activated when some convergence criteria are met. However, the rate of convergence remains a challenge for determination. There are two main types of iterative methods comprising of non-stationary, such as those based on the Krylov subspaces, and stationary techniques.

### 3.2 Krylov subspace iterative methods

Krylov subspace iterative solver is based on the application of projection processes for the extraction of an approximate solution from a specified low-dimensional subspace, called the Krylov subspace. The original idea of the Krylov subspace is based on the Cayley-Hamilton theorem [76] which states that the inverse of a  $N \times N$  invertible matrix  $\mathbf{Z}$  can be expressed by an  $(N - 1)^{\text{th}}$  degree polynomial in  $\mathbf{Z}$ . Therefore, the inverse of the matrix  $\mathbf{Z}$  can be demonstrated as

$$\mathbf{Z}^{-1} = \alpha_1 \mathbf{I} + \alpha_2 \mathbf{Z} + \alpha_3 \mathbf{Z}^2 + \cdots + \alpha_N \mathbf{Z}^{N-1} \quad (3.2)$$

where  $\alpha_n$  are corresponding coefficients. Consequently, the solution of Equation 3.1 can be given by

$$\mathbf{x} = \mathbf{Z}^{-1} \mathbf{v} = \alpha_1 \mathbf{v} + \alpha_2 \mathbf{Z} \mathbf{v} + \alpha_3 \mathbf{Z}^2 \mathbf{v} + \cdots + \alpha_N \mathbf{Z}^{N-1} \mathbf{v}. \quad (3.3)$$

In other words, the accurate solution of Equation 3.1 is a linear combination of bases forming the Krylov subspace associated with the matrix  $\mathbf{Z}$  and defined by

$$\mathcal{K}_N(\mathbf{Z}, \mathbf{v}) = \text{span} \left\{ \mathbf{v}, \mathbf{Z} \mathbf{v}, \mathbf{Z}^2 \mathbf{v}, \cdots, \mathbf{Z}^{N-1} \mathbf{v} \right\}. \quad (3.4)$$

As the result, the approximation of the solution requires the iterative computation of the bases of the Krylov subspace by mean of the power iteration. The computation of a newly generated basis and an approximate solution is required for each iteration until the desired accuracy is achieved. The satisfactory solution is usually obtained by the  $i^{\text{th}}$  iteration where  $i \ll N$ . The Krylov solvers attempt to minimise the corresponding residual vector at the  $i^{\text{th}}$  iteration defined as

$$\mathbf{r}^{(i)} = \mathbf{v} - \mathbf{Z} \mathbf{x}^{(i)} \quad (3.5)$$

where  $\mathbf{x}^{(i)}$  is the approximate solution at the  $i^{\text{th}}$  iteration.  $\mathbf{x}^{(i)}$  can be expressed as

$$\mathbf{x}^{(i)} = \mathbf{K}_{N \times i} \mathbf{a}_i \quad (3.6)$$

where

$$\mathbf{K}_{N \times i} = \left( \mathbf{v}, \mathbf{Z} \mathbf{v}, \mathbf{Z}^2 \mathbf{v}, \cdots, \mathbf{Z}^{i-1} \mathbf{v} \right) \quad (3.7)$$

$$\mathbf{a}_i = (\alpha_1, \alpha_2, \cdots, \alpha_i)^T. \quad (3.8)$$

$T$  denotes the transpose of a matrix. The coefficient vector  $\mathbf{a}_i$  is found by the mechanism of minimising the corresponding residuals. Different approaches for the minimisation result in different kinds of Krylov subspace iterations.

### 3.2.1 Arnoldi iteration

The application of the power iteration to the formation of the Krylov subspace usually leads to instability of the generated subspace. According to the properties of the power iteration, the computed basis  $\mathbf{Z}^{i-1}\mathbf{v}$  at the  $i^{\text{th}}$  iteration is gradually getting close to the direction of the largest eigenvector of  $\mathbf{Z}$  as  $i$  increases, causing most of the basis vectors to have nearly the same direction. The similarity in direction makes the resultant Krylov subspace ill-conditioned. The condition of the basis can be improved by using the Gram-Schmidt orthogonalisation process. Details about the application of the Gram-Schmidt process to an arbitrary basis  $\{\mathbf{u}_1, \mathbf{u}_2, \dots, \mathbf{u}_N\}$  for the construction of an equivalent orthogonal basis  $\{\mathbf{q}_1, \mathbf{q}_2, \dots, \mathbf{q}_N\}$  are outlined in Algorithm 3.1.

Assuming that  $\{\mathbf{q}_1, \mathbf{q}_2, \dots, \mathbf{q}_i\}$  is a set of orthogonal basis for a Krylov subspace  $\mathcal{K}_i(\mathbf{Z}, \mathbf{v})$ , the subspace can be represented as

$$\begin{aligned}\mathcal{K}_i(\mathbf{Z}, \mathbf{v}) &= \text{span}\{\mathbf{v}, \mathbf{Z}\mathbf{v}, \mathbf{Z}^2\mathbf{v}, \dots, \mathbf{Z}^{i-1}\mathbf{v}\} \\ &= \text{span}\{\mathbf{q}_1, \mathbf{Z}\mathbf{q}_1, \mathbf{Z}^2\mathbf{q}_1, \dots, \mathbf{Z}^{i-1}\mathbf{q}_1\}\end{aligned}\tag{3.9}$$

where  $\mathbf{q}_1 = \mathbf{v}$ . The application of the Gram-Schmidt procedure allows the representation of  $\mathbf{Z}\mathbf{v}$  using  $\mathbf{q}_1$  and  $\mathbf{q}_2$  as

$$\mathbf{Z}\mathbf{v} = \alpha\mathbf{q}_1 + \beta\mathbf{q}_2.\tag{3.10}$$

Therefore, Equation 3.9 can be rewritten as

$$\mathcal{K}_i(\mathbf{Z}, \mathbf{v}) = \text{span}\{\mathbf{q}_1, \alpha\mathbf{q}_1 + \beta\mathbf{q}_2, \mathbf{Z}(\alpha\mathbf{q}_1 + \beta\mathbf{q}_2), \dots, \mathbf{Z}^{i-2}(\alpha\mathbf{q}_1 + \beta\mathbf{q}_2)\}.\tag{3.11}$$

Because each basis in Equation 3.11 can be decomposed into a linear combination of  $\mathbf{q}_1$ ,  $\mathbf{q}_2$  and  $\mathbf{Z}^m\mathbf{q}_2$  where  $m = 1 \dots i - 2$

$$\begin{aligned}\mathbf{Z}(\alpha\mathbf{q}_1 + \beta\mathbf{q}_2) &= \alpha\mathbf{Z}\mathbf{q}_1 + \beta\mathbf{Z}\mathbf{q}_2 = \alpha(\alpha\mathbf{q}_1 + \beta\mathbf{q}_2) + \beta\mathbf{Z}\mathbf{q}_2 \\ \mathbf{Z}^2(\alpha\mathbf{q}_1 + \beta\mathbf{q}_2) &= \mathbf{Z}(\alpha(\alpha\mathbf{q}_1 + \beta\mathbf{q}_2) + \beta\mathbf{Z}\mathbf{q}_2) \\ &= \alpha^2\mathbf{Z}\mathbf{q}_1 + \alpha\beta\mathbf{Z}\mathbf{q}_2 + \beta\mathbf{Z}^2\mathbf{q}_2 \\ &= \alpha^2(\alpha\mathbf{q}_1 + \beta\mathbf{q}_2) + \alpha\beta\mathbf{Z}\mathbf{q}_2 + \beta\mathbf{Z}^2\mathbf{q}_2 \\ \dots &\dots \dots\end{aligned}\tag{3.12}$$

Equation 3.11 can be changed to

$$\begin{aligned}
 \mathcal{K}_i(\mathbf{Z}, \mathbf{v}) &= \text{span} \{ \mathbf{q}_1, \mathbf{q}_2, \mathbf{Z}\mathbf{q}_2, \mathbf{Z}^2\mathbf{q}_2, \mathbf{Z}^3\mathbf{q}_2, \dots, \mathbf{Z}^{i-2}\mathbf{q}_2 \} \\
 &= \text{span} \{ \mathbf{q}_1, \mathbf{q}_2, \mathbf{q}_3, \mathbf{Z}\mathbf{q}_3, \mathbf{Z}^2\mathbf{q}_3, \dots, \mathbf{Z}^{i-3}\mathbf{q}_3 \} \\
 &= \dots \\
 &= \text{span} \{ \mathbf{q}_1, \mathbf{q}_2, \mathbf{q}_3, \mathbf{q}_4, \mathbf{q}_5, \dots, \mathbf{q}_{i-1}, \mathbf{Z}\mathbf{q}_{i-1} \}.
 \end{aligned} \tag{3.13}$$

As the result, instead of orthogonalising  $\mathbf{Z}^{i-1}\mathbf{q}_1$  against  $\mathbf{q}_1, \dots, \mathbf{q}_{i-1}$ ,  $\mathbf{q}_i$  can be obtained by orthogonalising  $\mathbf{Z}\mathbf{q}_{i-1}$  against  $\mathbf{q}_1, \dots, \mathbf{q}_{i-1}$ . This formulation of the Krylov basis is generally called the Arnoldi iteration. To minimise the loss of orthogonality due to the round-off error of the classical Gram-Schmidt process, the Arnoldi iteration takes advantage of the modified Gram-Schmidt process to produce a set of orthonormal bases for the Krylov subspace. The Arnoldi algorithm using the modified Gram-Schmidt process is outlined in Algorithm 3.2. Applying the Arnoldi process generates an upper Hessenberg matrix [38] formed by the coefficients  $h_{m,n}$  computed by the algorithm

$$\mathbf{H}_{i \times i} = \begin{pmatrix} h_{1,1} & h_{1,2} & h_{1,3} & \cdots & \cdots & h_{1,n} & \cdots & \cdots & h_{1,i} \\ h_{2,1} & h_{2,2} & h_{2,3} & \cdots & \cdots & h_{2,n} & \cdots & \cdots & h_{2,i} \\ 0 & h_{3,2} & h_{3,3} & \cdots & \cdots & h_{3,n} & \cdots & \cdots & h_{3,i} \\ \vdots & 0 & h_{4,3} & \cdots & \cdots & \vdots & \cdots & \cdots & \vdots \\ \vdots & \cdots & 0 & \ddots & h_{n-1,n-1} & \vdots & \cdots & \cdots & \vdots \\ \vdots & \cdots & \cdots & \ddots & h_{n,n-1} & h_{n,n} & \cdots & \cdots & \vdots \\ \vdots & \cdots & \cdots & \cdots & 0 & h_{n+1,n} & \cdots & \cdots & \vdots \\ \vdots & \cdots & \cdots & \cdots & \cdots & \ddots & \ddots & \ddots & \vdots \\ 0 & 0 & 0 & \cdots & \cdots & \cdots & 0 & h_{i,i-1} & h_{i,i} \end{pmatrix} \tag{3.14}$$

and a matrix  $\mathbf{Q}$  whose columns are the Arnoldi vectors  $\mathbf{q}_1, \mathbf{q}_2, \dots, \mathbf{q}_i$ .

$$\mathbf{Q}_i = (\mathbf{q}_1, \mathbf{q}_2, \dots, \mathbf{q}_i) \tag{3.15}$$

The property of orthonormalisation of the Arnoldi vectors implies that

$$\mathbf{Q}^H \mathbf{Q} = \mathbf{I} \tag{3.16}$$

where  $H$  denotes the Hermitian transpose of a matrix. In addition, there is a relation between the matrix  $\mathbf{Z}$ ,  $\mathbf{Q}$  and the Hessenberg matrix  $\mathbf{H}$  as follows

$$\mathbf{Z}\mathbf{Q} = \mathbf{Q}\mathbf{H}. \tag{3.17}$$

Inserting Equation 3.16 into 3.17 results in

---

**Algorithm 3.1** The classical Gram-Schmidt process.

---

For  $n = 1 \cdots N$  $\mathbf{q}_n = \mathbf{u}_n$  (assign an initial value to the next vector spanning the subspace)For  $m = 1 \cdots n - 1$  $h_{m,n} = \langle \mathbf{u}_n, \mathbf{q}_m \rangle$  (compute the projection of the vector  $\mathbf{u}_n$  onto  $\mathbf{q}_m$ ) $\mathbf{q}_n = \mathbf{q}_n - h_{m,n} \mathbf{q}_m$  (make the new vector orthogonal to  $\mathbf{q}_m$ )

End

 $h_{n,n} = \|\mathbf{q}_n\|_2$ If  $h_{n,n} == 0$ 

Quit

End

 $\mathbf{q}_n = \frac{\mathbf{q}_n}{h_{n,n}}$  (make  $\mathbf{q}_n$  a unit vector)End

---

---

**Algorithm 3.2** The Arnoldi - modified Gram-Schmidt iteration.

---

 $\mathbf{q}_1 = \frac{\mathbf{v}}{\|\mathbf{v}\|_2}$ For  $n = 2 \cdots i$  $\mathbf{q}_n = \mathbf{Z}\mathbf{q}_{n-1}$  (assign an initial value to the next vector spanning the subspace  $\mathbf{q}_m$ )For  $m = 1 \cdots n - 1$  $h_{m,n-1} = \langle \mathbf{q}_n, \mathbf{q}_m \rangle$  (compute the projection of the vector  $\mathbf{q}_n$  onto  $\mathbf{q}_m$ ) $\mathbf{q}_n = \mathbf{q}_n - h_{m,n-1} \mathbf{q}_m$  (make the new vector orthogonal to  $\mathbf{q}_m$ )

End

 $h_{n,n-1} = \|\mathbf{q}_n\|_2$ If  $h_{n,n-1} == 0$ 

Quit

End

 $\mathbf{q}_n = \frac{\mathbf{q}_n}{h_{n,n-1}}$  (make  $\mathbf{q}_n$  a unit vector)End

---

$$\boxed{\mathbf{H} = \mathbf{Q}^H \mathbf{Z} \mathbf{Q}}. \quad (3.18)$$

Equation 3.18 is another interpretation of the Arnoldi iteration as an orthogonal transformation of matrix  $\mathbf{Z}$  to an upper Hessenberg matrix. As the value of  $i$  is sufficiently large, the eigenvalues of the Hessenberg matrix  $\mathbf{H}$  are good approximations of the  $i$  largest eigenvalues of  $\mathbf{Z}$ . Therefore, the Arnoldi iteration is efficient for the computation of eigenvalues due to the reduction of the large and unmanageable matrix  $\mathbf{Z}$  to the significantly smaller and more structural upper Hessenberg matrix  $\mathbf{H}$ . To derive the relation between the matrices  $\mathbf{Q}$  in successive iterations, we consider the matrix  $\mathbf{Q}_{i+1}$  and the partial Hessenberg matrix  $\tilde{\mathbf{H}}$  at the  $(i+1)^{\text{th}}$  iteration

$$\mathbf{Q}_{i+1} = (\mathbf{q}_1, \mathbf{q}_2, \dots, \mathbf{q}_{i+1}) \quad (3.19)$$

$$\tilde{\mathbf{H}}_{(i+1) \times i} = \begin{pmatrix} h_{1,1} & h_{1,2} & h_{1,3} & \cdots & h_{1,i-1} & h_{1,i} \\ h_{2,1} & h_{2,2} & h_{2,3} & \cdots & h_{2,i-1} & h_{2,i} \\ 0 & h_{3,2} & h_{3,3} & \cdots & h_{2,i-1} & h_{3,i} \\ 0 & 0 & h_{4,3} & \ddots & \vdots & \vdots \\ 0 & 0 & 0 & \ddots & h_{i-1,i-1} & \vdots \\ \vdots & \vdots & \vdots & \ddots & h_{i,i-1} & h_{i,i} \\ 0 & 0 & 0 & \cdots & 0 & h_{i+1,i} \end{pmatrix} \quad (3.20)$$

From Equation 3.17, the relation is expressed as

$$\boxed{\mathbf{Z} \mathbf{Q}_i = \mathbf{Q}_{i+1} \tilde{\mathbf{H}}}. \quad (3.21)$$

### 3.2.2 Conjugate gradient method

The conjugate gradient algorithm is a Krylov subspace method for the solution of Equation 3.1 where  $\mathbf{Z}$  is a real, symmetric and positive-definite matrix. The solution of Equation 3.1 is equivalent to the minimisation of a quadratic equation

$$\phi(\mathbf{x}) = \frac{1}{2} \mathbf{x}^T \mathbf{Z} \mathbf{x} - \mathbf{x}^T \mathbf{v}. \quad (3.22)$$

The minimisation of Equation 3.22 is achieved at  $\mathbf{x} = \mathbf{Z}^{-1} \mathbf{v}$ , which is also the solution of Equation 3.1. Therefore, instead of solving Equation 3.1, we aim to minimise Equation 3.22. The solution of Equation 3.22 is obtained by iteratively creating a sequence of approximate solutions. We denote  $\mathbf{x}^{(i)}$  and  $\mathbf{r}^{(i)}$  as the approximation and the residual at the  $i^{\text{th}}$  iteration. The residual is defined as

**Algorithm 3.3** Algorithm for the minimisation of Equation 3.22 using general direction vectors.

---

$\mathbf{x}^{(0)}$  = initial guess

$\mathbf{r}^{(0)} = \mathbf{v} - \mathbf{Z}\mathbf{x}^{(0)}$

For  $i = 1 \cdots n$

    Choose a direction  $\mathbf{d}^{(i)}$

$$\alpha_i = \frac{\mathbf{d}^{(i)T} \mathbf{r}^{(i-1)}}{\mathbf{d}^{(i)T} \mathbf{Z} \mathbf{d}^{(i)}}$$

$$\mathbf{x}^{(i)} = \mathbf{x}^{(i-1)} + \alpha_i \mathbf{d}^{(i)}$$

$$\mathbf{r}^{(i)} = \mathbf{v} - \mathbf{Z}\mathbf{x}^{(i)}$$

    If  $\|\mathbf{r}^{(i)}\|_2 < \text{tolerance}$

        Quit

    End

End

---

**Algorithm 3.4** The conjugate gradient method.

---

$\mathbf{x}^{(0)} = 0$

$\mathbf{r}^{(0)} = \mathbf{v} - \mathbf{Z}\mathbf{x}^{(0)}$

For  $i = 1 \cdots n$

    If  $i == 1$

$$\mathbf{d}^{(i)} = \mathbf{r}^{(0)}$$

    Else

$$\beta_i = \frac{\mathbf{r}^{(i-1)T} \mathbf{r}^{(i-1)}}{\mathbf{r}^{(i-2)T} \mathbf{r}^{(i-2)}}$$

$$\mathbf{d}^{(i)} = \mathbf{r}^{(i-1)} + \beta_i \mathbf{d}^{(i-1)}$$

    End

$$\alpha_i = \frac{\mathbf{r}^{(i-1)T} \mathbf{r}^{(i-1)}}{\mathbf{d}^{(i)T} \mathbf{Z} \mathbf{d}^{(i)}}$$

$$\mathbf{x}^{(i)} = \mathbf{x}^{(i-1)} + \alpha_i \mathbf{d}^{(i)}$$

$$\mathbf{r}^{(i)} = \mathbf{r}^{(i-1)} - \alpha_i \mathbf{Z} \mathbf{d}^{(i)}$$

    If  $\|\mathbf{r}^{(i)}\|_2 < \text{tolerance}$

        Quit

    End

End

---



$$\mathbf{r}^{(i)} = \mathbf{v} - \mathbf{Z}\mathbf{x}^{(i)}. \quad (3.23)$$

We assume that an approximation at iteration  $i + 1$  is a linear combination of the previous approximated solution and a direction vector  $\mathbf{d}^{(i+1)}$

$$\mathbf{x}^{(i+1)} = \mathbf{x}^{(i)} + \alpha_{i+1}\mathbf{d}^{(i+1)} \quad (3.24)$$

where  $\alpha_{i+1}$  is a coefficient for the minimisation along the direction vector  $\mathbf{d}^{(i+1)}$ . Substituting Equation 3.24 into Equation 3.22 results in

$$\phi\left(\mathbf{x}^{(i)} + \alpha_{i+1}\mathbf{d}^{(i+1)}\right) = \phi\left(\mathbf{x}^{(i)}\right) + \frac{1}{2}\alpha_{i+1}^2\mathbf{d}^{(i+1)T}\mathbf{Z}\mathbf{d}^{(i+1)} - \alpha_{i+1}\mathbf{d}^{(i+1)T}\mathbf{r}^{(i)}. \quad (3.25)$$

In the method of steepest descent, the minimisation of Equation 3.25 with respect to  $\alpha_{i+1}$  is obtained at

$$\alpha_{i+1} = \frac{\mathbf{d}^{(i+1)T}\mathbf{r}^{(i)}}{\mathbf{d}^{(i+1)T}\mathbf{Z}\mathbf{d}^{(i+1)}}. \quad (3.26)$$

The algorithm for the minimisation of Equation 3.22 using general direction vectors is presented in Algorithm 3.3. We can represent the approximation and the residual at iteration  $i$  as

$$\mathbf{x}^{(i)} = \mathbf{x}^{(0)} + \alpha_1\mathbf{d}^{(1)} + \alpha_2\mathbf{d}^{(2)} + \dots + \alpha_i\mathbf{d}^{(i)} \quad (3.27)$$

$$\begin{aligned} \mathbf{r}^{(i)} &= \mathbf{v} - \mathbf{Z}\mathbf{x}^{(i)} \\ &= \mathbf{r}^{(0)} - \alpha_1\mathbf{Z}\mathbf{d}^{(1)} - \alpha_2\mathbf{Z}\mathbf{d}^{(2)} - \dots - \alpha_i\mathbf{Z}\mathbf{d}^{(i)} \\ &= \mathbf{r}^{(i-1)} - \alpha_i\mathbf{Z}\mathbf{d}^{(i)}. \end{aligned} \quad (3.28)$$

A new direction vector  $\mathbf{d}^{(i)}$  at iteration  $i$  should be chosen so as to avoid reversing of the effects made by the previous direction vectors  $\mathbf{d}^{(j)}$  with  $j < i$ . This means that the direction vectors are chosen to be linearly independent. Therefore, the direction vectors can be selected to be  $\mathbf{Z}$ -orthogonal or orthogonal with respect to  $\mathbf{Z}$ .

$$\mathbf{d}^{(i)T}\mathbf{Z}\mathbf{d}^{(j)} = 0 \quad i \neq j \quad (3.29)$$

In addition, a newly generated direction vector  $\mathbf{d}^{(i)}$  is required to be the closest vector to  $\mathbf{r}^{(i-1)}$ . In other words, the generation of  $\mathbf{d}^{(i)}$  minimises the distance  $\left\|\mathbf{d} - \mathbf{r}^{(i-1)}\right\|_2$  where  $\mathbf{d} = \text{span}\left\{\mathbf{Z}\mathbf{d}^{(1)}, \mathbf{Z}\mathbf{d}^{(2)}, \dots, \mathbf{Z}\mathbf{d}^{(i-1)}\right\}^\perp$ . The fulfillment of the requirements draws the relation between the search directions  $\mathbf{d}^{(i)}$ , the residuals  $\mathbf{r}^{(i)}$  and the Krylov subspace as follows

$$\text{span} \{ \mathbf{d}^{(1)}, \mathbf{d}^{(2)}, \dots, \mathbf{d}^{(i)} \} = \text{span} \{ \mathbf{r}^{(0)}, \mathbf{r}^{(1)}, \dots, \mathbf{r}^{(i-1)} \} = \mathcal{K}_i(\mathbf{Z}, \mathbf{r}^{(0)}) \quad (3.30)$$

$$\mathbf{d}^{(i)} \in \text{span} \{ \mathbf{r}^{(i-1)}, \mathbf{d}^{(i-1)} \} \quad (3.31)$$

$$\mathbf{r}^{(i)T} \mathbf{r}^{(j)} = 0 \quad i \neq j. \quad (3.32)$$

Further analysis for the conclusions of Equation 3.30-3.32 is presented in [38]. From Equation 3.31, we assume a newly generated direction vector is in a form of

$$\mathbf{d}^{(i)} = \mathbf{r}^{(i-1)} + \beta_i \mathbf{d}^{(i-1)}. \quad (3.33)$$

Left multiplying both sides of Equation 3.33 with  $\mathbf{d}^{(i-1)T} \mathbf{Z}$  and applying  $\mathbf{d}^{(i-1)T} \mathbf{Z} \mathbf{d}^{(i)} = 0$  result in

$$\beta_i = -\frac{\mathbf{d}^{(i-1)T} \mathbf{Z} \mathbf{r}^{(i-1)}}{\mathbf{d}^{(i-1)T} \mathbf{Z} \mathbf{d}^{(i-1)}}. \quad (3.34)$$

Applying the orthogonality of the residuals to Equation 3.28 leads to

$$\mathbf{r}^{(i-1)T} \mathbf{r}^{(i-1)} = -\alpha_{i-1} \mathbf{r}^{(i-1)T} \mathbf{Z} \mathbf{d}^{(i-1)} \quad (3.35)$$

$$\mathbf{r}^{(i-2)T} \mathbf{r}^{(i-2)} = \alpha_{i-1} \mathbf{d}^{(i-1)T} \mathbf{Z} \mathbf{d}^{(i-1)}. \quad (3.36)$$

Substituting Equation 3.35-3.36 into Equation 3.34, we obtain

$$\beta_i = \frac{\mathbf{r}^{(i-1)T} \mathbf{r}^{(i-1)}}{\mathbf{r}^{(i-2)T} \mathbf{r}^{(i-2)}}. \quad (3.37)$$

The complete CG is shown in Algorithm 3.4. From Equation 3.30 and 3.32, the conjugate gradient method is considered to approximate the solution on the Krylov subspace using the orthogonality of the residuals to  $\mathcal{K}_i$ .

### 3.2.3 Biconjugate gradient method

The biconjugate gradient method (BiCG) is an improvement to the CG which makes it applicable to non-symmetric systems. The BiCG proceeds by generating of two mutually orthogonal sequences of residuals instead of a single sequence as in the CG. One sequence is based on the original matrix  $\mathbf{Z}$  and the other is derived from the transpose of the original matrix  $\mathbf{Z}^T$ . Thus, the BiCG involves the computation of two different sets of residuals and direction vectors in each iteration, causing the requirement for two MVPs. The search direction vectors are given by

**Algorithm 3.5** The biconjugate gradient method.

---

$$\mathbf{x}^{(0)} = 0$$

$$\mathbf{r}^{(0)} = \mathbf{v} - \mathbf{Z}\mathbf{x}^{(0)}$$

$$\tilde{\mathbf{r}}^{(0)} = \mathbf{r}^{(0)}$$

For  $i = 1 \cdots n$   If  $i == 1$ 

$$\mathbf{d}^{(i)} = \mathbf{r}^{(0)}$$

$$\tilde{\mathbf{d}}^{(i)} = \tilde{\mathbf{r}}^{(0)}$$

Else

$$\beta_i = \frac{\tilde{\mathbf{r}}^{(i-1)T} \mathbf{r}^{(i-1)}}{\tilde{\mathbf{r}}^{(i-2)T} \mathbf{r}^{(i-2)}}$$

$$\mathbf{d}^{(i)} = \mathbf{r}^{(i-1)} + \beta_i \mathbf{d}^{(i-1)}$$

$$\tilde{\mathbf{d}}^{(i)} = \tilde{\mathbf{r}}^{(i-1)} + \beta_i \tilde{\mathbf{d}}^{(i-1)}$$

End

$$\alpha_i = \frac{\tilde{\mathbf{r}}^{(i-1)T} \mathbf{r}^{(i-1)}}{\tilde{\mathbf{d}}^{(i)T} \mathbf{Z}\mathbf{d}^{(i)}}$$

$$\mathbf{x}^{(i)} = \mathbf{x}^{(i-1)} + \alpha_i \mathbf{d}^{(i)}$$

$$\mathbf{r}^{(i)} = \mathbf{r}^{(i-1)} - \alpha_i \mathbf{Z}\mathbf{d}^{(i)}$$

$$\tilde{\mathbf{r}}^{(i)} = \tilde{\mathbf{r}}^{(i-1)} - \alpha_i \mathbf{Z}^T \tilde{\mathbf{d}}^{(i)}$$

  If  $\|\mathbf{r}^{(i)}\|_2 < \text{tolerance}$ 

Quit

End

End

---

$$\mathbf{d}^{(i)} = \mathbf{r}^{(i-1)} + \beta_i \mathbf{d}^{(i-1)} \quad (3.38)$$

$$\tilde{\mathbf{d}}^{(i)} = \tilde{\mathbf{r}}^{(i-1)} + \beta_i \tilde{\mathbf{d}}^{(i-1)} \quad (3.39)$$

where the updated residuals are defined as

$$\mathbf{r}^{(i)} = \mathbf{r}^{(i-1)} - \alpha_i \mathbf{Z} \mathbf{d}^{(i)} \quad (3.40)$$

$$\tilde{\mathbf{r}}^{(i)} = \tilde{\mathbf{r}}^{(i-1)} - \alpha_i \mathbf{Z}^T \tilde{\mathbf{d}}^{(i)}. \quad (3.41)$$

The coefficients  $\alpha$  and  $\beta$  are specified as

$$\alpha_i = \frac{\tilde{\mathbf{r}}^{(i-1)T} \mathbf{r}^{(i-1)}}{\tilde{\mathbf{d}}^{(i)T} \mathbf{Z} \mathbf{d}^{(i)}} \quad (3.42)$$

$$\beta_i = \frac{\tilde{\mathbf{r}}^{(i-1)T} \mathbf{r}^{(i-1)}}{\tilde{\mathbf{r}}^{(i-2)T} \mathbf{r}^{(i-2)}}. \quad (3.43)$$

The BiCG generates a sequence of approximate solutions  $\mathbf{x}^{(i)}$  belonging to the subspace  $\mathbf{x}^{(0)} + \mathcal{K}_i$  and a sequence of residuals which is orthogonal to  $\mathcal{K}_i(\mathbf{Z}^T, \mathbf{r}^{(0)})$ . However, the BiCG eliminates the minimisation in the CG, resulting in unreliability. The outline of the BiCG is shown in Algorithm 3.5. The biconjugate stabilised method is an extension of the BiCG for a faster and smoother convergence rate.

### 3.2.4 Biconjugate gradient stabilised method

The biconjugate gradient stabilised method is an improved version of the BiCG for the solution of nonsymmetric linear systems intended to reduce the irregularity in the convergence rate of the BiCG. The recurrence relations in Equation 3.38-3.41 can be transformed into

$$\mathbf{d}^{(i+1)} = T_i(\mathbf{Z}) \mathbf{r}^{(0)} \quad (3.44)$$

$$\tilde{\mathbf{d}}^{(i+1)} = T_i(\mathbf{Z}^T) \tilde{\mathbf{r}}^{(0)} \quad (3.45)$$

$$\mathbf{r}^{(i)} = P_i(\mathbf{Z}) \mathbf{r}^{(0)} \quad (3.46)$$

$$\tilde{\mathbf{r}}^{(i)} = P_i(\mathbf{Z}^T) \tilde{\mathbf{r}}^{(0)} \quad (3.47)$$

**Algorithm 3.6** The biconjugate gradient stabilised method.

---

$\mathbf{x}^{(0)} = 0$   
 $\bar{\mathbf{r}}^{(0)} = \mathbf{v} - \mathbf{Z}\mathbf{x}^{(0)}$   
 $\tilde{\mathbf{r}} = \bar{\mathbf{r}}^{(0)}$   
For  $i = 1 \cdots n$   
     $\rho_{i-1} = \tilde{\mathbf{r}}^T \bar{\mathbf{r}}^{(i-1)}$   
    If  $i == 1$   
         $\bar{\mathbf{d}}^{(i)} = \bar{\mathbf{r}}^{(i-1)}$   
    Else  
         $\beta_i = \frac{\rho_i \alpha_i}{\rho_{i-1} \gamma_{i-1}}$   
         $\bar{\mathbf{d}}^{(i)} = \bar{\mathbf{r}}^{(i-1)} + \beta_i (\bar{\mathbf{d}}^{(i-1)} - \gamma_{i-1} \mathbf{u}^{(i-1)})$   
    End  
     $\mathbf{u}^{(i)} = \mathbf{Z}\bar{\mathbf{d}}^{(i)}$   
     $\alpha_i = \frac{\rho_{i-1}}{\tilde{\mathbf{r}}^T \mathbf{u}^{(i)}}$   
     $\mathbf{s} = \mathbf{r}^{(i-1)} - \alpha_i \mathbf{u}^{(i)}$   
     $\mathbf{t} = \mathbf{Z}\mathbf{s}$   
     $\gamma_i = \frac{\mathbf{t}^T \mathbf{s}}{\mathbf{t}^T \mathbf{t}}$   
     $\mathbf{x}^{(i)} = \mathbf{x}^{(i-1)} + \alpha_i \bar{\mathbf{d}}^{(i)} + \gamma_i \mathbf{s}$   
     $\bar{\mathbf{r}}^{(i)} = \mathbf{s} - \gamma_i \mathbf{t}$   
    If  $\|\bar{\mathbf{r}}^{(i)}\|_2 < \text{tolerance}$   
        Quit  
    End  
End  
End

---

where  $T_i(\mathbf{Z})$  and  $P_i(\mathbf{Z})$  are  $i^{\text{th}}$ -order polynomials in  $\mathbf{Z}$ . From Equation 3.46-3.47, the product of residuals and the product of direction vectors are rewritten as

$$\rho_i = \tilde{\mathbf{r}}^{(i)T} \mathbf{r}^{(i)} = \left( P_i(\mathbf{Z}^T) \tilde{\mathbf{r}}^{(0)} \right)^T P_i(\mathbf{Z}) \mathbf{r}^{(0)} = \tilde{\mathbf{r}}^{(0)T} P_i^2(\mathbf{Z}) \mathbf{r}^{(0)} \quad (3.48)$$

$$\chi_{i+1} = \tilde{\mathbf{d}}^{(i+1)T} \mathbf{d}^{(i+1)} = \left( T_i(\mathbf{Z}^T) \tilde{\mathbf{r}}^{(0)} \right)^T T_i(\mathbf{Z}) \mathbf{r}^{(0)} = \tilde{\mathbf{r}}^{(0)T} T_i^2(\mathbf{Z}) \mathbf{r}^{(0)}. \quad (3.49)$$

As a consequence, it becomes unnecessary to separately compute  $\tilde{\mathbf{r}}^{(i)}$  and  $\mathbf{r}^{(i)}$  as in the BiCG. The redundancy of the explicit record keeping of the direction vectors and residuals in the BiCG can be replaced in the biconjugate gradient squared method [77]. In the biconjugate gradient squared method, the residuals are defined by

$$\bar{\mathbf{r}}^{(i)} = P_i^2(\mathbf{Z}) \mathbf{r}^{(0)} \quad (3.50)$$

to duplicate the effect of  $P_i(\mathbf{Z})$  on  $\mathbf{r}^{(0)}$  with an expectation that  $\|P_i^2(\mathbf{Z}) \mathbf{r}^{(0)}\|_2$  is much smaller than  $\|P_i(\mathbf{Z}) \mathbf{r}^{(0)}\|_2$ . However, this frequently is not the case. The BiCGSTAB instead describes the residual vectors as

$$\bar{\mathbf{r}}^{(i)} = Q_i(\mathbf{Z}) P_i(\mathbf{Z}) \mathbf{r}^{(0)} \quad (3.51)$$

where  $Q_i(\mathbf{Z})$  are  $i^{\text{th}}$ -order polynomials in  $\mathbf{Z}$ .

$$Q_i(\mathbf{Z}) = (\mathbf{I} - \gamma_1 \mathbf{Z}) (\mathbf{I} - \gamma_2 \mathbf{Z}) \dots (\mathbf{I} - \gamma_i \mathbf{Z}) \quad (3.52)$$

$\gamma_i$  are suitable coefficients to be found at each iteration to minimise the residual norm. From Equations 3.52, 3.46, 3.44 and 3.40, the new form of Equation 3.51 is

$$\begin{aligned} \bar{\mathbf{r}}^{(i)} &= Q_i(\mathbf{Z}) P_i(\mathbf{Z}) \mathbf{r}^{(0)} \\ &= (\mathbf{I} - \gamma_i \mathbf{Z}) Q_{i-1}(\mathbf{Z}) \left( \mathbf{r}^{(i-1)} - \alpha_i \mathbf{Z} \mathbf{d}^{(i)} \right) \\ &= (\mathbf{I} - \gamma_i \mathbf{Z}) Q_{i-1}(\mathbf{Z}) (P_{i-1}(\mathbf{Z}) - \alpha_i \mathbf{Z} T_{i-1}(\mathbf{Z})) \mathbf{r}^{(0)}. \end{aligned} \quad (3.53)$$

Similarly, the BiCGSTAB defines the direction vector  $\bar{\mathbf{d}}^{(i+1)}$  as

$$\begin{aligned} \bar{\mathbf{d}}^{(i+1)} &= Q_i(\mathbf{Z}) T_i(\mathbf{Z}) \mathbf{r}^{(0)} \\ &= Q_i(\mathbf{Z}) \left( \mathbf{r}^{(i)} + \beta_{i+1} \mathbf{d}^{(i)} \right) \\ &= Q_i(\mathbf{Z}) (P_i(\mathbf{Z}) + \beta_{i+1} T_{i-1}(\mathbf{Z})) \mathbf{r}^{(0)}. \end{aligned} \quad (3.54)$$

Equations 3.53-3.54 can be written in the form of a recurrence relation as

$$\bar{\mathbf{r}}^{(i)} = (\mathbf{I} - \gamma_i \mathbf{Z}) \left( \bar{\mathbf{r}}^{(i-1)} - \alpha_i \mathbf{Z} \bar{\mathbf{d}}^{(i)} \right) \quad (3.55)$$

$$\bar{\mathbf{d}}^{(i)} = \bar{\mathbf{r}}^{(i-1)} + \beta_i (\mathbf{I} - \gamma_{i-1} \mathbf{Z}) \bar{\mathbf{d}}^{(i-1)}. \quad (3.56)$$

To represent the approximate solution in a recurrence relation, we define

$$\mathbf{s}^{(i)} = \bar{\mathbf{r}}^{(i-1)} - \alpha_i \mathbf{Z} \bar{\mathbf{d}}^{(i)}. \quad (3.57)$$

Consequently, the residual and the approximation are rewritten

$$\bar{\mathbf{r}}^{(i)} = \bar{\mathbf{r}}^{(i-1)} - \alpha_i \mathbf{Z} \bar{\mathbf{d}}^{(i)} - \gamma_i \mathbf{Z} \mathbf{s}^{(i)} \quad (3.58)$$

$$\mathbf{x}^{(i)} = \mathbf{x}^{(i-1)} + \alpha_i \bar{\mathbf{d}}^{(i)} + \gamma_i \mathbf{s}^{(i)}. \quad (3.59)$$

The values of  $\alpha_i$  and  $\beta_i$  can be derived from their definition in the BiCG while the values of  $\gamma_i$  are chosen to minimise the Euclidean norm of  $(\mathbf{I} - \gamma_i \mathbf{Z}) \mathbf{s}^{(i)}$ . Details about the derivation of the constants are discussed in [39]. The BiCGSTAB requires two MVPs within each iteration. The algorithm is outlined in Algorithm 3.6.

### 3.2.5 Generalised minimal residual method

The generalised minimal residual method [40] is an iterative technique for the solution of nonsymmetric linear problems. The principles of the GMRES are the establishment of the approximate solution using the Krylov subspace and the minimisation of the residual norm at each iteration. The GMRES is extensively applied for the solution of linear systems because of its superior convergence rate, resulting in a small number of iterations  $i$  ( $i \ll N$ ) required to obtain an acceptable solution. The construction of the GMRES iterates are represented using the Arnoldi vectors in Equation 3.15

$$\mathbf{x}^{(i)} = \mathbf{x}^{(0)} + y_1 \mathbf{q}_1 + y_2 \mathbf{q}_2 + \cdots + y_i \mathbf{q}_i \quad (3.60)$$

Equation 3.60 can be rewritten as

$$\mathbf{x}^{(i)} = \mathbf{x}^{(0)} + \mathbf{Q}_i \mathbf{y}_i \quad (3.61)$$

where  $\mathbf{Q}_i$  is the matrix defined in Equation 3.19 and  $\mathbf{y}_i$  is an  $i$ -element vector containing the coefficients  $y_j$  ( $1 \leq j \leq i$ )

$$\mathbf{y}_i = \begin{pmatrix} y_1 & y_2 & \cdots & y_i \end{pmatrix}^T. \quad (3.62)$$

Therefore, the residual at iteration  $i$  is

$$\begin{aligned} \mathbf{r}^{(i)} &= \mathbf{v} - \mathbf{Z} \left( \mathbf{x}^{(0)} + \mathbf{Q}_i \mathbf{y}_i \right) \\ &= \mathbf{r}^{(0)} - \mathbf{Z} \mathbf{Q}_i \mathbf{y}_i. \end{aligned} \quad (3.63)$$

Substituting the relation between the partial Hessenberg matrix and the matrix  $\mathbf{Q}$  in consecutive iterations in Equation 3.21 into Equation 3.63, we obtain

$$\mathbf{r}^{(i)} = \mathbf{r}^{(0)} - \mathbf{Q}_{i+1} \tilde{\mathbf{H}} \mathbf{y}_i. \quad (3.64)$$

If the first Arnoldi vector is defined as

$$\mathbf{q}_1 = \frac{\mathbf{r}^{(0)}}{\rho_0} \quad (3.65)$$

where  $\rho_0 = \|\mathbf{r}^{(0)}\|$ , the initial residual becomes

$$\begin{aligned} \mathbf{r}^{(0)} &= \rho_0 \mathbf{q}_1 \\ &= \rho_0 \mathbf{Q}_{i+1} \mathbf{e}_1 \end{aligned} \quad (3.66)$$

where  $\mathbf{e}_1 = \begin{pmatrix} 1 & 0 & \dots & 0 \end{pmatrix}^T$ . Substituting Equation 3.66 into 3.64, the residual can be interpreted as

$$\mathbf{r}^{(i)} = \mathbf{Q}_{i+1} \left( \rho_0 \mathbf{e}_1 - \tilde{\mathbf{H}} \mathbf{y}_i \right). \quad (3.67)$$

Because  $\mathbf{Q}$  is an orthonormal matrix, the residual norm at iteration  $i$  becomes

$$\|\mathbf{r}^{(i)}\|_2 = \|\rho_0 \mathbf{e}_1 - \tilde{\mathbf{H}} \mathbf{y}_i\|_2. \quad (3.68)$$

The GMRES aims to minimise Equation 3.68 by solving a least squares problem to find an optimal  $\mathbf{y}_i$ . The GMRES method is outlined in Algorithm 3.7.

The main disadvantage of the GMRES is the linear increase of the storage for the Arnoldi vectors and increase in the work required for the solution of a least-squares problem within each iteration. In some cases, the solution requires a large number of iterations, leading to a prohibitive cost of storage and workload per iteration. To reduce the undesired cost, the original GMRES is modified to allow a restart scheme after  $m$  iterations. However, it remains a challenge to select an appropriate value for  $m$ .

### 3.3 Stationary iterative methods

Stationary iterative methods approximate the solution of Equation 3.1 as a stationary point of a fixed-point iteration.

$$\mathbf{x}^{(i)} = \mathcal{F} \left( \mathbf{x}^{(i-1)} \right) \quad (3.69)$$



**Algorithm 3.7** The generalised minimal residual method.

---

 $\mathbf{x}^{(0)}$  = initial guess $\mathbf{r}^{(0)} = \mathbf{v} - \mathbf{Z}\mathbf{x}^{(0)}$  $\rho_0 = \|\mathbf{r}^{(0)}\|_2$  $\mathbf{q}_1 = \frac{\mathbf{r}^{(0)}}{\rho_0}$ For  $i = 1 \cdots n$      $\mathbf{u} = \mathbf{Z}\mathbf{q}_i$     For  $j = 1 \cdots i$          $h_{j,i} = \langle \mathbf{u}, \mathbf{q}_j \rangle$          $\mathbf{u} = \mathbf{u} - h_{j,i}\mathbf{q}_j$ 

End

 $h_{i+1,i} = \|\mathbf{u}\|_2$      $\mathbf{q}_{i+1} = \frac{\mathbf{u}}{h_{i+1,i}}$     Find  $\mathbf{y}$  that minimises  $\|\rho_0\mathbf{e}_1 - \tilde{\mathbf{H}}\mathbf{y}\|_2$      $\mathbf{x}^{(i)} = \mathbf{x}^{(0)} + \mathbf{Q}_i\mathbf{y}$     If  $\|\mathbf{r}^{(i)}\|_2 < \text{tolerance}$ 

Quit

End

End

---

For the satisfaction of the stationary condition, it generally makes sense to choose a fixed point iteration where the mapping  $\mathcal{F}$  is affine. The fixed point iteration can be expressed using a splitting of matrix  $\mathbf{Z}$

$$\mathbf{Z} = \mathbf{P} - \mathbf{K} \quad (3.70)$$

where  $\mathbf{P}$  is a nonsingular matrix. Substituting Equation 3.70 into Equation 3.1, we obtain

$$\mathbf{P}\mathbf{x} = \mathbf{K}\mathbf{x} + \mathbf{v} \quad (3.71)$$

or, equivalently

$$\mathbf{x} = \mathbf{P}^{-1}(\mathbf{K}\mathbf{x} + \mathbf{v}). \quad (3.72)$$

Arising from Equation 3.72, stationary iterative methods generate successive approximations by the process

$$\mathbf{x}^{(i)} = \mathbf{M}\mathbf{x}^{(i-1)} + \mathbf{b} \quad (3.73)$$

where the matrix  $\mathbf{M}$  and the vector  $\mathbf{b}$  are constant and are defined as

$$\mathbf{M} = \mathbf{P}^{-1}\mathbf{K} \quad (3.74)$$

$$\mathbf{b} = \mathbf{P}^{-1}\mathbf{v}. \quad (3.75)$$

The matrix  $\mathbf{M}$  is called the iteration matrix. All stationary iterative schemes can be expressed using the form of Equation 3.73. The choice of the iteration matrix  $\mathbf{M}$  defines different stationary techniques. Assuming that  $\mathbf{x}^{\text{exact}}$  is the exact solution of Equation 3.1, we denote the error vectors at iteration  $(i-1)$  and  $i$  as follows

$$\boldsymbol{\varepsilon}^{(i-1)} = \mathbf{x}^{\text{exact}} - \mathbf{x}^{(i-1)} \quad (3.76)$$

$$\boldsymbol{\varepsilon}^{(i)} = \mathbf{x}^{\text{exact}} - \mathbf{x}^{(i)}. \quad (3.77)$$

Substituting Equation 3.76-3.77 into 3.73, we obtain

$$\mathbf{x}^{\text{exact}} - \boldsymbol{\varepsilon}^{(i)} = \mathbf{M}(\mathbf{x}^{\text{exact}} - \boldsymbol{\varepsilon}^{(i-1)}) + \mathbf{b}. \quad (3.78)$$

Substituting Equation 3.70, 3.74 and 3.75 into 3.78 results in

$$\begin{aligned}
 \boldsymbol{\varepsilon}^{(i)} &= \mathbf{M}\boldsymbol{\varepsilon}^{(i-1)} - \mathbf{M}\mathbf{x}^{\text{exact}} + \mathbf{x}^{\text{exact}} - \mathbf{b} \\
 &= \mathbf{M}\boldsymbol{\varepsilon}^{(i-1)} - (\mathbf{M} - \mathbf{I})\mathbf{x}^{\text{exact}} - \mathbf{P}^{-1}\mathbf{v} \\
 &= \mathbf{M}\boldsymbol{\varepsilon}^{(i-1)} - \mathbf{P}^{-1}(\mathbf{P}(\mathbf{M} - \mathbf{I})\mathbf{x}^{\text{exact}} + \mathbf{v}) \\
 &= \mathbf{M}\boldsymbol{\varepsilon}^{(i-1)} - \mathbf{P}^{-1}((\mathbf{K} - \mathbf{P})\mathbf{x}^{\text{exact}} + \mathbf{v}) \\
 &= \mathbf{M}\boldsymbol{\varepsilon}^{(i-1)} - \mathbf{P}^{-1}(-\mathbf{Z}\mathbf{x}^{\text{exact}} + \mathbf{v}) \\
 &= \mathbf{M}\boldsymbol{\varepsilon}^{(i-1)}.
 \end{aligned} \tag{3.79}$$

Therefore, the relation between the successive errors can be expressed as

$$\boldsymbol{\varepsilon}^{(i)} = \mathbf{M}\boldsymbol{\varepsilon}^{(i-1)} \tag{3.80}$$

or, equivalently

$$\boldsymbol{\varepsilon}^{(i)} = \mathbf{M}^i \boldsymbol{\varepsilon}^{(0)}. \tag{3.81}$$

Thus, the convergence rate of a stationary iterative method depends on the spectral radius of the iteration matrix  $\mathbf{M}$ . The spectral radius is defined as

$$\rho(\mathbf{M}) = \max_{i=1}^N (|\lambda_i|) \tag{3.82}$$

where  $\lambda_i$  ( $1 \leq i \leq N$ ) are the eigenvalues of  $\mathbf{M}$ . To be able to converge, a stationary method must satisfy the following condition

$$\rho(\mathbf{M}) < 1. \tag{3.83}$$

At this stage, we give another decomposition of the matrix  $\mathbf{Z}$ . This definition will be repeatedly used in the rest of this section. The matrix  $\mathbf{Z}$  can be split into 3 component matrices

$$\mathbf{Z} = \mathbf{U} + \mathbf{L} + \mathbf{D} \tag{3.84}$$

where  $\mathbf{U}$  and  $\mathbf{L}$  are the strictly upper and lower triangular submatrices of  $\mathbf{Z}$ , respectively while  $\mathbf{D}$  is the diagonal matrix of  $\mathbf{Z}$

$$\mathbf{U} = \begin{pmatrix} 0 & z_{1,2} & \cdots & z_{1,N} \\ 0 & 0 & \cdots & z_{2,N} \\ \vdots & \vdots & \ddots & \vdots \\ 0 & 0 & \cdots & 0 \end{pmatrix} \tag{3.85}$$

$$\mathbf{L} = \begin{pmatrix} 0 & 0 & \cdots & 0 \\ z_{2,1} & 0 & \cdots & 0 \\ \vdots & \vdots & \ddots & \vdots \\ z_{N,1} & z_{N,2} & \cdots & 0 \end{pmatrix} \quad (3.86)$$

$$\mathbf{D} = \begin{pmatrix} z_{1,1} & 0 & \cdots & 0 \\ 0 & z_{2,2} & \cdots & 0 \\ \vdots & \vdots & \ddots & \vdots \\ 0 & 0 & 0 & z_{N,N} \end{pmatrix} \quad (3.87)$$

### 3.3.1 Jacobi method

For the construction of the Jacobi method, we place Equation 3.84 into 3.1 as follows

$$\begin{aligned} \mathbf{Z}\mathbf{x} &= \mathbf{v} \\ (\mathbf{U} + \mathbf{D} + \mathbf{L})\mathbf{x} &= \mathbf{v} \\ \mathbf{x} &= -\mathbf{D}^{-1}(\mathbf{U} + \mathbf{L})\mathbf{x} + \mathbf{D}^{-1}\mathbf{v}. \end{aligned} \quad (3.88)$$

For the Jacobi method, the definitions of the iteration matrix  $\mathbf{M}$  and the vector  $\mathbf{b}$  are

$$\mathbf{M} = -\mathbf{D}^{-1}(\mathbf{U} + \mathbf{L}) \quad (3.89)$$

$$\mathbf{b} = \mathbf{D}^{-1}\mathbf{v}. \quad (3.90)$$

The Jacobi iteration can be generalised by an updating process given by

$$\mathbf{x}^{(i+1)} = -\mathbf{D}^{-1}(\mathbf{U} + \mathbf{L})\mathbf{x}^{(i)} + \mathbf{D}^{-1}\mathbf{v}. \quad (3.91)$$

Equation 3.91 can be expressed in component-wise form as

$$x_m^{(i+1)} = \frac{v_m - \sum_{n \neq m} z_{m,n} x_n^{(i)}}{z_{m,m}} \quad m = 1, \dots, N \quad (3.92)$$

where  $z_{m,n}$ ,  $x_m$ ,  $v_m$  are elements of  $\mathbf{Z}$ ,  $\mathbf{x}$  and  $\mathbf{v}$ , respectively. Equation 3.92 implies that each element in the approximate solution  $\mathbf{x}$  is treated independently. Therefore, the updating process for each of the elements can be performed simultaneously. This leads to an ease of parallelising the method. Though the Jacobi method is easy to understand and implement, the slow and irregular convergence rate is its main drawback. The Jacobi method is described in Algorithm 3.8.

---

**Algorithm 3.8** The Jacobi method.

---

$\mathbf{x}^{(0)}$  = initial guess  
For  $i = 1, 2, \dots$   
  For  $m = 1 \cdots N$   
     $a = 0$   
    For  $n = 1 \cdots N$   
      If  $(m \neq n)$   
         $a = a + z_{m,n}x_n^{(i-1)}$   
      End  
    End  
     $x_m^{(i)} = \frac{v_m - a}{z_{m,m}}$   
  End  
  If  $\frac{\|\mathbf{v} - \mathbf{Z}\mathbf{x}^{(i)}\|_2}{\|\mathbf{v}\|_2} < \text{tolerance}$   
    Quit  
  End  
End

---

---

**Algorithm 3.9** The Gauss-Seidel method.

---

$\mathbf{x}^{(0)}$  = initial guess  
For  $i = 1, 2, \dots$   
  For  $m = 1 \cdots N$   
     $a = 0$   
    For  $n = 1 \cdots m - 1$   
       $a = a + z_{m,n}x_n^{(i)}$   
    End  
    For  $n = m + 1 \cdots N$   
       $a = a + z_{m,n}x_n^{(i-1)}$   
    End  
     $x_m^{(i)} = \frac{v_m - a}{z_{m,m}}$   
  End  
  If  $\frac{\|\mathbf{v} - \mathbf{Z}\mathbf{x}^{(i)}\|_2}{\|\mathbf{v}\|_2} < \text{tolerance}$   
    Quit  
  End  
End

---

### 3.3.2 Gauss-Seidel method

The Gauss-Seidel method is given by the re-arrangement of Equation 3.88 to obtain

$$\mathbf{x} = -(\mathbf{L} + \mathbf{D})^{-1} \mathbf{U}\mathbf{x} + (\mathbf{L} + \mathbf{D})^{-1} \mathbf{v}. \quad (3.93)$$

For the Gauss-Seidel method, the iteration matrix  $\mathbf{M}$  and vector  $\mathbf{b}$  are defined as

$$\mathbf{M} = -(\mathbf{L} + \mathbf{D})^{-1} \mathbf{U} \quad (3.94)$$

$$\mathbf{b} = (\mathbf{L} + \mathbf{D})^{-1} \mathbf{v}. \quad (3.95)$$

Consequently, the updating process for the Gauss-Seidel method is given by

$$\mathbf{x}^{(i+1)} = -(\mathbf{L} + \mathbf{D})^{-1} \mathbf{U}\mathbf{x}^{(i)} + (\mathbf{L} + \mathbf{D})^{-1} \mathbf{v}. \quad (3.96)$$

The component-wise form of the Gauss-Seidel method can be written as

$$x_m^{(i+1)} = \frac{1}{z_{m,m}} \left( v_m - \sum_{n < m} z_{m,n} x_n^{(i+1)} - \sum_{n > m} z_{m,n} x_n^{(i)} \right) \quad m = 1 \cdots N. \quad (3.97)$$

It is noticed that the most recently updated components  $x_m$  are used where possible in the Gauss-Seidel method. Thus, the Gauss-Seidel method generally converges faster than the Jacobi method. The sequential updating process due to the use of the most updated components may cause difficulties in parallelising the Gauss-Seidel method. The Gauss-Seidel algorithm is outlined in Algorithm 3.9.

### 3.3.3 Successive overrelaxation method

The derivation of the successive overrelaxation (SOR) method from Equation 3.1 is presented as

$$\begin{aligned} \mathbf{Z}\mathbf{x} &= \mathbf{v} \\ \varpi(\mathbf{D} + \mathbf{L} + \mathbf{U})\mathbf{x} &= \varpi\mathbf{v} \\ (\mathbf{D} + \varpi\mathbf{L})\mathbf{x} &= ((1 - \varpi)\mathbf{D} - \varpi\mathbf{U})\mathbf{x} + \varpi\mathbf{v} \\ \mathbf{x} &= (\mathbf{D} + \varpi\mathbf{L})^{-1} ((1 - \varpi)\mathbf{D} - \varpi\mathbf{U})\mathbf{x} + \varpi\mathbf{v}. \end{aligned} \quad (3.98)$$

The iteration matrix  $\mathbf{M}$  and the vector  $\mathbf{b}$  are defined as follows

$$\mathbf{M} = (\mathbf{D} + \varpi\mathbf{L})^{-1} ((1 - \varpi)\mathbf{D} - \varpi\mathbf{U}) \quad (3.99)$$

$$\mathbf{b} = \varpi(\mathbf{D} + \varpi\mathbf{L})^{-1} \mathbf{v}. \quad (3.100)$$

---

**Algorithm 3.10** The successive overrelaxation method.

---

$\mathbf{x}^{(0)}$  = initial guess  
For  $i = 1, 2, \dots$   
  For  $m = 1 \dots N$   
     $a = 0$   
    For  $n = 1 \dots m - 1$   
       $a = a + z_{m,n}x_n^{(i)}$   
    End  
    For  $n = m + 1 \dots N$   
       $a = a + z_{m,n}x_n^{(i-1)}$   
    End  
     $a = \frac{v_m - a}{z_{m,m}}$   
     $x_m^{(i)} = (1 - \varpi) x_m^{(i-1)} + \varpi a$   
  End  
  If  $\frac{\|\mathbf{v} - \mathbf{Z}\mathbf{x}^{(i)}\|_2}{\|\mathbf{v}\|_2} < \text{tolerance}$   
    Quit  
  End  
End

---

Therefore, the updating process for the SOR is

$$\mathbf{x}^{(i+1)} = (\mathbf{D} + \varpi \mathbf{L})^{-1} \left( ((1 - \varpi) \mathbf{D} - \varpi \mathbf{U}) \mathbf{x}^{(i)} + \varpi \mathbf{v} \right) \quad (3.101)$$

where the constant  $\varpi$  denotes the relaxation factor. The SOR in component-wise form is

$$x_m^{(i+1)} = (1 - \varpi) x_m^{(i)} + \frac{\varpi}{z_{m,m}} \left( v_m - \sum_{n < m} z_{m,n} x_n^{(i+1)} - \sum_{n > m} z_{m,n} x_n^{(i)} \right) \quad m = 1 \cdots N. \quad (3.102)$$

When the relaxation factor is 1, the SOR becomes the Gauss-Seidel method. In other words, the application of extrapolation, using a weighted average between the current and the previous iterate, to the Gauss-Seidel method results in the SOR, often leading to a better spectral radius of the iteration matrix. Thus, the convergence rate of the SOR is usually faster than that of the Gauss-Seidel. Choosing the optimal value of  $\varpi$  to maximise the convergence rate of the SOR is not possible in general. Some suggestions for the determination of the value of  $\varpi$  can be found in [78, 79]. The combination of two SOR sweeps, which update the unknowns in reverse directions, forms the symmetric successive overrelaxation (SSOR) method.

### 3.3.4 Forward backward method

The Krylov subspace iterative methods are favourable due to their robustness and their assurance of being convergent and achieving the exact solution within at most  $N$  iterations. However, the Krylov subspace methods may require a large number of iterations to obtain a solution with a desired accuracy for a large system because of being purely algebraic and lacking physical intuition. In addition, the implementation process of the Krylov subspace iterations are mathematically more complicated than that of the stationary iterative methods. Recently, much research effort has focused on the development of stationary solvers for application to EM problems [64, 65, 80, 81]. In order to enhance the convergence rate of stationary methods, some EM characteristics are implicitly embedded into the operating procedure.

For illustration of the EM mechanism in such stationary methods, we investigate a 1-D propagation problem shown in Figure 3.1a where the source located in the upper left corner radiates the fields in the entire region. The total fields in free-space are expected to be computed as would be the case for wireless network planning. For the calculation of the total fields, the equivalent surface currents are required. Applying the MoM to the problem in Figure 3.1a leads to the discretisation of the 1D dielectric surface into small flat segments in Figure 3.1b. Assuming that we examine the surface current of the red discretisation  $m$  in Figure 3.1b, the total current consists of two components

$$x_m = x_m^{\text{for-scat}} + x_m^{\text{back-scat}} \quad (3.103)$$



where  $x_m^{\text{for-scat}}$  denotes the current due to the incident fields and forward contribution or scattering from the discretisations in front of the discretisation  $m$ , while  $x_m^{\text{back-scat}}$  stands for the current due to backscattering from discretisations beyond the discretisation  $m$ . Vectors containing information about the forward and backward scattering are denoted by  $\mathbf{x}^{\text{for-scat}}$  and  $\mathbf{x}^{\text{back-scat}}$ , respectively

$$\begin{aligned}\mathbf{x}^{\text{for-scat}} &= \begin{pmatrix} x_1^{\text{for-scat}} & \dots & x_N^{\text{for-scat}} \end{pmatrix}^T \\ \mathbf{x}^{\text{back-scat}} &= \begin{pmatrix} x_1^{\text{back-scat}} & \dots & x_N^{\text{back-scat}} \end{pmatrix}^T\end{aligned}\quad (3.104)$$

and

$$\mathbf{x} = \mathbf{x}^{\text{for-scat}} + \mathbf{x}^{\text{back-scat}} \quad (3.105)$$

The forward scattering current  $\mathbf{x}^{\text{for-scat}}$  can be computed from knowledge about the backward scattering current  $\mathbf{x}^{\text{back-scat}}$  by solving the Volterra integral equation in [64]. Likewise, the backward scattering current  $\mathbf{x}^{\text{back-scat}}$  can be estimated by the value of the forward scattering current  $\mathbf{x}^{\text{for-scat}}$ . The procedure of sequentially solving the  $\mathbf{x}^{\text{for-scat}}$  and  $\mathbf{x}^{\text{back-scat}}$  results in a good approximation of a solution  $\mathbf{x}$ . This forms the basic idea of the forward backward method which consists of two sweeps in each iteration. The forward sweep is responsible for the computation of the  $\mathbf{x}^{\text{for-scat}}$  contribution while the backward sweep computes the value of the  $\mathbf{x}^{\text{back-scat}}$  contribution. In the forward sweep, the current discretisations are computed sequentially with respect to the propagation direction. Similarly, they are computed sequentially in the reverse direction for the backward sweep. This process of updating currents imitates the physical process of wave propagation, leading to a better convergence rate of the forward backward method. The method was simultaneously proposed by Holliday [64], and Kapp and Brown [80], and is termed by the forward backward method (FBM) and the method of ordered multiple interactions (MOMI), respectively. According to [65], the current discretisation at iteration  $i$  can be computed as follows

$$\begin{aligned}\text{forward sweep:} \quad & (\mathbf{D} + \mathbf{L}) \mathbf{x}^{\text{for-scat}^{(i)}} = \mathbf{v} - \mathbf{L} \mathbf{x}^{\text{back-scat}^{(i-1)}} \\ \text{backward sweep:} \quad & (\mathbf{D} + \mathbf{U}) \mathbf{x}^{\text{back-scat}^{(i)}} = -\mathbf{U} \mathbf{x}^{\text{for-scat}^{(i)}}.\end{aligned}\quad (3.106)$$

The summation of the backward part at the  $(i-1)^{\text{th}}$  iteration and the forward part at the  $i^{\text{th}}$  iteration of Equation 3.106 leads to

$$\begin{aligned}\mathbf{D} \left( \mathbf{x}^{\text{for-scat}^{(i)}} + \mathbf{x}^{\text{back-scat}^{(i-1)}} \right) &= \mathbf{v} - \mathbf{L} \left( \mathbf{x}^{\text{for-scat}^{(i)}} + \mathbf{x}^{\text{back-scat}^{(i-1)}} \right) \\ &\quad - \mathbf{U} \left( \mathbf{x}^{\text{for-scat}^{(i-1)}} + \mathbf{x}^{\text{back-scat}^{(i-1)}} \right).\end{aligned}\quad (3.107)$$

In the similar manner, we can derive the following equation

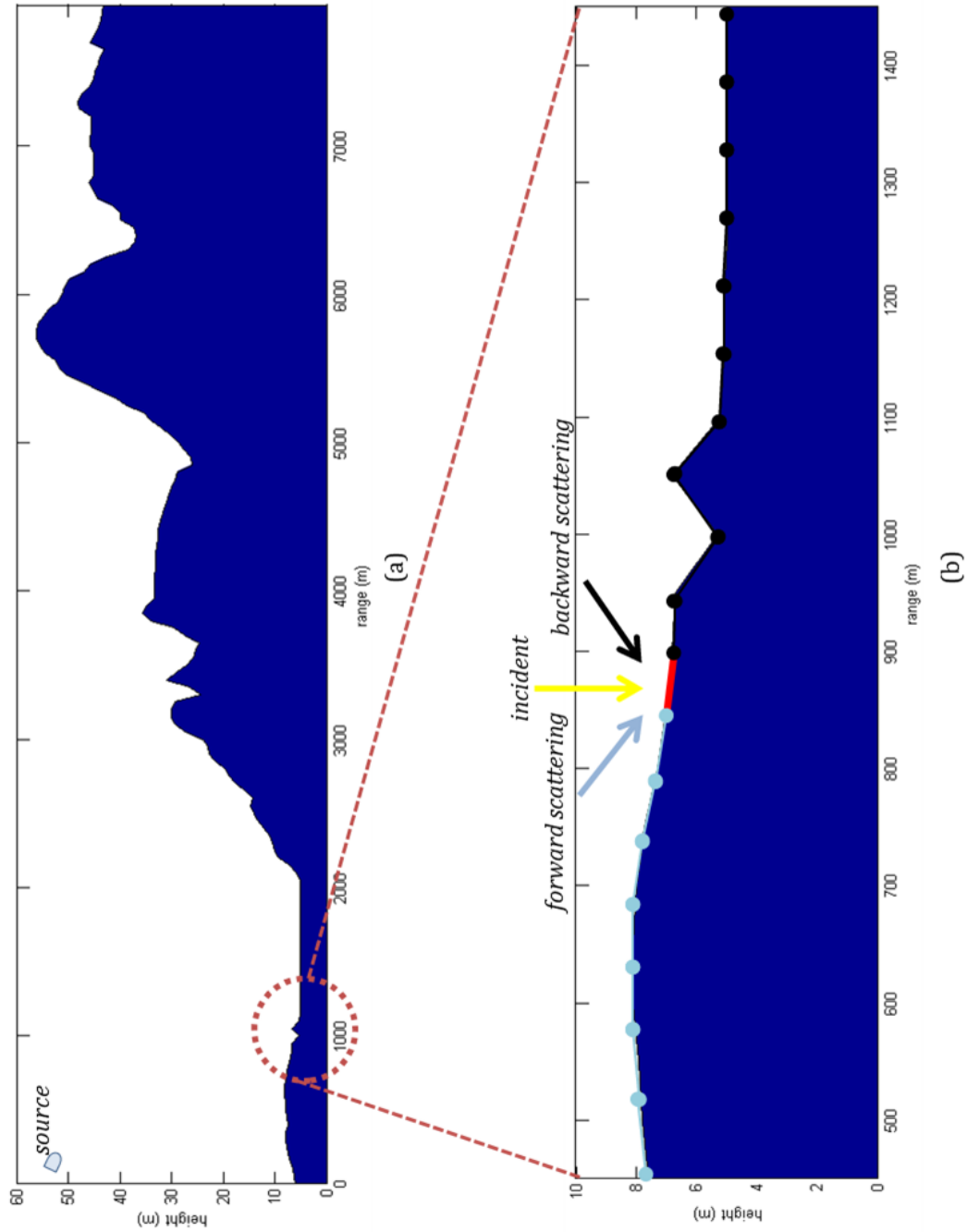


**Figure 3.1:** Forward and backward scattering in the forward backward method. Coloured segments refer to pulse basis function domains which are locally flat segments. Red segment is a segment under consideration. Blue segments refer to segments nearer to the source than the segment under consideration, causing forward scattering. Black segments refer to basis functions further away from the source, generating backward scattering.

$$\begin{aligned} \mathbf{D} \left( \mathbf{x}^{\text{for-scat}^{(i)}} + \mathbf{x}^{\text{back-scat}^{(i)}} \right) &= \mathbf{v} - \mathbf{L} \left( \mathbf{x}^{\text{for-scat}^{(i)}} + \mathbf{x}^{\text{back-scat}^{(i-1)}} \right) \\ &\quad - \mathbf{U} \left( \mathbf{x}^{\text{for-scat}^{(i)}} + \mathbf{x}^{\text{back-scat}^{(i)}} \right). \end{aligned} \quad (3.108)$$

Consequently, the FBM is re-arranged into the following form

$$\begin{aligned} \text{forward sweep:} \quad \mathbf{D}\mathbf{x}^{(i-1/2)} &= \mathbf{v} - \mathbf{L}\mathbf{x}^{(i-1/2)} - \mathbf{U}\mathbf{x}^{(i-1)} \\ \text{backward sweep:} \quad \mathbf{D}\mathbf{x}^{(i)} &= \mathbf{v} - \mathbf{L}\mathbf{x}^{(i-1/2)} - \mathbf{U}\mathbf{x}^{(i)} \end{aligned} \quad (3.109)$$

where

$$\begin{aligned} \mathbf{x}^{(i-1)} &= \mathbf{x}^{\text{for-scat}^{(i-1)}} + \mathbf{x}^{\text{back-scat}^{(i-1)}} \\ \mathbf{x}^{(i-1/2)} &= \mathbf{x}^{\text{for-scat}^{(i)}} + \mathbf{x}^{\text{back-scat}^{(i-1)}} \\ \mathbf{x}^{(i)} &= \mathbf{x}^{\text{for-scat}^{(i)}} + \mathbf{x}^{\text{back-scat}^{(i)}}. \end{aligned} \quad (3.110)$$

The FBM in element-wise form is

$$\begin{aligned} \text{forward sweep:} \quad x_m^{(i-1/2)} &= \frac{1}{z_{m,m}} \left( v_m - \sum_{n < m} z_{m,n} x_n^{(i-1/2)} - \sum_{n > m} z_{m,n} x_n^{(i-1)} \right) \\ m &= 1 \cdots N \\ \text{backward sweep:} \quad x_m^{(i)} &= \frac{1}{z_{m,m}} \left( v_m - \sum_{n < m} z_{m,n} x_n^{(i-1/2)} - \sum_{n > m} z_{m,n} x_n^{(i)} \right) \\ m &= N \cdots 1 \end{aligned} \quad (3.111)$$

Generally, the current discretisations are sequentially approximated in two sweeps and the computation of each discretisation uses the most up-to-date information from other discretisations. Comparing Equation 3.111 and 3.97 draws a conclusion that the FBM comprises of two separate Gauss-Seidel iterations which are in reverse directions. In other words, the FBM is equivalent to the SSOR with  $\varpi = 1$ . This leads to a small number of iterations required to achieve a desired solution. The advantage has been demonstrated in numerous 1-D applications for random rough surface scattering problems [65, 68, 69] or 2-D wave propagation [82].

### 3.3.5 Block forward backward method

The block forward backward method (BFBM) is an extension of the FBM for the improvement of the convergence rate in certain cases. Though the performance of the FBM is excellent due to the requirement of a small number of iterations, it is only applicable to low-grazing angle scattering problems or rural propagation without abrupt changes in the height of terrain profile. Some examples of abrupt changes in the terrain surfaces are the appearance of a ship over a sea surface in Figure 3.2a, the shape edges of buildings in

a terrain profile for urban areas in Figure 3.2b or very rough surface scattering problems. Abrupt changes or obstacles along the propagation path cause strong local scattering effects that cannot be computed using the forward backward process. The fields must be computed exactly in these regions before the iterative process can progress further. This is done using a block technique which inverts a local sub-matrix, implicitly incorporating all backward and forward scattering within the obstacle. An alternative way of thinking about the effect of the block forward backward method is to consider that its use is equivalent to preconditioning the linear system before applying the forward backward method. The BFBM applies the FBM scheme to groups of current discretisations. Instead of using the discretisation-by-discretisation updating scheme in the FBM, the BFBM assembles current discretisations into groups and then updates the surface currents using the group-by-group scheme shown in Figure 3.3. Assuming that the problem of  $N$  current discretisations are divided into  $M$  groups, the BFBM in group-wise form is

$$\begin{aligned}
 \text{forward sweep: } \quad \bar{\mathbf{x}}_m^{(i-1/2)} &= \bar{\mathbf{Z}}_{m,m}^{-1} \left( \bar{\mathbf{v}}_m - \sum_{n < m} \bar{\mathbf{Z}}_{m,n} \bar{\mathbf{x}}_n^{(i-1/2)} - \sum_{n > m} \bar{\mathbf{Z}}_{m,n} \bar{\mathbf{x}}_n^{(i-1)} \right) \\
 m &= 1 \cdots M \\
 \text{backward sweep: } \quad \bar{\mathbf{x}}_m^{(i)} &= \bar{\mathbf{Z}}_{m,m}^{-1} \left( \bar{\mathbf{v}}_m - \sum_{n < m} \bar{\mathbf{Z}}_{m,n} \bar{\mathbf{x}}_n^{(i-1/2)} - \sum_{n > m} \bar{\mathbf{Z}}_{m,n} \bar{\mathbf{x}}_n^{(i)} \right) \\
 m &= M \cdots 1
 \end{aligned} \tag{3.112}$$

where  $\bar{\mathbf{x}}_m$  is a vector containing information about current discretisations in group  $m$ ,  $\bar{\mathbf{v}}_m$  is a vector containing information about incident fields impinging on discretisations in group  $m$ .  $\bar{\mathbf{Z}}_{m,n}$  is a matrix containing information about interactions between discretisations in group  $m$  and those in group  $n$ . The representations of  $\mathbf{Z}$ ,  $\mathbf{x}$  and  $\mathbf{v}$  using  $\bar{\mathbf{Z}}_{m,n}$ ,  $\bar{\mathbf{x}}_m$  and  $\bar{\mathbf{v}}_m$  are

$$\mathbf{Z} = \begin{pmatrix} \bar{\mathbf{Z}}_{1,1} & \bar{\mathbf{Z}}_{1,2} & \cdots & \bar{\mathbf{Z}}_{1,M} \\ \bar{\mathbf{Z}}_{2,1} & \bar{\mathbf{Z}}_{2,2} & \cdots & \bar{\mathbf{Z}}_{2,M} \\ \vdots & \vdots & \ddots & \vdots \\ \bar{\mathbf{Z}}_{M,1} & \bar{\mathbf{Z}}_{M,2} & \cdots & \bar{\mathbf{Z}}_{M,M} \end{pmatrix} \tag{3.113}$$

$$\mathbf{x} = \begin{pmatrix} \bar{\mathbf{x}}_1 & \bar{\mathbf{x}}_2 & \cdots & \bar{\mathbf{x}}_M \end{pmatrix}^T \tag{3.114}$$

$$\mathbf{v} = \begin{pmatrix} \bar{\mathbf{v}}_1 & \bar{\mathbf{v}}_2 & \cdots & \bar{\mathbf{v}}_M \end{pmatrix}^T. \tag{3.115}$$

To derive the iteration matrix of the BFBM, we define the block-diagonal, block-upper-triangular and block-lower-triangular matrices as follows, respectively

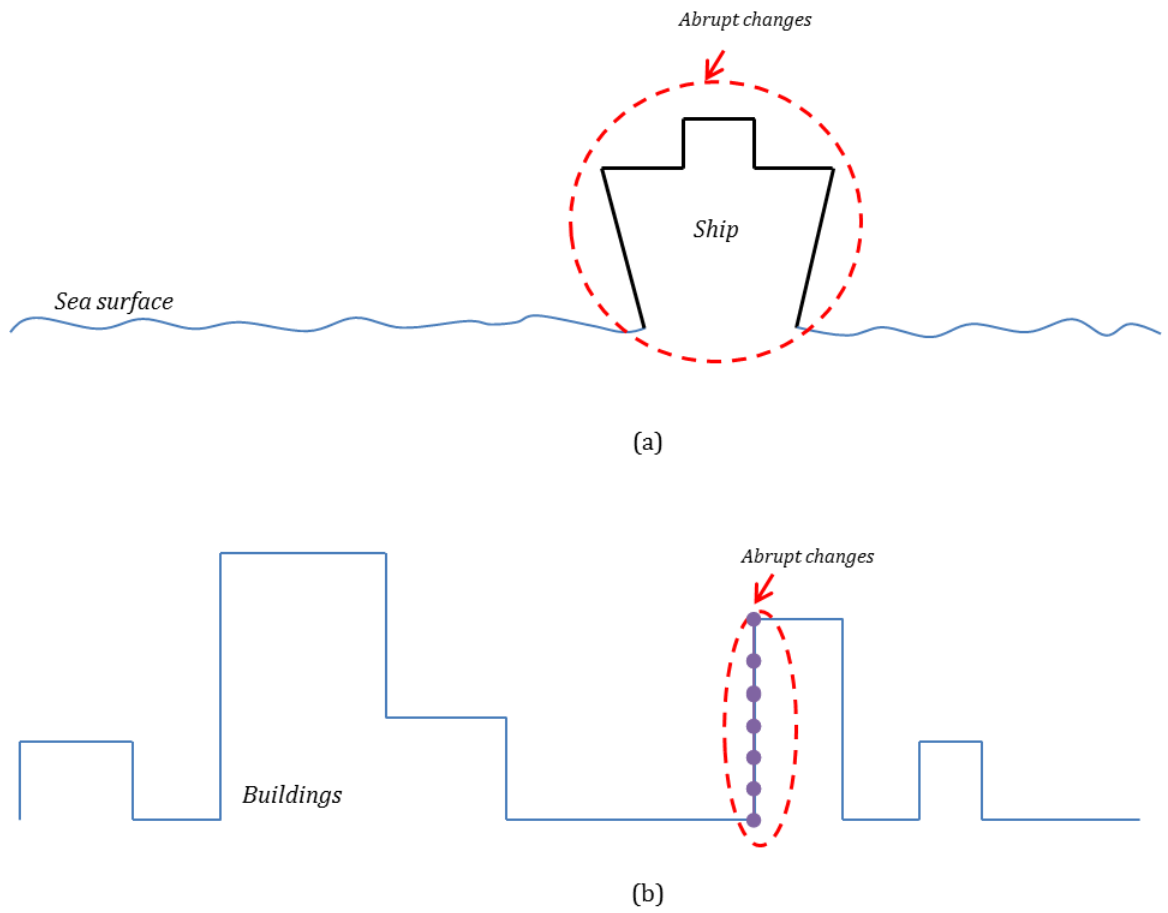


**Figure 3.2:** Block forward backward method for problems with abrupt changes in height.

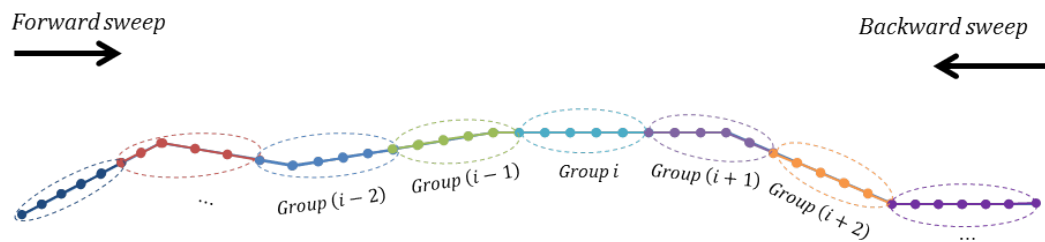


**Figure 3.3:** Group-by-group scheme of the block forward backward method.

$$\bar{\mathbf{D}} = \begin{pmatrix} \bar{\mathbf{Z}}_{1,1} & 0 & \cdots & 0 \\ 0 & \bar{\mathbf{Z}}_{2,2} & \cdots & 0 \\ \vdots & \vdots & \ddots & \vdots \\ 0 & 0 & \cdots & \bar{\mathbf{Z}}_{M,M} \end{pmatrix} \quad (3.116)$$

$$\bar{\mathbf{U}} = \begin{pmatrix} 0 & \bar{\mathbf{Z}}_{1,2} & \cdots & \bar{\mathbf{Z}}_{1,M} \\ 0 & 0 & \cdots & \bar{\mathbf{Z}}_{2,M} \\ \vdots & \vdots & \ddots & \vdots \\ 0 & 0 & \cdots & 0 \end{pmatrix} \quad (3.117)$$

$$\bar{\mathbf{L}} = \begin{pmatrix} 0 & 0 & \cdots & 0 \\ \bar{\mathbf{Z}}_{2,1} & 0 & \cdots & 0 \\ \vdots & \vdots & \ddots & \vdots \\ \bar{\mathbf{Z}}_{M,1} & \bar{\mathbf{Z}}_{M,2} & \cdots & 0 \end{pmatrix}. \quad (3.118)$$

We denote  $\bar{\mathbf{M}}^f$  and  $\bar{\mathbf{M}}^b$  as the iteration matrices for the forward sweep and for the backward sweep, respectively. They are defined as follows

$$\bar{\mathbf{M}}^f = -(\bar{\mathbf{L}} + \bar{\mathbf{D}})^{-1} \bar{\mathbf{U}} \quad (3.119)$$

$$\bar{\mathbf{M}}^b = -(\bar{\mathbf{U}} + \bar{\mathbf{D}})^{-1} \bar{\mathbf{L}}. \quad (3.120)$$

Thus, the iteration matrix of the BFBM is presented as

$$\mathbf{M} = \bar{\mathbf{M}}^f \bar{\mathbf{M}}^b. \quad (3.121)$$

The BFBM is applied for the solution of propagation in urban areas [82, 83], random rough surface scattering [65] or inhomogeneous problems [84]. The convergence rate of the BFBM increases with the size of the blocks but this creates a storage burden because the inverse of the block-diagonal matrices, which are used repeatedly in each iteration, need to be computed and stored for the efficient operation of the BFBM.

### 3.3.6 Buffered block forward backward method

The buffered block forward backward method is a modified version of the BFBM for application to 3-D scattering problems. Though the BFBM is extensively applied for 2-D problems, its application to 3-D is limited due to spurious edge effects which may

lead to the divergence of the BFBM. The artificial decomposition of the surface in the BFBM shown in Figure 3.4a causes unrealistic current densities with high values along the boundaries between groups or sub-regions, which are defined as specific physical areas on the surface of the problem. This phenomenon is termed the spurious edge effect and is demonstrated later in Section 3.3.6.2. To minimise this undesired edge effect, the BBFB [67, 81, 85] introduces local buffer regions for each group or sub-region. There are two sweeps in each iteration of the BBFB: the forward sweep and the backward sweep. It is noted that the associated buffer regions for the same sub-region are different in the forward sweep and the backward sweep, and they are chosen to be the area following the sub-region with regard to the marching direction as shown in Figure 3.4b,c. Similar to the BFBM, the current discretisations are updated sequentially from the sub-region 1 to  $M$  as the BBFB marches across the surface of the scatterer in the forward sweep. In the backward sweep, the current discretisations are updated in the reverse direction from the sub-region  $M$  to 1. The forward and backward sweeps of the BBFB are illustrated in the following matrix equations

$$\begin{aligned}
 \text{forward sweep:} \quad \hat{\mathbf{x}}_m^{(i-1/2)} &= \hat{\mathbf{Z}}_{m,m}^{-1} \left( \hat{\mathbf{v}}_m - \hat{\mathbf{p}}_m^{(i-1/2)} - \hat{\mathbf{s}}_m^{(i-1)} \right) \\
 & m = 1 \cdots M \\
 \text{backward sweep:} \quad \hat{\mathbf{x}}_m^{(i)} &= \hat{\mathbf{Z}}_{m,m}^{-1} \left( \hat{\mathbf{v}}_m - \hat{\mathbf{p}}_m^{(i-1/2)} - \hat{\mathbf{s}}_m^{(i)} \right) \\
 & m = M \cdots 1
 \end{aligned} \tag{3.122}$$

The linear matrix systems in the forward and backward sweeps illustrated in Equation 3.122 are called the local problems.  $\hat{\mathbf{Z}}_{m,m}$  denotes a matrix containing information about the mutual interaction between basis functions in the sub-region  $m$  and those in its associated buffer region  $b(m)$  as shown in Equation 3.123.

$$\hat{\mathbf{Z}}_{m,m} = \begin{pmatrix} \bar{\mathbf{Z}}_{m,m} & \bar{\mathbf{Z}}_{m,b(m)} \\ \bar{\mathbf{Z}}_{b(m),m} & \bar{\mathbf{Z}}_{b(m),b(m)} \end{pmatrix} \tag{3.123}$$

A similar interpretation is applied to  $\hat{\mathbf{x}}_m$  and  $\hat{\mathbf{v}}_m$

$$\hat{\mathbf{x}}_m = \begin{pmatrix} \bar{\mathbf{x}}_m \\ \bar{\mathbf{x}}_{b(m)} \end{pmatrix} \tag{3.124}$$

$$\hat{\mathbf{v}}_m = \begin{pmatrix} \bar{\mathbf{v}}_m \\ \bar{\mathbf{v}}_{b(m)} \end{pmatrix} \tag{3.125}$$

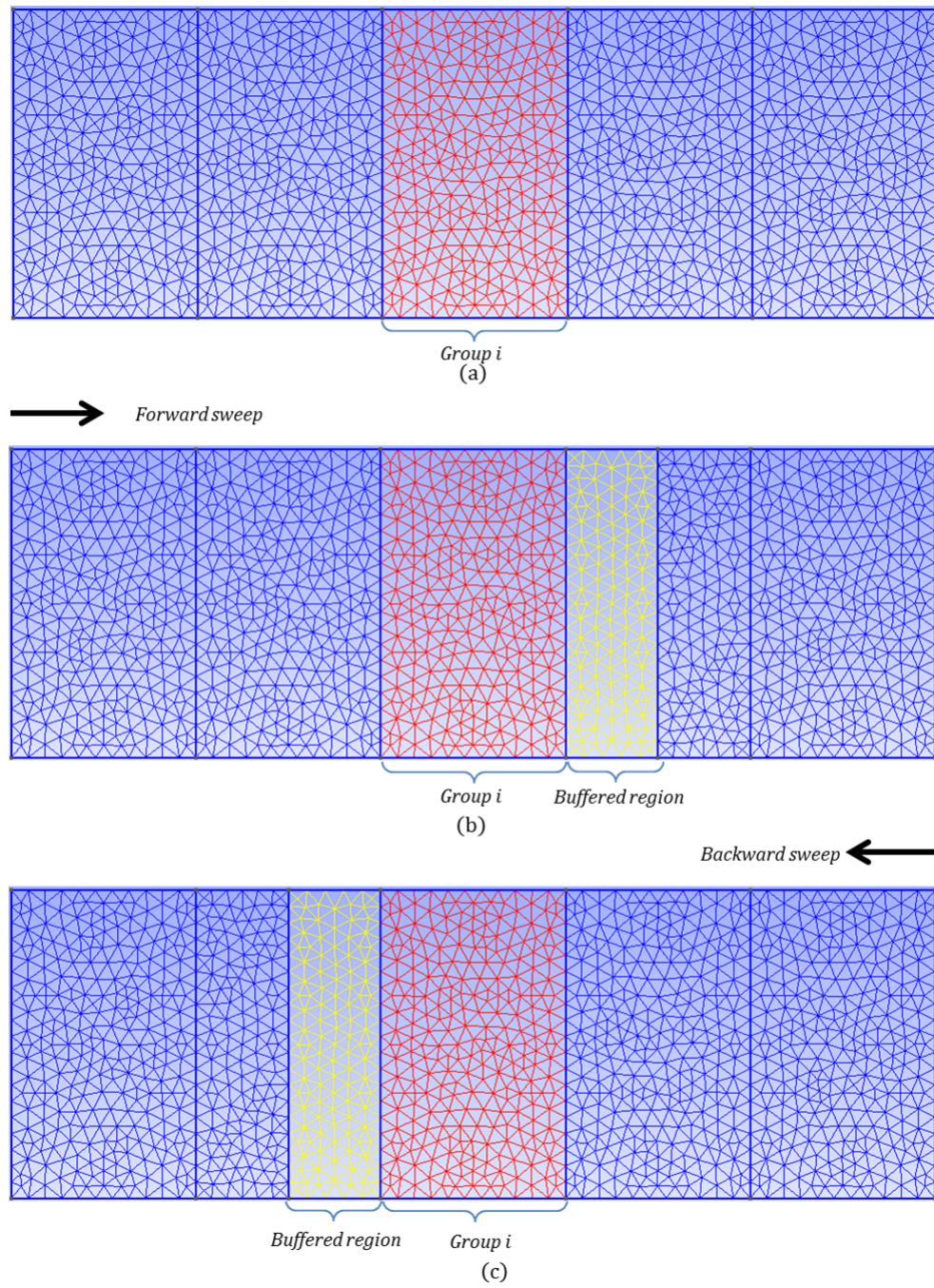


**Figure 3.4:** Buffer regions in the buffered block forward backward method.



$\hat{\mathbf{p}}_m^{(i)}$  and  $\hat{\mathbf{s}}_m^{(i)}$  are vectors holding information about the most up-to-date scattered fields (from the  $i^{\text{th}}$  iteration of the current) radiated from the prior and subsequent regions, respectively, onto the domain comprising of the sub-region  $m$  and its buffer region  $b(m)$ . For example we can write

$$\hat{\mathbf{p}}_m^{(i-1/2)} = \sum_{n=1}^{m-1} \begin{pmatrix} \bar{\mathbf{Z}}_{m,n} \\ \bar{\mathbf{Z}}_{b(m),n} \end{pmatrix} \hat{\mathbf{x}}_n^{(i-1/2)} \quad (3.126)$$

$$\hat{\mathbf{s}}_m^{(i)} = \sum_{n=b(m)+1}^M \begin{pmatrix} \bar{\mathbf{Z}}_{m,n} \\ \bar{\mathbf{Z}}_{b(m),n} \end{pmatrix} \hat{\mathbf{x}}_n^{(i)} \quad (3.127)$$

The local problems illustrated in Equation 3.122 are solved at each step in the forward and the backward sweeps. At each step, the buffer region is used to aid the accuracy of the updated current in that sub-region. Therefore, only the currents on the sub-region are retained while those on the associated buffer region are discarded and overwritten as one moves to the next local problem.

To examine the enhanced convergence properties of the BBFB, the iteration matrix of the BBFB is derived as shown below. The object is divided into sub-regions and the buffer region in each case is the entirety of the next sub-region. In other words, we assume that the sub-region and the buffer region are the same size to ease the derivation, though, they can be different. Each sweep of the BBFB can be represented in the form of an augmented matrix equation. The augmented linear equation for the forward sweep is given by

$$\mathbf{Z}^f \mathbf{x}^f = \mathbf{v}^f \quad (3.128)$$

where

$$\mathbf{Z}^f = \begin{pmatrix} \bar{\mathbf{Z}}_{1,1} & \bar{\mathbf{Z}}_{1,2} & 0 & 0 & \bar{\mathbf{Z}}_{1,3} & 0 & \cdots & \bar{\mathbf{Z}}_{1,M} \\ \bar{\mathbf{Z}}_{2,1} & \bar{\mathbf{Z}}_{2,2} & 0 & 0 & \bar{\mathbf{Z}}_{2,3} & 0 & \cdots & \bar{\mathbf{Z}}_{2,M} \\ \bar{\mathbf{Z}}_{2,1} & 0 & \bar{\mathbf{Z}}_{2,2} & \bar{\mathbf{Z}}_{2,3} & 0 & 0 & \cdots & \bar{\mathbf{Z}}_{2,M} \\ \bar{\mathbf{Z}}_{3,1} & 0 & \bar{\mathbf{Z}}_{3,2} & \bar{\mathbf{Z}}_{3,3} & 0 & 0 & \cdots & \bar{\mathbf{Z}}_{3,M} \\ \bar{\mathbf{Z}}_{3,1} & 0 & \bar{\mathbf{Z}}_{3,2} & 0 & \bar{\mathbf{Z}}_{3,3} & \bar{\mathbf{Z}}_{3,4} & \cdots & \bar{\mathbf{Z}}_{3,M} \\ \bar{\mathbf{Z}}_{4,1} & 0 & \bar{\mathbf{Z}}_{4,2} & 0 & \bar{\mathbf{Z}}_{4,3} & \bar{\mathbf{Z}}_{4,4} & \cdots & \bar{\mathbf{Z}}_{4,M} \\ \vdots & \vdots & \vdots & \vdots & \vdots & \vdots & \ddots & \vdots \\ \bar{\mathbf{Z}}_{M,1} & 0 & \bar{\mathbf{Z}}_{M,2} & 0 & \bar{\mathbf{Z}}_{M,3} & 0 & \cdots & \bar{\mathbf{Z}}_{M,M} \end{pmatrix} \quad (3.129)$$

and

$$\mathbf{x}^f = \left[ \bar{\mathbf{x}}_1 \quad \bar{\mathbf{d}}_2 \mid \bar{\mathbf{x}}_2 \quad \bar{\mathbf{d}}_3 \mid \cdots \mid \bar{\mathbf{x}}_M \right]^T \quad (3.130)$$

$$\mathbf{v}^f = \left[ \bar{\mathbf{v}}_1 \quad \bar{\mathbf{v}}_2 \mid \bar{\mathbf{v}}_2 \quad \bar{\mathbf{v}}_3 \mid \cdots \mid \bar{\mathbf{v}}_M \right]^T \quad (3.131)$$

where  $\bar{\mathbf{d}}_m$  is a vector containing temporary information about current segments in sub-region  $m$ . We denote the solution before the process of the forward sweep as  $\mathbf{x}^{f(0)}$  and the approximate solution after the completion of the forward sweep as  $\mathbf{x}^{f(1)}$ . The solution after one forward sweep is formulated as

$$\left( \mathbf{L}^f + \mathbf{D}^f \right) \mathbf{x}^{f(1)} = \mathbf{v}^f - \mathbf{U}^f \mathbf{x}^{f(0)} \quad (3.132)$$

where  $\mathbf{D}^f$ ,  $\mathbf{L}^f$  and  $\mathbf{U}^f$  denote the block-diagonal, block-lower-triangular and block-upper-triangular parts of  $\mathbf{Z}^f$ , respectively. As the result, the iteration matrix of the forward sweep is defined as

$$\mathbf{M}^f = \left( \mathbf{L}^f + \mathbf{D}^f \right)^{-1} \mathbf{U}^f. \quad (3.133)$$

Similarly, the iteration matrix of the backward sweep is

$$\mathbf{M}^b = \left( \mathbf{U}^b + \mathbf{D}^b \right)^{-1} \mathbf{L}^b \quad (3.134)$$

where  $\mathbf{D}^b$ ,  $\mathbf{L}^b$  and  $\mathbf{U}^b$  denote the block-diagonal, block-lower-triangular and block-upper-triangular parts of  $\mathbf{Z}^b$ , which is the augmented matrix in the backward sweep. The spectral radius of these matrices determines the convergence rate of the BBFB. This is examined in the next examples. The main disadvantage of the BBFB is the requirement of creating and storing the inverses of the local matrices defined in Equation 3.123, which are used repeatedly in each iteration. However, this burden can be reduced by the use of matrix compression techniques such as the MS-CBD [25, 26, 27].

### 3.3.6.1 Test case 1: spectral radius of the iteration matrices - perfectly conducting square plate

The spectral radius of the iteration matrices of the BBFB, which determines the convergence rate of the method, is investigated in this test case to demonstrate the advantage of the BBFB as compared to the BFBM. The eigenvalue distributions of the iteration matrices in the BBFB and the BFBM are examined separately in the forward sweep and in the backward sweep to study the convergence properties of the BBFB against the BFBM and to highlight the importance of the buffer region. A perfect electric conducting (PEC) square plate of  $\lambda \times \lambda$ , where  $\lambda$  is the wavelength at the operating frequency, placed on the  $XZ$  plane is discretised into 1,267 RWG basis functions. The plate is split into 5 equal slices along the  $x$ -axis. In the BFBM (without buffer region), the sub-region size is 2 slices. The size of the sub-region and buffer region is 1 slice each in the BBFB (with

buffer region). Elements in the impedance matrix  $\mathbf{Z}$  is computed using the combined field integral equation (CFIE) with the coefficient  $\alpha = 0.3$ . We give the derivation of the CFIE in chapter 4 where it is used most.

Figure 3.5 shows the eigenvalue distributions for two sweeps in the BBFB (with buffer region) and the BFBM (without buffer region). The eigenvalue spectrum of the BFBM shown in Figure 3.5 c,d is unacceptable for both sweeps since many eigenvalues are outside the unit circle, resulting in the divergence of the method. The buffer region in the BBFB significantly improves the eigenvalue spectrum shown in Figure 3.5 a,b, forcing most eigenvalues within the unit circle. It is worthwhile to note that the dimensions of the iteration matrices of the BBFB are not equal. Therefore, they have to be examined individually. We illuminate the plate with a vertically polarised plane wave with an incident angle of  $(\theta = \pi/2; \varphi = 2\pi/3)$  and use the BBFB and the BFBM to solve the problem. Figure 3.6 compares the convergence rate of the BBFB and the BFBM in terms of iteration. Residual norms shown in the figure are computed by

$$\text{residual norm} = \frac{\|\mathbf{Z}\mathbf{x}^{(i)} - \mathbf{v}\|_2}{\|\mathbf{v}\|_2}. \quad (3.135)$$

It can be seen that the BFBM start to diverge after few iterations while the BBFB remains to converge to a correct solution.

### 3.3.6.2 Test case 2: spurious edge effect - NASA almond

The edge effect is visualised in this test case to emphasize the importance of the buffer region. We investigate a scattering problem shown in Figure 3.7 a. A NASA almond defined in [1] is laid along the  $x$ -axis with the tail-to-head direction aligning with the positive direction of the  $x$ -axis. The scatterer is illuminated using a vertically polarised plane wave source of 7.0 GHz at the azimuth angle of  $120^\circ$  and the elevation angle of  $0^\circ$ . The almond is discretised using 12,834 RWG basis functions as shown in Figure 3.7a and the CFIE is applied and discretised using the MoM. The scatterer is decomposed into 23 equal slices along the  $x$ -axis. The sub-region and the buffer region comprise 3 and 1 slices, respectively.

The BBFB processes with the direction of the forward sweep coinciding with the tail-to-head direction and the initial guess set to zero. At the first step of the forward sweep in the 1<sup>st</sup> iteration, the current segments of the first sub-region including the associated buffer region are updated as shown in Figure 3.7 c. The presence of the spurious current densities at the boundary between the first and the second sub-regions can be seen in Figure 3.7 c. These are eliminated at the end of the step, leading to more natural current densities in the first sub-region as shown in Figure 3.7 d. A similar process is used for updating the current densities in the other sub-regions as shown in Figure 3.7 e,f,g,h. The approximate solution converges within 1 iteration with a residual norm of 0.003 which is defined in Equation 3.135. The surface current after one iteration is illustrated in Figure 3.7 b. Although the BBFB is applied to symmetrical problems (a square plate in Section Section 3.3.6.1 and

a NASA almond in Section Section 3.3.6.2), it is not necessary that the geometry of the problems be symmetrical in order to apply the BBFB.

### 3.3.7 Overlapping domain decomposition method

The overlapping domain decomposition method [86, 87] is a variant of the BBFB for more general EM problems. In the BBFB, a problem is usually decomposed into slices along the largest extent of the geometry. Instead of using an inflexible partition scheme, the O-DDM randomly divides a problem into non-overlapping sub-regions which are nearly the same size as shown in Figure 3.8b. The decomposition can be achieved by using graph partitioning techniques [88, 89] such as METIS [75, 90, 91] or Chaco [92]. The creation of the buffer region is the main difference between the O-DDM and the BBFB. While the associated buffer region in the BBFB must be the area following the sub-region with respect to the marching direction, the buffer region in the O-DDM is formed by the extension of the boundary of each sub-region. Therefore, the associated buffer region in the O-DDM entirely wraps the sub-region of a closed geometry as shown in Figure 3.8b. This property of the buffer region allows the O-DDM to be defined by a single sweep in each iteration instead of two sweeps as in the BBFB. Assuming that a geometry is partitioned into  $M$  non-overlapping sub-regions, the algorithm of the O-DDM is described by the following equation

$$\hat{\mathbf{x}}_m^{(i)} = \hat{\mathbf{Z}}_{m,m}^{-1} \left( \hat{\mathbf{v}}_m - \hat{\mathbf{p}}_m^{(i)} - \hat{\mathbf{s}}_m^{(i)} \right) \quad m = 1 \cdots M \quad (3.136)$$

where the definitions of  $\hat{\mathbf{x}}_m^{(i)}$ ,  $\hat{\mathbf{v}}_m$ ,  $\hat{\mathbf{p}}_m^{(i)}$ ,  $\hat{\mathbf{s}}_m^{(i)}$  and  $\hat{\mathbf{Z}}_{m,m}$  are presented in Equations 3.124, 3.125, 3.126, 3.127 and 3.123, respectively.

## 3.4 Preconditioning techniques

Preconditioning techniques [38, 77, 93] are a vital element in the development of iterative methods for the solution of challenging problems. For large linear problems in scientific computation, a large number of iterations is usually required for an accurate solution due to the unfavourable spectral properties of the matrix  $\mathbf{Z}$ . The most crucial property of preconditioning techniques is the efficient transformation of the original problem to an equivalent problem which is more favourable in terms of spectral properties. A preconditioner is a matrix that enables this type of transformation. There are three main types of preconditioning techniques namely the left, right and left-right preconditioning. The preconditioner matrix  $\mathbf{M}$  is generally chosen to be close in some sense to the matrix  $\mathbf{Z}$ . Left preconditioning transforms the original matrix system into the following matrix system

$$\mathbf{M}^{-1}\mathbf{Z}\mathbf{x} = \mathbf{M}^{-1}\mathbf{v} \quad (3.137)$$

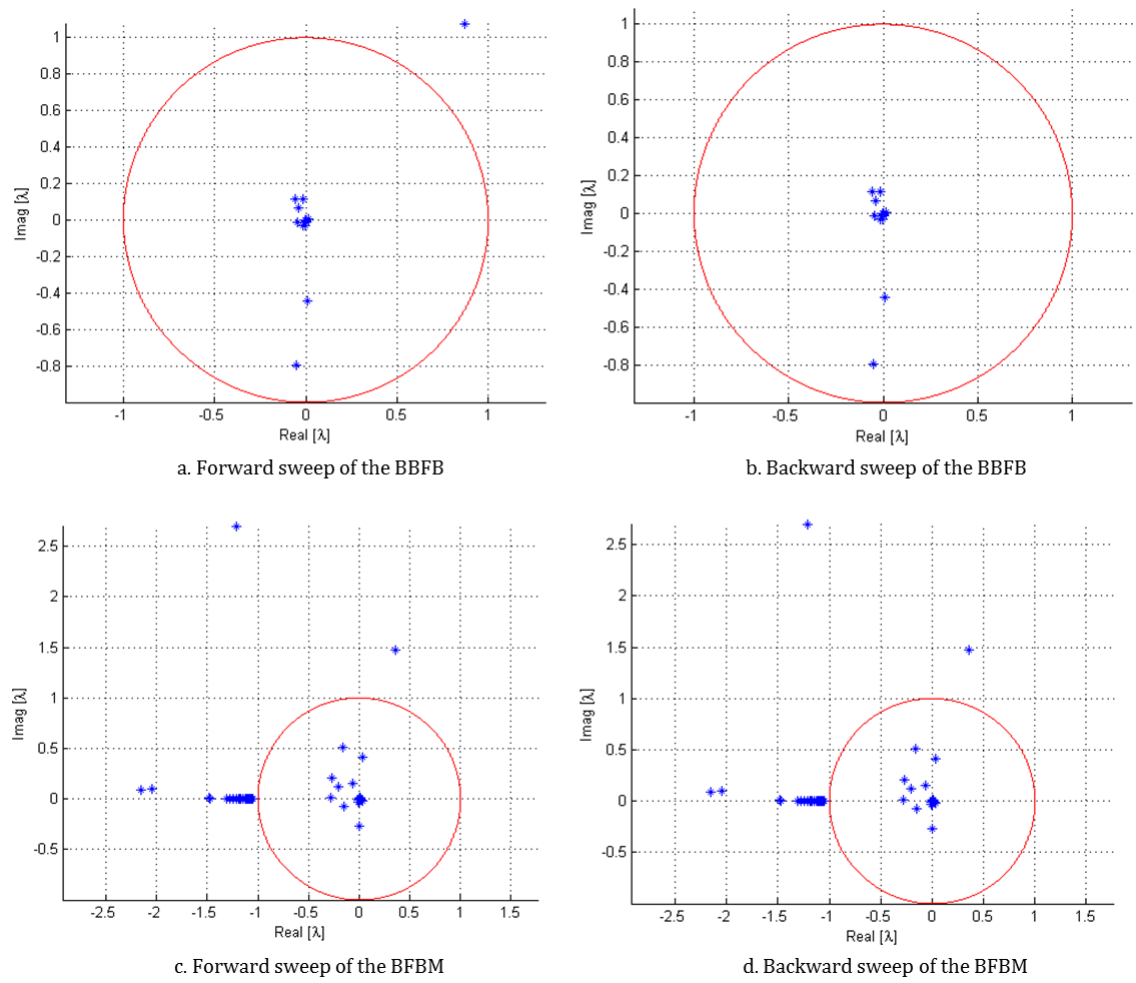


**Figure 3.5:** Eigenvalue distributions for a square plate.

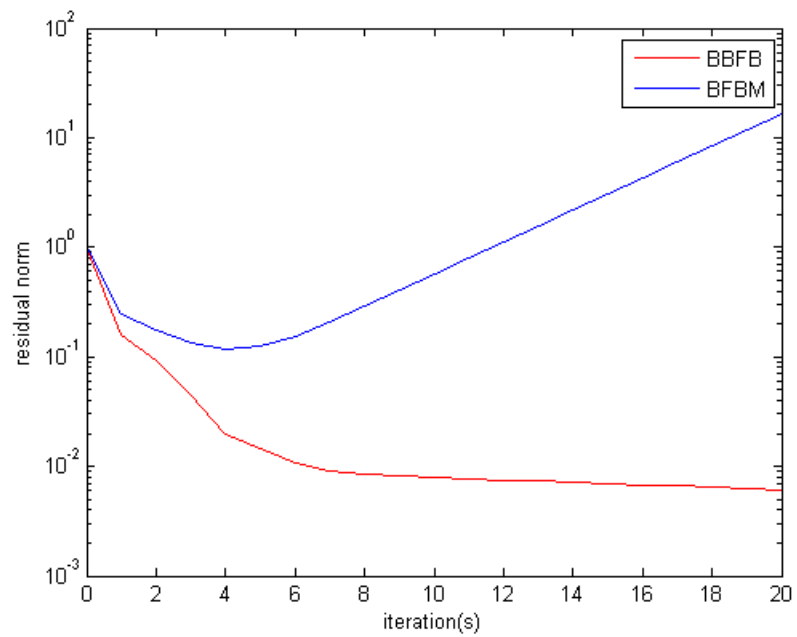


**Figure 3.6:** Comparison between the BBFB and the BFBM for a PEC square plate.

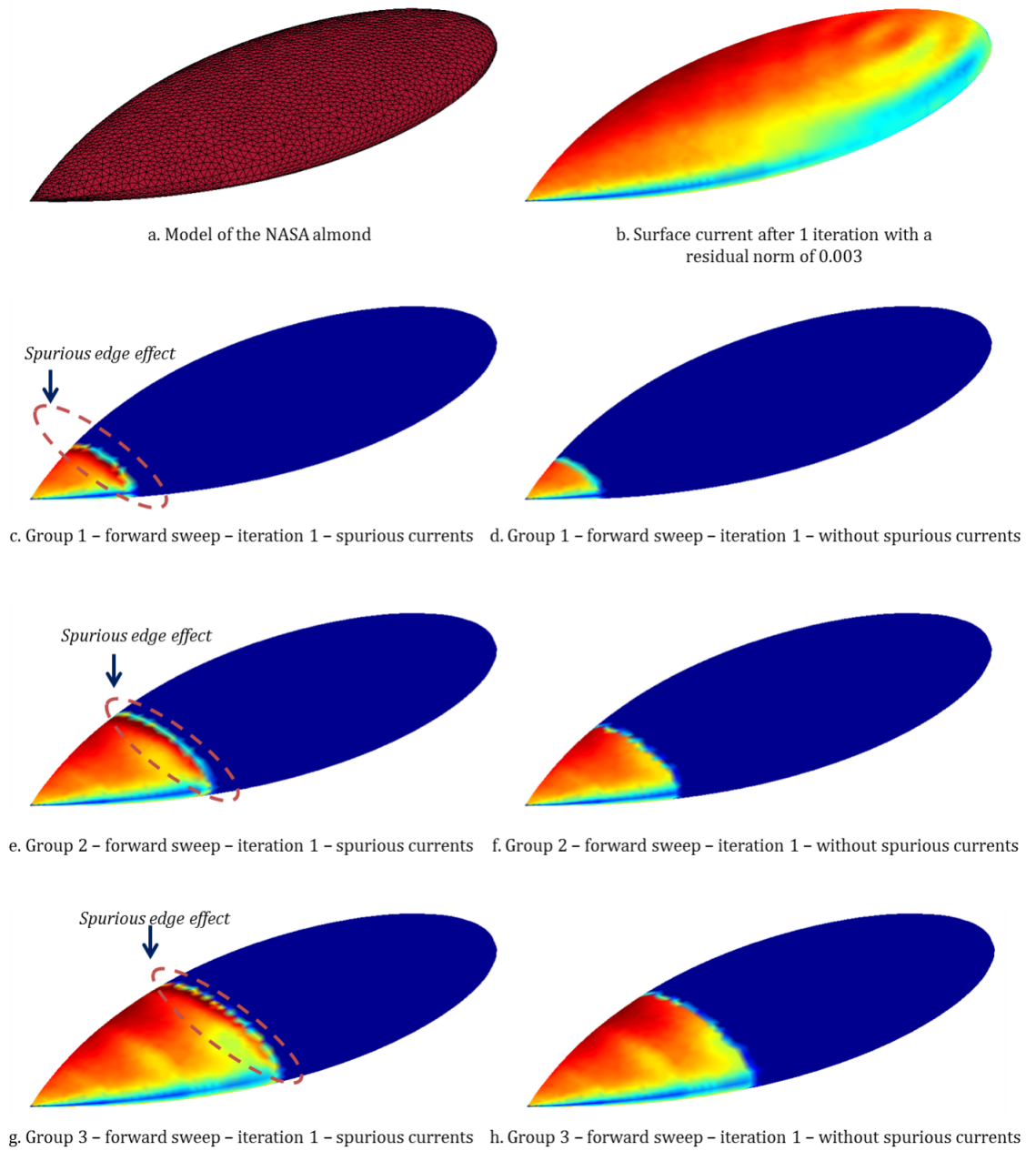


**Figure 3.7:** Spurious edge effects in the case of a NASA almond.

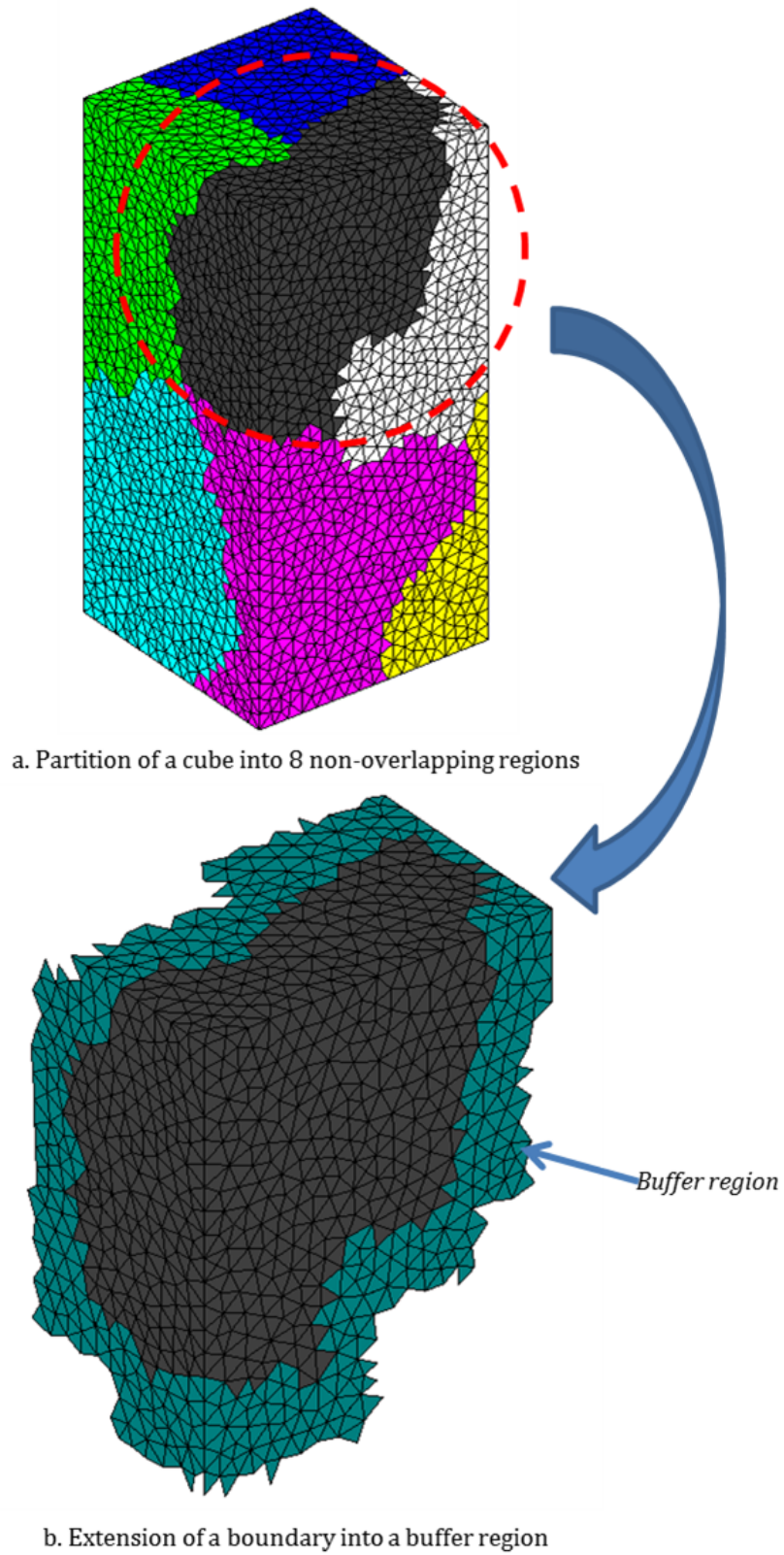


**Figure 3.8:** Sub-region and buffer region in the overlapping domain decomposition method.

where  $\mathbf{M}$  is a non-singular matrix. The new system is equivalent to Equation 3.1 but the newly transformed matrix  $\mathbf{M}^{-1}\mathbf{Z}$  may have a better spectral properties, leading to fewer iteration being required to solve the problem. The application of right preconditioning to Equation 3.1 results in the following equation

$$\mathbf{Z}\mathbf{M}^{-1}\mathbf{y} = \mathbf{v} \quad \text{where} \quad \mathbf{x} = \mathbf{M}^{-1}\mathbf{y} \quad (3.138)$$

The left-right preconditioning for Equation 3.1 is presented as follows

$$\mathbf{M}_1^{-1}\mathbf{Z}\mathbf{M}_2^{-1}\mathbf{y} = \mathbf{M}_1^{-1}\mathbf{b} \quad \text{where} \quad \mathbf{x} = \mathbf{M}_2^{-1}\mathbf{y} \quad (3.139)$$

where  $\mathbf{M}_1$  and  $\mathbf{M}_2$  are left and right preconditioners, respectively. It should be noted that the matrix-matrix products of  $\mathbf{M}^{-1}\mathbf{Z}$ ,  $\mathbf{Z}\mathbf{M}^{-1}$  and  $\mathbf{M}_1^{-1}\mathbf{Z}\mathbf{M}_2^{-1}$  are not created explicitly because of the expensive computation and the loss of sparsity of the preconditioners. The main criteria for the selection of a suitable preconditioning technique are the generation of a preconditioned system with better spectral properties and a reasonable cost of construction and application of the preconditioner.

### 3.4.1 Block Jacobi preconditioner

The simplest preconditioning applied in EM problems is the block Jacobi preconditioner [56, 94] where the preconditioner  $\mathbf{M}$  approximates the impedance matrix  $\mathbf{Z}$  in the form of a block-diagonal matrix.

$$\mathbf{M} = \begin{pmatrix} \bar{\mathbf{Z}}_{1,1} & 0 & \cdots & 0 \\ 0 & \bar{\mathbf{Z}}_{2,2} & \cdots & 0 \\ \vdots & \vdots & \ddots & \vdots \\ 0 & 0 & \cdots & \bar{\mathbf{Z}}_{M,M} \end{pmatrix} \quad (3.140)$$

The main diagonal block square matrices of  $\mathbf{M}$  are taken from the corresponding parts of the impedance matrix  $\mathbf{Z}$ . The inverse of the preconditioner, therefore, is

$$\mathbf{M}^{-1} = \begin{pmatrix} \bar{\mathbf{Z}}_{1,1}^{-1} & 0 & \cdots & 0 \\ 0 & \bar{\mathbf{Z}}_{2,2}^{-1} & \cdots & 0 \\ \vdots & \vdots & \ddots & \vdots \\ 0 & 0 & \cdots & \bar{\mathbf{Z}}_{M,M}^{-1} \end{pmatrix}. \quad (3.141)$$

The implementation of the block Jacobi preconditioner is straightforward and well suited for parallelisation. However, the efficiency of the block Jacobi preconditioner is limited when compared with more complicated preconditioners.



### 3.4.2 Incomplete LU preconditioner

In EM problems, the impedance matrix  $\mathbf{Z}$  can be decomposed into two parts comprised of the near-zone contributions and the far-zone contribution as follows

$$\mathbf{Z} = \mathbf{Z}^{\text{nf}} + \mathbf{Z}^{\text{ff}} \quad (3.142)$$

where  $\mathbf{Z}^{\text{nf}}$  and  $\mathbf{Z}^{\text{ff}}$  denote the matrices that contain information about the near-zone and the far-zone contributions, respectively. The near-zone matrix can be used to construct a preconditioner

$$\mathbf{M} = \mathbf{Z}^{\text{nf}} \quad (3.143)$$

The inverse of the preconditioner is obtained using direct methods involving the generation of the lower-triangular  $\mathbf{L}$  and the upper-triangular  $\mathbf{U}$  matrices. However, this process of matrix decomposition causes fill-in [95], leading to the loss of sparsity. To preserve the computational advantage of sparse matrices, some parts of fill-in can be discarded resulting in

$$\mathbf{LU} \approx \mathbf{Z}^{\text{nf}}. \quad (3.144)$$

Different strategies to remove fill-in results in various types of the incomplete LU preconditioners [96, 97, 98].

### 3.4.3 Sparse approximate inverse preconditioner

The main drawback of the incomplete LU preconditioner is the incompatibility with parallelisation and a large storage requirement for the lower-triangular and the upper triangular matrices. Thus, the sparse approximate inverse preconditioners (SPAI) [61, 98, 99] are more popular for the solution of large-scale problems. The basic idea of the SPAI is to compute a matrix  $\mathbf{M}$  that minimises the following Frobenius norm

$$\left\| \mathbf{I} - \mathbf{Z}^{\text{nf}} \mathbf{M}^{-1} \right\|_F = \sum_{j=1}^n \left\| e_j - \mathbf{Z}^{\text{nf}} m_j \right\|_2 \quad (3.145)$$

where the size of the near-zone matrix  $\mathbf{Z}^{\text{nf}}$  is  $n \times n$ ,  $e_j$  is the  $j^{\text{th}}$  canonical unit vector and  $m_j$  is the  $m^{\text{th}}$  column of  $\mathbf{M}^{-1}$ . We denote the inverse of  $\mathbf{M}$  as  $\mathbf{P}$ . The main challenge of the SPAI is to select a suitable  $\mathbf{P}$  which is sparse and contains large entries of the inverse, which are expected to improve the quality of the preconditioner. The selection of different sparsity patterns [100, 101] of  $\mathbf{P}$  leads to different kinds of SPAI. There are two main approaches for the selection of the sparsity including adaptive techniques and static techniques. Adaptive techniques dynamically attempt to identify the best pattern for  $\mathbf{P}$ , resulting in sophisticated and costly algorithms. Static techniques determine the sparsity pattern in advance based on some heuristics. In electromagnetic scattering problems,

an effective pattern can be pre-determined by exploiting the physical and geometrical properties [102, 103].

## 3.5 Conclusion

This chapter described a number of iterative methods applied to the solution of integral equations, which are discretised using the method of moments. Both stationary and non-stationary iterative methods are presented. Stationary methods are applied to solve electromagnetic scattering problems in chapter 4 and chapter 5. The buffered block forward backward method and the overlapping domain decomposition method are applied to solve three-dimensional perfectly conducting problems in chapter 4 while the forward backward method and the block forward backward method are applied to the solution of electromagnetic scattering from one-dimensional and two-dimensional random rough surfaces in chapter 5, respectively. Non-stationary methods, the generalised minimal residual method and the biconjugate gradient stabilised method, are applied to solve electromagnetic scattering problems in chapter 6 and chapter 7.

## 4 Modified multilevel fast multipole algorithm for stationary iterative methods

In this chapter, a modified multilevel fast multipole algorithm (MLFMA) is presented for the acceleration of the partial matrix-vector products (MVPs) required in each iteration of stationary iterative solvers used for the solution of electromagnetic wave propagation and scattering problems. Applying the standard MLFMA to the computation of the partial MVPs leads to significant redundancy, causing a loss of efficiency of the stationary method. A modified MLFMA is proposed to regain the efficiency. The modified MLFMA is based on two small novel algorithms which are responsible for a precise determination of small subsets of cubes which are in need of having their associated fields recomputed in the MLFMA upward or downward process during each step of the stationary iteration process. The combination of the modified MLFMA and the stationary methods is applied for the solution of perfectly conducting 3D scattering problems. Numerical results are presented to demonstrate the efficiency of the proposed technique.

### 4.1 Introduction

The application of the MoM to IEs is an extensively used technique for the numerical solution of electromagnetic wave scattering problems. As discussed in chapter 3, the storage requirements and the impractical complexity to invert the resultant matrix  $\mathbf{Z}$  are the main challenges for the solution of large and dense linear systems. Iterative methods become a suitable approach for the solution of electrically large problems. Iterative solvers are categorised into two main classes including non-stationary methods and stationary methods. The non-stationary solvers approximate a solution using a linear combination of Krylov bases which forms the Krylov subspace. The GMRES [40] and the BiCGSTAB [39] are popular among Krylov iterative methods for their robust convergence. “*Current marching*” solvers based on stationary solvers, especially the FBM [64], have received much attention for their rapid convergence. The FBM gradually builds up a solution as it marches across the surface of the scatterer. It has been demonstrated to converge within considerably fewer iterations as compared to the Krylov methods for certain two dimensional scattering problems [68]. The FBM has also been extended to the BBFB which is applicable to three dimensional problems in [81, 85].

The stationary solver, particularly the BBFB, would at first glance appear to be a potentially powerful complement to acceleration methods such as the MLFMA [57]. The acceleration techniques reduce the cost of each iteration while the stationary solvers reduce the overall number of iterations required for the solution. Together they tackle the

overall computational burden associated with this type of full-wave solver. However, the situation is complicated by the nature of the iterations that occur in the stationary solvers. The main computational burden of a non-stationary solver is a *full* MVP, with a cost of  $\mathcal{O}(N^2)$  operations which can be reduced by, for example, the MLFMA to  $\mathcal{O}(N \log N)$ . In contrast, the stationary solvers such as the BBFB method require the computation of a large number of *partial* MVPs, the overall cost of which is also  $\mathcal{O}(N^2)$ . However, the application of the standard MLFMA to the computation of these partial MVPs results in considerable computational redundancy which means that the speed up achieved by the MLFMA is greatly reduced, potentially offsetting the computational gains achieved due to the reduced number of iterations.

The modified MLFMA is presented in this chapter to efficiently perform these partial MVPs. The modified MLFMA is combined with the stationary solvers, the BBFB and the O-DDM, for the computation of scattering from three dimensional perfectly conducting scatterers. The chapter is organised as follows. Firstly, the combined field integral equation and the MLFMA are briefly reviewed prior to the explanation of the need for the modified MLFMA. Then, details about the proposed method are presented. Finally, numerical results are shown to demonstrate the accuracy and efficiency of the modified MLFMA.

## 4.2 Combined field integral equation for 3D perfectly conducting problems

The SEFIE and SMFIE in Equations 2.87-2.88 for a perfectly conducting scatterer located in free-space become, respectively

$$\hat{\mathbf{n}} \times \mathbf{E}^i = -\hat{\mathbf{n}} \times \left\{ \frac{\eta_0}{jk_0} \left( k_0^2 \mathbf{J}_s + \nabla (\nabla \cdot \mathbf{J}_s) \right) \right\}_{S^+} * \mathbf{G} \quad (4.1)$$

$$\hat{\mathbf{n}} \times \mathbf{H}^i = \mathbf{J}_s - \hat{\mathbf{n}} \times \{ \nabla \times \mathbf{J}_s \}_{S^+} * \mathbf{G}. \quad (4.2)$$

The EFIE is applicable for both thin-shell structures and solid bodies while the MFIE is only suitable for closed-surface scatterers [104]. In addition, both equations are singular for closed-surface scatterers at interior resonant frequencies [57, 105, 106, 107], leading to incorrect solutions of the surface current  $\mathbf{J}_s$ . The CFIE proposed by J. R. Mautz et al [105] is considered as an efficient treatment for the interior Maxwell resonances. The CFIE is a linear combination of the EFIE and the MFIE as

$$\text{CFIE} = \alpha \text{EFIE} + (1 - \alpha) \eta_0 \hat{\mathbf{n}} \times \text{MFIE} \quad (4.3)$$

where  $\alpha$  is a coefficient chosen as  $0 < \alpha < 1$ . The RWG basis functions [24] are used to expand the surface currents as

$$\mathbf{J}_s(\mathbf{r}) = \sum_{n=1}^N x_n \mathbf{f}_n(\mathbf{r}) \quad (4.4)$$

where  $N$  is a number of basis functions required for the discretisation and  $\mathbf{f}_n(\mathbf{r})$  denotes the RWG basis functions [24]. These are the most commonly applied sub-domain basis functions for MoM problems. The choice of basis functions is discussed further in [20, 104]. The EFIE part and the MFIE part of the CFIE is tested by the div-conforming RWG  $\mathbf{f}_n(\mathbf{r})$  and the curl-conforming RWG  $\hat{\mathbf{n}} \times \mathbf{f}_n(\mathbf{r})$ , respectively. The resultant elements of the impedance matrix  $\mathbf{Z}$  can be represented as

$$z_{m,n} = \alpha z_{m,n}^{\text{EFIE}} + (1 - \alpha) \eta_0 z_{m,n}^{\text{MFIE}} \quad (4.5)$$

where

$$\begin{aligned} z_{m,n}^{\text{EFIE}} &= -\frac{\eta_0}{jk_0} \left( k_0^2 \int_{T_m} \mathbf{f}_m(\mathbf{r}) \cdot \int_{T_n} G(\mathbf{r}, \mathbf{r}') \mathbf{f}_n(\mathbf{r}') dS' dS + \right. \\ &\quad \left. + \int_{T_m} \mathbf{f}_m(\mathbf{r}) \cdot \nabla \int_{T_n} G(\mathbf{r}, \mathbf{r}') \nabla' \cdot \mathbf{f}_n(\mathbf{r}') dS' dS \right) \\ &= j\omega\mu_0 \left( \int_{T_m} \mathbf{f}_m(\mathbf{r}) \cdot \int_{T_n} \left( \mathbf{I} + \frac{1}{k_0^2} \nabla \nabla' \right) G(\mathbf{r}, \mathbf{r}') \mathbf{f}_n(\mathbf{r}') dS' dS \right) \end{aligned} \quad (4.6)$$

and

$$z_{m,n}^{\text{MFIE}} = -\int_{T_m} (\hat{\mathbf{n}} \times \mathbf{f}_m(\mathbf{r})) \cdot \nabla \times \int_{T_n} G(\mathbf{r}, \mathbf{r}') \mathbf{f}_n(\mathbf{r}') dS' dS \quad (4.7)$$

where  $T_m$  is the support of the basis function  $\mathbf{f}_m$ . The computation of the above integrals should be performed with care to avoid singularities by using singularity extraction techniques or singularity cancellation techniques. Treatment of singularities is beyond the scope of this thesis. Several subtraction and cancellation techniques are presented in [108, 109, 110]. The specific subtraction technique used in this thesis is presented in [108].

### 4.3 Multilevel fast multipole algorithm

Most acceleration techniques start by separating the computational electromagnetic domain into a near-zone region and a far-zone region. Therefore, the MVP in Equation 3.1 can be rewritten as

$$\mathbf{Z}\mathbf{x} = \mathbf{Z}^{\text{near}}\mathbf{x} + \mathbf{Z}^{\text{far}}\mathbf{x} \quad (4.8)$$

where  $\mathbf{Z}^{\text{near}}$  is a sparse matrix containing information about coefficients representing interaction between basis functions which are in the near-zone range of each other.  $\mathbf{Z}^{\text{far}}$  is a dense matrix containing information about coefficients representing interaction between basis functions in the far-zone range. Most computations of Equation 4.8 are performed in the second part of the right hand side. The first part of the right hand side of Equation

4.8 is computed directly using Equations 4.6-4.7, while the second part is approximated to reduce the computational cost.

The FMM [54] optimises the computational cost of the second part by grouping basis functions and expanding the basis functions' interactions into *outgoing* and *incoming* plane waves. Assume that the testing function  $m$  and the basis function  $n$  are in the far-zone range of each other and belong to groups  $i$  and  $j$ , respectively. Gegenbauer's addition theorem [111] is applied to the diagonalisation and the factorisation of the kernel function [57, 98]. As the result, the coefficients of the impedance matrix in Equations 4.6-4.7 can be expressed as [57, 112, 113]

$$z_{m,n}^{\text{EFIE}} = \eta_0 \left(\frac{k_0}{4\pi}\right)^2 \oint d^2\hat{\mathbf{k}} \mathbf{V}_{mi}^{\text{EFIE}} T_{ij}(\hat{\mathbf{k}} \cdot \hat{\mathbf{r}}_{ij}) \cdot \mathbf{V}_{nj} \quad (4.9)$$

$$z_{m,n}^{\text{MFIE}} = \left(\frac{k_0}{4\pi}\right)^2 \oint d^2\hat{\mathbf{k}} \mathbf{V}_{mi}^{\text{MFIE}} T_{ij}(\hat{\mathbf{k}} \cdot \hat{\mathbf{r}}_{ij}) \cdot \mathbf{V}_{nj} \quad (4.10)$$

where

$$\mathbf{V}_{mi}^{\text{EFIE}} = \int_{T_m} e^{-j\mathbf{k}_0(\mathbf{r}-\mathbf{r}_i)} (\bar{\mathbf{I}} - \hat{\mathbf{k}}\hat{\mathbf{k}}) \mathbf{f}_m(\mathbf{r}) dS \quad (4.11)$$

$$\mathbf{V}_{mi}^{\text{MFIE}} = \int_{T_m} e^{-j\mathbf{k}_0(\mathbf{r}-\mathbf{r}_i)} (\hat{\mathbf{k}} \times \hat{\mathbf{n}} \times \mathbf{f}_m(\mathbf{r})) dS \quad (4.12)$$

$$\mathbf{V}_{nj} = \int_{T_n} e^{j\mathbf{k}_0(\mathbf{r}-\mathbf{r}_j)} (\bar{\mathbf{I}} - \hat{\mathbf{k}}\hat{\mathbf{k}}) \mathbf{f}_n(\mathbf{r}) dS \quad (4.13)$$

$$T_{ij}(\hat{\mathbf{k}} \cdot \hat{\mathbf{r}}_{ij}) = \sum_{l=0}^L (-j)^l (2l+1) h_l^{(2)}(k_0 r_{ij}) P_l(\hat{\mathbf{r}}_{ij} \cdot \hat{\mathbf{k}}). \quad (4.14)$$

Integrals in Equations 4.9-4.10 are over the surface of a unit sphere. Centres of groups  $i$  and  $j$  are denoted by  $\mathbf{r}_i$  and  $\mathbf{r}_j$ , respectively. The spherical Hankel function of the second kind and the Legendre polynomial of degree  $l$  are denoted by  $h_l^{(2)}$  and  $P_l$ , respectively. A vector pointing from the centre of group  $j$  to the centre of group  $i$  is defined as

$$\mathbf{r}_{ij} = \mathbf{r}_i - \mathbf{r}_j \quad r_{ij} = \|\mathbf{r}_{ij}\| \quad \hat{\mathbf{r}}_{ij} = \frac{\mathbf{r}_{ij}}{r_{ij}}. \quad (4.15)$$

$\bar{\mathbf{I}} = \hat{\mathbf{k}}\hat{\mathbf{k}} + \hat{\boldsymbol{\theta}}\hat{\boldsymbol{\theta}} + \hat{\boldsymbol{\varphi}}\hat{\boldsymbol{\varphi}}$  where  $\hat{\mathbf{k}}$ ,  $\hat{\boldsymbol{\theta}}$  and  $\hat{\boldsymbol{\varphi}}$  are the orthogonal unit vectors in oriented directions of the radial, polar and azimuth in the spherical coordinate system of the expanded plane waves, respectively. The expression  $(\bar{\mathbf{I}} - \hat{\mathbf{k}}\hat{\mathbf{k}})$  in Equations 4.11 and 4.13 represents the removal of the components of the integral along  $\hat{\mathbf{k}}$ . It can be seen from Figure 4.1 that the contribution of basis functions (blue dots) in group  $j$  to testing functions (red dots) in group  $i$  is separated into three steps. In the first step, the contribution is expanded into outgoing plane waves (green arrows) centred at  $\mathbf{r}_j$  using Equation 4.13. Then, the outgoing

plane waves are translated into incoming plane waves (blue arrows) centred at  $\mathbf{r}_i$  using the translation Equation 4.14. Finally, the incoming plane waves are converted into the real contribution using Equations 4.11-4.12. As a consequence, the MVP in the FMM is divided into two parts as shown in Figure 4.2. The near-zone contribution of basis functions inside the nearby groups (grey cubes) is computed analytically while the contribution of basis functions belonging to non-nearby groups (yellow cubes) is approximated using Equations 4.9-4.10. The approximation in the FMM allows the reduction of the storage requirements and the complexity of the MVP to  $\mathcal{O}(N^{3/2})$  [54].

The idea of the FMM can be extended to the multilevel scheme to further optimise the complexity. In the MLFMA, the size of groups increase with the distance between the source and the testing groups to reduce the computational cost associated with these groups. For example, in Figure 4.3 the contribution of basis functions (blue dots) in group  $j$  (smaller blue cube) to testing functions (red dots) in group  $i$  (smaller red cube) can be computed via their *parents* (larger cubes). Thus, the outgoing and incoming plane waves centred at the centre of the parent cubes are required to be computed. The outgoing plane waves of the source parent cube  $j'$  (green arrows in Figure 4.4b) can be obtained from the wave expansions of the children cube  $j$  (red arrows in Figure 4.4b) by using shifting and interpolation. The shifting for outgoing waves is expressed as

$$\mathbf{V}_{nj'} = e^{j\mathbf{k}_0\mathbf{r}_{jj'}} \mathbf{V}_{nj} \quad (4.16)$$

where

$$\mathbf{r}_{jj'} = \mathbf{r}_j - \mathbf{r}_{j'}. \quad (4.17)$$

$\mathbf{r}_{j'}$  denotes the centre of group  $j'$ . As the size of groups increases, the number of outgoing plane waves, required for the representation of the radiation, increases to preserve the accuracy of the MLFMA. Thus, the outgoing plane waves resulting from Equation 4.16 are interpolated to obtain suitable outgoing plane waves in Figure 4.4b. Conversely, the incoming plane waves of the children cube  $i$  (blue arrows in Figure 4.4a) are computed from the expansions of its parent  $i'$  (green arrows in Figure 4.4a) as

$$\mathbf{V}_{mi}^{\text{EFIE}} = e^{-j\mathbf{k}_0\mathbf{r}_{ii'}} \mathbf{V}_{mi'}^{\text{EFIE}} \quad (4.18)$$

$$\mathbf{V}_{mi}^{\text{MFIE}} = e^{-j\mathbf{k}_0\mathbf{r}_{ii'}} \mathbf{V}_{mi'}^{\text{MFIE}} \quad (4.19)$$

where

$$\mathbf{r}_{ii'} = \mathbf{r}_i - \mathbf{r}_{i'}. \quad (4.20)$$

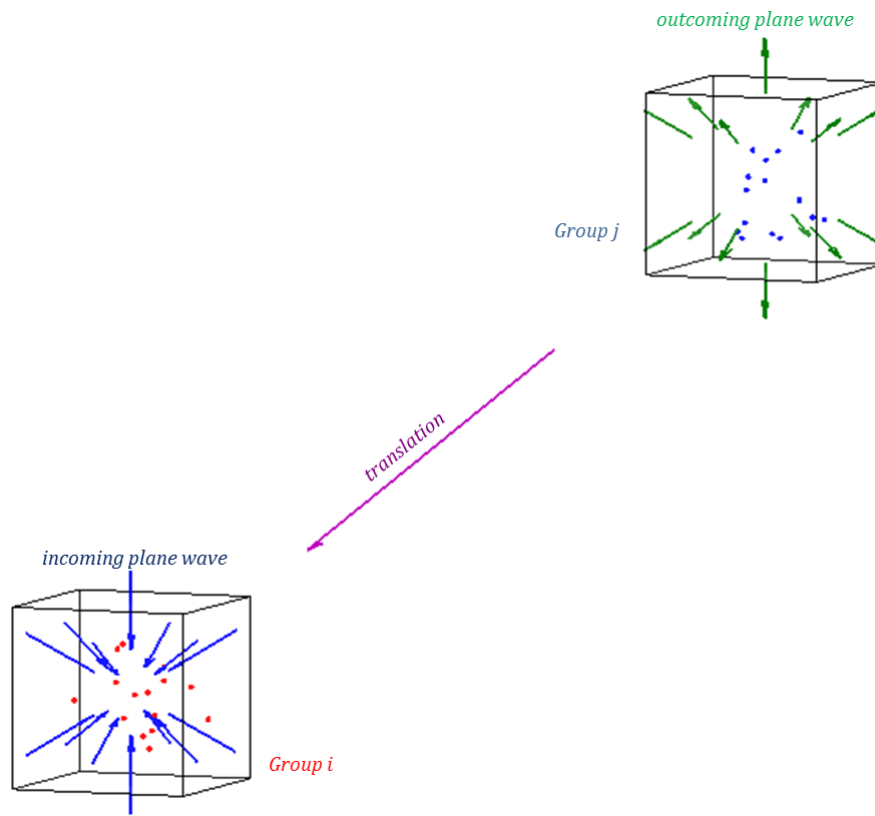


**Figure 4.1:** Illustration of the fast multipole method.

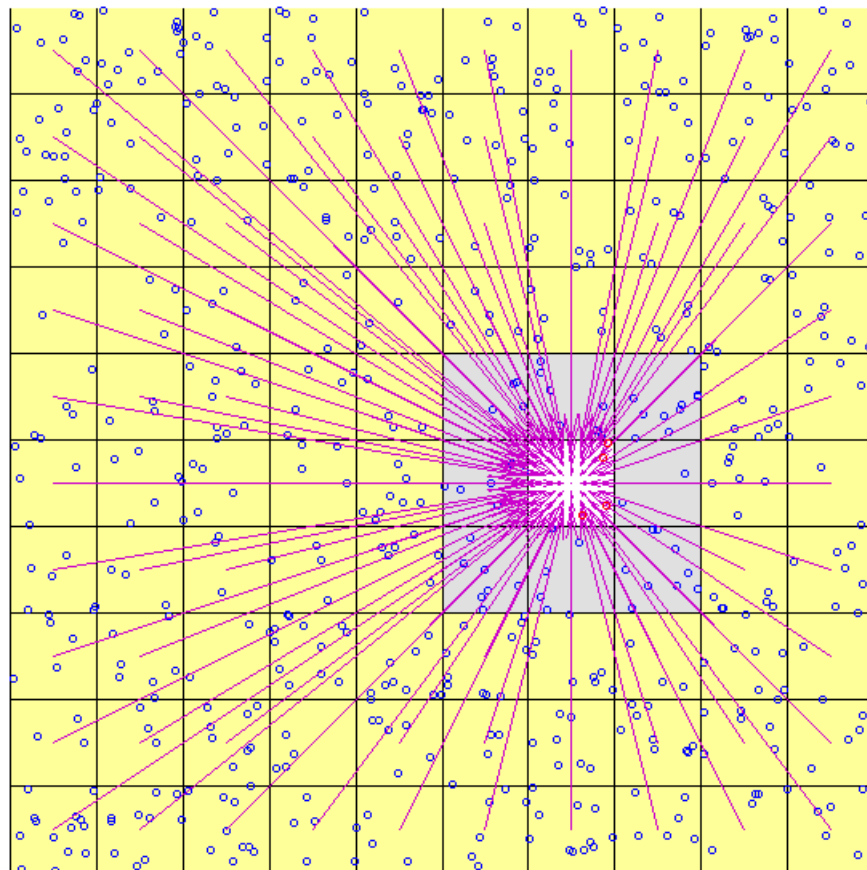


**Figure 4.2:** Translations in the fast multipole method.



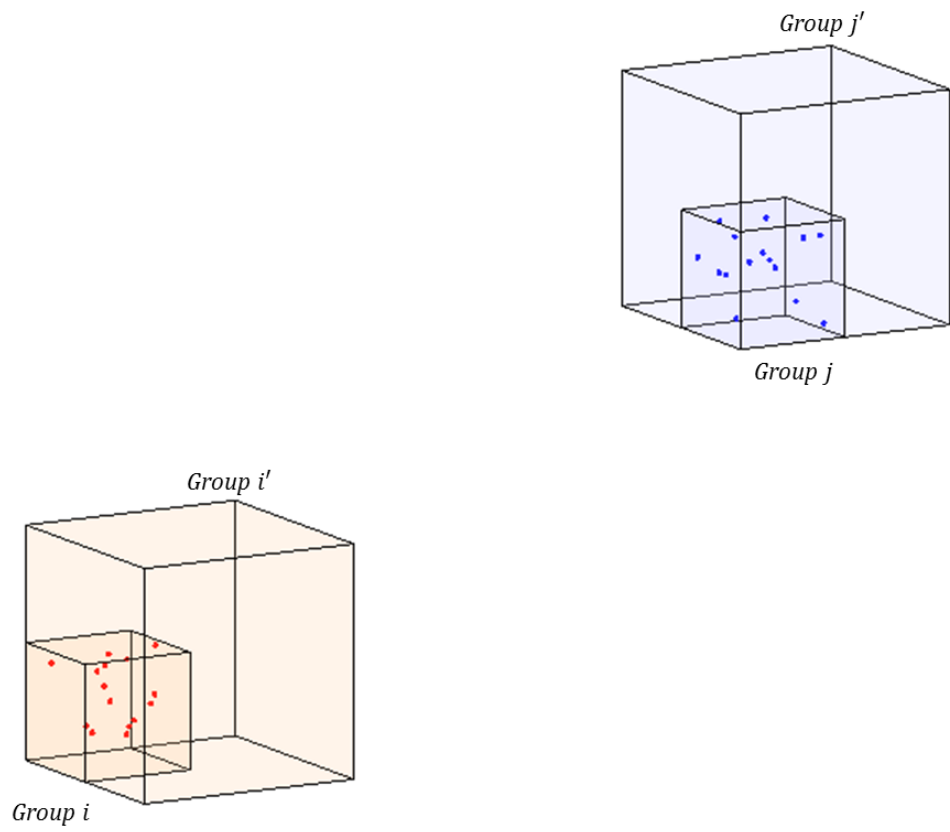


**Figure 4.3:** Parent cubes of source and testing groups.

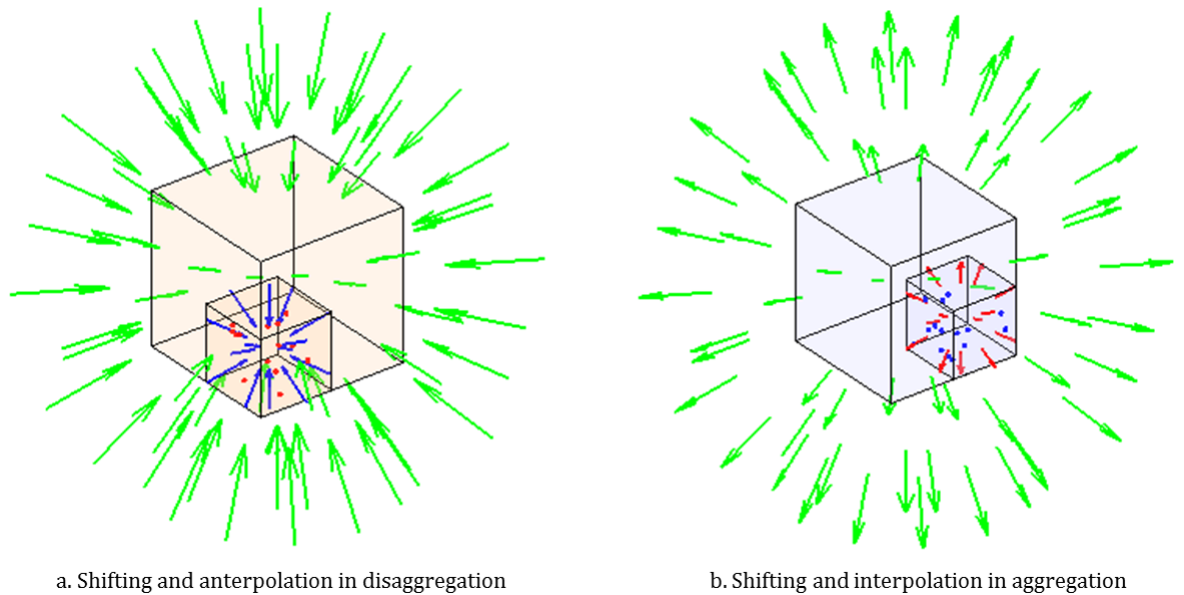


**Figure 4.4:** Shifting and interpolation/antepolation in the multilevel fast multipole algorithm.

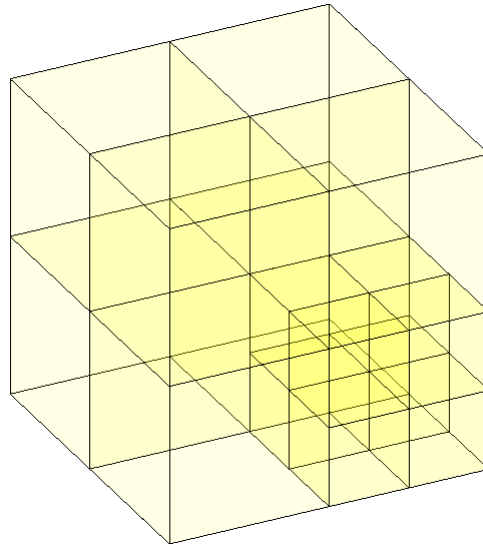


**Figure 4.5:** Recursive division of a cube into smaller cubes in the multilevel fast multipole algorithm.

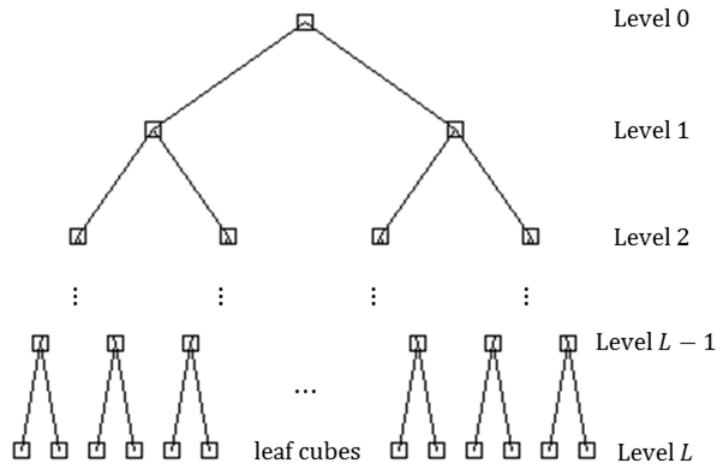


**Figure 4.6:** Octtree structure of the multilevel fast multipole algorithm.

$\mathbf{r}_{i'}$  denotes the centre of group  $i'$ . The incoming plane waves resulting from Equations 4.18-4.19 are interpolated to obtain suitable expansions in Figure 4.4a. Discussion about interpolation/interpolation schemes can be found in [57, 114, 115]. Consequently, the contribution of basis functions in group  $j$  to testing functions in group  $i$  can be obtained through five steps. Firstly, the outgoing plane waves of cube  $j$  are computed. In the second step, the expansions of cube  $j'$  are calculated using shifting and interpolation. Then the plane wave translation from cube  $j'$  to cube  $i'$  is performed. The incoming plane waves of cube  $i$  is computed from those of cube  $i'$  before the final step of conversion to the real contribution is performed.

For a discussion of the mathematical aspects of the MLFMA, the reader is referred to [57, 98]. In this chapter, the workflow of the MLFMA is revisited as it will be required to understand later sections. The MLFMA proceeds by the establishment of an octree structure. The entire scatterer is placed inside a large box which is decomposed into eight smaller and identical cubes. Each of the smaller cubes is again subdivided into eight smaller cubes. This recursive division shown in Figure 4.5 is performed until the size of the smallest cubes (called leaf cubes) is of a quarter wavelength. Cubes with no basis function are simply discarded. At the end of the recursive division, an octree structure is constructed where the root of the tree is the largest cube and the leaf cubes are located at the bottom of the tree as shown in Figure 4.6. The number of octet divisions or the number of the MLFMA levels is denoted by  $L$ . The coarsest level of the largest cube is level 0 while the finest level of the leaf cubes is level  $L$ .

The operation of the MLFMA can be separated into three phases: aggregation, translation and disaggregation. In the aggregation step, the outgoing plane waves are computed for every cube. At the leaf level, the outgoing plane waves are computed from the radiation patterns of the basis functions inside individual leaf cubes. At the next coarser level, the outgoing plane waves of a cube are obtained by means of shifting and summation of the outgoing expansions of its children. This is similar to the explanation for Figure 4.4. The aggregation step is propagated in the upward direction of the octree until reaching level 2. It results in the computation of the outgoing plane waves of every cube from level  $L$  to level 2 at the end of the step.

For ease of illustration of the translation and disaggregation steps, we investigate the application of the MLFMA to a two dimensional problem as shown in Figure 4.7. The testing functions (blue dots) are enclosed in a leaf cube (blue square). The parent and grand-parent of the testing cube are indicated by green and red squares, respectively. Yellow circles located at the centre of the cubes represent the outgoing plane waves of the corresponding cubes. The translation converts the outgoing plane waves of a radiating cube to the incoming plane waves of a testing cube at the same level. To preserve accuracy, the translation step is only performed between non-nearby cubes which are spaced by at least one cube. The MLFMA performs simultaneously the translation and disaggregation steps which start from level 2 as shown in Figure 4.8. The figure illustrates the translation step performed at the grand-parent cube (red square in Figure 4.7). The parent of the red cube is presented by the orange square in Figure 4.8. The scattering cubes at this step are those that satisfy two requirements. The first is that they are the children of the

neighbours of the orange square. The second is that they are non-nearby cubes of the red-square. The outgoing plane waves of the scattering cubes are translated into the incoming fields of the red square. After that, these incoming plane waves are shifted to the centre of the parent cube. A similar procedure is performed for the next finer level. The outgoing expansions of the children of the neighbours of the grand-parent cube are transformed into the incoming expansions of the parent cube as shown in Figure 4.9. At this stage, the incoming plane waves centred at the parent cube consist of two components: one from the shifted incoming fields of the grand-parent cube and another resulting from the translation step at this level. The total incoming plane waves are then shifted to the testing cube at the next finer level. This procedure of translation and disaggregation propagates downward the octtree until reaching the leaf level. At the end of the translation and disaggregation steps, the incoming plane waves of a leaf cube comprise the contribution of all basis functions except for those inside the nearby cubes. This conclusion is applied for a general MLFMA case with  $L$  levels. Finally, the near-zone contribution of the nearby cubes shown in Figure 4.10 is included to form the total interaction of all basis functions to the testing functions. It is worth noticing that the translation and disaggregation of all cubes at each level is performed simultaneously. In addition, the computed outgoing and incoming plane waves are shared between cubes, leading to the efficiency of the MLFMA. The MLMFA reduces the computational cost to  $\mathcal{O}(N \log N)$ .

## 4.4 Modified MLFMA for buffered block forward backward method

The matrix equation 3.122 of the buffered block forward backward method for the  $i^{\text{th}}$  step can be rewritten as

$$\begin{aligned}
 \text{forward sweep:} \quad & \hat{\mathbf{Z}}_{m,m} \hat{\mathbf{x}}_m^{(i-1/2)} = \hat{\mathbf{v}}_m - \hat{\mathbf{p}}_m^{(i-1/2)} - \hat{\mathbf{s}}_m^{(i-1)} \\
 & m = 1 \cdots M \\
 \text{backward sweep:} \quad & \hat{\mathbf{Z}}_{m,m} \hat{\mathbf{x}}_m^{(i)} = \hat{\mathbf{v}}_m - \hat{\mathbf{p}}_m^{(i-1/2)} - \hat{\mathbf{s}}_m^{(i)} \\
 & m = M \cdots 1
 \end{aligned} \tag{4.21}$$

The inverses of the impedance matrices  $\hat{\mathbf{Z}}_{m,m}$  are used constantly throughout the process of the BBFB. Instead of repeatedly making these inverses, it is beneficial to have them precomputed and stored in advance. Several matrix compression techniques such as the MS-CBD [25, 26, 27] can be applied to efficiently compute the impedance matrices and their inverse. Consequently, it is the computation of the right hand sides of Equation 4.21 that constitutes the significant burden for the solution of the local problem,  $\hat{\mathbf{x}}_m$ . The first component of the right hand side represents the incident fields impinging on the testing region which is comprised of the sub-region  $m$  and the buffer region  $b(m)$ . The testing region is shown by the red region in Figure 4.11. The latter two components on the right hand side represent the fields scattered from other regions (blue region in Figure 4.11). While the first component is known, the sum of the others is in need of computation at

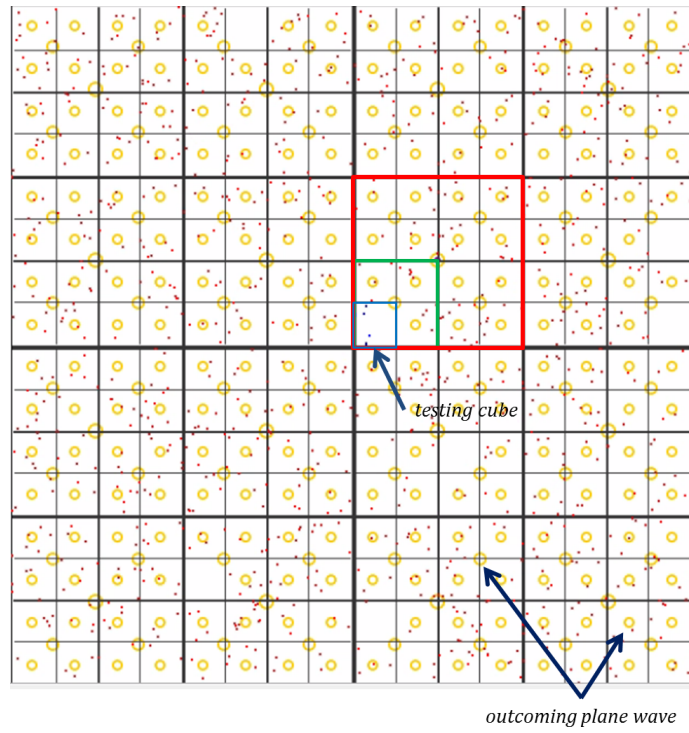


**Figure 4.7:** Illustration of the translation and disaggregation steps of the multilevel fast multipole method.

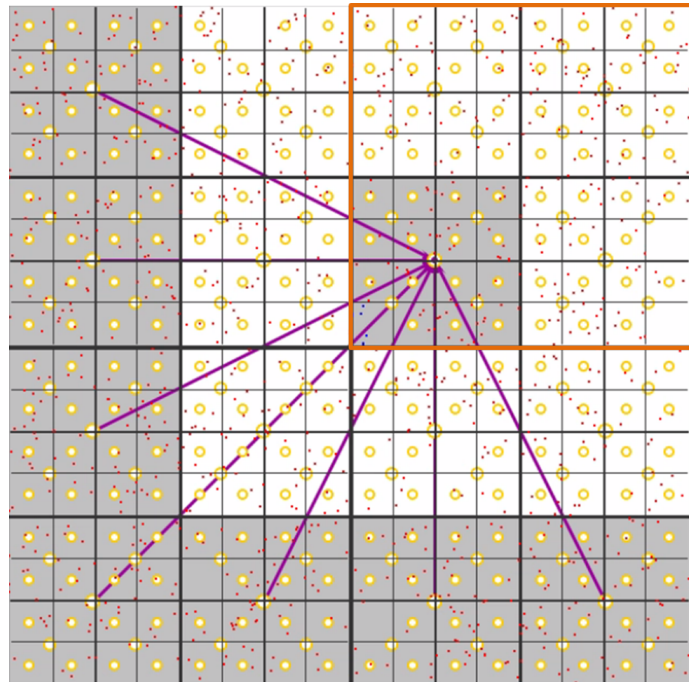


**Figure 4.8:** Translation and disaggregation at level 2 of an example in Figure 4.7.

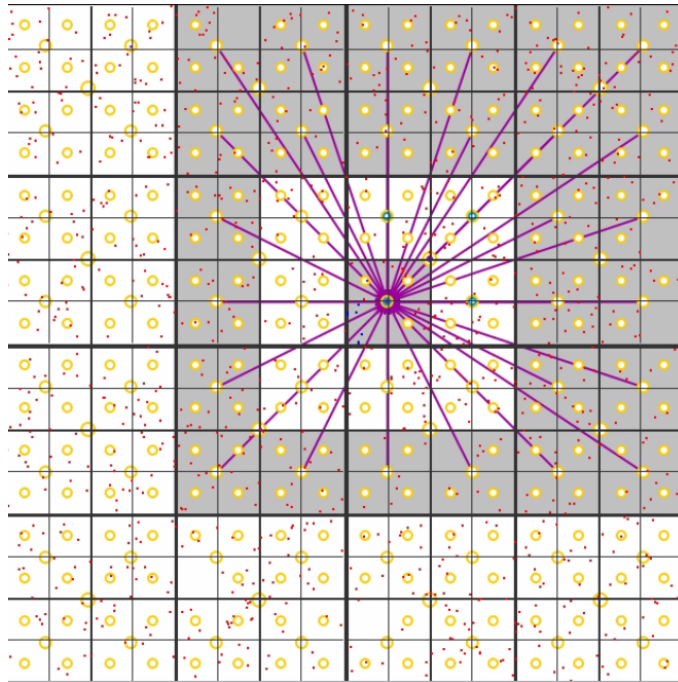


**Figure 4.9:** Translation and disaggregation at level 3 of an example in Figure 4.7.

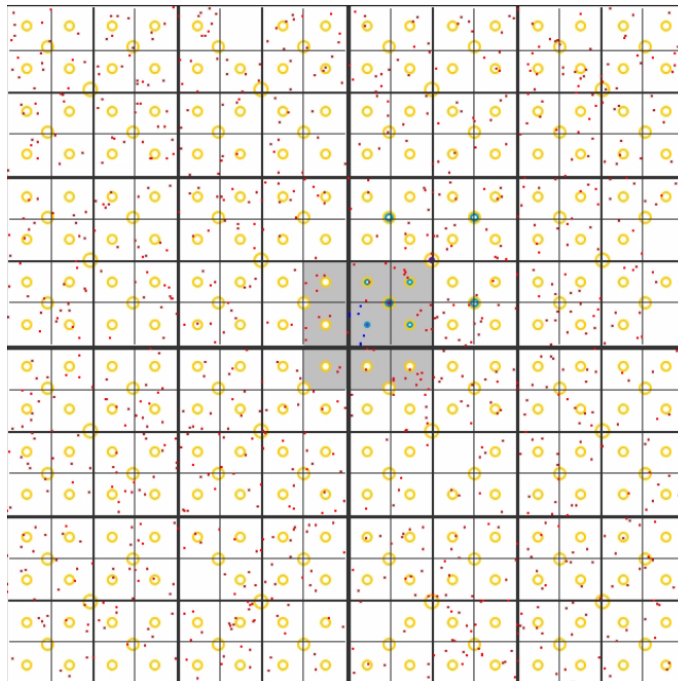


**Figure 4.10:** Near-zone contribution of an example in Figure 4.7.

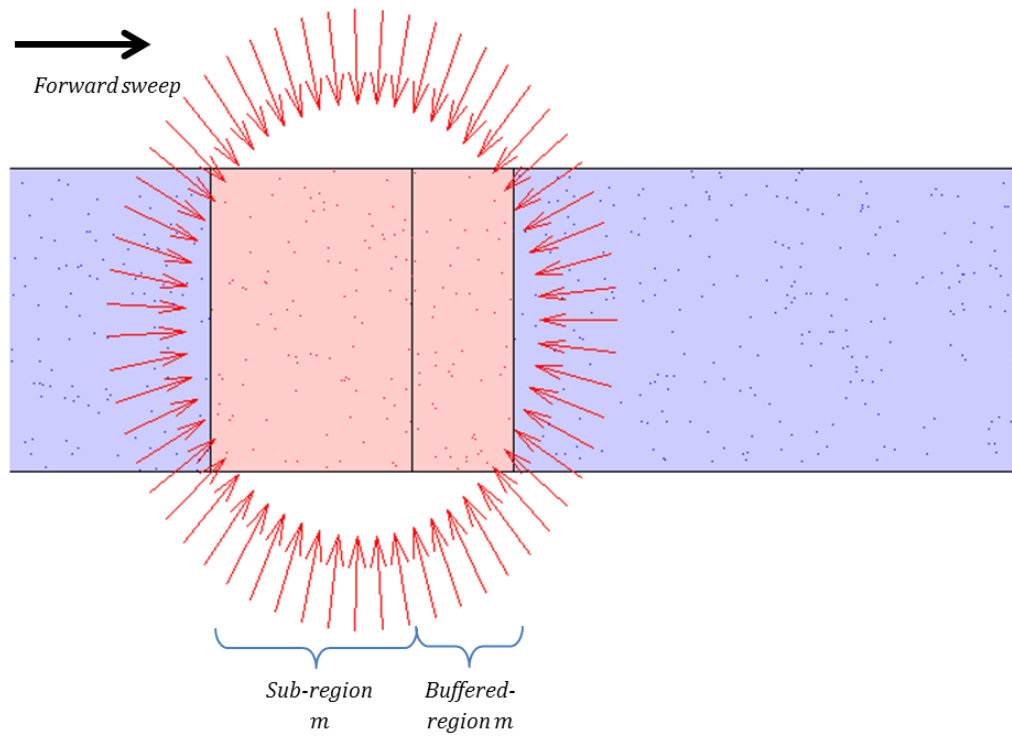


**Figure 4.11:** Illustration of the scattered fields at step  $m$  of the forward sweep of the BBFB.

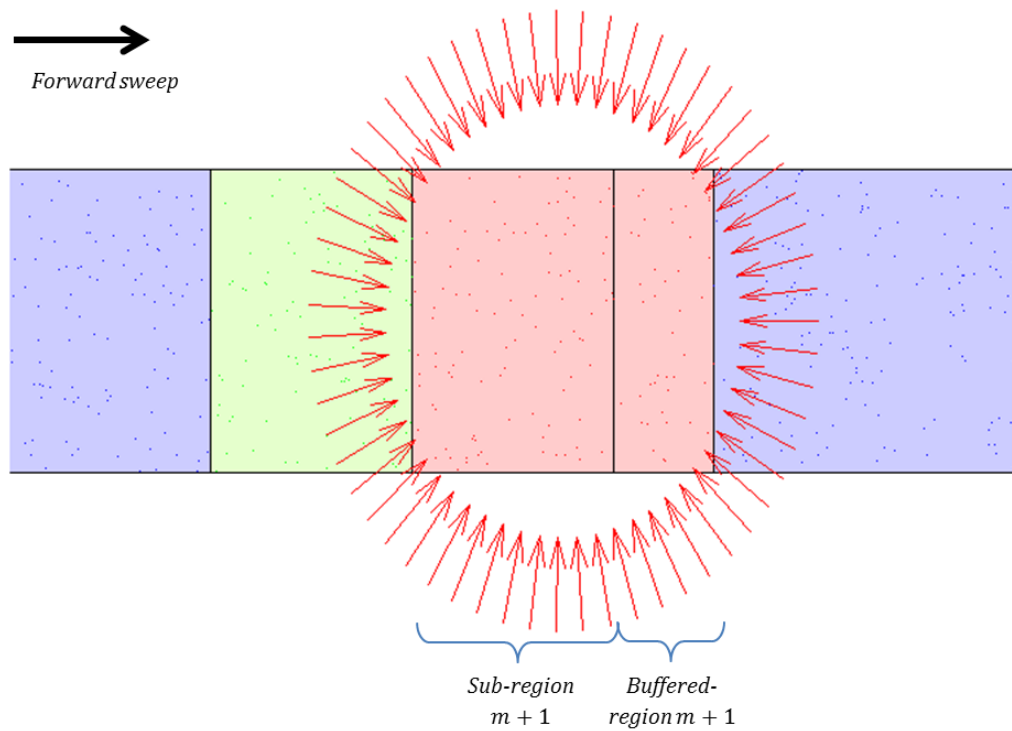


**Figure 4.12:** Illustration of the scattered fields at step  $(m + 1)$  of the forward sweep of the BBFB.

every single step of the forward and backward sweeps. The computation of the scattered fields represents the significant computational burden of the method. The computation can be considered a partial MVP involving some of the overall impedance matrix  $\mathbf{Z}$  and some of the unknown vector  $\mathbf{x}$ . Specifically, if sub-region  $m$  and buffer region  $b(m)$  contain unknowns between  $i$  and  $j$ , we are required to compute Equation 4.22 as follows

$$\begin{pmatrix} z_{1,1} & \cdots & z_{1,i-1} & z_{1,i} & \cdots & z_{1,j} & z_{1,j+1} & \cdots & z_{1,N} \\ \vdots & \ddots & \vdots & \vdots & \vdots & \vdots & \vdots & \vdots & \vdots \\ z_{i-1,1} & \cdots & z_{i-1,i-1} & z_{i-1,i} & \cdots & z_{i-1,j} & z_{i-1,j+1} & \cdots & z_{i-1,N} \\ z_{i,1} & \cdots & z_{i,i-1} & z_{i,i} & \cdots & z_{i,j} & z_{i,j+1} & \cdots & z_{i,N} \\ \vdots & \cdots & \vdots & \vdots & \ddots & \vdots & \vdots & \vdots & \vdots \\ z_{j,1} & \cdots & z_{j,i-1} & z_{j,i} & \cdots & z_{j,j} & z_{j,j+1} & \cdots & z_{j,N} \\ z_{j+1,1} & \cdots & z_{j+1,i-1} & z_{j+1,i} & \cdots & z_{j+1,j} & z_{j+1,j+1} & \cdots & z_{j+1,N} \\ \vdots & \cdots & \vdots & \vdots & \cdots & \vdots & \vdots & \ddots & \vdots \\ z_{N,1} & \cdots & z_{N,i-1} & z_{N,i} & \cdots & z_{N,j} & z_{N,j+1} & \cdots & z_{N,N} \end{pmatrix} \begin{pmatrix} x_1 \\ \vdots \\ x_{i-1} \\ 0 \\ \vdots \\ 0 \\ x_{j+1} \\ \vdots \\ x_N \end{pmatrix} = \begin{pmatrix} t_1 \\ \vdots \\ t_{i-1} \\ t_i \\ \vdots \\ t_j \\ t_{j+1} \\ \vdots \\ t_N \end{pmatrix}. \quad (4.22)$$

Blue elements of the vector  $\mathbf{x}$  denote the amplitudes of the basis functions located in the scattering region (blue region) which are required in the computation. Red elements correspond to the unknowns in sub-region  $m$  and its associated buffer region  $b(m)$ , and have been set to zero. Similarly, we highlight in red the elements in the right hand side vector that we need to compute, namely fields scattered to unknowns in the testing region. Equation 4.22 is called a partial MVP because it does not involve the entirety of the unknown vector  $\mathbf{x}$  and needs only be computed for some unknowns. Note that computing this partial MVP is not in itself a difficult problem. One can easily multiply by the relevant rows of the  $\mathbf{Z}$  matrix (coloured in both blue and red) by  $\mathbf{x}$  with the appropriate elements set to zero to produce the desired (red-coloured) components on the right hand side. However, doing this independently for each sub-problem will result in a method that is  $\mathcal{O}(N^2)$  in complexity. The challenge is in computing it in an efficient manner. To do this, it is preferable to use an acceleration technique such as the MLFMA. A naive application of the MLFMA to the BBFB would commence with such a decomposition of the whole scattering structure. Each partial MVP occurring in Equation 4.21 as illustrated in Equation 4.22 can then be performed using the MLFMA, resulting in the computation of the complete right hand side vector  $\mathbf{t}$ . However, for any given local sub-problem only a few elements of this right hand side vector (namely  $t_l$  where  $l = i \cdots j$ ) are of interest. Thus the application of the standard MLFMA to the computation of Equation 4.22 can result in significant redundancy as more fields are computed than necessary.

A further problem is that the computation of the fields in sub-region  $m$  requires that we use the most up-to-date amplitudes of the current elements in the vector  $\mathbf{x}$ . This requires that we re-perform the aggregation phase at the scattering cubes each time currents are



updated. However, for any given sub-problem of the BBFB, only several cubes have updated currents as compared to the previous sub-problem. It is only these updated current amplitudes that need be considered in a re-calculation of the aggregation phase. Performing a full aggregation computation is wasteful.

For example, suppose the BBFB is marching from sub-region  $m$  to sub-region  $(m + 1)$  as shown in Figure 4.11 and Figure 4.12. The computation of the current elements in the sub-region  $(m + 1)$  and the associated buffer region  $b(m + 1)$  (red region in Figure 4.12) requires knowledge of the current elements in other regions including the blue and green regions. However, only the current elements in the green region have changed between this sub-problem and the previous one. Consequently, only the recomputation of the aggregation of fields associated with the green region is required.

If the MLFMA is applied naively, the three phases are recomputed across the octree structure at a cost of a full MVP for each of the  $M$  sub-problems of the forward and backward sweeps. As a result, each iteration of the BBFB requires a computation of  $\mathcal{O}(2MN \log N)$ , considerably slowing down the performance of the BBFB. A similar problem would hamper the application of the MLFMA to other stationary methods such as the overlapping domain decomposition method [86, 87]. Instead, we proposed a modified MLFMA algorithm which only recomputes the fields within the octree structure where necessary. The proposed algorithm is also applicable to other stationary methods.

#### 4.4.1 Modified MLFMA

In a manner similar to the MLFMA, the modified MLFMA separates the partial MVP into two components: the near-zone component and the far-zone component. The near-zone component is for neighbouring cells and is computed exactly, while the far-zone component is expedited using the aggregation-translation-disaggregation ideas underpinning the MLFMA. The modified MLFMA optimises the computational cost for both calculations.

##### 4.4.1.1 Near-zone computation

The conventional computation of the near-zone in the MLFMA becomes less onerous in the case of a partial MVP. For illustration, we assume that we wish to compute the scattered fields from scattering regions (blue regions) to the  $m^{\text{th}}$  sub-problem region (red region) of the forward sweep as shown in Figure 4.13. The computation of the mutual interactions between basis functions within the sub-problem region is neglected (as it is included on the left hand side of Equation 4.21). Thus, for many leaf cubes in the red region no near field calculation is required at all, such as the red cube marked **X**. Red cubes which are adjacent to the scattering regions do require a near-zone computation. However, only a few cubes in the scattering region are involved in the near-zone computation. They are represented by dark blue cubes in Figure 4.13. For example, the computation of the near-zone contribution of the leaf cube marked with the **■** involves only the two cubes marked **⊗**.

The modified MLFMA incorporates such information and reduces the cost of the near-zone computation by a process of two steps. In the first step, only sub-problem (red)

leaf cubes adjacent to the scattering regions are selected for near-zone computation while the near-zone contribution to other cubes is set to zero. Near-zone cubes of each selected sub-problem leaf cube are determined in the second step. Only leaf cubes in the near-zone region and belonging to the dark blue regions are used for the computation of the near-zone. The computation of the near-zones is thus given by Equation 4.23 where  $\hat{\mathbf{t}}^{\text{near}-C}$  is a vector denoting the near-zone interaction of the leaf cube  $C$  which is inside the testing region.  $\mathbf{Z}^{C,C'}$  is an impedance matrix representing interactions between basis functions inside the leaf cubes  $C$  and  $C'$ .  $\mathbf{x}^{C'}$  is a vector containing the most up-to-date amplitudes of current elements inside  $C'$ .  $\text{NF}(C)$  denotes the set of indices of leaf cubes which are both inside the near-zone range of  $C$  and inside the scattering region.

$$\hat{\mathbf{t}}^{\text{near}-C} = \sum_{C' \in \text{NF}(C)} \mathbf{Z}^{C,C'} \mathbf{x}^{C'} \quad (4.23)$$

#### 4.4.1.2 Far-zone computation

In the MLFMA, far-zones are computed in a three step process, namely aggregation, translation and disaggregation. In what follows, we denote the aggregation phase as the upward process while the translation-disaggregation phase is denoted as the downward process. Assume that the BBFB is marching from the sub-region  $(m-1)$  to the sub-region  $m$  in the forward sweep. In other words, we are solving Equation 4.21 for some sub-region  $m$ , having just solved it for sub-region  $(m-1)$ . Specification of the right hand side of Equation 4.21 requires the computation of a partial MVP of the form Equation 4.22. The cubes at the leaf level belonging to the *previous* sub-problem  $(m-1)$  are denoted by  $C_{m-1}$ .  $C_{m-1}$  is thus comprised of leaf cubes in the sub-region  $(m-1)$  and the associated buffer region  $b(m-1)$ . Similarly, the leaf cubes which are in the *current* sub-problem are denoted by  $C_m$ . Thus at the leaf level, the incoming and outgoing fields remain unchanged for all cubes except for the few cubes in  $C_{m-1}$  (whose currents are the most recently updated) and  $C_m$  (whose currents are being updated at this step of the sweep). This requirement propagates upward to the root of the octree structure. At higher levels, cubes associated with  $C_{m-1}$  and  $C_m$  (i.e. their parents, grand parents, etc.) must have those fields changed. Therefore, only a subset of cubes at each level of the octree structure are in need of field re-computation during the upward and downward processes. We refer to  $C_{\text{total}} = C_{m-1} \cup C_m$ . These concepts are schematically illustrated in Figure 4.14. The recomputed-upward cubes are cubes where the upward process must be re-calculated (and are shown in blue). Similarly, the downward process should be re-calculated for the recomputed-downward cubes (shown in red). Green cubes are cubes which feature in both processes.

To implement the modified MLFMA we introduce four flags named: flag-down, flag-up, flag-recomputed-down, and flag-recomputed-up denoted by FD, FU, FRD and FRU, respectively. These flags are used to identify cubes whose fields are in need of re-computation. The flags FD and FU are used to notify whether a cube is present in the downward process and the upward process, respectively. The flags FRD and FRU respectively indicate that a cube must have its incoming fields and outgoing fields recomputed. Thus, the outgoing

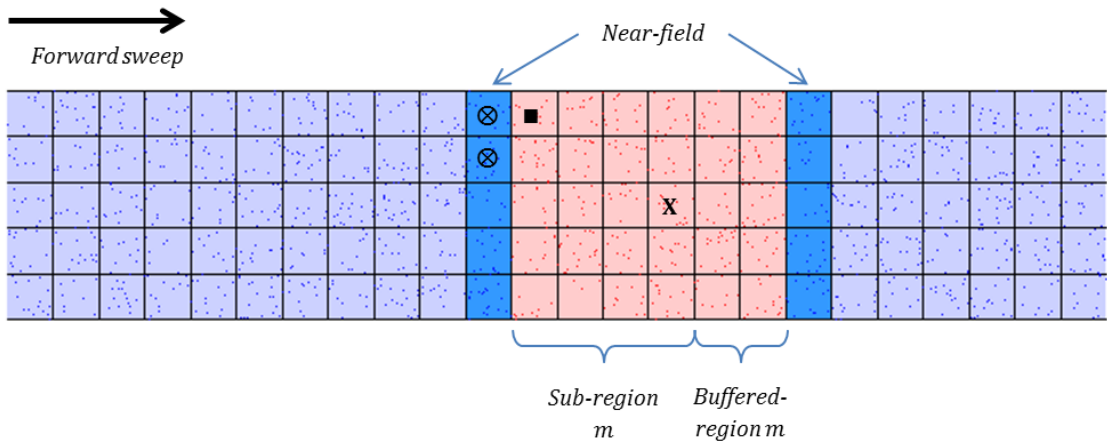


**Figure 4.13:** Near-zone computation in the modified MLFMA.

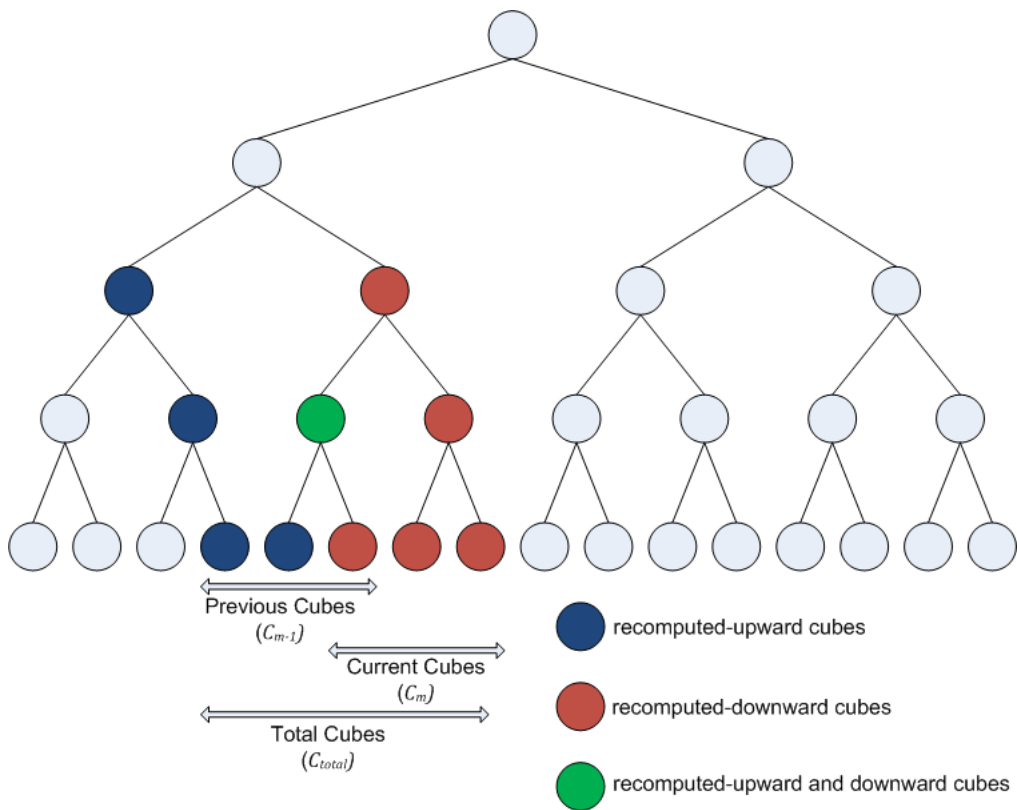


**Figure 4.14:** Illustration of the recombination of the upward and downward processes in the modified MLFMA.

---

**Algorithm 4.1** Indication of flags of leaf cubes in the modified MLFMA.

---

For (all cubes in the leaf level)

set FU

clear FD

clear FRU

clear FRD

End

For (all cubes in the leaf level)

    If (a cube is in  $C_m$ )

clear FU

set FD

set FRD

End

End

For (all cubes in the leaf level)

    If (a cube is in  $C_{total}$ )

set FRU

End

End

---

**Algorithm 4.2** Indication of flags of cubes at the higher levels in the modified MLFMA.

---

```
For (the second lowest level to the highest level)
  For (all cubes in the level)
    If (there is any son with a FD set)
      set FD
    End
    If (there is any son with a FU set)
      set FU
    End
    If (there is any son with a FRD set)
      set FRD
    End
    If (there is any son with a FRU set)
      set FRU
    End
  End
End
For (all cubes in the level)
  If (FRU is set)
    If (there is any other cube at the same level has FD set)
      set FRU
    Else
      clear FRU
    End
  End
End
For (all cubes in the level)
  If (FRD is set)
    If (all other cubes at the same level have FU set and FRU clear)
      clear FRD
    Else
      set FRD
    End
  End
End
End
```

---

fields are recomputed during the upward process for only cubes with both flags FU and FRU set. The outgoing fields of these cubes are recomputed by means of interpolation and shifting of the outgoing fields of their children, which in turn have flag FU set. Similarly, the downward process is recomputed for only cubes having both FD and FRD set.

Algorithm 4.1 determines the flags of cubes at the leaf level from the information about  $C_{\text{total}}$  and  $C_m$ . At first, we assume that all leaf cubes are involved in the aggregation process and their outgoing/incoming fields are unchanged. The downward process is assumed to be unnecessary. Secondly, cubes in  $C_m$  have flags FD and FRD set to indicate a requirement of recomputing the downward process. The mutual contributions between unknowns within sub-problem  $m$  is neglected, resulting in cleared FUs. Finally, the FRUs are set for only cubes in  $C_{\text{total}}$  because the amplitudes of current elements in the *previous* sub-problem  $C_{m-1}$  have been updated and the current elements in  $C_m$  are not involved in the partial MVP at the *current* step. At the end of Algorithm 4.1, only cubes in  $C_m$  have FD and FRD set to perform the downward process and only cubes in  $C_{\text{total}} \setminus C_m$  have both FU and FRU set for the performance of the upward process.

The flags of cubes at the higher (non-leaf) levels are indicated by the application of Algorithm 4.2. The indication is based on flags at the lower levels. Algorithm 4.2 is divided into three main steps. At the first step, the flags of the parent cubes are a logical sum of the flags of their children cubes because a parent cube is in need of recomputation if at least one of its children is recomputed. Step one is a preliminary for the second step where the FRUs are determined. Cubes with FRUs set are re-examined to ensure that there is no redundant computation in the upward process. The recomputation of the upward process is only necessary when the computed outgoing fields are used in the downward process of at least one cube at the same level. The second step will check whether any other cube at the same level has the FD set. In the case that there is no cube with FD set, the FRU of the examined cube is cleared. The FRDs are re-examined in the third step for the elimination of redundant computation in the downward process. The recomputation of the downward process is required when there is a change in the upward direction at the same level. Cubes with FRD set are examined to guarantee that at least one cube at the same level has the outgoing fields changed. Otherwise, the FRD of the examined cube is cleared. The three steps are applied for every level except for the leaf level.

After the determination of the flags, the upward and downward processes are recomputed. The upward process is performed from the leaf level to the highest level. At the leaf level, the upward process is recomputed for cubes with both FU and FRU set. The computation of the outgoing fields is given in Equation 4.24

$$\mathbf{S}^C = \sum_{j \in C} x_j \mathbf{S}_j^C \quad (4.24)$$

where  $C$  is a leaf cube with FU and FRU set.  $\mathbf{S}_j^C$  represents the radiation pattern of a basis function  $j$  inside  $C$  and  $\mathbf{S}^C$  denotes the combined radiation pattern of all basis functions inside the cube. At higher levels, the outgoing fields are again re-calculated for cubes with both FU and FRU set. They are a combination of the outgoing fields of the

children cubes and are presented as follows

$$\mathbf{S}^C = \sum_{C' \in \mathcal{C}} \beta^{C,C'} \mathbf{S}^{C'} \quad (4.25)$$

where  $C'$  is a child cube with FU set.  $\beta^{C,C'}$  is a function which shifts the radiation patterns centred at  $C'$  to be centred at  $C$ . If  $C'$  has FRU set,  $\mathbf{S}^{C'}$  is obtained from the recomputation of the outgoing fields at the lower level. Otherwise,  $\mathbf{S}^{C'}$  remains the same from the previous step. After the recomputation of the upward process, we recompute the downward process. The translation-disaggregation is performed only for cubes with both FD and FRD set. The translation stage is illustrated in the following equation

$$\mathbf{G}^C = \sum_{C' \in \text{FF}(C)} \alpha^{C,C'} \mathbf{S}^{C'} \quad (4.26)$$

where  $\text{FF}(C)$  denotes a list containing indices of cubes in the far-zone range of  $C$ .  $C'$  is a cube in the list  $\text{FF}(C)$  and has FU set.  $\alpha^{C,C'}$  is a translation function which converts the outgoing fields centred at  $C'$  to the incoming fields centred at  $C$ . The disaggregation stage is recomputed from the highest level to the leaf level. The incoming fields of the cube having both FD and FRD set is a combination of the translated fields and the shifted fields centred at its parent

$$\mathbf{I}^C = \mathbf{G}^C + \beta^{C,C'} \mathbf{I}^{C'} \quad (4.27)$$

where  $C'$  is the parent of  $C$ .  $\mathbf{I}^C$  is the total incoming fields centred at  $C$ . At the leaf level, the actual scattered fields at an individual testing function  $j$  is given by

$$t_j^{\text{far}-C} = \mathbf{I}^C \mathbf{F}_j^C \quad (4.28)$$

where  $\mathbf{F}_j^C$  represents the receiving pattern of the testing function  $j$  inside  $C$ . As the result, the total scattering fields at the cube  $C$  is computed as

$$\hat{\mathbf{t}}^C = \hat{\mathbf{t}}^{\text{near}-C} + \hat{\mathbf{t}}^{\text{far}-C} \quad (4.29)$$

where

$$\hat{\mathbf{t}}^{\text{far}-C} = \left( t_i^{\text{far}-C} \quad \dots \quad t_j^{\text{far}-C} \right)^T. \quad (4.30)$$

The index of the testing functions inside  $C$  ranges from  $i$  to  $j$ . Algorithm 4.1 and Algorithm 4.2 are repeatedly performed as the BBFB marches over the surface of the scatterer. They allow the use of the MLFMA to perform partial MVPs without having to entirely recompute the far-zone tree structure and perform the entire aggregation-translation-disaggregation for each sub-problem, thereby retaining the efficiency of the MLFMA.

### 4.4.2 Computational complexity

In this section, we estimate the computational cost of a single BBFB iteration using the modified MLFMA routine as introduced in Section 4.4.1. The computational cost of each BBFB iteration is comprised of two parts: the cost for the solution of the local problems (by premultiplying both side of Equation 4.21 by  $\hat{\mathbf{Z}}_{m,m}^{-1}$ ) and the cost to perform the modified MLFMA in order to compute the right hand sides of the equation. The local problems are assumed to be negligible in terms of physical size as compared to the entire scatterer. Thus, the computational complexity of each BBFB iteration is dominated by the complexity of the modified MLFMA. By using the original MLFMA, each sub-problem of the BBFB (i.e. solving Equation 4.21 for a given  $m$ ) requires a full MVP, leading to a cost of  $\mathcal{O}(MN \log N)$  for each sweep. A full MVP implies that each cube in the octtree structure performs the upward and the downward processes once. The modified MLFMA reduces the computational cost by implementing Algorithm 4.1 and Algorithm 4.2 which results in individual cubes only sometimes having fields re-computed as part of the upward-downward processes. The complexity of each BBFB iteration, when using the modified MLFMA, can be estimated by the number of the upward and downward processes performed by each cube. We call them the number of updates of the upward and downward processes.

Several quantities must be defined for the estimation of the complexity. The extent of the sub-region and the buffer region are denoted by  $GS$  and  $BS$ , respectively as shown in Figure 4.15.  $GS$  and  $BS$  are measured in terms of the size of a leaf cube. For example, the values of  $GS$  and  $BS$  in Figure 4.15 are 3 and 1, respectively. As shown in Figure 4.15, a testing region is represented by a rectangular cube extending over a three dimensional space. A spanning-level of the testing region over one extent is defined as the number of hierarchical tree levels over which the region spreads. A spanning-level is denoted by  $SL_a$  where  $a$  represents a direction.  $SL_1$  is a spanning-level along the marching direction. For example, the value of  $(SL_1, SL_2, SL_3)$  in Figure 4.15 is  $(2, 2, 1)$  as it has 4 leaf cubes in two directions and two in the other. The four leaf cubes span two hierarchical tree levels, while the two leaf cubes span one ( $2^2 = 4, 2^2 = 4, 2^1 = 2$ ). The largest value of  $\{SL_1, SL_2, SL_3\}$  is denoted by  $SL$ .

$$SL = \max \{SL_1, SL_2, SL_3\} \quad (4.31)$$

Application of Algorithm 4.1 and Algorithm 4.2 results in different numbers of updates of individual leaf cubes, depending on the problem geometry and choice of sub-regions, buffer regions, etc. This variation propagates upward to the root of the octtree structure and it is difficult to therefore give precise values for the complexity. However, we estimate it for the simplified case of scattering from a rectangular plate in what follows. We denote  $l$  as a level of the octtree structure where the complexity is analysed. To ease the analysis, the number of updates of the upward process and the downward process are analysed separately.



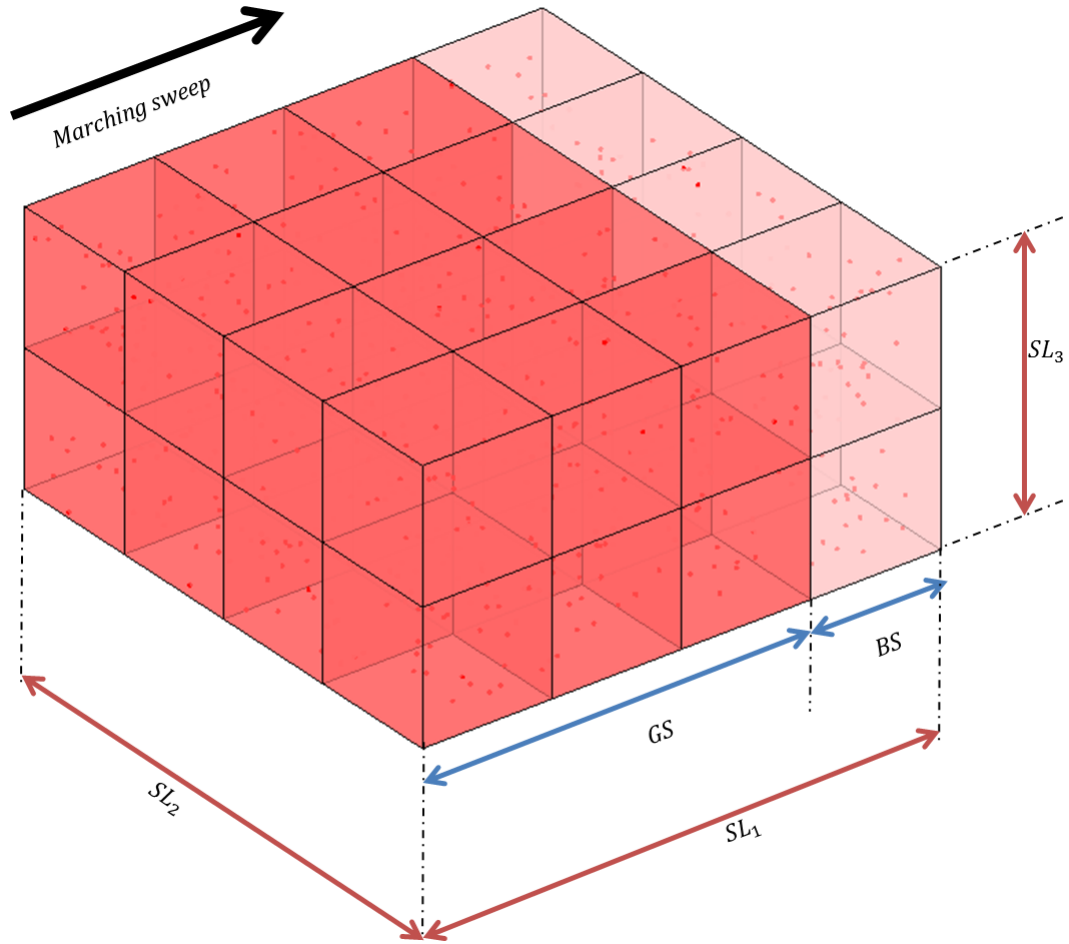


**Figure 4.15:** Illustration of a sub-region size ( $GS$ ) and a buffer region size ( $BS$ ).

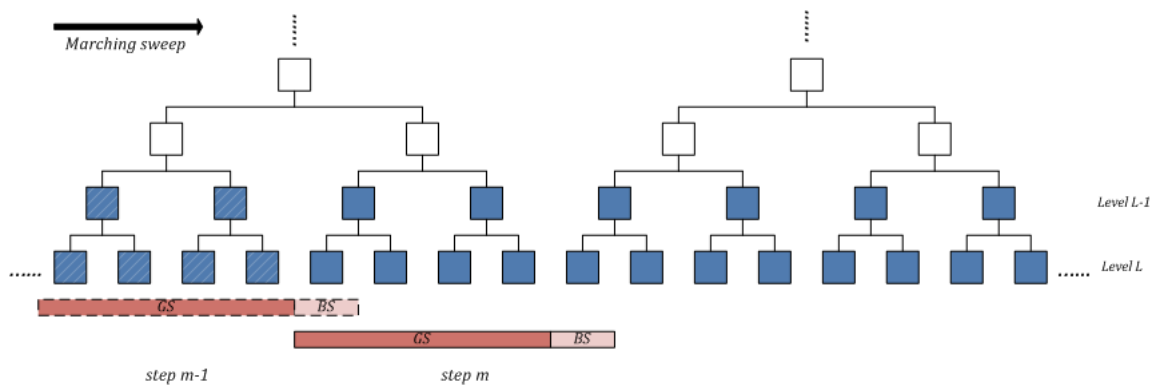


**Figure 4.16:** Illustration of the complexity of the upward process -  $c_1^u$ .

To ensure the clarity of Figures 4.16 – 4.20, some explanations of the coloured shaped are provided as follows. Dashed and solid bars represent the previous and the current steps of the marching sweep, respectively. The dark and light orange parts of the bar illustrate the sub-region and the buffer region, respectively. The dark blue cube represents the investigated cube while the light blue cubes represent the children of the investigated cube.

#### 4.4.2.1 Numbers of updates of the upward process

An update of the upward process is needed if the following two conditions are to be fulfilled. The first requirement is that an investigated cube or any of its children has the outgoing fields changed. The second is that at least one cube at the same level needs the updated outgoing fields for the computation of the incoming fields.

For cubes belonging to levels  $l$  where  $L - \log_2 GS < l \leq L$ , the number of upward updates is 1. An illustration is shown in Figure 4.16 where  $GS = 4$  and  $BS = 1$ . The iteration is marching from sub-region  $(m - 1)$  to sub-region  $m$ . Thus, cubes belonging to sub-region  $(m - 1)$  (strip-blue cubes) will have their outgoing fields updated at step  $m$ . The blue cubes, which are of levels  $l$  where  $L - \log_2 GS < l \leq L$ , are sequentially updated once when the iteration marches over the surface of a scatterer. The number of upward updates of cubes of these levels is denoted by  $c_1^u = 1$ .

Cubes, belonging to levels  $l$  where  $L - SL_1 < l \leq L - \log_2 GS$ , may have to update their outgoing fields if any of their children are in the *current* testing region. Figure 4.17a demonstrates that the dark blue cube may have the outgoing fields updated from step  $m$  to step  $n$ . Its children are shown in light blue. The first child of this cube involves in step  $m$  while its last child participates in step  $n$ . The number of possible updates  $n_{2a}^u$  is shown in Equation 4.32. However, when the cube is entirely inside the testing region as shown in Figure 4.17b, updating the upward process becomes unnecessary. It is because the cube is entirely outside the scattering region. The number of unnecessary updates  $n_{2b}^u$  is given in Equation 4.33. Consequently, the number of updates of cubes belonging to these levels  $c_2^u$  is given in Equation 4.34.

$$n_{2a}^u = \frac{2^{L-l} + GS + BS - 1}{GS} \quad (4.32)$$

$$n_{2b}^u = \frac{GS + BS - 2^{L-l}}{GS} \quad (4.33)$$

$$c_2^u = n_{2a}^u - n_{2b}^u = \frac{2^{L-l+1} - 1}{GS} \quad (4.34)$$

An availability of levels  $l$ , where  $L - SL < l \leq L - SL_1$ , is subject to the condition of  $SL \neq SL_1$ . This means that the marching extent of the testing region is not the largest extent. Thus, the upward update is required whenever any of its children is involved in the testing region. Consequently, the number of upward updates is computed as follows

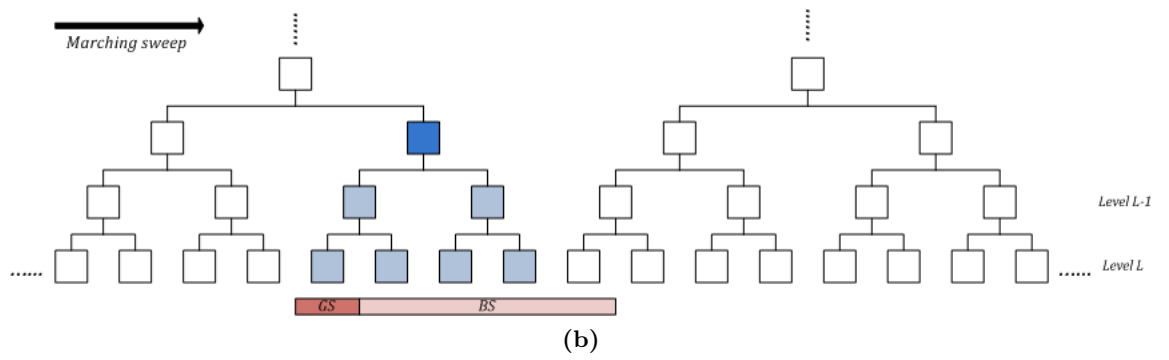
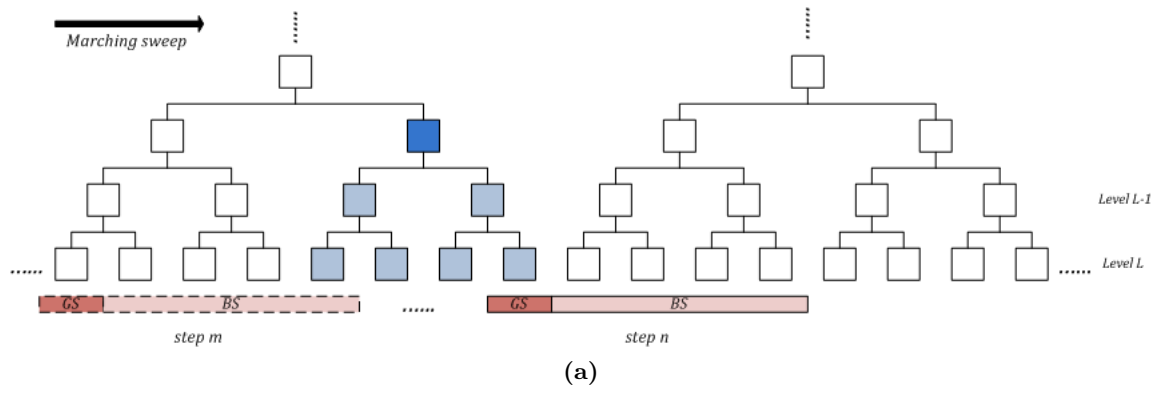


**Figure 4.17:** Illustration of the complexity of the upward process -  $C_2^u$ .

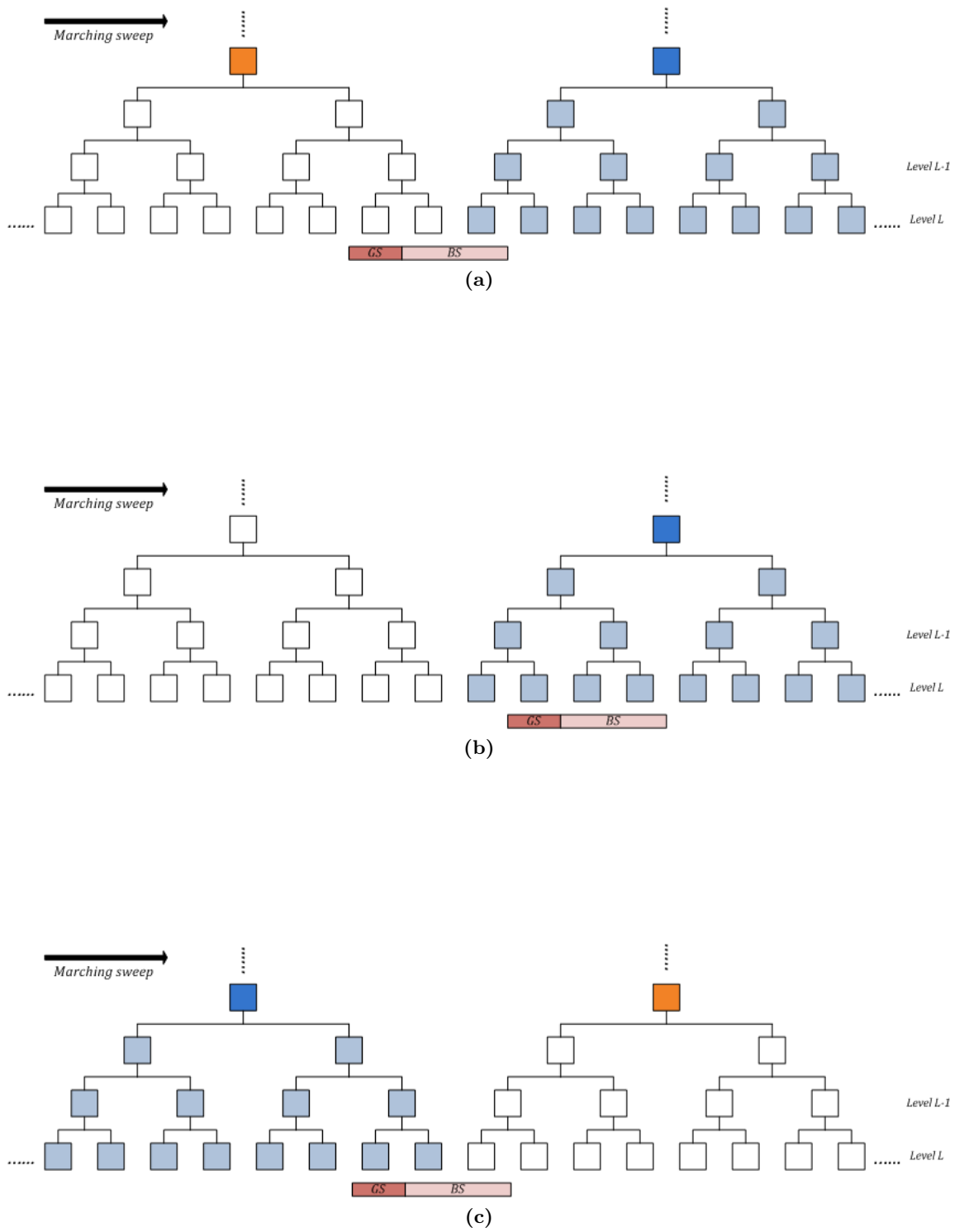


**Figure 4.18:** Illustration of the complexity of the upward process -  $c_4^u$ .

$$c_3^u = \frac{2^{L-l} + GS + BS - 1}{GS}. \quad (4.35)$$

For cubes of levels  $l$  where  $2 \leq l \leq L - SL$ , the complexity can be divided into three components. The first component is the complexity of the first phase when the testing region is marching into the dark blue cube as shown in Figure 4.18a. When the testing region partially belongs to two different cubes (the dark blue cube and the orange cube) at the investigated level, it causes the upward process to be updated for both cubes. The number of updates during the first phase  $n_{4a}^u$  is given in Equation 4.36. The second component is the complexity of the second phase when the testing region is entirely inside the investigated cube as shown in Figure 4.18b. In this phase, updating the upward process of the investigated cube becomes redundant. The complexity of the third phase, when the testing region is marching out the investigated cube, is analysed in a similar manner to that of the first phase. The complexity of this phase  $n_{4c}^u$  is given in Equation 4.37. Finally, the complexity of cubes belong to these levels  $c_4^u$  is expressed in Equation 4.38.

$$n_{4a}^u = \frac{GS + BS - 1}{GS} \quad (4.36)$$

$$n_{4c}^u = \frac{GS + BS - 1}{GS} + 1 \quad (4.37)$$

$$c_4^u = n_{4a}^u + n_{4c}^u = 2 \frac{GS + BS - 1}{GS} + 1 \quad (4.38)$$

#### 4.4.2.2 Numbers of updates of the downward process

There are two conditions for the performance of the update of the downward process of a cube. The first condition is that an investigated cube or any of its children is in need of the recomputation of the incoming fields. Secondly, at least one cube at the same level has the outgoing fields changed, leading to a requirement of downward updating.

For cubes belonging to levels  $l$  where  $L - SL_1 < l \leq L$ , the number of downward updates is larger than 1 due to the buffer region. Cubes inside buffer regions may require multiple recomputations of the downward process. An average number of the downward updates  $c_1^d$  is computed as follows

$$c_1^d = 1 + \frac{BS}{GS}. \quad (4.39)$$

The inequality of the largest extent and the marching extent of the testing region leads to the appearance of levels  $l$  where  $L - SL < l \leq L - SL_1$ . The complexity of cubes of these levels comprises three parts. The first part corresponds to a phase when the testing region starts approaching an investigated cube. Figure 4.19a shows that the testing region is partially inside one child (blue cube with a marker  $\mathbf{X}$ ) of the investigated cube (dark blue cube). Therefore, the incoming fields of the investigated cube is only shifted and antepolated to the single cube with a marker  $\mathbf{X}$ . It means that this computational cost

is half of the cost to perform the full downward process of the investigated cube. The complexity of the first phase is given in Equation 4.40. The second phase corresponds to a situation when the testing region is partially inside both children as illustrated in Figure 4.19b. Consequently, the incoming fields of the dark blue cube are shifted and antepolated to both children with markers  $\mathbf{X}$ . The complexity of the second phase is expressed in Equation 4.41. The third phase is illustrated in Figure 4.19c. The complexity of this phase  $c_{2c}^d$  is derived in a similar manner to that of the first phase.  $c_{2c}^d$  is given in Equation 4.42. As the result, the total complexity of cubes belong to these levels is expressed by Equation 4.43.

$$c_{2a}^d = \frac{1}{2}n_{2a}^d = \frac{1}{2} \frac{2^{L-l}}{2GS} = \frac{2^{L-l}}{4GS} \quad (4.40)$$

$$c_{2b}^d = n_{2b}^d = \frac{2^{L-l} + GS + BS - 1}{GS} - 2 \frac{2^{L-l}}{2GS} \quad (4.41)$$

$$c_{2c}^d = c_{2a}^d = \frac{2^{L-l}}{4GS} \quad (4.42)$$

$$c_2^d = c_{2a}^d + c_{2b}^d + c_{2c}^d = 1 + \frac{2^{L-l}}{2GS} + \frac{BS - 1}{GS} \quad (4.43)$$

For cubes belonging to levels  $l$  where  $2 \leq l \leq L - SL$ , their computational cost has three components. The first phase is shown in Figure 4.20a. The testing region is across two cubes (dark blue cube and orange cube) at the investigated level. The incoming fields are computed only for the child on the left hand side of the dark blue cube. Thus, the complexity of each update is a half of the full disaggregation of the investigated cube. The complexity of the first phase is shown in Equation 4.44. The next phase is demonstrated in Figure 4.20b. In this phase, the testing region is partially inside both children of the investigated cube. The complexity of this phase is given in Equation 4.45. The derivation of the complexity of the third phase shown in Figure 4.20c is similar to that of the first phase. The computation of the third phase is given in Equation 4.46.  $n_{3a}^d$ ,  $n_{3b}^d$  and  $n_{3c}^d$  are the number of updates performed in the first, second and third phase, respectively. The total complexity of cubes in these levels are expressed in Equation 4.47.

$$c_{3a}^d = \frac{1}{2}n_{3a}^d = \frac{1}{2} \left( \frac{GS + BS - 1}{GS} + 1 \right) \quad (4.44)$$

$$c_{3b}^d = n_{3b}^d = \frac{GS + BS - 1}{GS} + \frac{1}{2} \quad (4.45)$$

$$c_{3c}^d = \frac{1}{2}n_{3c}^d = \frac{1}{2} \frac{GS + BS - 1}{GS} \quad (4.46)$$

$$c_3^d = c_{3a}^d + c_{3b}^d + c_{3c}^d = 2 \frac{GS + BS - 1}{GS} + 1 \quad (4.47)$$

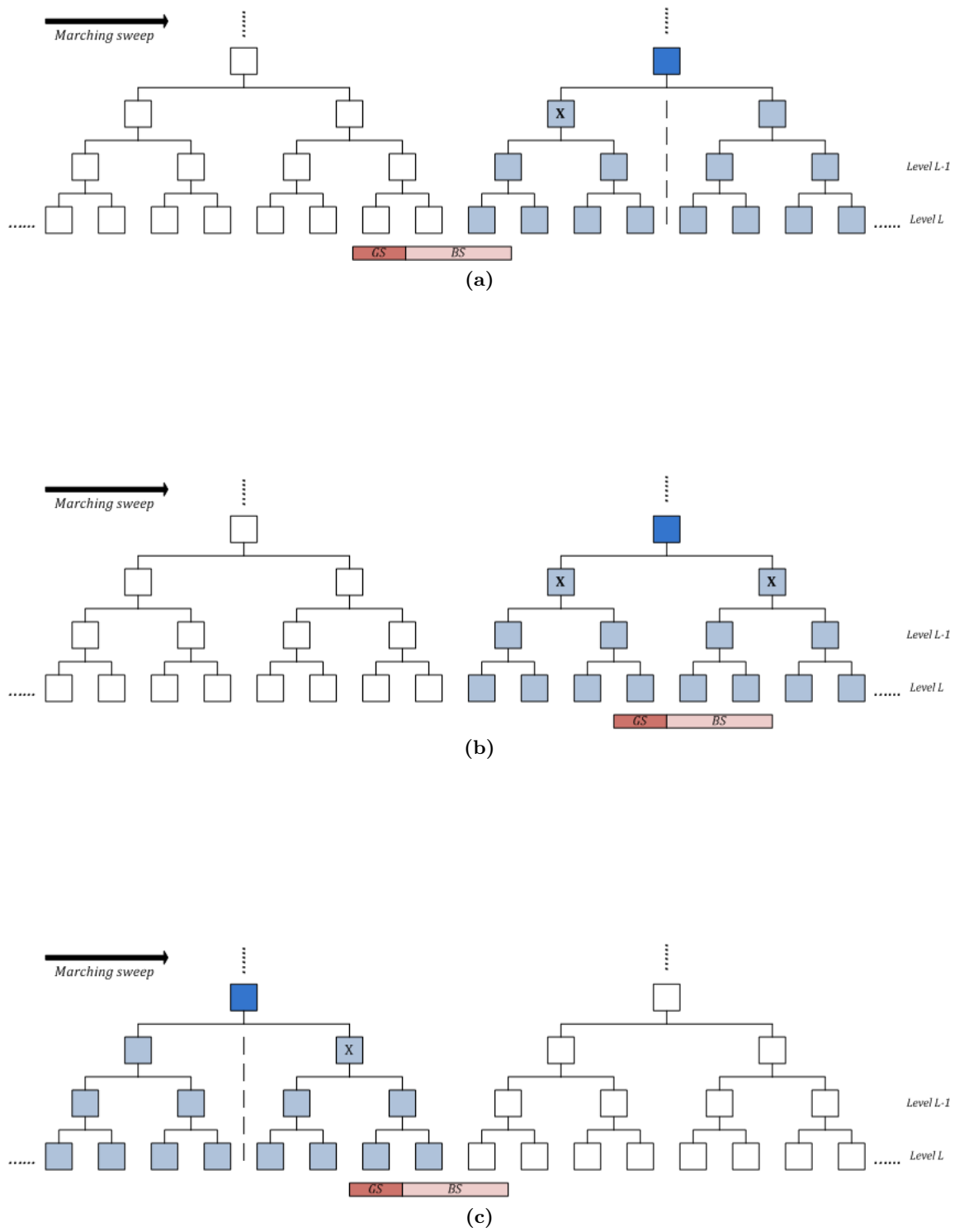


**Figure 4.19:** Illustration of the complexity of the downward process -  $c_2^d$ .

The number of updates required for cubes at different levels for a rectangular plate was analysed is shown in Table 4.1. They are based on consideration of typical cubes located in the centre of the scatterer (where the sub-region and the buffer region size is constant - note that as we approach the ends of the scatterer, the sub-region and the buffer region can sometimes change in order to properly fit the structure). We note also that it is only applicable to the case of a rectangular plate. Nonetheless, the table is useful in that it give some quantification of the complexity of the modified MLFMA.

Several principles regarding the optimisation of the performance of the modified MLFMA can be inferred from Table 4.1. Firstly, a decrease in the computational cost can be achieved by an increase of the sub-region size  $GS$  and a reduction of the buffer region size  $BS$ . An increase of the sub-region size may also lead to a better convergence rate of the BBFB. However, the size of the regions is limited by our ability to compute and store the local sub-matrix inverses  $\hat{\mathbf{Z}}_{m,m}^{-1}$ . Secondly, the complexity can considerably increase for cubes belonging to levels  $l$  where  $L - SL_1 < l \leq L - \log_2 GS$  and  $L - SL < l \leq L - SL_1$ . The increase is mainly due to the term  $2^{L-l}$ . The undesirable increase can be avoided by a decrease of the buffer region size, and equality of  $SL_1$  and  $SL$ . However, a decrease in a size of the buffer region can impact negatively on the convergence rate of the BBFB. Therefore, a determination of the size of these regions should be carried out carefully. The expressions in Table 4.1 are validated numerically in the next section.

If the sizes of the sub-regions and the buffer regions are chosen in accordance with the above, the complexity of a single BBFB sweep is approximately  $(1 + BS/GS)$  times that of a full MVP. As the result, our estimation of the computational cost of each BBFB iteration is  $\mathcal{O}(2(1 + BS/GS)N \log N)$ , which is significantly smaller than the complexity of  $\mathcal{O}(2MN \log N)$  if the standard MLFMA is applied.

## 4.5 Numerical results and validations

Some numerical experiments were conducted to examine the efficiency and the accuracy of the proposed algorithm. The proposed algorithm was developed using an open-source MLFMA code PUMA-EM [116] and an open-source linear algebra library LAPACK [117]. Firstly, the verification of the complexity estimation against some simulation results is presented. Next, comparisons between the proposed method and several popular solvers are shown to demonstrate its efficiency. Finally, the proposed method is applied in combination with a low-rank matrix decomposition for a fast generation of RCS results. All experiments presented in this section were carried out on a Dell-Precision Workstation 670 with a 3.0 GHz Xeon CPU and 3.0 GB of RAM.

### 4.5.1 Verification of the complexity estimation

Numbers of updates computed using formulations in Section 4.4.2 are verified by comparison with the numbers of updates counted in simulations. The simulations count the number of upward and downward updates of all cubes from the finest to the coarsest level.



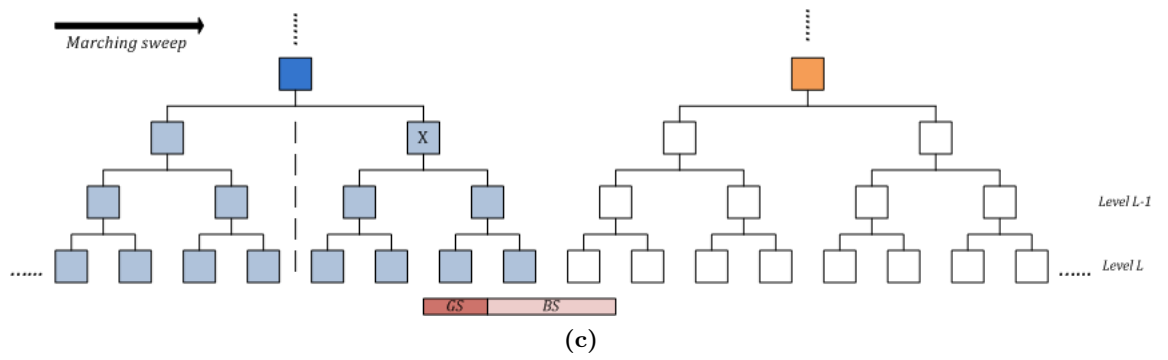
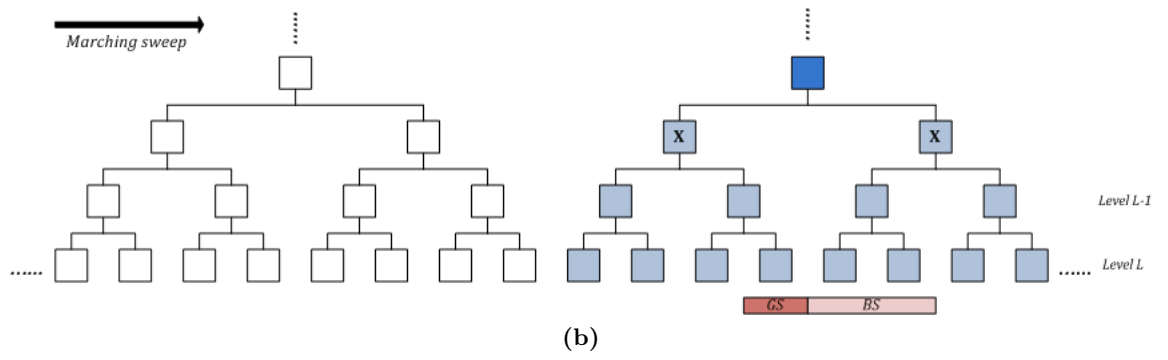
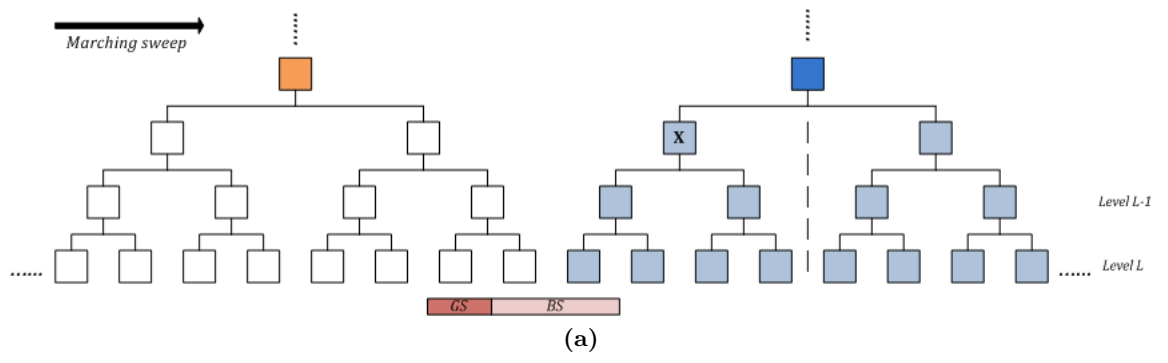


Figure 4.20: Illustration of the complexity of the downward process -  $c_3^d$ .

Level ( $l$ )	Number of updates	
	Upward process	Downward process
$2 \leq l \leq L - SL$	$2^{\frac{GS+BS-1}{GS}} + 1$	$2^{\frac{GS+BS-1}{GS}} + 1$
$L - SL < l \leq L - SL_1$	$\frac{2^{L-l} + GS + BS - 1}{GS}$	$1 + \frac{2^{L-l}}{2GS} + \frac{BS-1}{GS}$
$L - SL_1 < l \leq L - \log_2 GS$	$\frac{2^{L-l+1} - 1}{GS}$	$1 + \frac{BS}{GS}$
$L - \log_2 GS < l \leq L$	1	

**Table 4.1:** Numbers of updates of the upward and downward processes for a single sweep of the BBFB using the modified MLFMA.

Level	Upward process			Downward process		
	Formulation	Middle	Average	Formulation	Middle	Average
2	3	–	1.5	3	–	2
3	3	3	2	3	3	2.33
4	3	3	2.16	3	3	2.5
5	3	3	2.55	3	3	2.73
6	3	3	2.76	3	2.34	2.26
7	2.33	2.33	2.24	1.66	1.66	1.64
8	1	1.3	1.3	1.33	1.33	1.32
9	1	1	1	1.33	1.34	1.33

Formulation: the number of updates computed using formulations in Table 4.1.

Middle: the number of updates of cubes in the middle of a plate.

Average: the average number of updates.

**Table 4.2:** Numbers of process updates for a rectangular PEC plate with a size of  $1.5\lambda \times 40\lambda$  using the BBFB accelerated by the modified MLFMA.

For example, an investigated cube has  $n$  children. The number of upward or downward updates will increase by  $1/n$  if one of its children performs a corresponding process.

#### **4.5.1.1 Test case 1: Complexity estimation for a rectangular PEC plate size of $1.5\lambda \times 40\lambda$**

A rectangular PEC plate size of  $1.5\lambda \times 40\lambda$  is illuminated by a vertically polarised plane wave at a frequency of 500MHz, where  $\lambda$  is the associated wavelength of an excitation. RWG basis functions are used for the discretisation of the surface of the scatterer. The marching direction of the BBFB is chosen to be the largest extent of the plate. The application of the modified MLFMA allows a partition of the entire scatterer into cubes where leaf cubes are size of  $\lambda/4$ . The number of octtree levels is  $L = 9$ . Consequently, there are 161 leaf cubes along the greatest extent of the plate. The sizes of the sub-region and the buffer region are chosen as  $GS = 3$  and  $BS = 1$ , respectively. The numbers of downward and upward updates that actually occurred in the simulation are shown in Table 4.2. The number of updates estimated using the formulations in Table 4.1 are shown in “Formulation” columns. The “Middle” columns contain an average number of updates of cubes located in the middle of the scatterer where the estimate should be most accurate. The overall average numbers of updates of each level are given in “Average” columns. It can be seen that values estimated using the formulations of Table 4.1 are close to those observed in the simulation for the middle cubes where the conditions used to make the estimate are best met.

#### **4.5.1.2 Test case 2: Complexity estimation for a rectangular PEC plate size of $0.5\lambda \times 20\lambda$**

A similar experiment is performed for a rectangular PEC plate size of  $0.5\lambda \times 20\lambda$ . The greatest extent of a scatterer is chosen to be the marching direction. The application of the modified MLFMA to the scatterer leads to an octtree structure of 8 levels. In this experiment, the size of the buffer region is increased to observe its effect on the performance of the modified MLFMA. The sizes of the sub-region and the buffer region are 1 and 4, respectively. The numbers of updates are presented in Table 4.3. Numbers computed using formulations are similar to those counted by the simulation. The enlargement of the buffer region leads to a significant increase in the number of updates. As a result, the larger size of the buffer region degrades the performance of the modified MLFMA. The comparison between the runtime of one BBFB iteration and that of one full MVP is shown in Table 4.4. The table confirms the estimated cost of  $\mathcal{O}(2(1 + BS/GS)N \log N)$  for each BBFB iteration.

#### **4.5.1.3 Test case 3: Comparison between the standard MLFMA and the modified MLFMA for a perfectly conducting NASA ogive with a length of 10 inches**

A comparison between the performance of the standard MLFMA and that of the modified MLFMA is presented in this experiment. The NASA ogive [1] is positioned along the  $x$ -

Level	Upward process			Downward process		
	Formulation	Middle	Average	Formulation	Middle	Average
2	9	—	4.5	9	—	5.75
3	9	9	6	9	9	7.5
4	9	9	6.8	9	9	7.9
5	9	8	6.95	9	8	7.55
6	7	5	4.65	5	6	5.8
7	3	2	1.91	5	5	4.88
8	1	1	0.99	5	5	4.87

Formulation: the number of updates computed using formulations in Table 4.1.

Middle: the number of updates of cubes in the middle of a plate.

Average: the average number of updates.

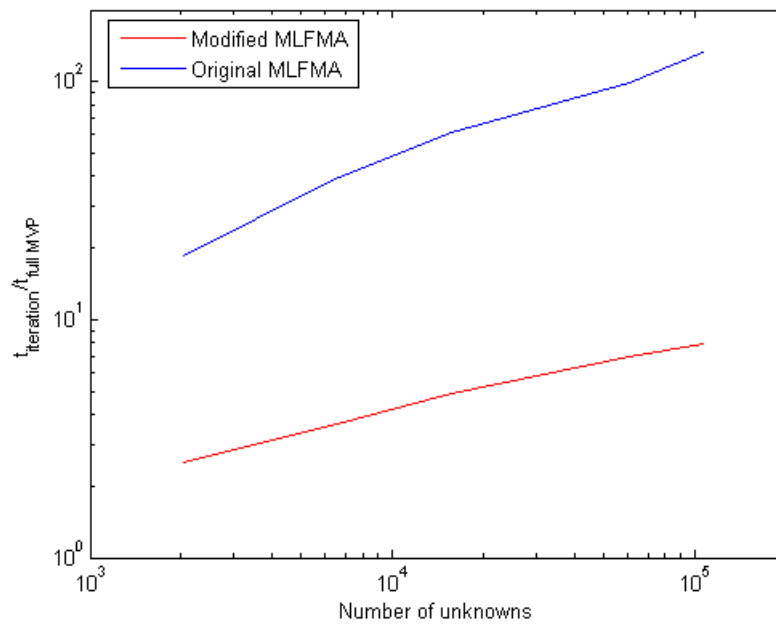
**Table 4.3:** Numbers of process updates for a rectangular PEC plate with a size of  $0.5\lambda \times 20\lambda$  using the BBFB accelerated by the modified MLFMA.

Plate size	$t_{\text{iter}}(\text{sec})$	$t_{\text{MVP}}(\text{sec})$	$t_{\text{iter}}/t_{\text{MVP}}$
$1.5\lambda \times 40\lambda$	38	13	2.92
$0.5\lambda \times 20\lambda$	14	2	7

$t_{\text{iter}}$ : time to perform one BBFB iteration

$t_{\text{MVP}}$ : time to perform one full matrix-vector product using the MLFMA

**Table 4.4:** Comparison of runtime of a BBFB iteration and that of a full matrix-vector product for rectangular PEC plates size of  $1.5\lambda \times 40\lambda$  and  $0.5\lambda \times 20\lambda$ .



**Figure 4.21:** Comparison of the runtime (divided by runtime of one full MVP) between the standard MLFMA and the modified MLFMA for the NASA ogive.

	Number of slices	Sub-region size ( $GS$ )	Buffer region size ( $BS$ )
Scenario 1	24	2	1
Scenario 2	24	3	1
Scenario 3	24	4	1

**Table 4.5:** List of scenarios performed in test case 4.

Local problems	Scenario 1		Scenario 2		Scenario 3	
	Forward	Backward	Forward	Backward	Forward	Backward
1	868	536	1204	868	1626	1204
2	1090	1062	1754	1570	2438	2259
3	1418	1238	2142	2016	3178	3004
4	1536	1501	2663	2499	3557	3520
5	1791	1626	2812	2796	3254	3431
6	2057	1984	2808	2873	1713	2336
7	2088	2063	2290	2509	–	–
8	2202	2133	1166	1713	–	–
9	2084	2140	–	–	–	–
10	1838	1962	–	–	–	–
11	1385	1622	–	–	–	–
12	714	1166	–	–	–	–

**Table 4.6:** Size of local problems of scenarios in test case 4.

Local problems	Forward	Backward
1	1520	232
2	2112	1520
3	1944	2112
4	1664	1944
5	1504	1664
6	1680	1504
7	1927	1680
8	1859	1927
9	1827	1859
10	1568	1827
11	928	1568
12	232	928

**Table 4.7:** Size of local problems in test case 6.

axis and is illuminated by an incident wave which has a frequency varying from 3GHz to 20GHz. Thus, a total number of unknowns is within a range of (2,040-106,125). The marching direction of the BBFB is the greatest extent of the problem. The size of the sub-region and the buffer region is fixed with  $GS = 1$  and  $BS = 1$ . The complexity of the methods is measured in terms of the ratio between the average runtime of one BBFB iteration and the runtime of one full MVP using the MLFMA (i.e. with complexity of  $\mathcal{O}(N \log N)$ ) and is shown in Figure 4.21. The complexity of the proposed method is considerably smaller than that of the BBFB with the standard MLFMA. The ratio for the case of the modified MLFMA slowly increases with the size of the problem. This is due to  $SL_1 \neq SL$  as the frequency increases. This leads to a larger complexity required to compute processes at levels  $l$  where  $L - SL < l \leq L - SL_1$  as shown in Table 4.1.

### 4.5.2 Efficiency and accuracy of the modified MLFMA applied to the BBFB

In this section, comparisons between the performance of the proposed method and that of some popular Krylov iterations are presented. An improvement step, which is analysed in detail in the next chapter, is performed at the end of each BBFB iteration for enhancement of the convergence rate. Two Krylov solvers, the GMRES and the BiCGSTAB, are chosen for comparison. They are preconditioned by the sparse approximate inverse technique. The combined field integral equation with a coupling parameter of  $\alpha = 0.3$  is applied to improve the condition number of the resultant impedance matrix. The threshold of the improvement step of the BBFB is  $\eta = 0.6$ . Residual norms, which are shown in the following test cases, are computed by

$$\text{residual norm} = \frac{\|\mathbf{Z}\mathbf{x}^{(i)} - \mathbf{v}\|_2}{\|\mathbf{v}\|_2}. \quad (4.48)$$

#### 4.5.2.1 Test case 4: Comparison for a perfectly conducting NASA almond with a length of 9.936 inches<sup>1</sup>

The NASA almond [1], placed along the  $x$ -axis as shown in Figure 4.22a, is illuminated by a vertically polarised plane wave with an incident angle of ( $\theta = \pi/2; \varphi = 2\pi/3$ ) at 7GHz. The scatterer is discretised by 12,858 RWG basis functions. The almond is decomposed into thin and equal slices along the marching direction which is the greatest extent of the problem ( $x$ -axis). The total number of slices is 24. The width of each slice is equal to a size of a leaf cube. Different scenarios of the BBFB are applied for the solution of the problem. The different scenarios correspond to the size of the sub-region as presented in Table 4.5. The number of basis functions within individual local problems for each scenario is given in Table 4.6. The comparisons between the BBFB and the preconditioned Krylov solvers are shown in Figure 4.22b and c. The number of iterations required by the proposed algorithm is significantly fewer than that of the Krylov solvers to achieve the same accuracy. Although the complexity of each BBFB iteration is larger than that of

<sup>1</sup>inch is used to describe the size of geometries such as NASA almond, NASA double-ogive in [1].

the SPAI-GMRES and the SPAI-BiCGSTAB, the overall performance of the proposed algorithm remains better than the others, due to the fact that fewer iterations are needed.

The main issue with application of the proposed method is the determination of the sizes of the sub-region and the buffer region. It can be seen clearly that when the size of the sub-region increases, the convergence rate of the proposed algorithm is improved. However, the increase would lead to more complexity for the solution of local problems. In our experience, the performance of the BBFB is acceptable for the size of the sub-region  $GS = 2$  when the CFIE with  $\alpha = 0.3$  is applied to the solution of smooth, long and narrow structures. The size of the buffer region is kept to be small to minimise redundant computations. In numerous experiments, the size of the buffer region  $BS = 1$  yields a desired accurate solution.

#### **4.5.2.2 Test case 5: Comparison for a perfectly conducting wind turbine blade with a length of 40 meters**

The application of the BBFB to a solution of a real-life problem is presented in this experiment. The scatterer is a PEC wind turbine blade with a length of 40 meters, placed along the  $z$ -axis as shown in Figure 4.23a. The geometry is discretised using 52,893 basis functions, and is partitioned into 136 equal slices along its greatest extent. The blade is illuminated by a vertically polarised plane wave at 200MHz with an incident angle of  $(\theta = \pi/2; \varphi = 2\pi/3)$ . The BBFB marches along the  $z$ -axis. The sizes of the sub-region and the buffer region are  $GS = 2$  and  $BS = 1$ , respectively. The performance of the algorithms are presented in Figure 4.23b and c. The proposed algorithm demonstrates a good convergence rate, reaching a residual norm of  $10^{-3}$  within 3 iterations. The overall performance of the BBFB remains considerably better than that of the Krylov iterations in terms of runtime.

#### **4.5.2.3 Test case 6: RCS computation of a perfectly conducting NASA double-ogive with a length of 7.5 inches**

The comparison between the measurement data in [1] and the results computed by the BBFB is presented in this experiment. A NASA double-ogive [1] is positioned along the  $x$ -axis as shown in Figure 4.24a. The scatterer is discretised into 12,552 RWG basis functions and is illuminated by plane waves at 9GHz. The double-ogive is partitioned into 23 equal slices along the marching direction which is the greatest extent of the problem. The width of each slice is  $\lambda/4$ , equal to the size of leaf cubes. The size of the sub-region and the buffer region are 2 and 1, respectively. The size of local problems is shown in Table 4.7. The RCS results are shown in dBsm (decibel relative to one square meter) as a function of  $\varphi$  with  $\theta = \pi/2$ . The RCS characteristics for both horizontal (HH) and vertical (VV) polarisations are computed using the proposed method. The simulated results are compared with the published measurement in Figure 4.24b. The results show a good agreement with the measured data for both polarisations at all aspect angles.

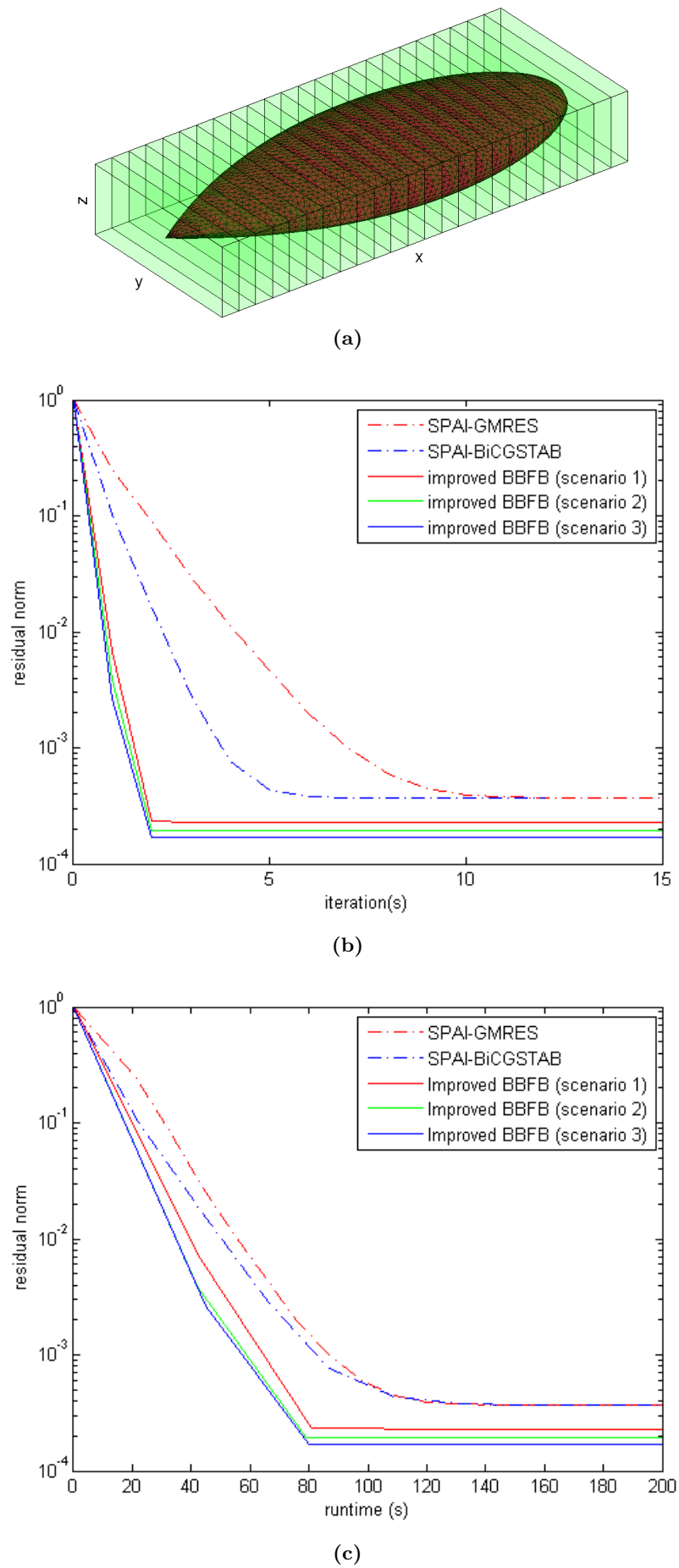


**Figure 4.22:** Comparison between the BBFB and the Krylov iterations for the NASA almond.



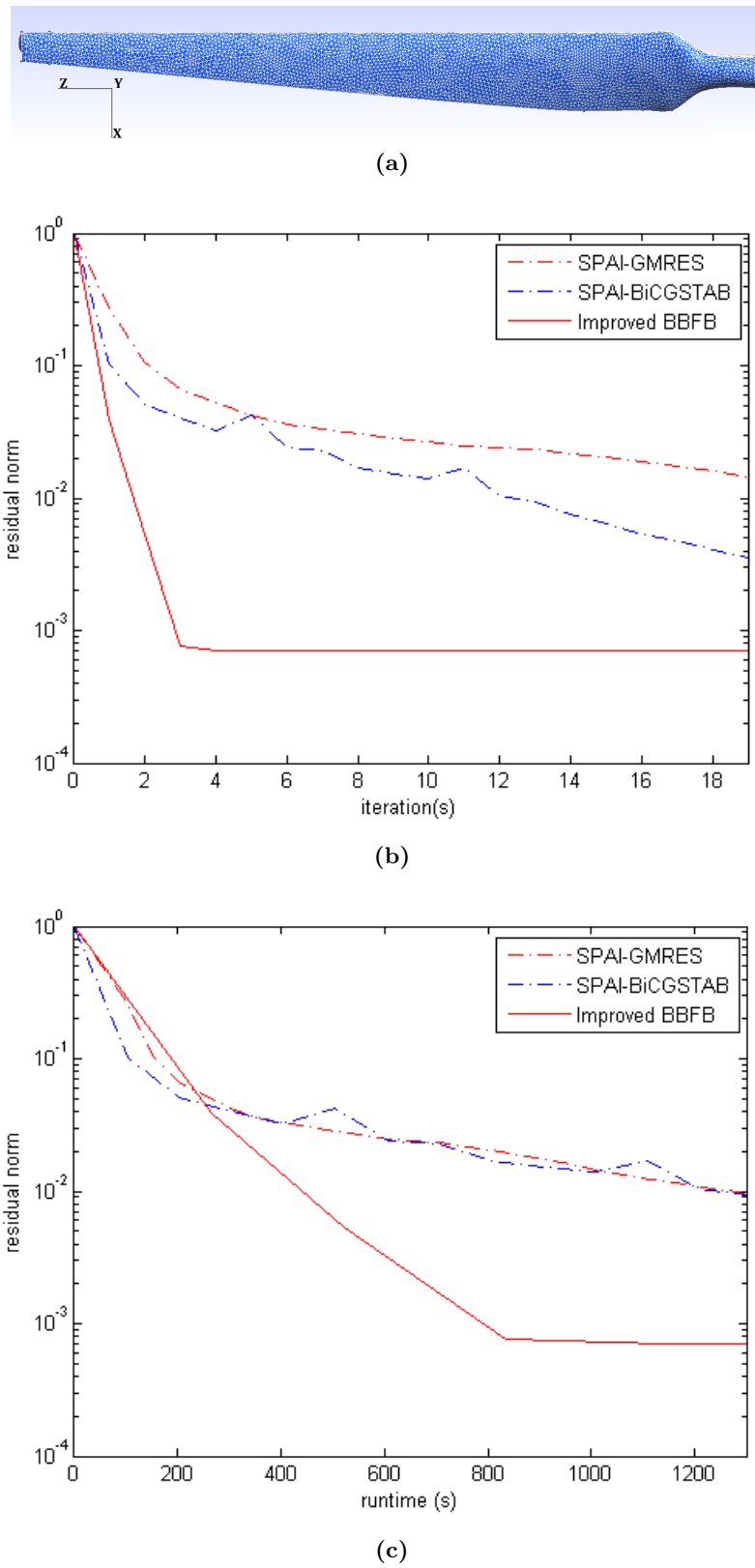


**Figure 4.23:** Comparison between the BBFB and the Krylov iterations for the wind turbine blade.

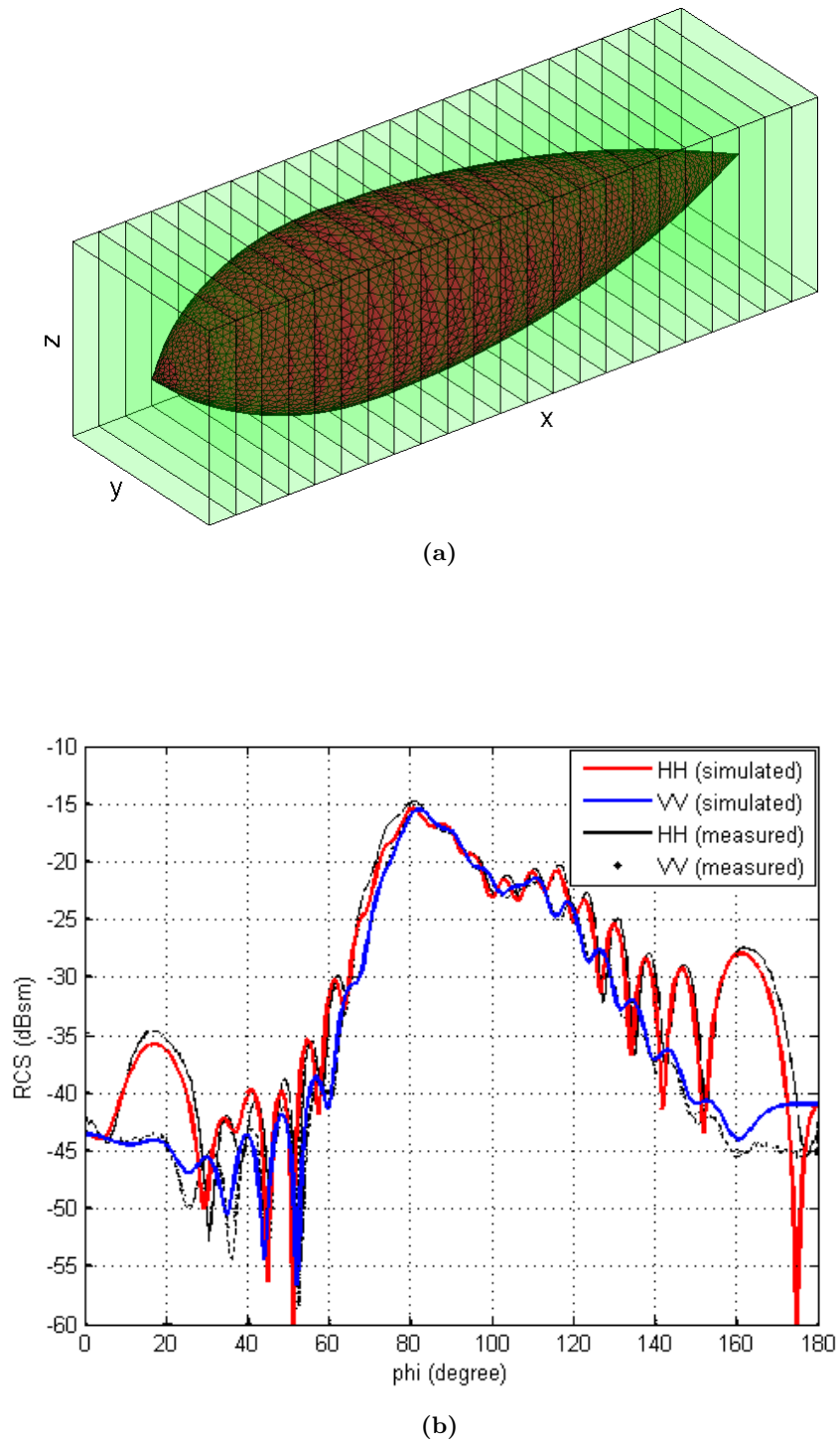


**Figure 4.24:** Comparison between the RCS results computed using the BBFB and the measurement data in [1].

### 4.5.3 Combination with the interpolative decomposition for an efficient computation of radar cross section

The ability to accurately and efficiently compute the radar cross section of three dimensional bodies for a large number of incident angles is important for many electromagnetic applications. The MoM discretisation of a surface integral equation representation of the problem remains a very popular solution method especially for electrically small bodies where one can directly compute the inverse of the associated impedance matrix and then use it to solve for multiple excitations. An advantage of such direct solvers is that the most burdensome computation of the inverse is performed only once. However, due to the dense nature of the impedance matrix, storage becomes an issue as the problem size grows and iterative solvers become more appropriate for the solution of medium and large problems. A disadvantage of iterative solvers is that the iterative process must be repeated independently for every excitation vector. Several approaches have been proposed to alleviate the drawback. One approach is to reduce the number of iterations for each incident excitation by improving the initial guess. The initial guess can be obtained from the previous solution with a phase correction [57] or established by reusing descent vectors computed in previous iterative processes [118]. Another approach is to reduce the number of right hand side vectors by application of matrix decomposition techniques such as the singular value decomposition (SVD) [119], interpolation models [120] or asymptotic models [121]. However, the lack of an error-controllable scheme or the computational burden of matrix decomposition techniques are disadvantages of the methods. The interpolative decomposition (ID) [122, 123] also reduces the number of right hand side vectors and demonstrates several desirable features. The algorithm offers an error-controllable scheme [122]. In addition, the cost to construct matrices in ID is cheaper than in SVD [122].

#### 4.5.3.1 Interpolative decomposition

We assume that there are  $N_{\text{inc}}$  distinct time harmonic sources (Figure 4.25) illuminating a scatterer. Thus, we can rewrite Equation 3.1 as

$$\mathbf{Z}\mathbf{X} = \mathbf{V} \quad (4.49)$$

where  $\mathbf{V}$  is a  $N \times N_{\text{inc}}$  matrix with column vectors containing information about  $N_{\text{inc}}$  excitations.  $\mathbf{X}$  is a  $N \times N_{\text{inc}}$  matrix with column vectors containing information about corresponding currents. These are unknowns and must be computed. A naive solution proceeds by solving  $N_{\text{inc}}$  distinct problems of the form Equation 3.1. A better way to solve the system in Equation 4.49 is to somehow reduce the number of vectors in  $\mathbf{V}$ , or equivalently the number of excitations under consideration. This is achieved by application of the ID to the excitation matrix  $\mathbf{V}$ . The right hand side of Equation 4.49 is decomposed into the product of a skeleton matrix and an interpolation matrix as

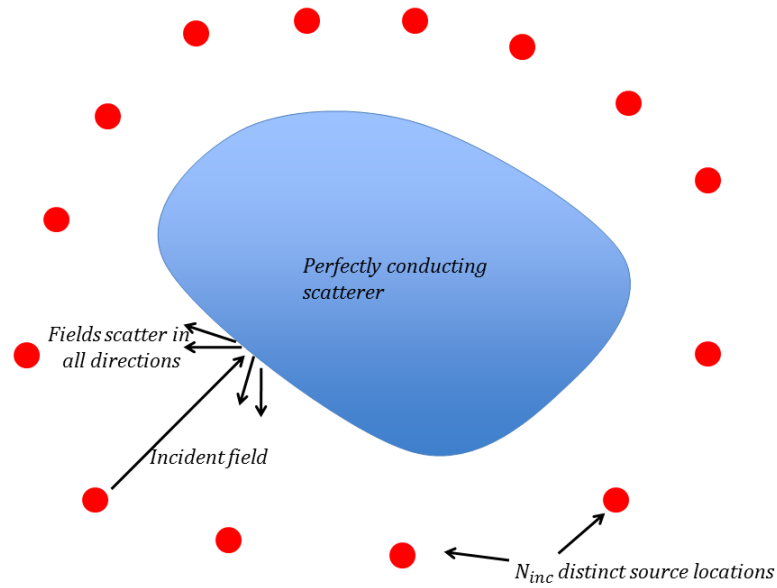
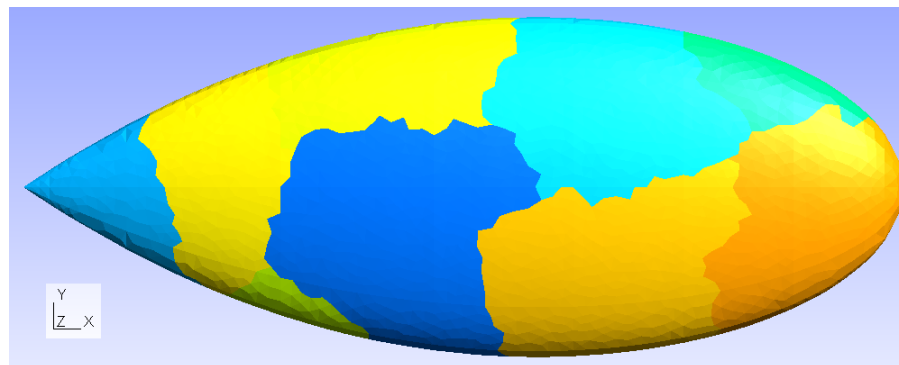


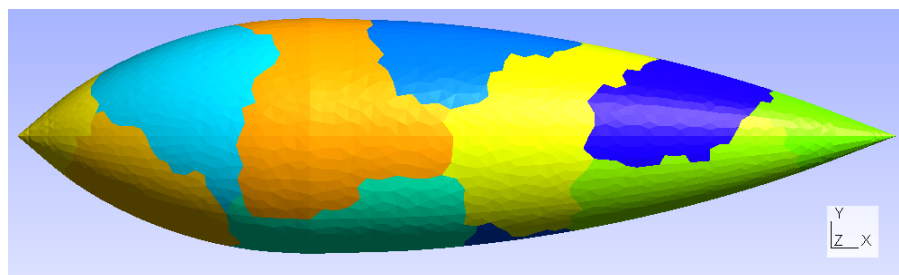
**Figure 4.25:** Illustration of multiple excitation angles in a mono RCS computation of a PEC problem.

	Original MLFMA	Modified MLFMA	Speed-up
Almond	90	33	2.73
Double-ogive	135	35	3.86

**Table 4.8:** Runtime in seconds for each O-DDM iteration when using the modified MLFMA and the original MLFMA for the NASA almond and the NASA double-ogive.



(a)



(b)

**Figure 4.26:** Partition of the NASA almond and the NASA double-ogive in the overlapping domain decomposition method.

$$\mathbf{V} = \bar{\mathbf{V}}\mathbf{P} \quad (4.50)$$

where  $\bar{\mathbf{V}}$  is a  $N \times K$  skeleton excitation matrix and  $\mathbf{P}$  is a  $K \times N_{\text{inc}}$  interpolation matrix ( $K \ll N_{\text{inc}}$ ). The representation of  $\mathbf{V}$  in Equation 4.50 allows us to rewrite Equation 4.49 as

$$\mathbf{Z}(\bar{\mathbf{X}}\mathbf{P}) = \bar{\mathbf{V}}\mathbf{P} \quad (4.51)$$

where  $\bar{\mathbf{X}}$  is a corresponding  $N \times K$  skeleton current matrix. Consequently, the application of ID reduces the original system Equation 4.49 with  $N_{\text{inc}}$  excitations to a reduced system with  $K$  excitations where  $K \ll N_{\text{inc}}$ .

$$\mathbf{Z}\bar{\mathbf{X}} = \bar{\mathbf{V}} \quad (4.52)$$

$\bar{\mathbf{X}}$  can be computed by solving  $K$  problems of the form 3.1. Having computed  $\bar{\mathbf{X}}$ , it is possible to reconstruct the full-solution  $\mathbf{X}$  by performing the product of the skeleton current matrix and the interpolation matrix.

$$\mathbf{X} = \bar{\mathbf{X}}\mathbf{P} \quad (4.53)$$

Individual linear systems in Equation 4.52 are solved by using the O-DDM accelerated by the modified MLFMA. In addition, the cube-based scheme proposed in [87] is applied to facilitate the performance of the modified MLFMA.

#### 4.5.3.2 Test case 7: Comparison between the modified MLFMA and the MLFMA applied to the O-DDM

The modified MLFMA is applied to the O-DDM for the solution of perfectly conducting three dimensional problems. To illustrate the advantage of using the modified MLFMA as opposed to the original MLFMA, we compare the runtime of each O-DDM iteration for both cases in Table 4.8. The methods are applied to the NASA almond and the NASA double-ogive which are discretised into 12,834 and 12,555 RWG basis functions at 7GHz and 9GHz, respectively. The almond and the double-ogive are partitioned into 10 and 15 overlapping domains as shown in Figure 4.26, respectively. In each case, the runtime required for the modified MLFMA O-DDM iteration is greatly reduced when compared to that of the original MLFMA O-DDM.

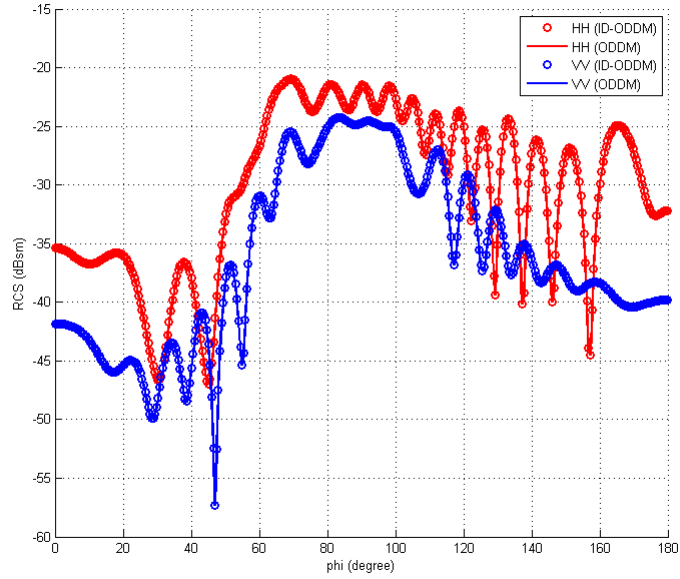


**Figure 4.27:** Comparison between the RCS computed using ID-ODDM and that computed using the ODDM for the NASA almond.

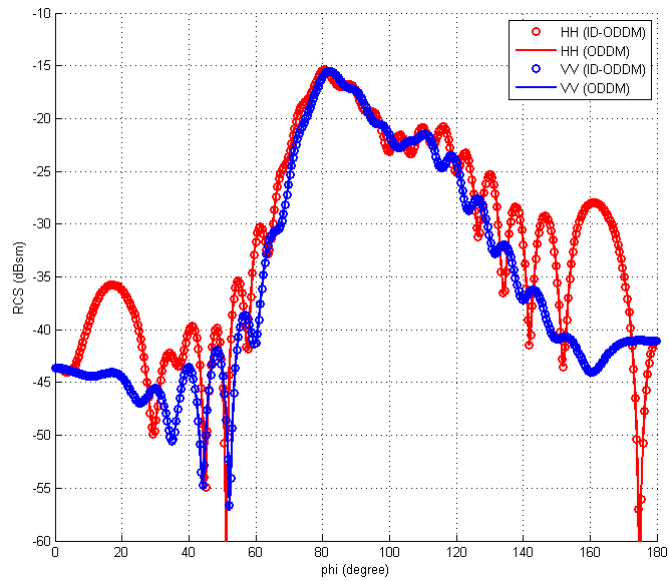


**Figure 4.28:** Comparison between the RCS computed using ID-ODDM and that computed using the ODDM for the NASA double-ogive.

	Method	$N_{inc}$	$K$	Runtime (sec)
Almond	ID-ODDM	776	63	9,764
	ODDM	776	N/A	80,365
Double-ogive	ID-ODDM	776	59	11,020
	ODDM	776	N/A	95,474

**Table 4.9:** Runtime for the computation of mono RCS using the ID-ODDM and the ODDM with a phase correction for the NASA almond and the NASA double-ogive.

### 4.5.3.3 Test case 8: Efficiency of ID applied to the O-DDM

The RCS results of the problems in test case 7 are investigated to examine the efficiency of ID applied to the O-DDM. The RCS of the almond is evaluated at 776 distinct incident angles. For each angle in the horizontal plane, we compute the monostatic RCS using the O-DDM with the modified MLFMA. To improve the convergence rate, the initial guess is obtained from the previous solution with a phase correction [57]. This is plotted in Figure 4.27 for both horizontal (red solid line) and vertical (blue solid line) polarisations. We then used ID to solve the same problem. It was possible to compress the right hand side matrix and instead solve  $K = 63$  distinct skeleton excitations. These were then used to solve for the surface currents for all 776 incident angles using the interpolative matrix  $\mathbf{P}$  and Equation 4.53. These were in turn used to compute the monostatic RCS, shown in Figure 4.27 using red and blue circles. The results for a similar simulation of the NASA double-ogive are also presented in Figure 4.28. The agreement is extremely good, with no error being discernible. The simulation results for both geometries also match the measured data in [1] very well. The runtime for the computation of RCS using the ID-ODDM and the ODDM with a phase correction is given in Table 4.9. Using ID method, the total time required to solve for the multiple right hand sides was reduced by a factor of 8.

## 4.6 Conclusion

A modified MLFMA is presented in this chapter to accelerate the partial matrix vector products required in each iteration of stationary solvers such as the buffered block forward backward method and the overlapping domain decomposition method. Applying the standard MLFMA to the performance of the partial matrix vector products results in significant redundancy, causing the loss of efficiency of the stationary methods. A reduction of the redundancy can be achieved by using the modified method which is based on two simple algorithms which can be used to set flags to determine what small subset of cubes is in need of having their associated fields recomputed in the MLFMA upward or downward processes. Numerical experiments are presented to demonstrate the efficiency and the accuracy of the proposed method over the standard method.

# 5 Modified improvement step for stationary iterative methods

In this chapter, the modified improvement step is proposed for the improvement of the convergence rate of stationary iterations. The proposed technique is an extension of the optimally sized correction (or the improvement step) introduced by Mullen et al in [124]. The optimal correction is modified for the use of multiple correction vectors instead of a single correction vector. The improvement step is briefly reviewed prior to the introduction of the modified technique. The mathematical derivation and a complexity analysis of the method are given in Section 5.3. Some numerical experiments are presented to illustrate the advantages of the technique.

## 5.1 Introduction

Stationary iterative methods have been proven to be efficient for application to specific problems such as scattering from randomly rough surfaces [125, 126]. However, the performance of the stationary methods is greatly dependent on the spectral radius of the associated iteration matrix as explained in chapter 3. Small values of the spectral radius lead to a good performance of the stationary solvers. Nevertheless, the operation of the methods deteriorates when the value of the spectral radius approaches 1. This happens to randomly rough surface scattering problems when the roughness of the surface increases, resulting in an unsatisfactory convergence rate. An improvement step [124] can be operated at the end of each FBM iteration when a certain criterion is met for better convergence behaviour. However, the successive process of stationary iterations may result in the loss of effectiveness of the previous improvement steps. In this chapter, the modified improvement step is proposed to alleviate the loss by using multiple correction vectors.

## 5.2 Improvement step

The error vector of the approximate solution at the  $i^{\text{th}}$  iteration is defined as

$$\boldsymbol{\varepsilon}^{(i)} = \mathbf{x} - \mathbf{x}^{(i)} \tag{5.1}$$

where  $\mathbf{x}$  is the exact solution. From Equation 3.80, the relationship between consecutive errors is given by

$$\boldsymbol{\varepsilon}^{(i)} = \mathbf{M}\boldsymbol{\varepsilon}^{(i-1)} \tag{5.2}$$



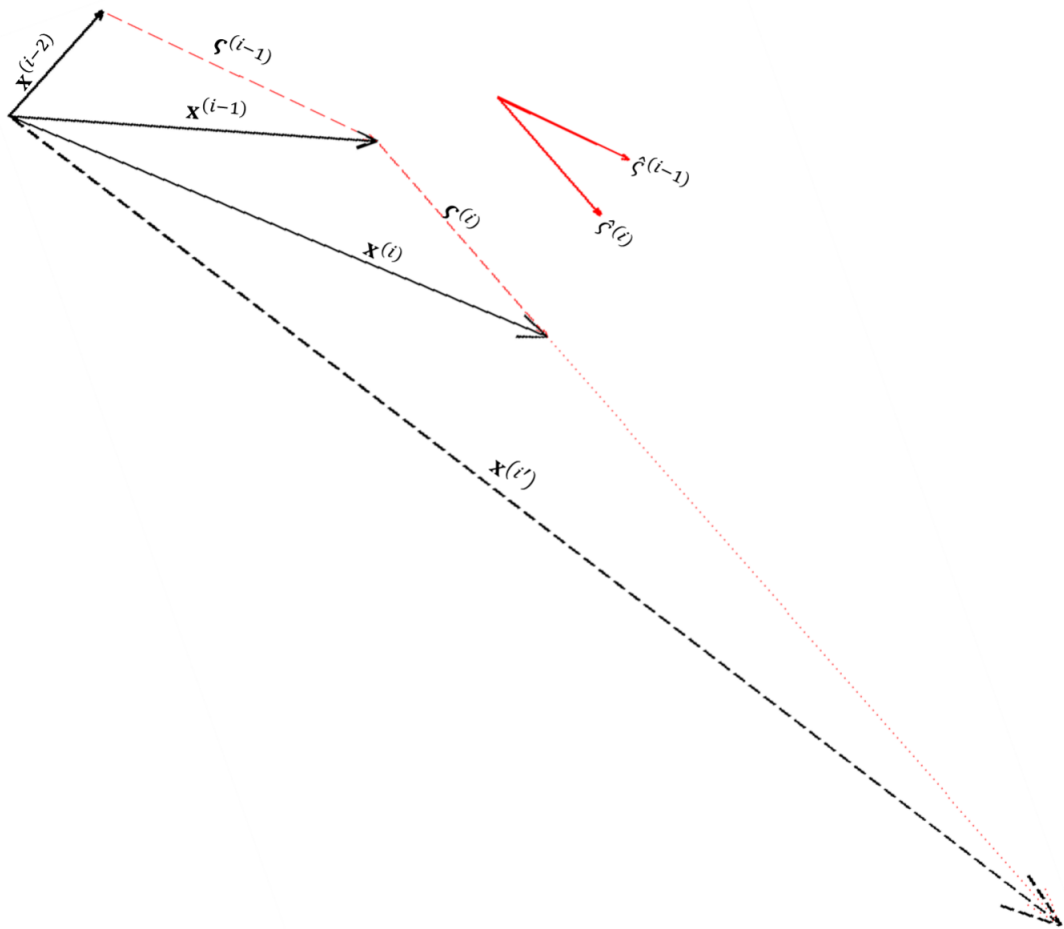


**Figure 5.1:** Illustration of the improvement step.

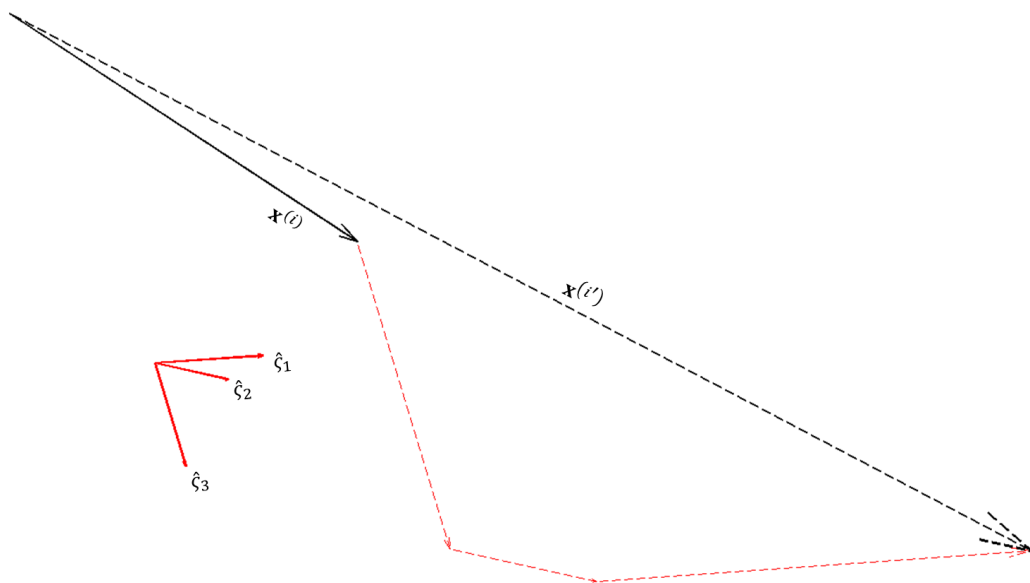


**Figure 5.2:** Illustration of the modified improvement step.

where  $\mathbf{M}$  is the iteration matrix of the stationary method. Assume that the representation of the initial error vector is given by

$$\boldsymbol{\varepsilon}^{(0)} = \sum_{n=1}^K \beta_n^{(0)} \mathbf{e}_n \quad (5.3)$$

where  $K$  is the rank of the iteration matrix.  $\beta_n^{(0)}$  are initial coefficients and  $\mathbf{e}_n$  are eigenvectors of the iteration matrix. The error vector at iteration  $i$  can be written in terms of the eigenvectors  $\mathbf{e}_n$  and the corresponding eigenvalues  $\lambda_n$ .

$$\boldsymbol{\varepsilon}^{(i)} = \sum_{n=1}^K \lambda_n^i \beta_n^{(0)} \mathbf{e}_n \quad (5.4)$$

It can be seen that the error vector is a linear combination of error components which are in the direction of eigenvectors  $\mathbf{e}_n$ . The magnitude of these components at the  $i^{\text{th}}$  iteration is given by  $\lambda_n^i \beta_n^{(0)}$ . This suggests that the error components associated with small  $\lambda_n$  will decay rapidly due to the multiplication by  $\lambda_n$  at each iteration. In contrast, the error components related to large  $\lambda_n$  will slowly decay. After a large number of iterations, the error vector  $\boldsymbol{\varepsilon}^{(i)}$  is dominated by error components associated with the largest eigenvalues of the iteration matrix. We denote the set of indices of the largest eigenvalues by  $\Omega$ . Therefore, the error vector in Equation 5.4 can be approximated by

$$\boldsymbol{\varepsilon}^{(i)} \simeq \sum_{n \in \Omega} \lambda_n^i \beta_n^{(0)} \mathbf{e}_n. \quad (5.5)$$

The largest eigenvalue of the iteration matrix is denoted by  $\lambda_{\text{dom}}$ . Equation 5.5 can be rewritten as

$$\boldsymbol{\varepsilon}^{(i)} \simeq \lambda_{\text{dom}}^i \mathbf{q} \quad (5.6)$$

where

$$\mathbf{q} = \sum_{n \in \Omega} \beta_n^{(0)} \mathbf{e}_n. \quad (5.7)$$

Equation 5.6 implies that  $\boldsymbol{\varepsilon}^{(i)}$  may lie essentially in the direction of vector  $\mathbf{q}$  after a number of iterations. In this situation, it is more beneficial to perform an error correction along the approximate direction  $\mathbf{q}$  instead of waiting for a slow decay of the error by a costly performance of a sequential left-multiplication by  $\mathbf{M}$ . Identification of this situation is based on a similarity of successive correction vectors defined as

$$\boldsymbol{\zeta}^{(i-1)} = \mathbf{x}^{(i-1)} - \mathbf{x}^{(i-2)} \quad (5.8)$$

$$\boldsymbol{\zeta}^{(i)} = \mathbf{x}^{(i)} - \mathbf{x}^{(i-1)}. \quad (5.9)$$

The similarity is estimated by the computation of a parameter  $\eta$

$$\eta = \left| \hat{\zeta}^{(i-1)} \cdot \hat{\zeta}^{(i)} \right| \quad (5.10)$$

where  $\hat{\zeta}^{(i-1)}$  and  $\hat{\zeta}^{(i)}$  are unit vectors in the direction of  $\zeta^{(i-1)}$  and  $\zeta^{(i)}$ , respectively. If  $\eta$  is greater than a pre-defined threshold, it means that corrections are taking place in the same direction and an improvement step is performed along the direction of vector  $\hat{\zeta}^{(i)}$ . The approximate solution after the improvement step is

$$\mathbf{x}^{(i')} = \mathbf{x}^{(i)} + \alpha \hat{\zeta}^{(i)} \quad (5.11)$$

where the coefficient  $\alpha$  is chosen to minimise the residual norm along the direction of vector  $\chi^{(i)}$  which is given by

$$\chi^{(i)} = \mathbf{Z} \hat{\zeta}^{(i)}. \quad (5.12)$$

The improvement step is illustrated in Figure 5.1. The corresponding residual of the approximate solution  $\mathbf{x}^{(i')}$  is defined as

$$\mathbf{r}^{(i')} = \mathbf{r}^{(i)} + \alpha \chi^{(i)} \quad (5.13)$$

where

$$\mathbf{r}^{(i)} = \mathbf{Z} \mathbf{x}^{(i)} - \mathbf{v}. \quad (5.14)$$

The square of the residual norm after the improvement step is

$$\begin{aligned} \left\| \mathbf{r}^{(i')} \right\|^2 &= \mathbf{r}^{(i')H} \cdot \mathbf{r}^{(i')} \\ &= \left( \mathbf{r}^{(i)H} + \alpha^{\text{re}} \chi^{(i)H} - j \alpha^{\text{im}} \chi^{(i)H} \right) \cdot \left( \mathbf{r}^{(i)} + \alpha^{\text{re}} \chi^{(i)} + j \alpha^{\text{im}} \chi^{(i)} \right) \end{aligned} \quad (5.15)$$

where  $\alpha^{\text{re}}$  and  $\alpha^{\text{im}}$  are the real and the imaginary components of the coefficient  $\alpha$ , respectively. Equation 5.15 is minimised if its partial derivatives with respect to  $\alpha^{\text{re}}$  and  $\alpha^{\text{im}}$  are forced to be zero. In other words, the residual norm is minimised along the direction of  $\chi^{(i)}$  if

$$\alpha^{\text{re}} = - \frac{\mathbf{r}^{(i)H} \cdot \chi^{(i)} + \chi^{(i)H} \cdot \mathbf{r}^{(i)}}{2 \chi^{(i)H} \cdot \chi^{(i)}} \quad (5.16)$$

$$\alpha^{\text{im}} = -j \frac{\mathbf{r}^{(i)H} \cdot \chi^{(i)} - \chi^{(i)H} \cdot \mathbf{r}^{(i)}}{2 \chi^{(i)H} \cdot \chi^{(i)}}. \quad (5.17)$$

It should be noticed that the improvement step is performed only if  $\eta$  is larger than the pre-defined parameter. However, the improvement step can be carried out several times

during the solution of a particular problem. The improvement step considerably enhances the convergence rate of the FBM as shown in [68].

## 5.3 Modified improvement step

### 5.3.1 Formulation

The minimisation of Equation 5.15 is similar to that applied in the method of steepest descent. Thus, updating the current elements along the previous correction vector becomes unnecessary. However, the stationary methods operate without guaranteeing that the currents along the previous correction vector will not be updated again. This may cancel the effect of the previous improvement steps. To preserve the effectiveness of the previous steps, the modified improvement step is proposed. The proposed method allows a simultaneous correction along multiple correction vectors.

We assume that the modified improvement step is performed at the end of iteration  $i$  where  $(n - 1)$  optimal corrections have previously been executed. This results in  $n$  computed correction vectors  $\hat{\boldsymbol{\zeta}}_1, \dots, \hat{\boldsymbol{\zeta}}_n$  at the end of iteration  $i$ . We assume that the correction vectors are in reverse chronological order where  $\hat{\boldsymbol{\zeta}}_1$  is the most recent correction direction. We define the corresponding products between the impedance matrix and the correction vectors as

$$\boldsymbol{\chi}_l = \mathbf{Z}\hat{\boldsymbol{\zeta}}_l \quad (5.18)$$

where  $l = 1, \dots, n$ . A residual which is minimised along  $n$  directions is represented as

$$\mathbf{r}^{(i')} = \mathbf{r}^{(i)} + \alpha_1\boldsymbol{\chi}_1 + \alpha_2\boldsymbol{\chi}_2 + \dots + \alpha_n\boldsymbol{\chi}_n \quad (5.19)$$

where  $\alpha_1, \dots, \alpha_n$  are unknown coefficients. Consequently, a square of the residual norm is computed by

$$\|\mathbf{r}^{(i')}\|^2 = \left( \mathbf{r}^{(i)H} + \sum_{l=1}^n (\alpha_l^{\text{re}} \boldsymbol{\chi}_l^H - j\alpha_l^{\text{im}} \boldsymbol{\chi}_l^H) \right) \cdot \left( \mathbf{r}^{(i)} + \sum_{l=1}^n (\alpha_l^{\text{re}} \boldsymbol{\chi}_l + j\alpha_l^{\text{im}} \boldsymbol{\chi}_l) \right) \quad (5.20)$$

where  $\alpha_l^{\text{re}}$  and  $\alpha_l^{\text{im}}$  are the real and the imaginary components of the corresponding coefficient  $\alpha_l$ . Forcing the partial derivatives of Equation 5.20 with respect to  $\alpha_1^{\text{re}}, \alpha_1^{\text{im}}, \dots, \alpha_n^{\text{re}}, \alpha_n^{\text{im}}$  to zero leads to a series of equations as

$$\begin{aligned} & \left( \mathbf{r}^{(i)H} \cdot \boldsymbol{\chi}_1 + \boldsymbol{\chi}_1^H \cdot \mathbf{r}^{(i)} \right) + 2\alpha_1^{\text{re}} \boldsymbol{\chi}_1^H \cdot \boldsymbol{\chi}_1 + \sum_{l \neq 1} \alpha_l^{\text{re}} (\boldsymbol{\chi}_1^H \cdot \boldsymbol{\chi}_l + \boldsymbol{\chi}_l^H \cdot \boldsymbol{\chi}_1) + \sum_{l \neq 1} j\alpha_l^{\text{im}} (\boldsymbol{\chi}_1^H \cdot \boldsymbol{\chi}_l - \boldsymbol{\chi}_l^H \cdot \boldsymbol{\chi}_1) = 0 \\ & \left( \mathbf{r}^{(i)H} \cdot \boldsymbol{\chi}_2 + \boldsymbol{\chi}_2^H \cdot \mathbf{r}^{(i)} \right) + 2\alpha_2^{\text{re}} \boldsymbol{\chi}_2^H \cdot \boldsymbol{\chi}_2 + \sum_{l \neq 2} \alpha_l^{\text{re}} (\boldsymbol{\chi}_2^H \cdot \boldsymbol{\chi}_l + \boldsymbol{\chi}_l^H \cdot \boldsymbol{\chi}_2) + \sum_{l \neq 2} j\alpha_l^{\text{im}} (\boldsymbol{\chi}_2^H \cdot \boldsymbol{\chi}_l - \boldsymbol{\chi}_l^H \cdot \boldsymbol{\chi}_2) = 0 \\ & \quad \vdots \\ & \left( \mathbf{r}^{(i)H} \cdot \boldsymbol{\chi}_n + \boldsymbol{\chi}_n^H \cdot \mathbf{r}^{(i)} \right) + 2\alpha_n^{\text{re}} \boldsymbol{\chi}_n^H \cdot \boldsymbol{\chi}_n + \sum_{l \neq n} \alpha_l^{\text{re}} (\boldsymbol{\chi}_n^H \cdot \boldsymbol{\chi}_l + \boldsymbol{\chi}_l^H \cdot \boldsymbol{\chi}_n) + \sum_{l \neq n} j\alpha_l^{\text{im}} (\boldsymbol{\chi}_n^H \cdot \boldsymbol{\chi}_l - \boldsymbol{\chi}_l^H \cdot \boldsymbol{\chi}_n) = 0 \end{aligned}$$

and

$$\begin{aligned}
 j \left( \mathbf{r}^{(i)H} \cdot \boldsymbol{\chi}_1 - \boldsymbol{\chi}_1^H \cdot \mathbf{r}^{(i)} \right) + 2\alpha_1^{\text{im}} \boldsymbol{\chi}_1^H \cdot \boldsymbol{\chi}_1 + \sum_{l \neq 1} j \alpha_l^{\text{re}} (\boldsymbol{\chi}_l^H \cdot \boldsymbol{\chi}_1 - \boldsymbol{\chi}_1^H \cdot \boldsymbol{\chi}_l) + \sum_{l \neq 1} \alpha_l^{\text{im}} (\boldsymbol{\chi}_1^H \cdot \boldsymbol{\chi}_l + \boldsymbol{\chi}_l^H \cdot \boldsymbol{\chi}_1) &= 0 \\
 j \left( \mathbf{r}^{(i)H} \cdot \boldsymbol{\chi}_2 - \boldsymbol{\chi}_2^H \cdot \mathbf{r}^{(i)} \right) + 2\alpha_2^{\text{im}} \boldsymbol{\chi}_2^H \cdot \boldsymbol{\chi}_2 + \sum_{l \neq 2} j \alpha_l^{\text{re}} (\boldsymbol{\chi}_l^H \cdot \boldsymbol{\chi}_2 - \boldsymbol{\chi}_2^H \cdot \boldsymbol{\chi}_l) + \sum_{l \neq 2} \alpha_l^{\text{im}} (\boldsymbol{\chi}_2^H \cdot \boldsymbol{\chi}_l + \boldsymbol{\chi}_l^H \cdot \boldsymbol{\chi}_2) &= 0 \\
 &\vdots \\
 j \left( \mathbf{r}^{(i)H} \cdot \boldsymbol{\chi}_n - \boldsymbol{\chi}_n^H \cdot \mathbf{r}^{(i)} \right) + 2\alpha_n^{\text{im}} \boldsymbol{\chi}_n^H \cdot \boldsymbol{\chi}_n + \sum_{l \neq n} j \alpha_l^{\text{re}} (\boldsymbol{\chi}_l^H \cdot \boldsymbol{\chi}_n - \boldsymbol{\chi}_n^H \cdot \boldsymbol{\chi}_l) + \sum_{l \neq n} \alpha_l^{\text{im}} (\boldsymbol{\chi}_n^H \cdot \boldsymbol{\chi}_l + \boldsymbol{\chi}_l^H \cdot \boldsymbol{\chi}_n) &= 0
 \end{aligned}$$

The above equations can be arranged into the following matrix equation

$$\begin{pmatrix} \mathbf{A}_{1,1} & \mathbf{A}_{1,2} & \cdots & \mathbf{A}_{1,n} \\ \mathbf{A}_{2,1} & \mathbf{A}_{2,2} & \cdots & \mathbf{A}_{2,n} \\ \vdots & \vdots & \ddots & \vdots \\ \mathbf{A}_{n,1} & \mathbf{A}_{n,2} & \cdots & \mathbf{A}_{n,n} \end{pmatrix} \begin{pmatrix} \mathbf{c}_1 \\ \mathbf{c}_2 \\ \vdots \\ \mathbf{c}_n \end{pmatrix} = \begin{pmatrix} \mathbf{d}_1 \\ \mathbf{d}_2 \\ \vdots \\ \mathbf{d}_n \end{pmatrix} \quad (5.21)$$

where

$$\mathbf{A}_{l,m} = \begin{pmatrix} \boldsymbol{\chi}_l^H \cdot \boldsymbol{\chi}_m + \boldsymbol{\chi}_m^H \cdot \boldsymbol{\chi}_l & j \left( \boldsymbol{\chi}_l^H \cdot \boldsymbol{\chi}_m - \boldsymbol{\chi}_m^H \cdot \boldsymbol{\chi}_l \right) \\ j \left( \boldsymbol{\chi}_m^H \cdot \boldsymbol{\chi}_l - \boldsymbol{\chi}_l^H \cdot \boldsymbol{\chi}_m \right) & \boldsymbol{\chi}_l^H \cdot \boldsymbol{\chi}_m + \boldsymbol{\chi}_m^H \cdot \boldsymbol{\chi}_l \end{pmatrix} \quad (5.22)$$

$$\mathbf{c}_l = \begin{pmatrix} \alpha_l^{\text{re}} \\ \alpha_l^{\text{im}} \end{pmatrix} \quad (5.23)$$

$$\mathbf{d}_l = \begin{pmatrix} - \left( \mathbf{r}^{(i)H} \cdot \boldsymbol{\chi}_l + \boldsymbol{\chi}_l^H \cdot \mathbf{r}^{(i)} \right) \\ -j \left( \mathbf{r}^{(i)H} \cdot \boldsymbol{\chi}_l - \boldsymbol{\chi}_l^H \cdot \mathbf{r}^{(i)} \right) \end{pmatrix}. \quad (5.24)$$

The coefficients  $\alpha_l$  are the solution of the  $2n \times 2n$  matrix equation 5.21. Having these coefficients computed, the approximate solution after the modified improvement step is given by

$$\mathbf{x}^{(i')} = \mathbf{x}^{(i)} + \alpha_1 \hat{\boldsymbol{\zeta}}_1 + \alpha_2 \hat{\boldsymbol{\zeta}}_2 + \cdots + \alpha_n \hat{\boldsymbol{\zeta}}_n. \quad (5.25)$$

Equation 5.25 minimises the resultant norm along the  $n$  directions of vectors  $\boldsymbol{\chi}_l$ , resulting in the preservation of the minimisation of the previous steps. Figure 5.2 illustrates the modified improvement step using three correction vectors. The modified improvement step reduces to the original method of Section 5.2 when  $n = 1$ .

### 5.3.2 Computational complexity

The computational complexity of the modified improvement step is comprised of three components. The first component is the complexity for the computation of  $\mathbf{r}^{(i)}$ ,  $\boldsymbol{\chi}_1, \dots, \boldsymbol{\chi}_n$  and  $\hat{\boldsymbol{\zeta}}_1, \dots, \hat{\boldsymbol{\zeta}}_n$ . The vectors  $\boldsymbol{\chi}_2, \dots, \boldsymbol{\chi}_n$  and  $\hat{\boldsymbol{\zeta}}_2, \dots, \hat{\boldsymbol{\zeta}}_n$  have been computed and stored in the previous modified improvement steps. Thus, the actual complexity of the first part is the cost to compute  $\mathbf{r}^{(i)}$ ,  $\boldsymbol{\chi}_1$  and  $\hat{\boldsymbol{\zeta}}_1$ . This cost is equal to the complexity of the similar process performed in the original technique, which is of one MVP as presented in [68]. The complexity of this part is of  $\mathcal{O}(N^2)$  which can be further reduced if acceleration techniques are applied. Therefore

$$c_1 = \mathcal{O}(N^2) \quad (5.26)$$

The second component is the complexity to establish the matrix Equation 5.21. Matrix elements  $\mathbf{A}_{l,m}$ , where  $2 \leq l, m \leq n$ , have been computed and stored in the previous step. In addition, the matrix in Equation 5.21 is symmetric. Therefore, the actual complexity of the second part is the cost to compute  $\mathbf{A}_{1,1}, \dots, \mathbf{A}_{1,n}$  and  $\mathbf{d}_1, \dots, \mathbf{d}_n$ . Consequently, the computation of this part is of order  $\mathcal{O}(nN + n)$ ,

$$c_2 = nN + n \simeq nN. \quad (5.27)$$

The last component is the complexity for the solution of Equation 5.21, which is of  $\mathcal{O}(n^3)$  if the direct matrix inversion is applied.

$$c_3 = n^3 \quad (5.28)$$

The total complexity of the modified improvement step is

$$c_{\text{total}} = c_1 + c_2 + c_3. \quad (5.29)$$

The extra-cost of the modified technique when compared to the original technique is the sum of the second and the third components.

$$c_{\text{extra}} = c_2 + c_3 \quad (5.30)$$

In practice, the number of correction vectors required in the modified step is very small when compared to the number of unknowns  $n \ll N$ . As a result, the complexity of the modified step is approximately equal to that of the original step.

$$c_{\text{total}} \simeq c_1 \quad (5.31)$$

## 5.4 Numerical results and validations

This section demonstrates the accuracy and the efficiency of the proposed method. Two applications of the modified improvement step are presented. The proposed technique is applied for the solution of scattering from one dimensional randomly rough surfaces, and the computation of scattering from two dimensional randomly rough surfaces. All experiments were carried out on a Dell-Precision Workstation 670 with a 3.0GHz Xeon CPU and 3.0GB of RAM.

### 5.4.1 Application to the solution of scattering from one dimensional randomly rough surface

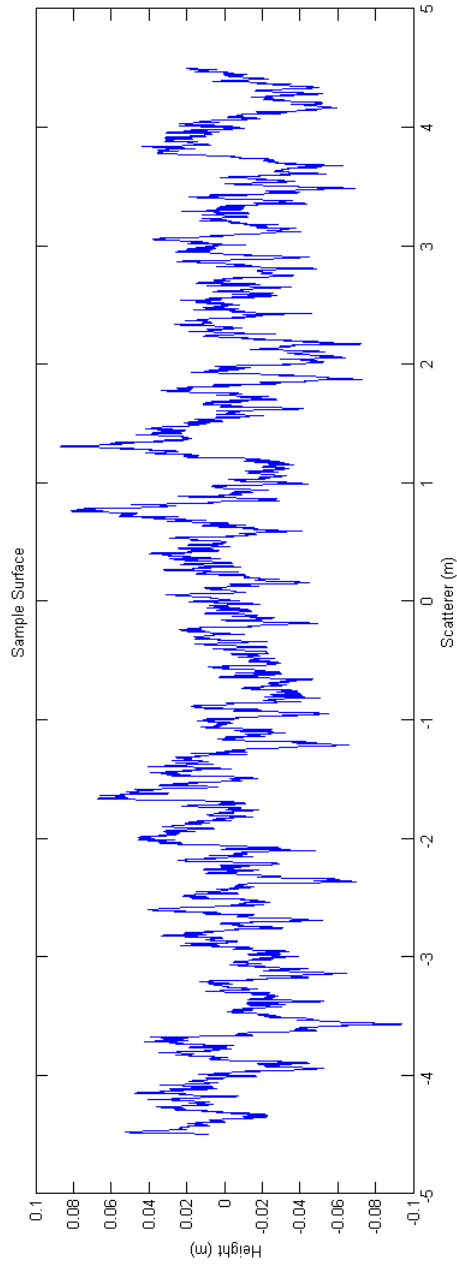
In this section, the modified improvement step is performed to enhance the convergence rate of the FBM. The FBM has been shown to be more efficient than non-stationary iterations when applied to randomly rough surface problems because of its rapid convergence rate [68]. The spectral acceleration (SA) [126] is applied for the acceleration of the MVPs performed in each FBM iteration. We denote the applied technique by IFBM-SA( $n$ ) where  $n$  is a number of correction vectors used in the modified improvement step. If more than  $n$  correction steps have been performed before the current iteration, only the  $n$  most recent correction vectors are retained for the next improvement step.

#### 5.4.1.1 Efficiency and accuracy of the IFBM-SA( $n$ )

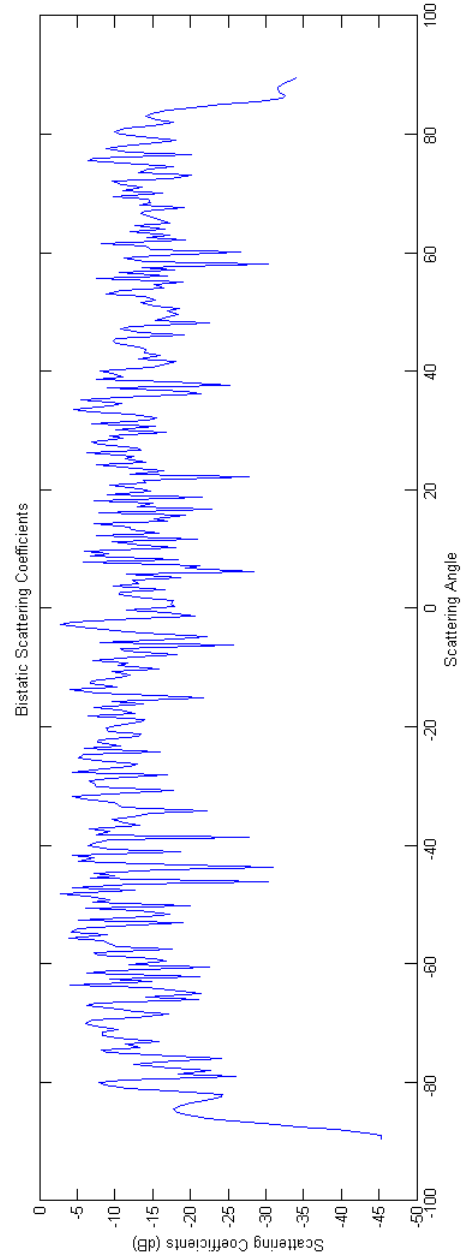
The efficiency and the accuracy of the proposed method is demonstrated by two test cases. The first test case presents that the rate of convergence improves with the number of correction vectors used while the second test case compares the performance of the IFBM-SA( $n$ ) against a reference method [125]. The configuration for the simulations relating to Figure 5.3a is as follows. The relative permittivity of the lower medium is of  $\epsilon_r = 14.15 + j5.21$ . An incident angle of  $50^\circ$  and a tapering parameter of  $g = L/4$  were used to remove edge effects where  $L$  is the length of the rough surfaces. Tapering parameters are further discussed in [127]. 128 basis functions per wavelength were used for the discretisation of the surface.

#### Performance of the modified improvement step with an increase in the number of correction vectors

The simulated exponential correlation surface has the root mean square height of  $h_{\text{rms}} = 0.88\lambda$ , correlation length of  $l_c = 2.8\lambda$  and length of  $L = 300\lambda$ .  $\lambda$  is the wavelength of a horizontally polarised incident wave of 10GHz. The total number of unknowns is 76,800. The IFBM-SA( $n$ ) is applied for the solution of the problem. The number of correction vectors is varied from 1 to 20 to observe the behaviour of the modified improvement step. IFBM-SA(1) corresponds to the original method of Section 5.2. A realisation of the simulated rough surface and the computed scattering coefficients are shown in Figure 5.3a and b, respectively.



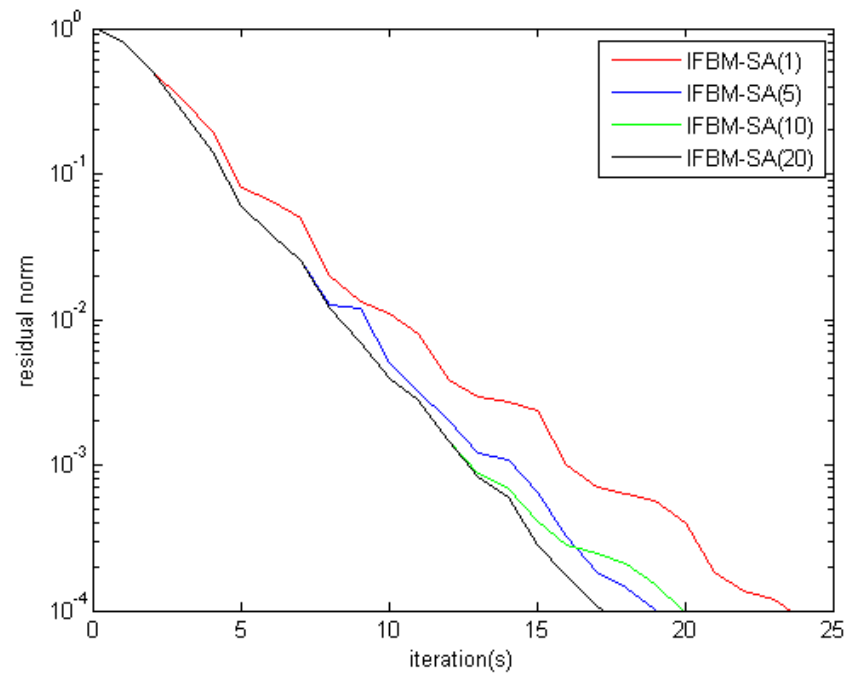
(a) A sample of an exponential surface.



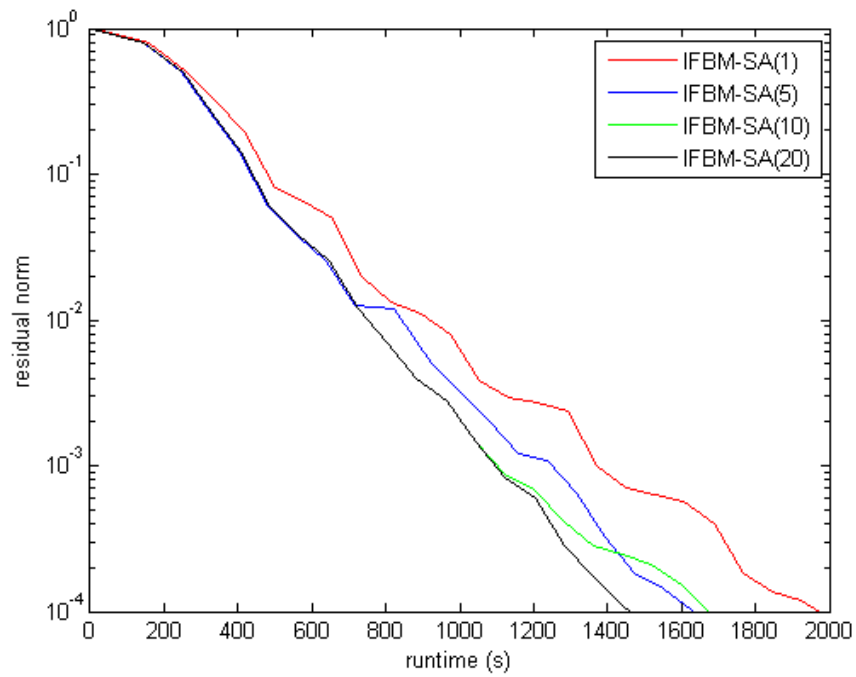
(b) Bistatic scattering coefficients of the sample surface

**Figure 5.3:** Bistatic scattering coefficients of an exponential surface: root mean square height of  $0.88\lambda$ ; correlation length of  $2.8\lambda$ ; incident angle of  $50^\circ$ .





(a)



(b)

**Figure 5.4:** Comparison of the performance of the modified improvement step using different numbers of correction vectors.

The comparison between the performance of different values of the number of correction vectors is shown in Figure 5.4. Figure 5.4a shows that as the number of correction vectors increases, the number of required iterations to achieve the desired residual norm of  $10^{-4}$  decreases. Thus, the convergence rate of the FBM increases with the number of correction vectors used. The improvement in terms of the number of iterations and runtime is shown in Figure 5.4a and b, respectively.

### **Comparison between the modified technique and the reference method**

The performance of the modified technique is compared to the original technique and the one in [125] which shall be termed the reference method to exhibit the efficiency of the proposed method. The reference method is based on stationary iterative methods with inner iterations solved by using the GMRES. Both SA and FFT are applied to expedite the reference method. Very rough exponential and Gaussian correlation surfaces with a root mean square height of  $2.0\lambda$  and a length of  $150\lambda$  are considered. The ratio of the root mean square height and the correlation length of the surface is varied from 0.2 to 0.6 to examine the robustness of the new technique. Two types of polarisations, horizontal and vertical, are considered. The total number of unknowns is 38,400. The tolerance of the iterative solvers is set to  $10^{-4}$ . The results for exponential surfaces are presented in Table 5.1 and Table 5.2 for horizontal and vertical polarisation, respectively. Similarly, the results for Gaussian surfaces are shown in Table 5.3 and Table 5.4. The number outside the parenthesis denotes the runtime in seconds while the number inside the parenthesis denotes the number of iterations required to achieve the desired residual norm.

For exponential cases, the proposed method outperforms the reference method and the original IFBM-SA. The reference method diverges for all cases due to the extreme roughness of the surface. The IFBM-SA(1), the original method, mostly diverges. If not, it requires a large number of iterations to achieve the accuracy of  $10^{-4}$ . The proposed method converges for all cases and can save up to 75% of the runtime when compared to the original method.

For Gaussian cases, the performance of the reference method and the original IFBM-SA is improved due to the difference in the roughness of exponential surfaces and Gaussian surfaces. However, the performance of the proposed method remains better than the reference method. In Table 5.3 and Table 5.4, an increase in the number of correction vectors barely results in a better performance of the proposed method because very few iterations are required to solve the problems, leading to negligible effect of the modified improvement step. However, the effect of the proposed method improves with the ratio  $h_{\text{rms}}/l_c$ . It can be seen clearly that the efficiency of the proposed method increases with the roughness of the surface, which results in an increase of the number of iterations required to solve the problems when the original IFBM-SA is applied.

$h_{\text{rms}}/l_c$	0.2	0.3	0.45	0.6
Reference method	diverge	diverge	diverge	diverge
IFBM-SA(1)	stagnate	stagnate	stagnate	stagnate
IFBM-SA(10)	1,842 (35)	1,881 (35)	1,613 (28)	2,429 (44)
IFBM-SA(20)	1,118 (21)	1,279 (23)	1,413 (25)	2,107 (38)
IFBM-SA(30)	1,120 (21)	1,250 (23)	1,391 (25)	1,511 (27)

**Table 5.1:** Runtime (outside parenthesis) in seconds and number of iterations (inside parenthesis) required to achieve a residual norm of  $10^{-4}$ . Exponential surface. Horizontal polarisation.

$h_{\text{rms}}/l_c$	0.2	0.3	0.45	0.6
Reference method	diverge	diverge	diverge	diverge
IFBM-SA(1)	2,217 (42)	4,112 (77)	stagnate	stagnate
IFBM-SA(10)	844 (15)	1,044 (17)	1,031 (17)	1,129 (19)
IFBM-SA(20)	843 (15)	990 (16)	1,036 (17)	1,080 (18)

**Table 5.2:** Runtime (outside parenthesis) in seconds and number of iterations (inside parenthesis) required to achieve a residual norm of  $10^{-4}$ . Exponential surface. Vertical polarisation.

$h_{\text{rms}}/l_c$	0.2	0.3	0.45	0.6
Reference method	987 (13)	1,452 (17)	2,616 (28)	diverge
IFBM-SA(1)	270 (6)	334 (7)	433 (9)	626 (13)
IFBM-SA(10)	271 (6)	330 (7)	391 (8)	448 (9)

**Table 5.3:** Runtime (outside parenthesis) in seconds and number of iterations (inside parenthesis) required to achieve a residual norm of  $10^{-4}$ . Gaussian surface. Horizontal polarisation.

$h_{\text{rms}}/l_c$	0.2	0.3	0.45	0.6
Reference method	stagnate	951 (17)	1,361 (22)	2,085 (33)
IFBM-SA(1)	267 (6)	373 (8)	389 (8)	454 (9)
IFBM-SA(10)	266 (6)	331 (7)	345 (7)	364 (7)

**Table 5.4:** Runtime (outside parenthesis) in seconds and number of iterations (inside parenthesis) required to achieve a residual norm of  $10^{-4}$ . Gaussian surface. Vertical polarisation.

### 5.4.1.2 Validation against measurement

To validate the proposed method, we compare the brightness temperature computed by the proposed method against the measured brightness temperature of actual soil surfaces. Brightness temperature is used to sense land surface soil moisture or to retrieve estimates of the surface wind speed, rain rate, etc [128]. More details about brightness temperature can be found in [129]. The exponential smooth surface with the root mean square height of  $h_{\text{rms}} = 0.88\text{cm}$  and the relative permittivity of  $\epsilon_r = 19.2 + j2.41$  [130] corresponding to a soil moisture of  $0.35\text{cm}^3/\text{cm}^3$  is investigated. Because the correlation length of the surface is not provided in measurement setup information [131], the correlation length is assumed to be  $8.4\text{cm}$  corresponding to the measurement in [132, 133]. The experiments were performed at the wavelength of  $21.4\text{cm}$  over a range of incident angles from  $20^\circ$  to  $50^\circ$ . Detail about the experiments are given in [131].

Polarisation	Incident angle	Brightness temperature (K)			
		Simulation	Measurement	Difference	% difference
Vertical	$20^\circ$	159.96	167.56	7.6	4.53%
Vertical	$35^\circ$	148.41	153.29	4.88	3.18%
Vertical	$50^\circ$	127.68	135.73	8.05	5.93%
Horizontal	$20^\circ$	191.97	181.46	10.51	5.79%
Horizontal	$35^\circ$	205.62	196.83	8.79	4.47%
Horizontal	$50^\circ$	230.19	223.81	6.38	2.85%

**Table 5.5:** Comparison of the brightness temperature between simulation and measurement.  $h_{\text{rms}} = 0.88\text{cm}$ .  $\epsilon_r = 19.2 + j2.41$

The comparison between the simulation results and the measurement data is presented in Table 5.5. It can be seen that there is a good agreement between the results generated by simulation and the measurement for different incident angles and polarisations. The difference between the measurement and the simulation is within 10K, guaranteeing adequate accuracy [129].

### 5.4.2 Application to the solution of scattering from two dimensional randomly rough surface

The convergence rate of the BFBM is enhanced by the application of the modified improvement step. The BFBM [129], which is expedited by using the spectral acceleration, is applied to the solution of scattering from two dimensional randomly rough surface. We denote the applied technique by IBFBM-SA( $n$ ) where  $n$  is a number of correction vectors used in the modified improvement step. The random rough surfaces are defined as follows. The lower medium is assumed to be wet soil with the relative permittivity of  $\epsilon_r = 15.57 + j3.71$  [134] at  $1.5\text{GHz}$ . An incident angle of  $40^\circ$  and a tapering parameter of  $g = L/3$  were applied to eliminate edge effects where  $L$  is the length of the surface along

both  $x$  and  $y$  directions as shown in Figure 5.5. Two types of random rough surfaces, the Gaussian and exponential surfaces illuminated by the horizontal polarised incidence, are investigated. The surface area is  $4\lambda \times 4\lambda$  and 32 basis functions per wavelength were used, resulting in totally 16,384 pulse basis functions or equivalent to 98,304 unknowns. The width of each slice in the BFBM-SA is  $\lambda/8$ , resulting in total to 32 groups. The correlation length is fixed with the value  $l_c = 0.3\lambda$  while the root mean square height is varied from  $0.2\lambda$  to  $0.27\lambda$  to examine the robustness of the new technique. The tolerance of the iterative solver is set to  $10^{-4}$ . The results are presented in Table 5.6 and Table 5.7 for the Gaussian and exponential surfaces, respectively. The number outside the parenthesis denotes the number of iterations required to achieve the desired residual norm. It can be seen clearly that the proposed method outperforms the standard IBFBM-SA. The number of iterations and the required runtime increase with the roughness of the surface. In addition, the convergence rate of the proposed method is improved with an increase in a number of correction vectors.

## 5.5 Conclusion

A novel technique is proposed for the solution of random rough surface scattering. The convergence rate of the IFBM-SA and the IBFBM-SA is enhanced by the application of the modified improvement step without significant extra complexity. Numerical results are presented to illustrate the advantages of the proposed algorithm and to validate the simulation results against measurement data.

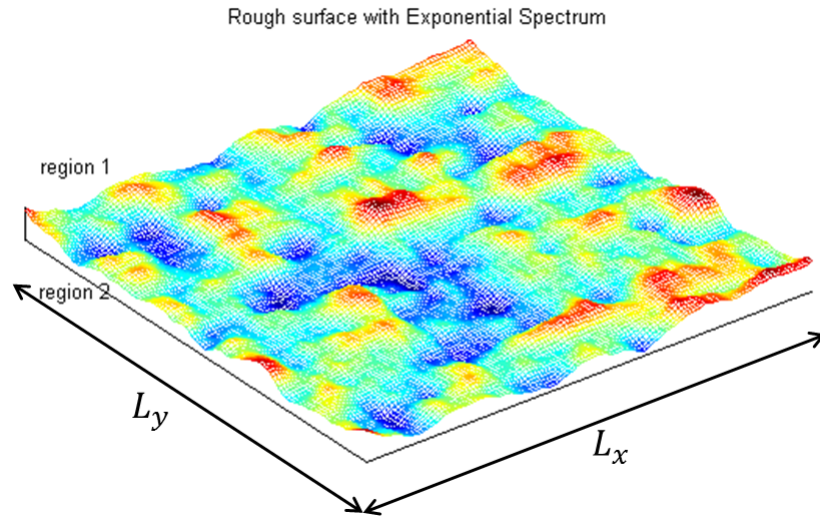


**Figure 5.5:** Two dimensional dielectric random rough surface profile.

$h_{\text{rms}}$	$0.2\lambda$	$0.25\lambda$	$0.27\lambda$
IFBM-SA(1)	50,680 (16)	65,094 (20)	72,214 (22)
IFBM-SA(5)	38,263 (12)	49,628 (15)	55,434 (17)
IFBM-SA(10)	35,039 (11)	46,326 (14)	52,169 (16)

**Table 5.6:** Runtime (outside parenthesis) in seconds and number of iterations (inside parenthesis) required to achieve a residual norm of  $10^{-4}$ . Gaussian surface. Horizontal polarisation.

$h_{\text{rms}}$	$0.2\lambda$	$0.25\lambda$	$0.27\lambda$
IFBM-SA(1)	61,342 (19)	89,714 (28)	176,252 (55)
IFBM-SA(5)	47,507 (15)	76,375 (24)	121,360 (37)
IFBM-SA(10)	47,463 (15)	73,480 (23)	117,161 (37)

**Table 5.7:** Runtime (outside parenthesis) in seconds and number of iterations (inside parenthesis) required to achieve a residual norm of  $10^{-4}$ . Exponential surface. Horizontal polarisation.

## 6 Integral equation approaches for indoor wave propagation

Two integral equation formulations for the analysis of two dimensional indoor EM wave propagation are investigated in this chapter. The volume and the surface electric field integral equations are discretised by the MoM, resulting in dense linear systems whose iterative solutions are accelerated by using acceleration techniques. The purpose of the investigation is to identify which formulation is more efficient with a view to future work analysing three dimensional indoor EM wave propagation. Numerical results are presented to compare the performance of the two approaches when applied to the same indoor propagation problem.

### 6.1 Introduction

Reliable and accurate electromagnetic wave propagation models are highly desirable for radio channel modelling and wireless system development. The unique characteristics of the indoor environment, such as the variety of materials and the geometrical complexity of structures, pose troublesome challenges in the development of indoor propagation models. New generations of mobile communication systems have introduced the use of low-powered radio access nodes operating in femto/pico-cells positioned inside buildings. These cells are vital to the improvement of service coverage and network capacity within the cellular-based system. Thus, there is a growing demand for accurate propagation models, served as design tools in base-station location optimisation, to estimate signal strength at various location within a cell. It is noted that signal strength monitoring is only a part of cell planning and optimisation. These models aim to include as much of the physics of the environment as possible but yield a solution within a reasonable runtime.

Empirical models, for example the Motley-Keenan model [70] and the COST 231 multi-wall model [135], are popular techniques to predict indoor wave propagation because of their speed and simplicity. However, the lack of accuracy and reliability are the main drawbacks of these models. Significant research efforts have focused on ray-tracing based models which originate from the approximation of Maxwell's equations at high frequencies. The GTD [9, 10] and the UTD [11, 12, 13] are applied in [136, 137] to include the diffraction phenomenon, leading to an enhanced accuracy of ray-tracing models. Nevertheless, the increase in geometrical complexity may cause significant additional computations when applying the asymptotic diffraction models, which further degrades the performance of these methods.

To the best of the author's knowledge, there are only a few attempts to develop full-wave models based on for example the FDTD or the MoM [58, 138, 139, 140]. In this chapter, the application of the MoM to the volume and the surface electric field integral equations for solving the indoor wave propagation problem is discussed. The dense linear systems resulting from the discretised integral equations are solved by using a Krylov-based iterative solver, the BiCGSTAB [39], instead of using the BBFB or the BFBM as in chapter 4 and chapter 5 because the application of the BBFB and the BFBM is only suitable for quasi-smooth, long and narrow problems which are unlikely to happen in indoor environment. The FFT and the fast far field approximation (FAFFA) are applied to accelerate MVPs performed within each iteration for the volume and the surface integral equations, respectively. Because the aim of the study is to investigate the efficiency of the integral equation formulations, the FFT and FAFFA are chosen for their implementation simplicity.

## 6.2 Volume integral equation accelerated by the fast Fourier transform

In this section, the analysis of two dimensional wave propagation problems is based on the discretisation of the volume integral equation.

### 6.2.1 Volume electric field integral equation for two dimensional TM<sup>z</sup> polarisation problem

The volume electric field integral equation can be applied to the analysis of a two dimensional inhomogeneous dielectric cylinder. In the case of two dimensional TM<sup>z</sup> polarisation problems, we assume that a scatterer is illuminated by an incident TM<sup>z</sup> wave which has three components including  $E_z^i$ ,  $H_x^i$  and  $H_y^i$ . Therefore, the representation of the scattered field in Equation 2.55 is rewritten as

$$E_z^s(\mathbf{r}) = -j\omega A_z(\mathbf{r}) \quad (6.1)$$

where

$$A_z(\mathbf{r}) = \mu_0 \int J_z(\mathbf{r}') \frac{1}{4j} H_0^{(2)}(k_0 |\mathbf{r} - \mathbf{r}'|) ds'. \quad (6.2)$$

$\epsilon_0$ ,  $\mu_0$  and  $k_0$  denote the permittivity, the permeability and the wavenumber of the background medium (free-space in this case), respectively.  $J_z$  is the  $z$ -component of the volume current and  $H_n^{(2)}$  denotes the  $n^{\text{th}}$  order Hankel function of the second kind. In addition, the relationship between the volume current and the total electric field in Equation 2.53 is transformed into

$$J_z(\mathbf{r}) = j\omega\epsilon_0 (\epsilon_r(\mathbf{r}) - 1) E_z(\mathbf{r}). \quad (6.3)$$



Substituting Equation 6.3 into Equation 6.1 results in

$$E_z^i(\mathbf{r}) = \frac{J_z(\mathbf{r})}{j\omega\epsilon_0(\epsilon_r(\mathbf{r}) - 1)} + j\omega A_z(\mathbf{r}). \quad (6.4)$$

Note that Equation 6.4 only holds for points inside the scatterers where the relative permittivity  $\epsilon_r(\mathbf{r}) \neq 1$  (blue region in Figure 6.1a). We can alternatively derive an integral equation which represents the incident field in terms of  $E_z(\mathbf{r})$  as follows

$$E_z^i(\mathbf{r}) = E_z(\mathbf{r}) + \frac{j}{4} \int \chi(\mathbf{r}') E_z(\mathbf{r}') H_0^{(2)}(k_0 |\mathbf{r} - \mathbf{r}'|) ds' \quad (6.5)$$

where

$$\chi(\mathbf{r}) = k^2(\mathbf{r}) - k_0^2 \quad (6.6)$$

$$k^2(\mathbf{r}) = \omega^2 \mu_0 \epsilon_0 \epsilon_r(\mathbf{r}) \quad ; \quad k_0^2 = \omega^2 \mu_0 \epsilon_0 \quad (6.7)$$

$\chi(\mathbf{r})$ , which expresses the difference between the wavenumber at point  $\mathbf{r}$  and the wavenumber of the background, is called the contrast value. Equation 6.5 holds for every point within an investigated space (both blue and white regions in Figure 6.1b). The MoM is applied to discretise Equation 6.5 using  $N = N_x \times N_y$  pulse basis functions defined on a uniform grid as shown in Figure 6.1b where  $N_x$  and  $N_y$  are numbers of discretisation points in the horizontal and vertical directions of the scenario, respectively. This results in a linear system

$$\mathbf{Z}\mathbf{x} = \mathbf{v} \quad (6.8)$$

where  $\mathbf{Z}$  is a  $N \times N$  impedance matrix,  $\mathbf{v}$  is a  $N \times 1$  vector containing incident field information and  $\mathbf{x}$  is a  $N \times 1$  vector containing the unknown total electric fields. The impedance matrix  $\mathbf{Z}$  can be expressed in the following form

$$\mathbf{Z} = \mathbf{I} + \mathbf{GD} \quad (6.9)$$

where  $\mathbf{I}$  is a  $N \times N$  identity matrix and  $\mathbf{D}$  is a  $N \times N$  diagonal matrix containing information about the contrast values of the basis functions

$$\mathbf{D} = \begin{pmatrix} \chi_1 & 0 & \cdots & 0 \\ 0 & \chi_2 & \cdots & 0 \\ \vdots & \vdots & \ddots & \vdots \\ 0 & 0 & \cdots & \chi_N \end{pmatrix} \quad (6.10)$$

$\mathbf{G}$  is a  $N \times N$  Green's function matrix

$$\mathbf{G} = \begin{pmatrix} g_{1,1} & g_{1,2} & \cdots & g_{1,N} \\ g_{2,1} & g_{2,2} & \cdots & g_{2,N} \\ \vdots & \vdots & \ddots & \vdots \\ g_{N,1} & g_{N,2} & \cdots & g_{N,N} \end{pmatrix} \quad (6.11)$$

where

$$\begin{aligned} g_{m,n} &= \frac{j}{4} \left( \frac{2\pi a}{k_0} H_1^{(2)}(k_0 a) - \frac{j^4}{k_0^2} \right) & ; \text{ for } m = n \\ g_{m,n} &= \frac{j}{4} \frac{2\pi a}{k_0} J_1(k_0 a) H_0^{(2)}(k_0 |\mathbf{r}_m - \mathbf{r}_n|) & ; \text{ for } m \neq n \end{aligned} \quad (6.12)$$

$J_1$  is the Bessel function of the first order and  $a$  is the radius of the equivalent circle defined in [20]. Because the entire investigated space is discretised into pulse basis functions located on a uniformly spaced grid as shown in Figure 6.1b,  $\mathbf{G}$  can be expressed in form of a block Toeplitz matrix as follows

$$\mathbf{G} = \begin{pmatrix} \bar{G}_{1,1} & \bar{G}_{1,2} & \bar{G}_{1,3} & \cdots & \bar{G}_{1,N_y} \\ \bar{G}_{1,2} & \bar{G}_{1,1} & \bar{G}_{1,2} & \cdots & \bar{G}_{1,N_y-1} \\ \bar{G}_{1,3} & \bar{G}_{1,2} & \bar{G}_{1,1} & \cdots & \bar{G}_{1,N_y-2} \\ \vdots & \vdots & \vdots & \ddots & \vdots \\ \bar{G}_{1,N_y} & \bar{G}_{1,N_y-1} & \bar{G}_{1,N_y-2} & \cdots & \bar{G}_{1,1} \end{pmatrix} \quad (6.13)$$

where  $\bar{G}_{m,n}$  are Toeplitz matrices with a size of  $N_x \times N_x$ . This allows the use of the FFT in the subsequent solution.

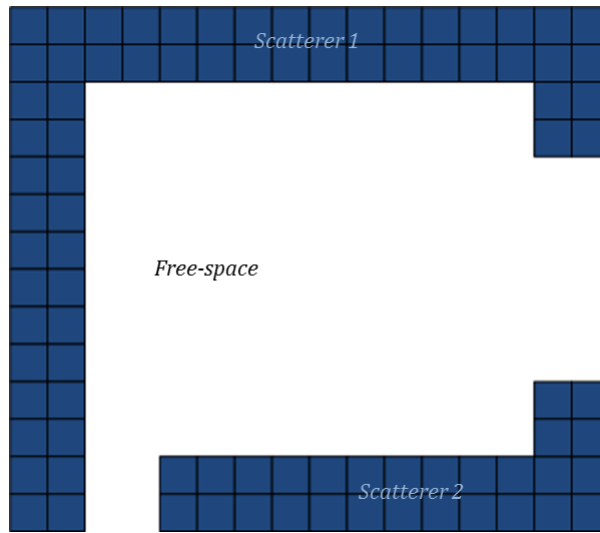
### 6.2.2 Fast Fourier transform applied to the discretised volume integral equation

Krylov-based iterative solvers can be applied for the solution of Equation 6.8. The approximation of the solution requires the performance of the MVPs at the cost of  $\mathcal{O}(N^2)$ . However, the particular form of  $\mathbf{Z}$  allows an efficient computation of the MVPs. By substituting Equation 6.9 into 6.8, the MVP in Equation 6.8 is rewritten as

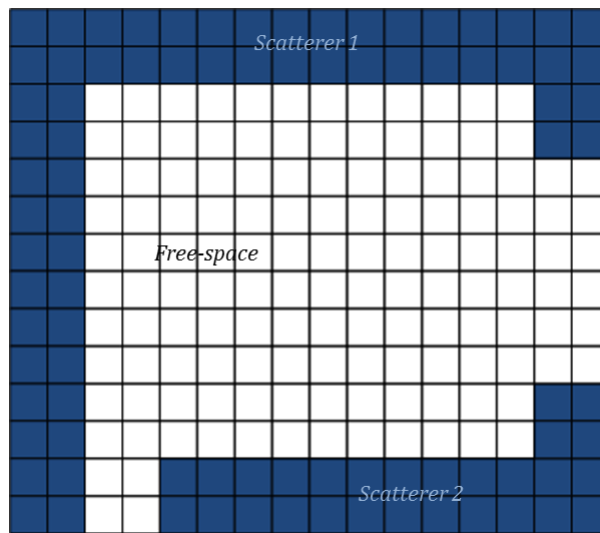
$$\mathbf{Z}\mathbf{x}^{(i)} = \mathbf{x}^{(i)} + \mathbf{G}\bar{\mathbf{x}}^{(i)} \quad (6.14)$$

where  $\mathbf{x}^{(i)}$  denotes the approximate solution at iteration  $i$  and  $\bar{\mathbf{x}}^{(i)}$  is defined as

$$\bar{\mathbf{x}}^{(i)} = \mathbf{D}\mathbf{x}^{(i)}. \quad (6.15)$$



(a) Discretisation of the volumetric scatterers.



(b) Discretisation of the entire volumetric space.

**Figure 6.1:** Discretisation of the volume integral equation using pulse basis functions.

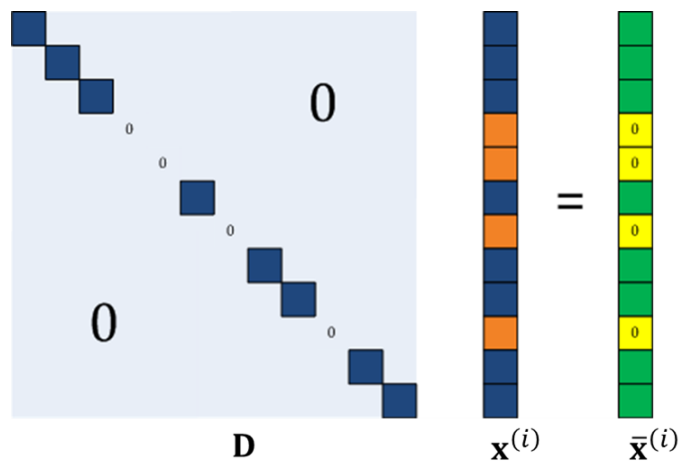


**Figure 6.2:** Illustration of the MVP in Equation 6.15.

Consequently, the cost to compute the product of  $\mathbf{Z}\mathbf{x}^{(i)}$  is comprised of two components: the cost  $c_1$  to perform the MVP in Equation 6.15 and the cost  $c_2$  to perform the MVP in the right hand side of Equation 6.14. Because  $\mathbf{D}$  is a diagonal matrix, the MVP in Equation 6.15 can be computed efficiently with the cost  $c_1$  of  $\mathcal{O}(N)$ . The Toeplitz form of  $\mathbf{G}$  suggests the application of the FFT to the computation of the MVP in Equation 6.14 with the cost  $c_2$  of  $\mathcal{O}(N \log N)$ . Thus, the total complexity to compute Equation 6.14 is proportional to  $\mathcal{O}(N \log N)$ . As the result, the FFT reduces the computational cost to perform the MVP in Equation 6.8 from  $\mathcal{O}(N^2)$  to  $\mathcal{O}(N \log N)$ .

The application of the MoM to Equation 6.4 requires only the discretisation of the scatterers as compared to Equation 6.5 which needs the discretisation of the entire investigated space as shown in Figure 6.1. Thus, the number of unknowns in the latter is larger than that in the former. However, the latter form of the VEFIE allows the use of the FFT to accelerate the performance of the MVP required in each Krylov iteration.

### 6.2.3 Reduced operator for the enhancement of convergence rate

Recasting Equation 6.4 into 6.5 permits the use of the FFT but significantly increases the number of unknowns because the entire environment is discretised instead of only the local scatterers. This may worsen the convergence rate of the iterative methods. However, we can distinguish between unknowns located in free-space, the values of which do not affect the values of unknowns elsewhere, and unknowns located in the scatterers which are more important and *do* influence the field elsewhere. It becomes more efficient to focus the iterative solver on correcting the latter unknowns and leaving the computation of the former to a post-processing step.

To see this more clearly, we denote  $l$  and  $m$  as the indices of basis functions which are located in free-space and inside the scatterers, respectively. The MVP in Equation 6.15 is illustrated in Figure 6.2. Because all elements of the diagonal matrix  $\mathbf{D}$  will be zero except for elements  $d_{m,m}$ , the product in Equation 6.15 will generate the same vector  $\bar{\mathbf{x}}^{(i)}$  regardless of the values of  $x_l^{(i)}$  (orange elements of  $\mathbf{x}^{(i)}$ ). When we keep the values of the scatterer unknowns  $x_m^{(i)}$  (blue elements of  $\mathbf{x}^{(i)}$ ) and vary the values of the free-space unknowns  $x_l^{(i)}$  (orange elements of  $\mathbf{x}^{(i)}$ ), the values of the resultant elements corresponding to the scatterer unknowns  $\bar{x}_m^{(i)}$  (green elements of  $\bar{\mathbf{x}}^{(i)}$ ) are unchanged while those corresponding to the free-space unknowns  $\bar{x}_l^{(i)}$  (yellow elements of  $\bar{\mathbf{x}}^{(i)}$ ) are always zero. Consequently, elements corresponding to the scatterer unknowns of the resultant vector  $\mathbf{v}^{(i)} = \mathbf{Z}\mathbf{x}^{(i)}$  remain the same regardless of the value of  $x_l^{(i)}$ . In other words, the free-space unknowns are merely present to enforce a regular grid and facilitate the use of the FFT. After each MVP, it is beneficial to extract only significant elements of  $\mathbf{v}^{(i)}$  and to concentrate the solver on correcting the corresponding unknowns. This technique, the reduced operator, is presented in detail in [141]. The application of the reduced operator leads to the improvement of the convergence rate of the Krylov solver, and counteracts the possible loss of efficiency introduced by the discretisation of the entire investigated space.

### 6.3 Surface integral equation accelerated by the fast far field approximation

In this section, we develop an alternative formulation for the analysis of two dimensional wave propagation problems. The alternative approach is based on the discretisation of the surface integral equation.

#### 6.3.1 Surface electric field integral equation for two dimensional TM<sup>z</sup> polarisation problem

The surface integral equation is mainly applied for homogeneous problems where it can take advantage of the boundary conditions to reduce the number of unknowns as compared to the volume integral equation. Assume that a homogeneous cylinder is illuminated by a TM<sup>z</sup> polarised incidence. The coupled EFIE in Equation 2.87 can be written as follows

$$\begin{aligned} E_z^i(\mathbf{r}) &= M_t(\mathbf{r}) + j\omega A_z^{(1)}(\mathbf{r}) + \frac{1}{\epsilon_1} \left\{ \frac{\partial F_y^{(1)}}{\partial x} - \frac{\partial F_x^{(1)}}{\partial y} \right\}_{S^+} \\ 0 &= -M_t(\mathbf{r}) + j\omega A_z^{(2)}(\mathbf{r}) + \frac{1}{\epsilon_2} \left\{ \frac{\partial F_y^{(2)}}{\partial x} - \frac{\partial F_x^{(2)}}{\partial y} \right\}_{S^-} \end{aligned} \quad (6.16)$$

where

$$A_z^{(\alpha)}(\mathbf{r}) = \mu_\alpha \int J_z(\mathbf{r}') \frac{1}{4j} H_0^{(2)}(k_\alpha |\mathbf{r} - \mathbf{r}'|) dl' \quad (6.17)$$

$$\bar{F}_t^{(\alpha)}(\mathbf{r}) = \epsilon_\alpha \int \hat{\mathbf{t}}(\mathbf{r}') M_t(\mathbf{r}') \frac{1}{4j} H_0^{(2)}(k_\alpha |\mathbf{r} - \mathbf{r}'|) dl'. \quad (6.18)$$

$\hat{\mathbf{t}}$  denotes a unit vector tangent to the contour of the cylinder as shown in Figure 6.3.  $k_1$  and  $k_2$  represent the wavenumbers of the exterior region and the interior region, respectively.  $(\mu_1, \epsilon_1)$  and  $(\mu_2, \epsilon_2)$  denote the permeability and the permittivity of the exterior medium and the interior medium, respectively. The expressions in brackets in Equation 6.16 depend on the side of the surface where the observer is located. We assume that pulse basis functions are used for the discretisation of the scatterer contour. The application of the MoM to Equation 6.16 yields a  $2N \times 2N$  linear system

$$\begin{pmatrix} \mathbf{Z}_a & \mathbf{Z}_b \\ \mathbf{Z}_c & \mathbf{Z}_d \end{pmatrix} \begin{pmatrix} \mathbf{j} \\ \mathbf{m} \end{pmatrix} = \begin{pmatrix} \mathbf{e}^i \\ 0 \end{pmatrix} \quad (6.19)$$

where  $N$  is the number of pulse basis functions used to discretise the boundary of the scatterer. It is assumed that the  $n^{\text{th}}$  segment is defined on a domain of length  $\Delta_n$  with a centre  $\mathbf{r}_n$  and a normal vector  $\hat{\mathbf{n}}_n$ .  $\mathbf{j}$  and  $\mathbf{m}$  are  $N \times 1$  vectors containing information about the electric current  $J_z$  and the magnetic current  $M_t$  on the surface of the scatterer, respectively.  $\mathbf{e}^i$  denotes a  $N \times 1$  vector containing information about incident fields impinging on the basis functions. Matrix entries are given by

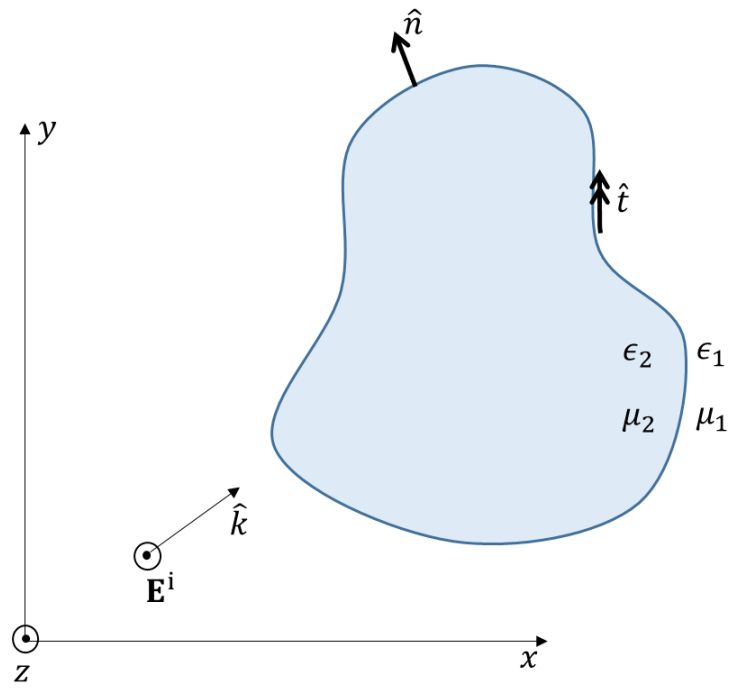


**Figure 6.3:** Illustration of a homogeneous cylinder illuminated by a  $TM^z$  incidence.

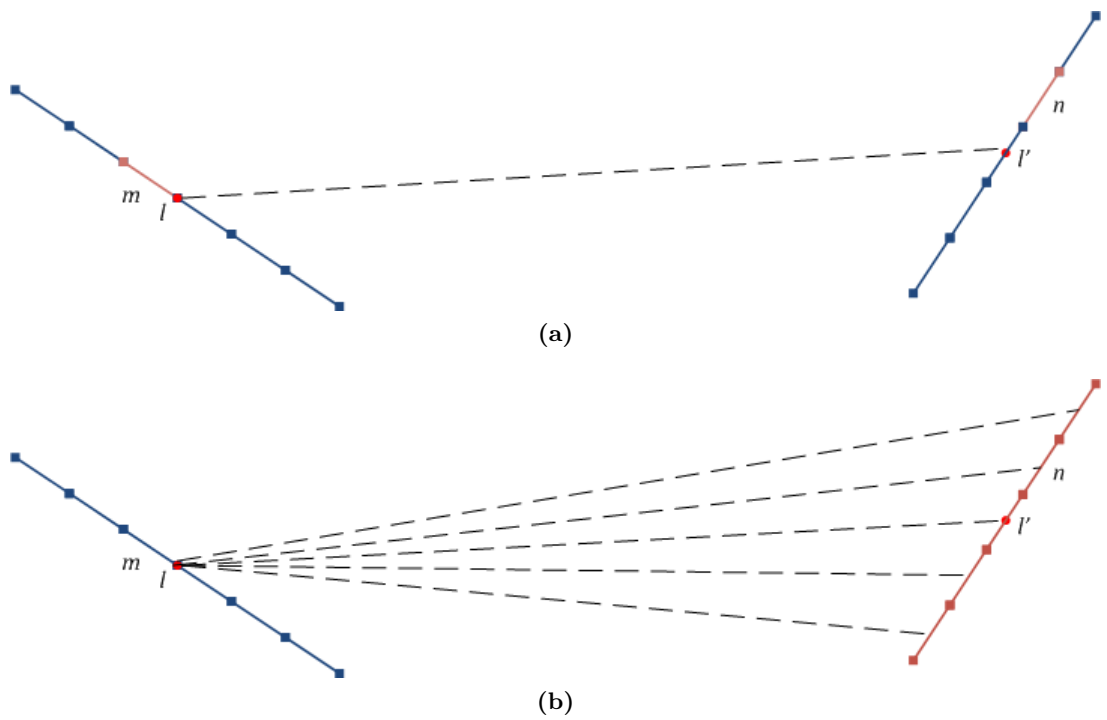


**Figure 6.4:** Illustration of the FAFFA.

$$z_{m,n}^{(a)} = \begin{cases} \frac{k_1 \eta_1}{4} H_0^{(2)}(k_1 r_{mn}) \Delta_n & m \neq n \\ \frac{k_1 \eta_1}{4} \Delta_m \left\{ 1 - j \frac{2}{\pi} \left[ \ln \left( \frac{\gamma k_1 \Delta_m}{4} - 1 \right) \right] \right\} & m = n \end{cases} \quad (6.20)$$

$$z_{m,n}^{(b)} = \begin{cases} -\frac{k_1}{4j} \hat{\mathbf{n}}_n \cdot \hat{\mathbf{r}}_{nm} H_1^{(2)}(k_1 r_{mn}) \Delta_n & m \neq n \\ \frac{1}{2} & m = n \end{cases} \quad (6.21)$$

$$z_{m,n}^{(c)} = \begin{cases} \frac{k_2 \eta_2}{4} H_0^{(2)}(k_2 r_{mn}) \Delta_n & m \neq n \\ \frac{k_2 \eta_2}{4} \Delta_m \left\{ 1 - j \frac{2}{\pi} \left[ \ln \left( \frac{\gamma k_2 \Delta_m}{4} - 1 \right) \right] \right\} & m = n \end{cases} \quad (6.22)$$

$$z_{m,n}^{(d)} = \begin{cases} -\frac{k_2}{4j} \hat{\mathbf{n}}_n \cdot \hat{\mathbf{r}}_{nm} H_1^{(2)}(k_2 r_{mn}) \Delta_n & m \neq n \\ -\frac{1}{2} & m = n \end{cases} \quad (6.23)$$

where  $\eta_i$  denotes the surface impedance of the corresponding medium and  $\gamma = 1.781$ .  $\hat{\mathbf{r}}_{nm}$  and  $r_{mn}$  are unit vectors and the length of  $\mathbf{r}_{nm}$  which is defined as follows

$$\mathbf{r}_{nm} = \mathbf{r}_n - \mathbf{r}_m. \quad (6.24)$$

### 6.3.2 Fast far field approximation applied to the surface integral equation

The FAFFA [50, 51, 82] can be applied to efficiently evaluate the MVP requested to solve Equation 6.19. A coarse grid is superimposed over the scatterer boundary, resulting in the collection of fine segments into large groups with associated centres. Considering a basis function  $m$  located in group  $G_l$  with a centre  $\mathbf{r}_l$ , contributions from other basis functions onto the basis function  $m$  can be divided into two parts: the near-zone contributions from groups close to  $G_l$  denoted by  $NF_l$ , and the far-zone contributions from the other groups denoted by  $FF_l$ . The near-zone contributions are computed exactly while the far-zone contributions are approximated using the FAFFA. The idea of the FAFFA is based on the far-field form of the Hankel function:

$$H_\alpha^{(2)}(x) \simeq \sqrt{\frac{2}{\pi x}} e^{-j(x - \alpha \frac{\pi}{2} - \frac{\pi}{4})} \quad (6.25)$$

For  $r_{mn} \gg r_{lm}$ , we can write

$$\begin{aligned} r_{mn} &\simeq r_{ln} - \hat{\mathbf{r}}_{ln} \cdot \mathbf{r}_{lm} \\ &\simeq r_{ln} - \hat{\mathbf{r}}_{l'l} \cdot \mathbf{r}_{lm} \end{aligned} \quad (6.26)$$

where  $\mathbf{r}_l$  and  $\mathbf{r}_{l'}$  are the centres of group  $G_l$  and  $G_{l'}$  as shown in Figure 6.4a, respectively. Inserting Equation 6.26 into 6.19 and applying the far-field form of the Hankel function allow us to write

$$\begin{aligned}
\bar{\mathbf{Z}}_{m,n} &= \begin{pmatrix} z_{m,n}^{(a)} & z_{m,n}^{(b)} \\ z_{m,n}^{(c)} & z_{m,n}^{(d)} \end{pmatrix} \\
&\simeq \begin{pmatrix} e^{j\psi_1} & 0 \\ 0 & e^{j\psi_2} \end{pmatrix} \begin{pmatrix} z_{l,n}^{(a)} & z_{l,n}^{(b)} \\ z_{l,n}^{(c)} & z_{l,n}^{(d)} \end{pmatrix} \\
&\equiv \bar{\mathbf{S}}\bar{\mathbf{Z}}_{l,n}
\end{aligned} \tag{6.27}$$

where the phase shifting functions are given by

$$\psi_\alpha = k_\alpha \hat{\mathbf{r}}_{l'l} \cdot \mathbf{r}_{lm}. \tag{6.28}$$

Therefore, the far-zone contributions onto the segment  $m$  can be expressed as

$$\sum_{G_{l'} \in \text{FF}_l} \sum_{n \in G_{l'}} \bar{\mathbf{Z}}_{m,n} \bar{\mathbf{x}}_n \simeq \sum_{G_{l'} \in \text{FF}_l} \bar{\mathbf{S}} \sum_{n \in G_{l'}} \bar{\mathbf{Z}}_{l,n} \bar{\mathbf{x}}_n \tag{6.29}$$

where  $\bar{\mathbf{x}}_n$  is a vector containing information about the electric and magnetic currents of segment  $n$

$$\bar{\mathbf{x}}_n = \begin{pmatrix} j_n \\ m_n \end{pmatrix} \tag{6.30}$$

The important point to note is that the final sum in Equation 6.29 needs only to be computed once per pair of groups. The shifting matrix  $\bar{\mathbf{S}}$  allows an efficient shift of the fields computed at the centre of group  $G_l$  to all the points in the group as illustrated in Figure 6.4b. The application of the FAFFA reduces the complexity to perform a MVP from  $\mathcal{O}(N^2)$  to  $\mathcal{O}(N^{1.5})$ . The efficiency of the FAFFA can be further improved without losing the overall accuracy of the method by the enlargement of the groups when the distance between the source and the test segments increases.

## 6.4 Numerical results and validations

In this section, numerical results are presented to compare the performance of two integral equation approaches applied to the solution of two dimensional indoor propagation problems. Experiments presented in this section were performed on a laptop with a 2.27GHz core i5 CPU and 4.0GB of RAM.

### 6.4.1 Efficiency of the reduced operator

To investigate the advantage of the reduced operator (described in Section 6.2.3), a two dimensional indoor problem with a size of 10m  $\times$  10m is examined as shown in Figure 6.5.



A line source radiating at 1GHz is positioned at  $(3, 2)$  inside the building. There are two types of material in the scenario concrete and glass with relative permittivities of  $\epsilon_r^{\text{concrete}} = 3.5 - j0.6$  and  $\epsilon_r^{\text{glass}} = 7.0 - j0.05$ , respectively. The values of the relative permittivities are referenced from [138]. A discretisation of 10 samples per wavelength was used in order to adequately describe the problem and resulted in 640,000 unknowns for the VEFIE. However, only 89,568 unknowns are located in non free-space regions. The BiCGSTAB is applied for the solution of the problem, is accelerated by the FFT. We compare the performance of the Krylov method with and without the aid of the reduced operator. The results are shown in Figure 6.6. The convergence rate of the BiCGSTAB is considerably improved by the use of the reduced operator.

### 6.4.2 Efficiency of the adaptive FAFFA

The same problem as in Section 6.4.1 is solved by using the surface electric field integral equation. The surface of the scatterers is sampled with a rate of 10 pulse basis functions per wavelength. This leads to a total number of 6,341 basis functions and 12,682 unknowns. The average length of each pulse basis function domain is 0.015m. Basis functions are assembled into leaf groups with a size of 0.2m. Groups which are within a range of 3m are considered the near-zone groups while the others are the far-zone groups. The BiCGSTAB which is accelerated by the FAFFA is used to solve the linear matrix system. The BiCGSTAB can be further accelerated by the enlargement of groups when the distance between the source and the testing groups increases. This method is denoted by the adaptive FAFFA. The size of groups is doubled everytime the distance increases by a factor of 2. The comparison between the performance of the FAFFA and the adaptive FAFFA is demonstrated in Figure 6.7. The total fields computed using the BiCGSTAB accelerated by the adaptive FAFFA are shown in Figure 6.8.

### 6.4.3 Comparison between the VEFIE and the SEFIE

The VEFIE and the SEFIE approaches are used for the solution of two dimensional indoor wave propagation. The volume and the surface integral equations are solved using the BiCGSTAB accelerated by the FFT and the adaptive FAFFA, respectively. In addition, the block diagonal preconditioning technique is implemented to enhance the convergence rate of the Krylov method. The indoor environment problem in Figure 6.9 has a size of  $15\text{m} \times 15\text{m}$ . A line source radiating at 1GHz is placed at  $(0, 0)$ . Three types of material in the scenario are concrete, glass and wood with relative permittivities, referenced from [138], of  $3.5 - j0.6$ ,  $7.0 - j0.05$  and  $1.8 - j0.045$ , respectively. The total numbers of unknowns are 1,440,000 and 40,952 for the VEFIE and the SEFIE, respectively. Note that in the VEFIE approach only 141,472 of the 1,440,000 unknowns corresponded to real scatterers. The total fields throughout the room computed using the two approaches are compared in Figure 6.10. The total fields along lines  $y = -1.2437\text{m}$  and  $x = -1.2437\text{m}$  are shown in Figure 6.11 and Figure 6.12, respectively. The lines are shown in blue and red dashed line in Figure 6.9, respectively. In Figure 6.11, the total fields in both approaches drop significantly around  $x = -3$  where the line passes out of sight. Similarly, the drops can be

observed around  $y = 3$  and  $y = -2$  in Figure 6.12. It can be seen clearly that there is a good agreement between results computed by the two approaches with the standard deviation of 2.03dB. The computation of the standard deviation is based on the dB values of the total fields evaluated at 1,440,000 points uniformly spaced throughout the scenario. Although the VEFIE has considerably more unknowns than the SEFIE, the overall performance of the VEFIE is far better than that of the SEFIE in terms of both iterations and runtime as shown in Table 6.1. The better convergence rate of the VEFIE as compared to the SEFIE may be due to the more efficient application of the block diagonal preconditioner when applied to the VEFIE. The block diagonal preconditioning technique enhances the convergence rate of iterative solvers using an assumption that interaction between basis functions only depends on the distance between them. The assumption is fulfilled in the VEFIE case as shown in Equation 6.12 where the mutual interaction is only dependent on the argument of the Green's function. The assumption is only partially fulfilled in the SEFIE case where the mutual interaction depends on both the distance between basis functions and their orientation as shown in Equation 6.21 and Equation 6.23. Therefore, two far-away basis functions may have great interaction or two close basis functions may have negligible effect on each other. This leads to the poorer performance of the block diagonal preconditioner when applied to the SEFIE.

	VEFIE-FFT	SEFIE-FAFFA
residual norm	$10^{-3}$	0.02
iterations	61	445
runtime (sec)	242.6	38,224

**Table 6.1:** Comparison of the two approaches for the scenario in Figure 6.9.

## 6.5 Conclusion

Two approaches, based on the SEFIE and the VEFIE, are applied to model the characteristics of 2D indoor wave propagation and the two techniques have been shown to yield similar results. However, the convergence rate of the VEFIE is considerably better than that of the SEFIE in terms of runtime. Possible future work can concentrate on the wideband analysis of 2D indoor wave propagation based on some wideband techniques such as the asymptotic waveform evaluation (AWE) [74].

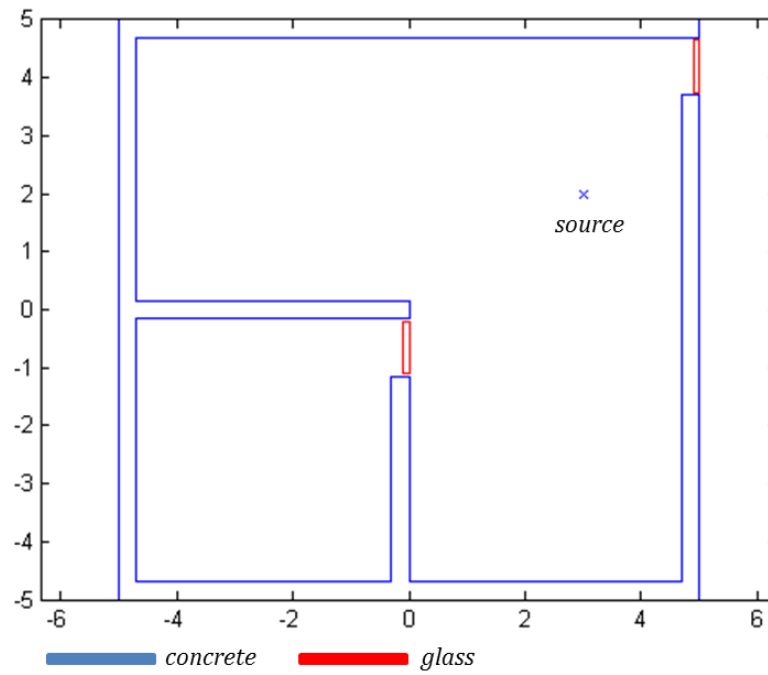


**Figure 6.5:** Two dimensional indoor environment with a size of  $10\text{m} \times 10\text{m}$ .

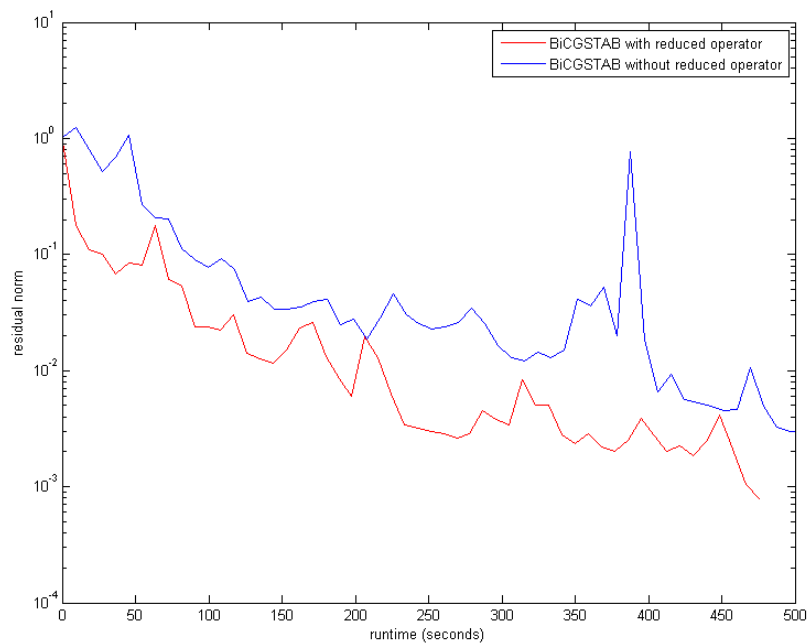


**Figure 6.6:** Comparison between the BiCGSTAB with and without the reduced operator for scenario in Figure 6.5.

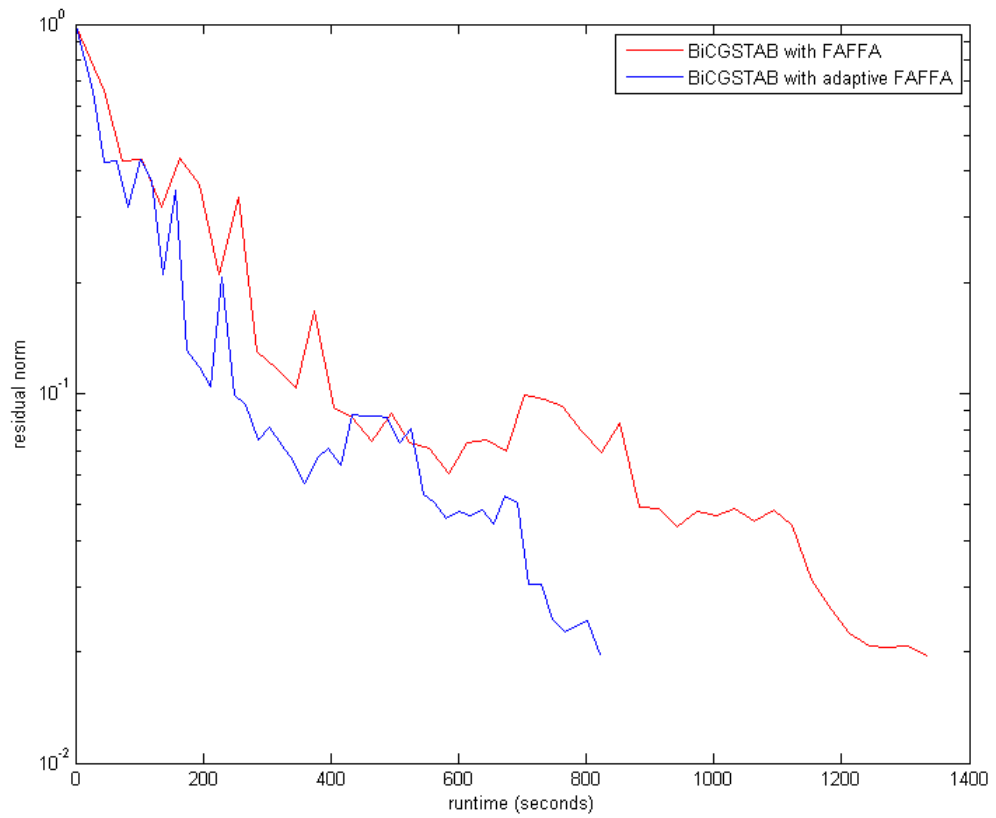


**Figure 6.7:** Comparison between the BiCGSTAB with the FAFFA and with the adaptive FAFFA for scenario in Figure 6.5.

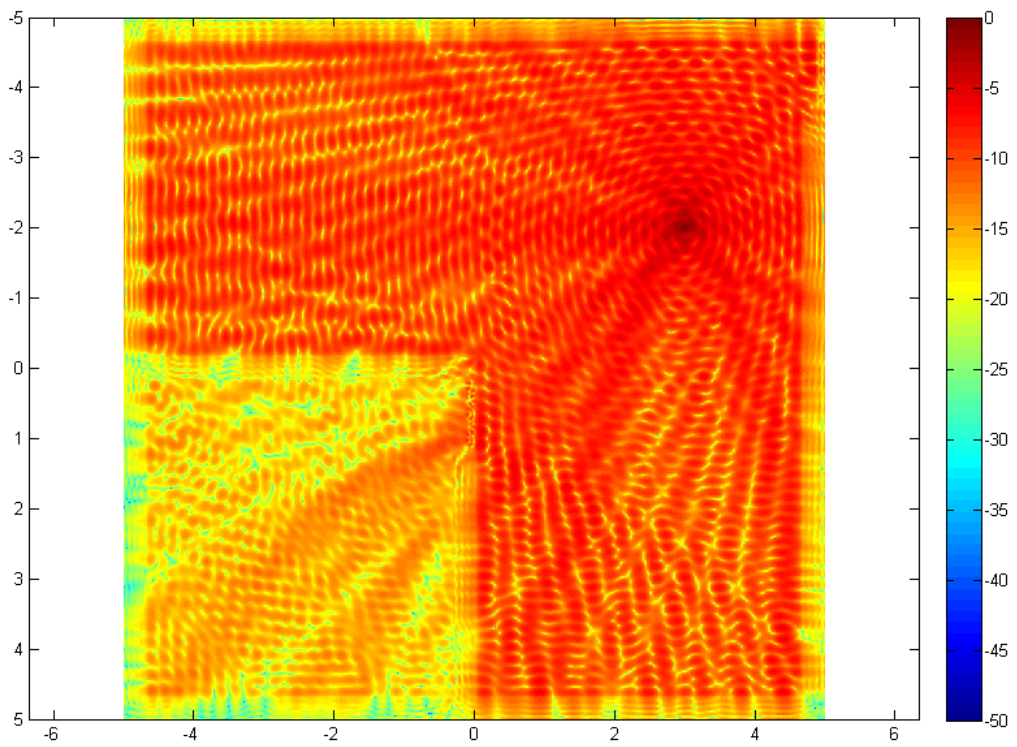


**Figure 6.8:** Total field throughout the room computed using the SEFIE.

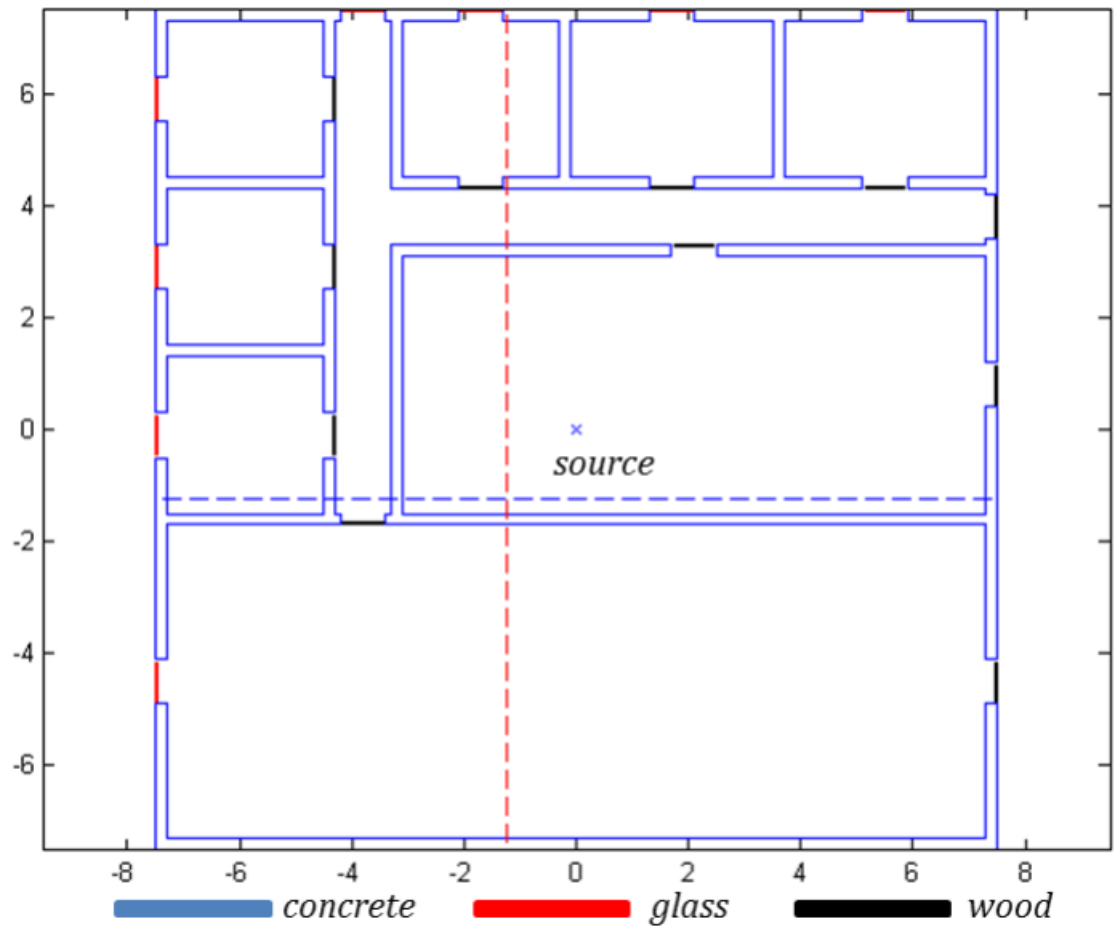


**Figure 6.9:** Two dimensional indoor environment with a size of  $15\text{m} \times 15\text{m}$ .

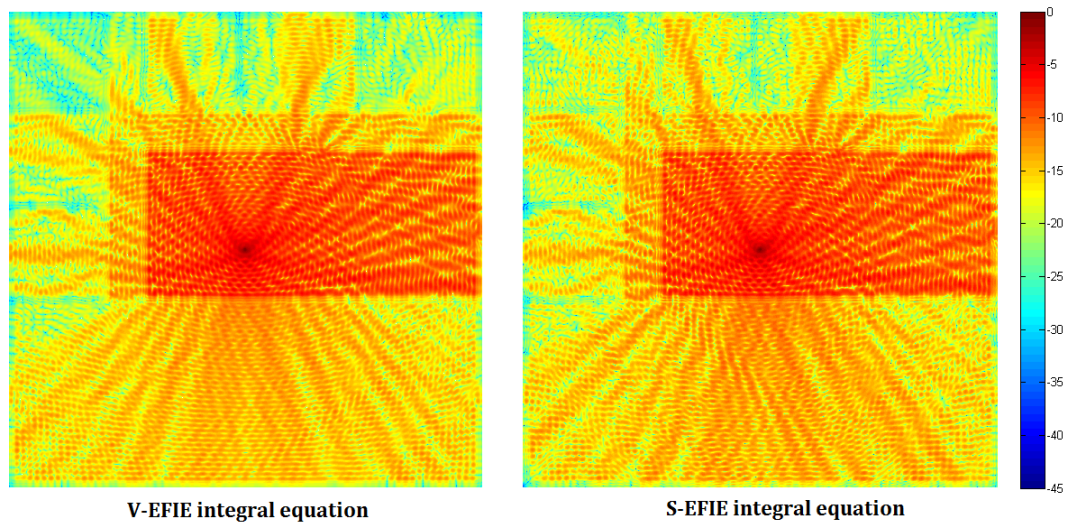


**Figure 6.10:** Total fields throughout the room using the VEFIE and the SEFIE approaches.

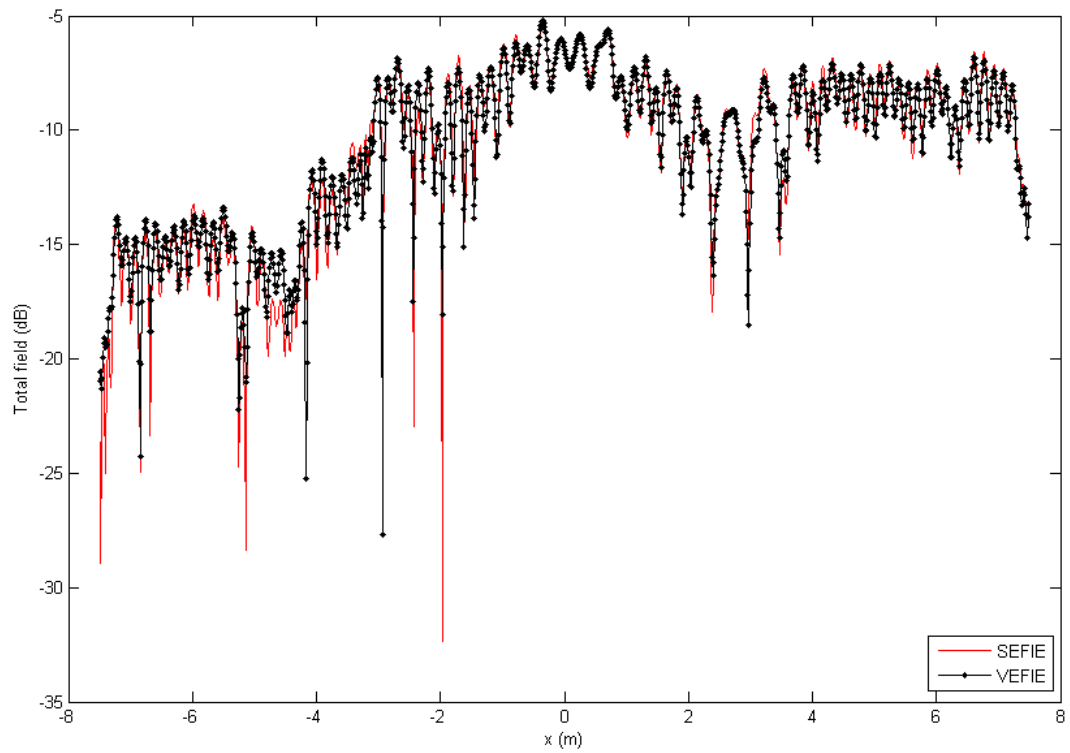


**Figure 6.11:** Total fields along the line  $y = -1.2437\text{m}$  in the scenario shown in Figure Figure 6.9.

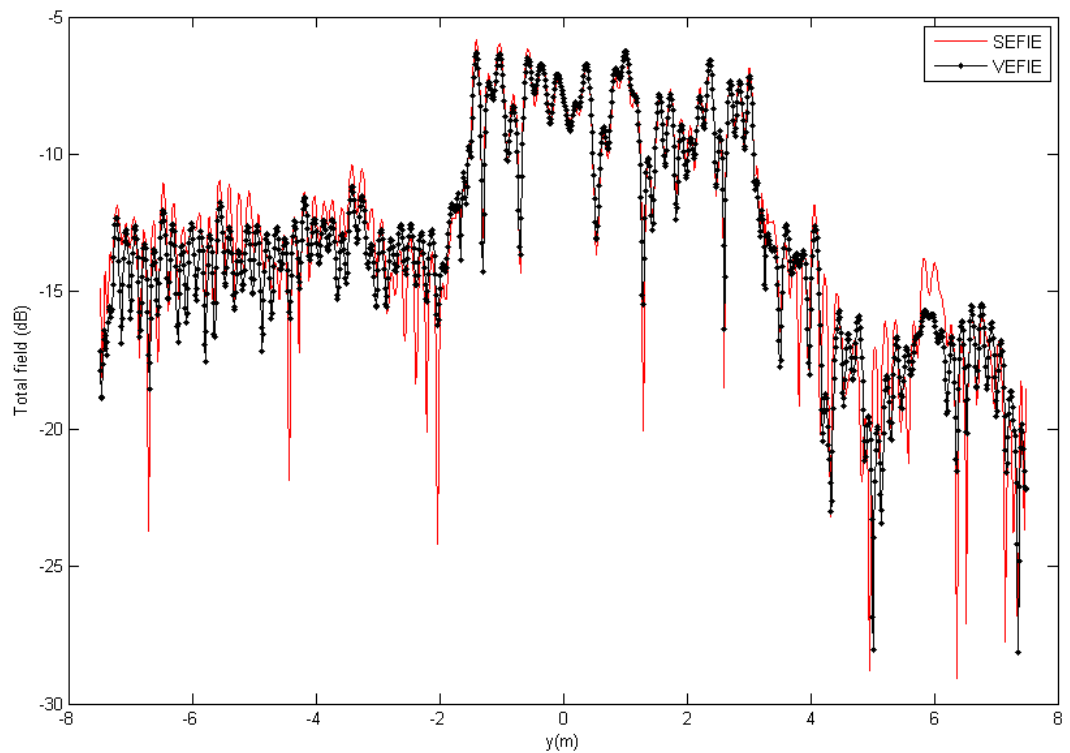


**Figure 6.12:** Total fields along the line  $x = -1.2437\text{m}$  in the scenario shown in Figure Figure 6.9.

# 7 Wideband solution for three dimensional forward scattering problems

In this chapter, a novel approach for wideband solution of three dimensional scattering problems is presented. The asymptotic waveform evaluation (AWE) is combined with the fast Fourier transform (FFT) for an efficient computation of scattered fields from three dimensional arbitrarily shaped dielectric objects over a wide range of frequencies. Numerical results are presented to demonstrate the accuracy and computational efficiency of the technique in comparison with analytical and conventional numerical methods.

## 7.1 Introduction

Accurate solution of three dimensional wave scattering problems is an important and on-going research topic, due to the diverse range of important applications such as breast cancer detection [142] and radar cross section computation. The MoM is one of the most popular techniques that have been developed and provides a purely numerical solution of such scattering problems. Historically, this approach has been limited to the analysis of scattering from electrically small bodies because of the intensive computational requirements, in terms of both time and storage. Recently, the development of more efficient algorithms has facilitated the examination of larger and more complicated bodies. In particular, the use of iterative solvers such as the GMRES [40] in conjunction with acceleration techniques such as the FFT [143] can significantly enhance the computational performance without compromising accuracy. In addition, if an analysis over a wide range of frequencies is of interest, it can be more efficient to use model-reduction methods such as the AWE [72, 73] and the Padé via Lanczos (PVL) algorithm [144] rather than repeated application of the MoM at many individual frequency points. Traditionally, the AWE has been applied by explicitly computing and applying the inverse of the impedance matrix at a central frequency in order to generate so-called moments [145]. This has restricted its application to relatively small problems, due to the dense nature of the impedance matrix. In this chapter, we investigate the use of the GMRES-FFT to iteratively solve for the moments which are used to approximate responses at other frequencies using the AWE. This allows a fast analysis of large-scale three dimensional problems over a wide frequency band.

## 7.2 Volume integral equation

### 7.2.1 Volume electric field integral equation

The volume electric field integral equation (VEFIE) formulation is applicable to the problem of wave scattering from inhomogeneous bodies and has the advantage that unknowns need only be iteratively solved within the scatterer volume. Fields exterior to the scatterer can be computed at a later step via a simple convolution with a Green's function. We consider a problem where an inhomogeneous body is located in a homogeneous background medium characterised by permittivity  $\epsilon_b$ , conductivity  $\sigma_b$  and permeability  $\mu_b$ . The inhomogeneous scatterer has a finite volume  $V$  and is specified by position-dependent permittivity  $\epsilon(\mathbf{r})$  and conductivity  $\sigma(\mathbf{r})$  while its permeability is assumed constant and equal to that of the background. Therefore, the scattered electric fields are generated by only the induced volume electric current  $\mathbf{J}_{\text{eq}}$  [57]. Equation 2.65 can be rewritten as follows

$$\mathbf{E}^s(\mathbf{r}) = -j\omega\mu_b \iiint_V \left( \mathbf{J}_{\text{eq}}(\mathbf{r}') + \frac{1}{k_b^2} \nabla' \nabla' \cdot \mathbf{J}_{\text{eq}}(\mathbf{r}') \right) \frac{e^{-jk_b|\mathbf{r}-\mathbf{r}'|}}{4\pi|\mathbf{r}-\mathbf{r}'|} dv'. \quad (7.1)$$

It should be noted that Equation 7.1 only holds for points inside the scatterers. We can apply a similar procedure as shown in Section 6.2.1 to derive an alternative integral equation which holds for every point within an investigated space by the introduction of a contrast function. Substituting Equation 2.53 into 7.1 results in

$$\mathbf{E}^s(\mathbf{r}) = \omega^2\mu_b\epsilon_b \iiint_V \left( \frac{\epsilon(\mathbf{r}')}{\epsilon_b} - 1 \right) \left( \mathbf{E}(\mathbf{r}') + \frac{1}{k_b^2} \nabla' \nabla' \cdot \mathbf{E}(\mathbf{r}') \right) \frac{e^{-jk_b|\mathbf{r}-\mathbf{r}'|}}{4\pi|\mathbf{r}-\mathbf{r}'|} dv'. \quad (7.2)$$

We define the magnetic vector potential  $\mathbf{A}$  as

$$\mathbf{A}(\mathbf{r}) = -j\omega\mu_b\epsilon_b \iiint_V \chi(\mathbf{r}') \mathbf{E}(\mathbf{r}') G(\mathbf{r}, \mathbf{r}') dv' \quad (7.3)$$

and the irrotational part of the scattered electric field as

$$\mathbf{E}^{\text{irr}}(\mathbf{r}) = \frac{j\omega}{k_b^2} \nabla \nabla \cdot \mathbf{A}(\mathbf{r}) \quad (7.4)$$

where the contrast function  $\chi(\mathbf{r})$  is defined as

$$\chi(\mathbf{r}) = \frac{\epsilon(\mathbf{r})}{\epsilon_b} - 1 \quad (7.5)$$

and  $G(\mathbf{r}, \mathbf{r}')$  is the scalar Green function for the background medium. Thus, Equation 7.2 is rewritten as

$$\mathbf{E}^s(\mathbf{r}) = j\omega\mathbf{A}(\mathbf{r}) + \mathbf{E}^{\text{irr}}(\mathbf{r}). \quad (7.6)$$



The VEFIE can be expressed as

$$\mathbf{E}^i(\mathbf{r}) = \mathbf{E}(\mathbf{r}) - j\omega\mathbf{A}(\mathbf{r}) - \mathbf{E}^{\text{irr}}(\mathbf{r}). \quad (7.7)$$

### 7.2.2 The weak-form discretisation

A weak-form discretisation [142, 146] is introduced to reduce the singularity in Equation 7.7. The volumetric scatterer is inscribed in a larger cube with dimension of  $L_x \times L_y \times L_z$ . The cube is discretised into a set of  $N_x \times N_y \times N_z$  uniform cells of volume  $\Delta V = \Delta x \Delta y \Delta z$  where  $\Delta \iota = L_\iota / N_\iota$  for  $\iota = x, y, z$ . The total number of cells is thus  $M = N_x N_y N_z$ . The centre of individual cells is positioned at

$$\mathbf{r}_{l,m,n} = (x_l, y_m, z_n) = [l. \Delta x, m. \Delta y, n. \Delta z] \quad (7.8)$$

where  $(l, m, n) \in [1, N_x] \otimes [1, N_y] \otimes [1, N_z]$  is a set of integers.  $\otimes$  denotes a Cartesian product. The application of the MoM to Equation 7.7 leads to

$$\mathbf{E}_{l,m,n}^i = \mathbf{E}_{l,m,n} - j\omega\mathbf{A}_{l,m,n} - \mathbf{E}_{l,m,n}^{\text{irr}} \quad (7.9)$$

where  $\mathbf{E}_{l,m,n} = \mathbf{E}(\mathbf{r}_{l,m,n})$ . A similar definition is applied for  $\mathbf{E}_{l,m,n}^i$ ,  $\mathbf{A}_{l,m,n}$  and  $\mathbf{E}_{l,m,n}^{\text{irr}}$ . The magnetic vector potential component  $\mathbf{A}_{l,m,n}$  can be obtained through Equation 7.3 as

$$\mathbf{A}_{l,m,n} = B_0 \sum_{l'=1}^{N_x} \sum_{m'=1}^{N_y} \sum_{n'=1}^{N_z} G_{l-l', m-m', n-n'} \chi_{l', m', n'} \mathbf{E}_{l', m', n'} \quad (7.10)$$

where  $B_0 = -j\omega\mu_b\epsilon_b \Delta V$  for  $(l, m, n) \in [0, N_x + 1] \otimes [0, N_y + 1] \otimes [0, N_z + 1]$ . The central finite difference is used to approximate  $\mathbf{E}_{l,m,n}^{\text{irr}}$  in Equation 7.4 as follows

$$\begin{aligned} E_{x;l,m,n}^{\text{irr}} &= \frac{j\omega}{k_b^2 \Delta x^2} (A_{x;l-1,m,n} - 2A_{x;l,m,n} + A_{x;l+1,m,n}) \\ &+ \frac{j\omega}{4k_b^2 \Delta x \Delta y} (A_{y;l-1,m-1,n} - A_{y;l-1,m+1,n} - A_{y;l+1,m-1,n} + A_{y;l+1,m+1,n}) \\ &+ \frac{j\omega}{4k_b^2 \Delta x \Delta z} (A_{z;l-1,m,n-1} - A_{z;l-1,m,n+1} - A_{z;l+1,m,n-1} + A_{z;l+1,m,n+1}) \end{aligned} \quad (7.11)$$

$$\begin{aligned} E_{y;l,m,n}^{\text{irr}} &= \frac{j\omega}{k_b^2 \Delta y^2} (A_{y;l,m-1,n} - 2A_{y;l,m,n} + A_{y;l,m+1,n}) \\ &+ \frac{j\omega}{4k_b^2 \Delta x \Delta y} (A_{x;l-1,m-1,n} - A_{x;l-1,m+1,n} - A_{x;l+1,m-1,n} + A_{x;l+1,m+1,n}) \\ &+ \frac{j\omega}{4k_b^2 \Delta y \Delta z} (A_{z;l,m-1,n-1} - A_{z;l,m-1,n+1} - A_{z;l,m+1,n-1} + A_{z;l,m+1,n+1}) \end{aligned} \quad (7.12)$$

$$\begin{aligned}
 E_{z;l,m,n}^{\text{irr}} &= \frac{j\omega}{k_b^2 \Delta z^2} (A_{z;l,m,n-1} - 2A_{z;l,m,n} + A_{z;l,m,n+1}) \\
 &+ \frac{j\omega}{4k_b^2 \Delta x \Delta z} (A_{x;l-1,m,n-1} - A_{x;l-1,m,n+1} - A_{x;l+1,m,n-1} + A_{x;l+1,m,n+1}) \\
 &+ \frac{j\omega}{4k_b^2 \Delta y \Delta z} (A_{y;l,m-1,n-1} - A_{y;l,m-1,n+1} - A_{y;l,m+1,n-1} + A_{y;l,m+1,n+1})
 \end{aligned} \tag{7.13}$$

We can rewrite Equation 7.10 in matrix notation as

$$\begin{pmatrix} \mathbf{A}_x \\ \mathbf{A}_y \\ \mathbf{A}_z \end{pmatrix} = B_0 \mathbf{G} \mathbf{D} \begin{pmatrix} \mathbf{E}_x \\ \mathbf{E}_y \\ \mathbf{E}_z \end{pmatrix} \tag{7.14}$$

where for example  $\mathbf{E}_x$  is a vector of length  $M$  which contains the unknown  $x$ -components of the electric field at the cell centres, with similar interpretations for the other quantities.  $\mathbf{G}$  is a Greens function matrix with three blocks on the diagonal.

$$\mathbf{G} = \begin{pmatrix} \mathbf{G}_1 & 0 & 0 \\ 0 & \mathbf{G}_2 & 0 \\ 0 & 0 & \mathbf{G}_3 \end{pmatrix} \tag{7.15}$$

Each of the  $\mathbf{G}_i$  has a block Toeplitz form while  $\mathbf{D}$  is a diagonal matrix containing contrast values. Equation 7.11-7.13 can be rewritten as

$$\begin{pmatrix} \mathbf{E}_x^{\text{irr}} \\ \mathbf{E}_y^{\text{irr}} \\ \mathbf{E}_z^{\text{irr}} \end{pmatrix} = \Delta \mathbf{V} \mathbf{H} \mathbf{G} \mathbf{D} \begin{pmatrix} \mathbf{E}_x \\ \mathbf{E}_y \\ \mathbf{E}_z \end{pmatrix} \tag{7.16}$$

where  $\mathbf{H}$  is a sparse matrix containing a suitable numerical approximation to the grad-div operation. Finally, Equation 7.9 can be rewritten as

$$\mathbf{Z} \cdot \mathbf{E} = \mathbf{E}^{\text{i}} \tag{7.17}$$

where

$$\mathbf{Z} = \mathbf{I} - k_b^2 \Delta \mathbf{V} \mathbf{G} \mathbf{D} - \Delta \mathbf{V} \mathbf{H} \mathbf{G} \mathbf{D} \tag{7.18}$$

and for example

$$\mathbf{E} = \begin{pmatrix} \mathbf{E}_x \\ \mathbf{E}_y \\ \mathbf{E}_z \end{pmatrix} \quad (7.19)$$

Equation 7.17 can be solved using an iterative method which requires  $\mathcal{O}(N^2)$  operations per iteration instead of  $\mathcal{O}(N^3)$  computations required for direct inversion where  $N = 3M$  is the total number of unknowns. However, because of the special form of  $\mathbf{G}$  and the sparsity of  $\mathbf{D}$  and  $\mathbf{H}$ , we can take advantage of the FFT for a fast MVP to reduce the number of operations per iteration to  $\mathcal{O}(N \log N)$ .

### 7.3 Asymptotic waveform evaluation

Because both the  $\mathbf{Z}$  matrix and incident field vector  $\mathbf{E}^i$  are frequency dependent, the total field  $\mathbf{E}$  also varies with frequency and hence with  $k_b$ . If a response over a certain band of frequency is of interest, then the repeated independent solution of Equation 7.17 at each frequency is computationally expensive and time-consuming. An alternative method in this situation is to use the AWE which generates a reduced order model, exact at the central frequency and approximate to a desired accuracy over the band of interest. Let the central frequency be  $f_0$  with a corresponding value of  $k_b$  given by  $k_{b0}$ . We create an approximate solution at a desired frequency  $f$  (with corresponding background wavenumber  $k_b$ ) by using a Taylor series

$$\mathbf{E}(k_b) = \sum_{k=0}^Q \mathbf{m}_k (k_b - k_{b0})^k \quad (7.20)$$

or more accurately by using Padé approximation

$$\mathbf{E}(k_b) = \frac{\sum_{i=0}^L \mathbf{a}_i (k_b - k_{b0})^i}{1 + \sum_{j=1}^P \mathbf{b}_j (k_b - k_{b0})^j} \quad (7.21)$$

where  $\mathbf{m}_k$  denotes the moments, given by the following recursive relation for  $k = 1 \dots Q$

$$\mathbf{Z}(k_{b0}) \mathbf{m}_k = \frac{\mathbf{E}^{i(k)}(k_{b0})}{k!} - \sum_{i=1}^k \frac{\mathbf{Z}^{(i)}(k_{b0})}{i!} \mathbf{m}_{k-i}. \quad (7.22)$$

$\mathbf{Z}^{(i)}(k_{b0})$  is the  $i^{\text{th}}$  derivative of  $\mathbf{Z}$  with respect to  $k_b$  and evaluated at  $k_{b0}$ . Other quantities have similar interpretations. In the Padé expression  $L + P = Q$  and the unknowns can be obtained by matching the moments

$$\mathbf{P}_f \begin{pmatrix} \mathbf{b}_1 \\ \mathbf{b}_2 \\ \vdots \\ \mathbf{b}_P \end{pmatrix} = \begin{pmatrix} \mathbf{m}_{L+1} \\ \mathbf{m}_{L+2} \\ \vdots \\ \mathbf{m}_{L+P} \end{pmatrix} \quad (7.23)$$

with

$$\mathbf{P}_f = \begin{pmatrix} \mathbf{m}_L & \mathbf{m}_{L-1} & \cdots & \mathbf{m}_{L-P+1} \\ \mathbf{m}_{L+1} & \mathbf{m}_L & \cdots & \mathbf{m}_{L-P+2} \\ \vdots & \vdots & \ddots & \vdots \\ \mathbf{m}_{L+P-1} & \mathbf{m}_{L+P-2} & \cdots & \mathbf{m}_L \end{pmatrix}. \quad (7.24)$$

$\mathbf{b}_j$  computed from Equation 7.23 are used for the calculation of  $\mathbf{a}_i$  as

$$\begin{aligned} \mathbf{a}_0 &= \mathbf{m}_0 \\ \mathbf{a}_1 &= \mathbf{m}_1 + \mathbf{b}_1 \mathbf{m}_0 \\ \mathbf{a}_2 &= \mathbf{m}_2 + \mathbf{b}_1 \mathbf{m}_1 + \mathbf{b}_2 \mathbf{m}_0 \\ &\vdots \\ \mathbf{a}_i &= \mathbf{m}_i + \sum_{j=1}^i \mathbf{b}_j \mathbf{m}_{i-j} \end{aligned} \quad (7.25)$$

A key part in the computation of the derivatives of  $\mathbf{Z}$  required in Equation 7.22 is to calculate the derivatives of  $\mathbf{K}$  where  $\mathbf{K}$  is defined as the product of  $\mathbf{G}$  and  $\mathbf{D}$ . We get

$$\mathbf{K}^{(i)}(k_{b0}) = \sum_{j=0}^i \binom{i}{j} \mathbf{G}^{(i-j)}(k_{b0}) \mathbf{D}^{(j)}(k_{b0}). \quad (7.26)$$

The GMRES-FFT is applied for the solution of Equation 7.22. The key observation is that  $\mathbf{H}$  is not frequency dependent and that both the derivatives of  $\mathbf{G}$  and  $\mathbf{D}$  retain their computationally efficient form, namely block Toeplitz and diagonal respectively, which permits the rapid  $\mathcal{O}(N \log N)$  computation of the right hand side vectors of Equation 7.22. This coupled with the use of GMRES to solve for the moments allows the use of the AWE for larger problems.

## 7.4 Numerical results and validations

Numerical results are presented in this section to illustrate and validate the proposed method. All of the simulations were performed on a core i5 CPU running at 2.27GHz.

The scatterer is a dielectric sphere with a radius of 0.09m centred at the origin and illuminated by an incident plane wave from the direction ( $\theta = 0; \varphi = 0$ ), with an electric field polarised along the  $x$ -axis. The sphere is centred in a cube with the side length of 0.3m. Each side is discretised using 36 cells resulting in a total of 139,968 unknowns as shown in Figure 7.1. The number of terms retained in the Taylor series is  $Q = 20$  and a Padé approximation with  $L = P = 10$  is created. The tolerance for the iteration scheme used to compute the moments is specified to be  $10^{-6}$ . Firstly, we examine the accuracy of the method by making a comparison of the monostatic RCS computed using an analytic method (Mie series), a conventional numerical method (MoM computed independently at each frequency) and our proposed method. The frequency band of interest is from 700MHz to 1.3GHz and the expansion frequency is 1.0GHz. In order to illustrate the ability of the model to handle frequency dependent parameters, the relative permittivity of the dielectric bodies is modelled as a cubic polynomial in  $k_b$  varying from 1.87 to 1.96 when the frequency changes from 700MHz to 1.3GHz as shown in Figure 7.2. A comparison is shown in Figure 7.3. It can be seen that the result from the described method agrees exactly with the numerical method and is in close agreement with the analytic method (small deviations are due to the simplistic nature of the basis functions used in the discretisation and can be reduced by increasing the number of basis functions used, at the expense of greater run times). The total fields at 1.3GHz along lines in  $x$ -,  $y$ -,  $z$ -directions are presented in Figure 7.4 – 7.6, respectively. The fields are computed using the three methods. Again the reduced order model agrees perfectly with the repeated MoM calculations. The efficiency of the proposed method is demonstrated in Table 7.1. The table outlines the computation time associated with the two numerical methods, for different numbers of frequency points spanning the range. The computational time of the MoM increases linearly with the number of frequency points while the computational time of the AWE is almost constant because the computation of moments comprises most complexity of the AWE. Once the moments are computed, the results at different frequency points can be calculated quickly. It can be seen that the AWE is more computationally efficient, and the speed-up increases with the number of desired frequencies.

Number of frequencies	41	61	81	101
MoM time (sec)	3,112	4,629	6,139	7,673
AWE time (sec)	2,384	2,422	2,468	2,494
Speed up	1.31	1.91	2.49	3.08

**Table 7.1:** Comparison of runtime using the conventional MoM and the AWE for the dielectric sphere.

## 7.5 Conclusion

This chapter presents an efficient method to analyse electromagnetic wave scattering from arbitrarily shaped bodies over a wideband of frequencies. The formulation is based on the three dimensional weak-form formulation of the VEFIE discretised using the MoM. AWE is used to rapidly compute the electromagnetic response over a wide frequency range. GMRES-FFT is used to solve for the individual moments and the form of the impedance matrix means that the right hand side of each moment equation retains a structure compatible with the use of the FFT. Numerical results for a dielectric lossless sphere with frequency-dependent permittivity have been shown to demonstrate the accuracy and computational efficiency in comparison with Mie series and conventional MoM.

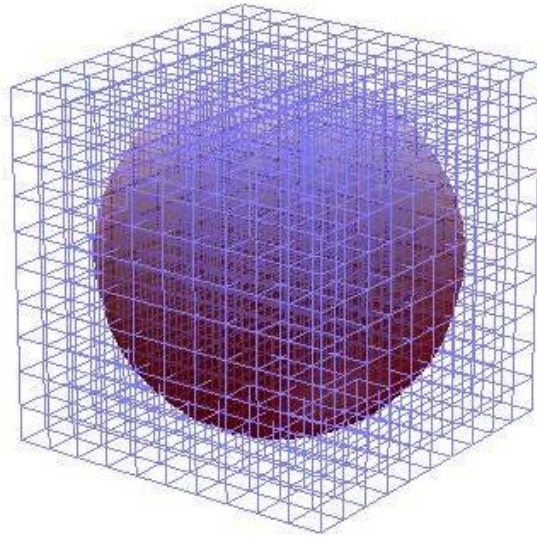


**Figure 7.1:** Discretisation of the dielectric sphere.

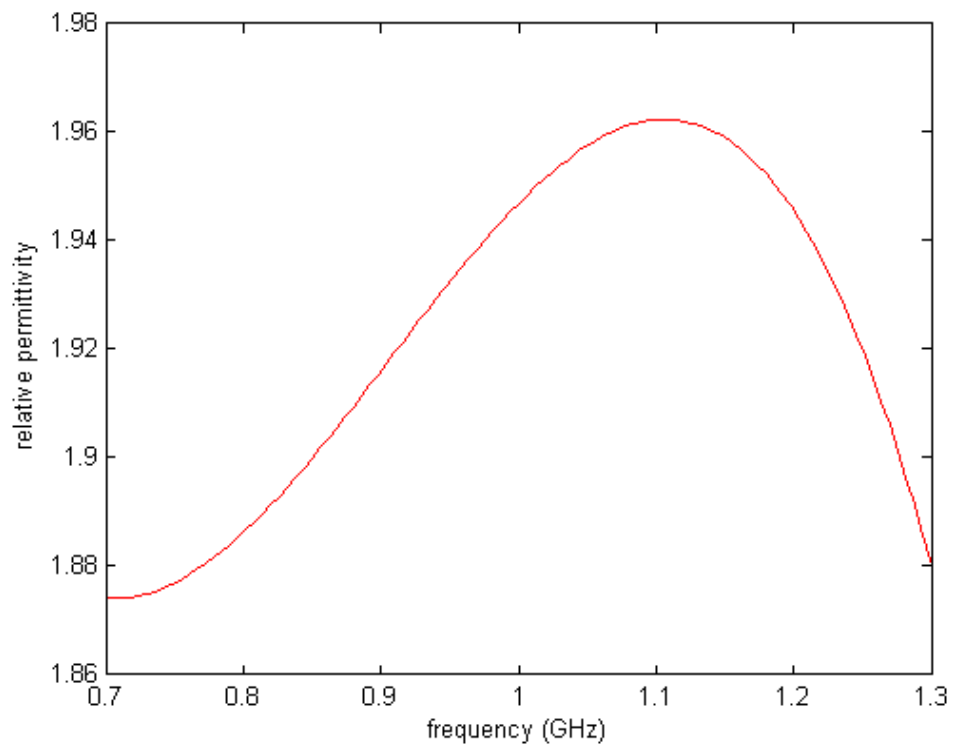


**Figure 7.2:** Value of the relative permittivity of the dielectric sphere with respect to frequency.

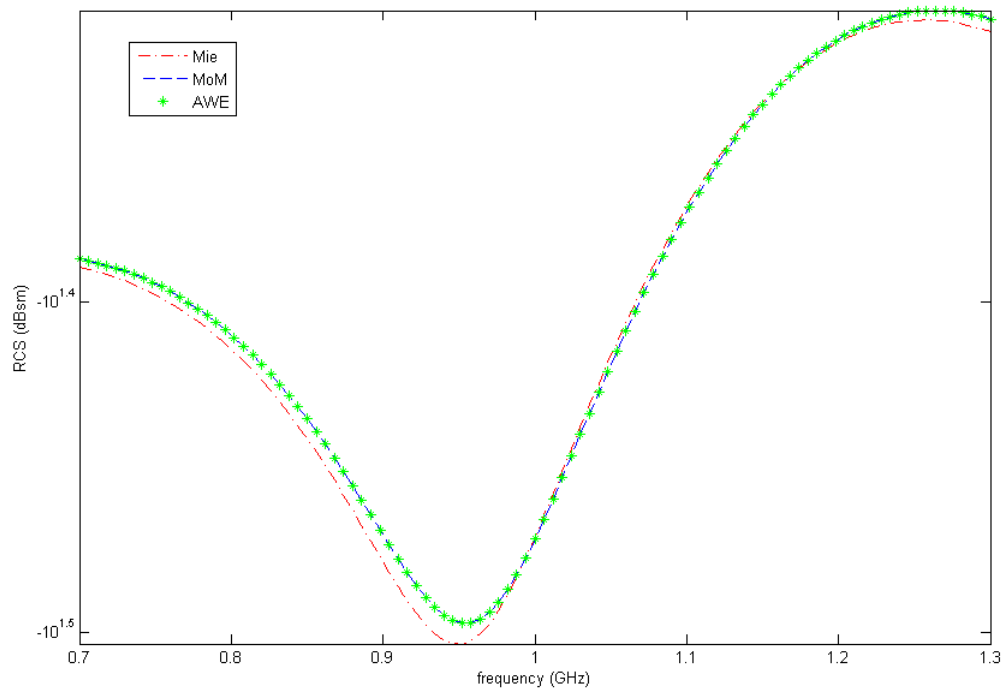


**Figure 7.3:** Radar cross section results of the dielectric sphere with the radius of 0.09m.

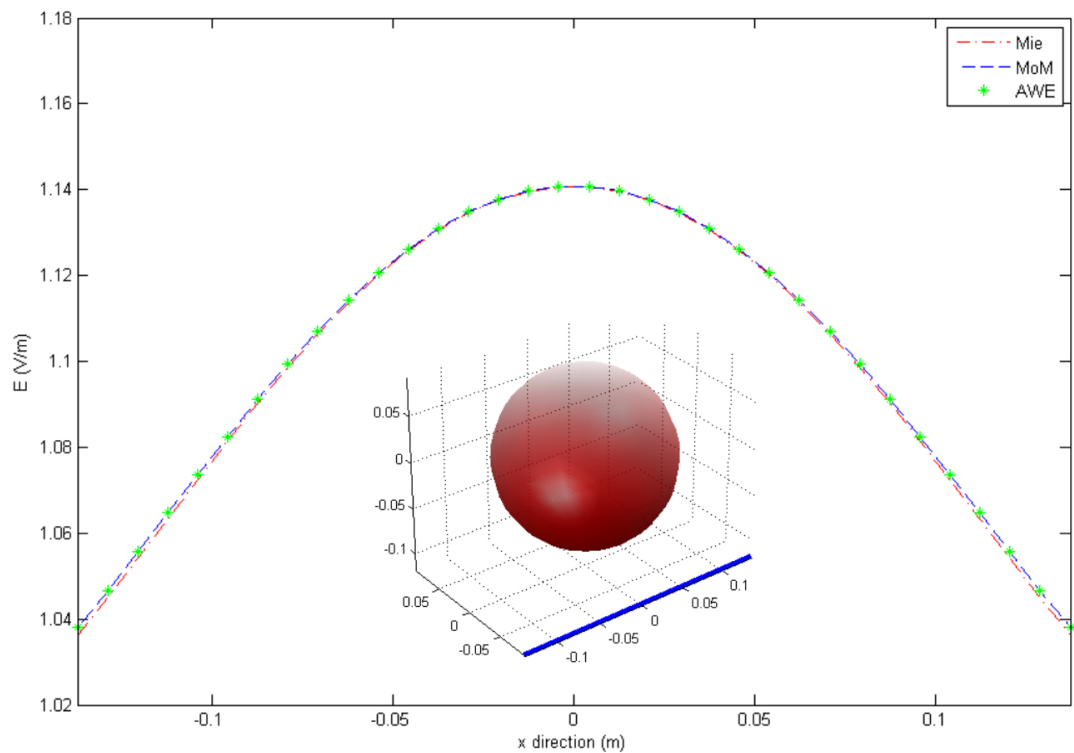


**Figure 7.4:** Total field along  $x$  direction with  $y = -0.0874\text{m}$  and  $z = -0.1208\text{m}$  at  $f = 1.3\text{GHz}$ .



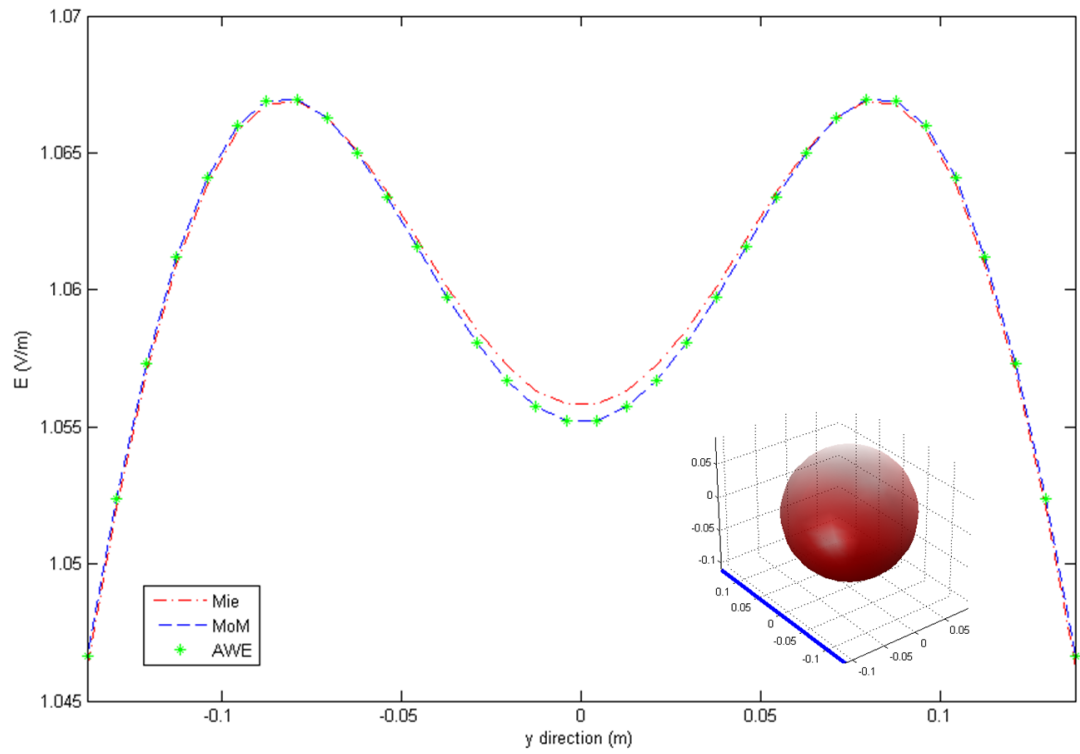


**Figure 7.5:** Total field along  $y$  direction with  $x = -0.1124\text{m}$  and  $z = -0.1124\text{m}$  at  $f = 1.3\text{GHz}$ .

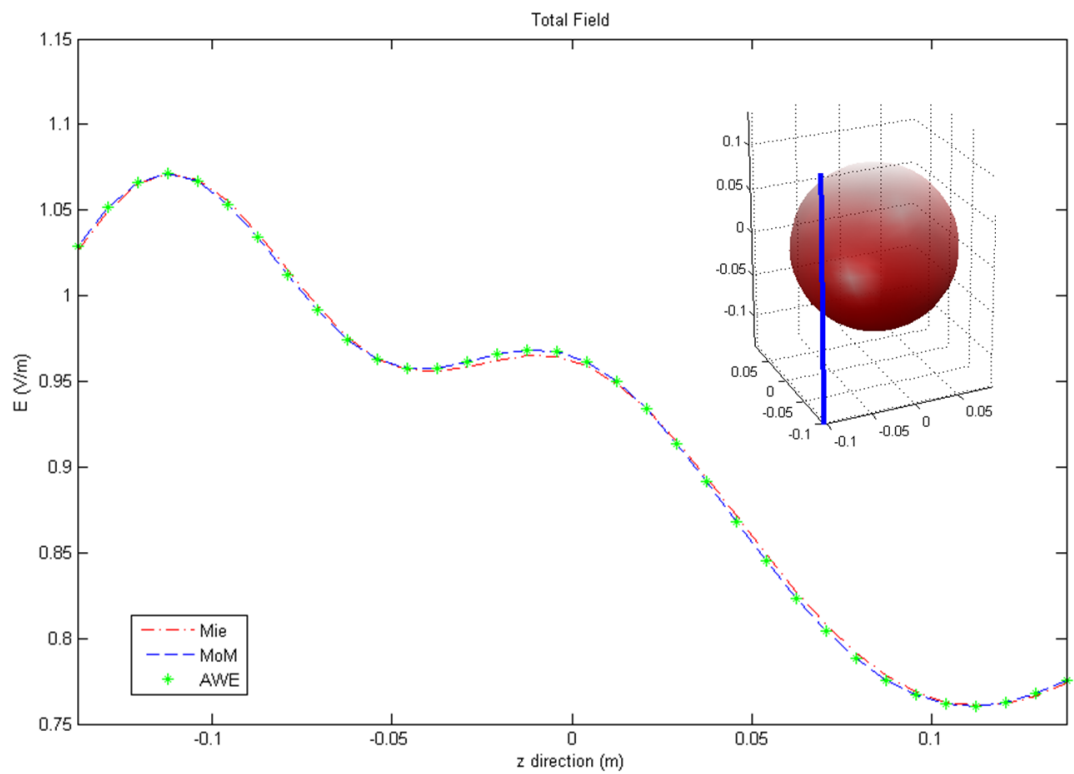


**Figure 7.6:** Total field along  $z$  direction with  $x = -0.1041\text{m}$  and  $y = -0.1041\text{m}$  at  $f = 1.3\text{GHz}$ .

## 8 Conclusions

The central focus of this dissertation is on the development of accelerated iterative algorithms, which are a combination of iterative methods and acceleration techniques, to efficiently solve electromagnetic (EM) scattering and wave propagation problems. There is a need for appropriate algorithms for fast solution of diverse applications in EM problems in spite of impressive recent improvements in computer technology and much research focusing on the area of accelerated iterative methods. Chapters 2 and 3 provide the basic materials necessary to understand the following chapters. Maxwells equations are reviewed in Chapter 2 to derive the electric field integral equations and the magnetic field integral equations which are used extensively in the later chapters. The method of moments is also presented as a numerical solution for the integral equations. Chapter 3 revisits popular iterative solvers which are categorised into non-stationary and stationary methods. The iterative solvers are reviewed as an appropriate approach for a solution of dense linear systems, resulting from the application of the method of moments to integral equations. Chapters 4 – 7 demonstrate the four main contributions of the dissertation. Chapters 4 and 5 focus on the use of stationary iterative methods in combination with several acceleration techniques such as the multilevel fast multipole method and the spectral acceleration for the solution of two and three dimensional scattering problems. Chapters 6 and 7 concentrate on using Krylov iterative methods to solve two dimensional indoor propagation problems and three dimensional wideband forward scattering problems, respectively.

In Chapter 4, the modified multilevel fast multipole algorithm is applied to improve the performance of stationary iterative solvers. The application of the standard MLFMA to stationary iterative methods cancels the advantage of the stationary methods due to an inefficient performance of partial MVPs which are required constantly in the process of the methods. The modified MLFMA is a variant of the standard one with two additional simple algorithms enabling a considerably better performance of the partial MVPs. Numerical experiments demonstrate the efficiency of the proposed method as compared to the standard MLFMA when applied to stationary iterative methods, in particular, the BBFB and the O-DDM. The proposed algorithm is applied for the solution of three dimensional perfectly conducting scattering problems. However, it is noteworthy that the modified algorithm is extendable to other applications, such as three dimensional scattering problems for dielectric geometries or random rough surface scattering problems, where the stationary methods and the MLFMA are used for the solution.

The improvement of the performance of the stationary iterative solvers is extended in Chapter 5. Despite focusing on acceleration techniques to reduce the computational complexity as in Chapter 4, Chapter 5 concentrates on improving the convergence rate of the iterative methods. The modified improvement step is the main contribution of the

chapter. The proposed algorithm is an extension of the original improvement step which uses a single correction vector for an enhancement of the convergence rate. The main disadvantage of the original method is that in the process of stationary methods updating currents along the previous correction vector may be performed, causing the loss of efficiency of the previous improvement step. The modified improvement step is proposed to preserve the effectiveness of the previous correction steps, leading to a better convergence rate with negligible additional complexity. The greater the number of correction vectors is, the better the achieved convergence rate is. Simulation results are shown to confirm the advantage of the proposed algorithm. Although the proposed algorithm is only applied for a solution of two and three dimensional random rough surface scattering problems in this chapter, it can be extended to other applications.

Chapter 6 turns our attention to the application of Krylov iterative solvers in conjunction with acceleration techniques to solve two dimensional indoor wave propagation problems. A contribution of Chapter 6 is a comparison between the volume and the surface integral equations for solving the problems. The fast Fourier transform and the fast far field approximation algorithm are implemented for the volume and the surface integral equations, respectively, to speed up the MVP performed within each iteration. Simulation results suggest that the volume integral equation approach converges to a desired accuracy significantly faster than the surface integral equation approach. Although the number of unknowns in the volumetric approach is considerably greater than that in the surface approach, the former converges within greatly fewer iterations. Further investigation is necessary for an explanation of the convergence rate. The AWE technique, presented in Chapter 7, could be applied to analyse indoor wave propagation problems over a wide range of frequency. In addition, the volume integral equation could be applied for the solution of three dimensional indoor propagation with the aid of graphic processing unit (GPU) and parallelisation techniques.

Chapter 7 is devoted to the last contribution of this dissertation. The chapter investigates the wideband solution of three dimensional scattering problems using Krylov iterative methods in combination with an acceleration technique, the fast Fourier transform, and a wideband technique, asymptotic waveform evaluation. The proposed method which combines several techniques approximates wideband results from information about moments at the central frequency while the conventional method has to separately compute the results at individual frequency points. Numerical results demonstrate that the proposed method is more computationally efficient for the computation of the wideband results as compared to the conventional method. Numerical experiments are presented for homogeneous dielectric spheres with frequency-dependent electrical parameters because this permits comparison with analytical solutions. However, it should be noted that the method can be readily applied to homogeneous lossy objects.

## 8.1 Future study

Several avenues of future research can be envisaged from this dissertation. The first is the potential application of the modified MLFMA to stationary iterative solvers for a

solution of larger and more complicated geometries made from imperfectly conductor or dielectric materials. The method has been applied to solve problems where the number of unknowns is of the order of hundred thousands. Larger and more complex problems may require further investigation into the use of graphic processing unit and parallelisation techniques.

Secondly, modified MLFMA concept is potentially applicable to three dimensional random rough surface scattering. The BBFB or the O-DDM accelerated by the steepest descent fast multiple method (FMM) could borrow the idea of the modified MLFMA to reduce the computational complexity of the partial MVPs and potential for the improvement of the convergence rate of the block forward backward method used in Chapter 5. For three dimensional random rough surface problems, the block forward backward method can easily diverge as the roughness of the surface increases with respect to the operating frequency. The BBFB and the O-DDM could be an effective resolution for the improvement of the convergence rate. The stationary methods can be accelerated by the steepest descent FMM which may adopt the idea of the modified MLFMA to efficiently perform the partial MVPs required.

Next, the work presented in Chapter 6 maybe potentially extended for three dimensional indoor wave propagation problems. Although the FFT is applied to accelerate the performance of the MVP and to reduce the computational complexity from  $\mathcal{O}(N^2)$  to  $\mathcal{O}(N\log N)$ , it is noted that the number of unknowns  $N$  is a large value because it includes the free-space unknowns which contain irrelevant information for iterative solvers. The large value of  $N$ , especially in three dimensional cases, leads to significant redundancy. Thus, there is a need for new acceleration algorithms which preserve the advantage of the FFT and also reduce the number of unknowns  $N$ . Knowledge about supercomputer and parallelisation may be necessary when the size of the problems is beyond the capability of the normal computer.

Another possible avenue for future work extends the application of wideband solutions for three dimensional forward scattering problem presented in Chapter 7. The asymptotic waveform evaluation technique may be replaced by the well-conditioned asymptotic waveform evaluation for a better accuracy over a wider range of frequency. In addition, a strict error control scheme needs to be developed to determine the number of moments required with respect to the pre-defined accuracy.

## Bibliography

- [1] A. Woo, H. Wang, M. Schuh, and M. Sanders, "EM Programmer's Notebook-Benchmark Radar Targets for the Validation of Computational Electromagnetics Programs," *IEEE Antennas and Propagation Magazine*, vol. 35, no. 1, pp. 84–89, Feb. 1993.
- [2] S. M. Yucedag, O. M. Yucedag, and H. A. Serim, "Analytical Method for Monostatic Radar Cross Section Calculation of a Perfectly Conducting Wind Turbine Model Located over Dielectric Lossy Half Space," *IET Radar, Sonar and Navigation*, vol. 8, no. 8, pp. 965–970, Oct. 2014.
- [3] K. Kim, J. H. Kim, and D. S. Cho, "Numerical Investigation on Dynamic Radar Cross Section of Naval Ship Considering Ocean Wave-Induced Motion," *Progress In Electromagnetic Research M*, vol. 27, pp. 11–26, 2012.
- [4] M. Alves, R. Port, and M. Rezende, "Simulations of the Radar Cross Section of a Stealth Aircraft," in *The 2007 SBMO/IEEE MTT-S International Microwave and Optoelectronics Conference*, Oct. 2007, pp. 409–412.
- [5] J. Shea, B. Van Veen, and S. Hagness, "A TSVD Analysis of Microwave Inverse Scattering for Breast Imaging," *IEEE Transactions on Biomedical Engineering*, vol. 59, no. 4, pp. 936–945, Apr. 2012.
- [6] M. Lakshmanan, B. Harrawood, G. Agasthya, and A. Kapadia, "Simulations of Breast Cancer Imaging Using Gamma-Ray Stimulated Emission Computed Tomography," *IEEE Transactions on Medical Imaging*, vol. 33, no. 2, pp. 546–555, Feb. 2014.
- [7] A. Fouda and F. Teixeira, "Ultra-Wideband Microwave Imaging of Breast Cancer Tumors via Bayesian Inverse Scattering," *Journal of Applied Physics*, vol. 115, no. 6, pp. 064 701–064 701–8, Feb. 2014.
- [8] M. Kline and I. Kay, *Electromagnetic Theory and Geometrical Optics*. New York: Wiley Interscience, 1965.
- [9] G. L. James, *Geometrical Theory of Diffraction for Electromagnetic Waves*, ser. Electromagnetic Waves. Institution of Engineering and Technology, 1979.
- [10] J. B. Keller, "Geometrical Theory of Diffraction," *Journal of the Optical Society of America*, vol. 52, no. 2, pp. 116–130, Feb. 1962.
- [11] P. Pathak and R. Kouyoumjian, "An Analysis of the Radiation from Apertures in Curved Surfaces by the Geometrical Theory of Diffraction," *Proceedings of the IEEE*, vol. 62, no. 11, pp. 1438–1447, Nov. 1974.

- [12] R. Kouyoumjian and P. Pathak, "A Uniform Geometrical Theory of Diffraction for an Edge in a Perfectly Conducting Surface," *Proceedings of the IEEE*, vol. 62, no. 11, pp. 1448–1461, Nov. 1974.
- [13] P. Pathak, "Techniques for High Frequency Problems," in *Antenna Handbook*. Springer US, 1988, pp. 195–311.
- [14] P. Y. Ufimtsev, "Elementary Edge Waves and the Physical Theory of Diffraction," *Electromagnetics*, vol. 11, no. 2, pp. 125–160, 1991.
- [15] —, *Fundamentals of the Physical Theory of Diffraction*. John Wiley & Sons Inc., 2006.
- [16] J. Jin, *The Finite Element Method in Electromagnetics*, 3rd ed. Wiley-IEEE Press, 2014.
- [17] J. Volakis, A. Chatterjee, and L. Kempel, *Finite Element Method Electromagnetics: Antennas, Microwave Circuits, and Scattering Applications*, 1st ed. Wiley-IEEE Press, 1998.
- [18] D. M. Sullivan, *Electromagnetic Simulation Using The FDTD Method*, 2nd ed. Wiley-IEEE Press, 2013.
- [19] A. Taflove and S. C. Hagness, *Computational Electrodynamics: The Finite-Difference Time-Domain Method*, 3rd ed. Artech House, 2005.
- [20] A. Peterson, S. Ray, and R. Mittra, *Computational Methods for Electromagnetics*. Wiley-IEEE Press, 1997.
- [21] W. C. Gibson, *The Method of Moments in Electromagnetics*, 2nd ed. Apple Academic Press Inc, 2014.
- [22] R. Harrington, *Field Computation by Moment Methods*. Wiley-IEEE Press, 1993.
- [23] K. Yee, "Numerical Solution of Initial Boundary Value Problems Involving Maxwell's Equations in Isotropic Media," *IEEE Transactions on Antennas and Propagation*, vol. 14, no. 3, pp. 302–307, May 1966.
- [24] S. Rao, D. Wilton, and A. Glisson, "Electromagnetic Scattering by Surfaces of Arbitrary Shape," *IEEE Transactions on Antennas and Propagation*, vol. 30, no. 3, pp. 409–418, May 1982.
- [25] A. Heldring, J. Rius, J. Tamayo, J. Parron, and E. Ubada, "Fast Direct Solution of Method of Moments Linear System," *IEEE Transactions on Antennas and Propagation*, vol. 55, no. 11, pp. 3220–3228, Nov. 2007.
- [26] —, "Multiscale Compressed Block Decomposition for Fast Direct Solution of Method of Moments Linear System," *IEEE Transactions on Antennas and Propagation*, vol. 59, no. 2, pp. 526–536, Feb. 2011.
- [27] A. Heldring, J. Tamayo, E. Ubada, and J. Rius, "Accelerated Direct Solution of the Method-of-Moments Linear System," *Proceedings of the IEEE*, vol. 101, no. 2, pp. 364–371, Feb. 2013.

- [28] K. Zhao, Vouvakis, N. Marinos, and J.-F. Lee, "The Adaptive Cross Approximation Algorithm for Accelerated Method of Moments Computations of EMC Problems," *IEEE Transactions on Electromagnetic Compatibility*, vol. 47, no. 4, pp. 763–773, Nov. 2005.
- [29] A. Heldring, J. Tamayo, C. Simon, E. Ubeda, and J. Rius, "Sparsified Adaptive Cross Approximation Algorithm for Accelerated Method of Moments Computations," *IEEE Transactions on Antennas and Propagation*, vol. 61, no. 1, pp. 240–246, Jan. 2013.
- [30] M. Bebendorf, "Approximation of Boundary Element Matrices," *Numerische Mathematik*, vol. 86, no. 4, pp. 565–589, Jun. 2000.
- [31] V. Le-Van, B. Bannwarth, A. Carpentier, O. Chadebec, J.-M. Guichon, and G. Meunier, "The Adaptive Cross Approximation Technique for a Volume Integral Equation Method Applied to Nonlinear Magnetostatic Problems," *IEEE Transactions on Magnetics*, vol. 50, no. 2, pp. 445–448, Feb. 2014.
- [32] E. Michielssen and A. Boag, "A Multilevel Matrix Decomposition Algorithm for Analyzing Scattering from Large Structures," *IEEE Transactions on Antennas and Propagation*, vol. 44, no. 8, pp. 1086–1093, Aug. 1996.
- [33] J. Parron, J. M. Rius, and J. R. Mosig, "Application of the Multilevel Matrix Decomposition Algorithm to the Frequency Analysis of Large Microstrip Antenna Arrays," *IEEE Transactions on Magnetics*, vol. 38, no. 2, pp. 721–724, Mar. 2002.
- [34] J. M. Rius, J. Parron, E. Ubeda, and J. R. Mosig, "Multilevel Matrix Decomposition Algorithm for Analysis of Electrically Large Electromagnetic Problems in 3-D," *Microwave and Optical Technology Letters*, vol. 22, no. 3, pp. 177–182, Aug. 1999.
- [35] R. Mittra and K. Du, "Characteristic Basis Function Method for Iteration-Free Solution of Large Method of Moments Problems," *Progress In Electromagnetics Research B*, vol. 6, pp. 307–336, 2008.
- [36] V. V. S. Prakash and R. Mittra, "Characteristic Basis Function Method: A New Technique for Efficient Solution of Method of Moments Matrix Equations," *Microwave and Optical Technology Letters*, vol. 36, no. 2, pp. 95–100, Jan. 2003.
- [37] A. Yagbasan, C. Tunc, V. Erturk, A. Altintas, and R. Mittra, "Characteristic Basis Function Method for Solving Electromagnetic Scattering Problems Over Rough Terrain Profiles," *IEEE Transactions on Antennas and Propagation*, vol. 58, no. 5, pp. 1579–1589, May 2010.
- [38] G. H. Golub and C. F. Van Loan, *Matrix Computations*, 3rd ed. Johns Hopkins University Press, 1996.
- [39] H. A. Van Der Vorst, "BI-CGSTAB: a Fast and Smoothly Converging Variant of BI-CG for the Solution of Nonsymmetric Linear Systems," *SIAM Journal on Scientific and Statistical Computing*, vol. 13, no. 2, pp. 631–644, Mar. 1992.
- [40] Y. Saad and M. H. Schultz, "GMRES: A Generalized Minimal Residual Algorithm for Solving Nonsymmetric Linear Systems," *SIAM Journal on Scientific and Statistical Computing*, vol. 7, no. 3, pp. 856–869, Jul. 1986.

- [41] Y. Saad, *Iterative Methods for Sparse Linear Systems*, 2nd ed. Society for Industrial and Applied Mathematics, 2003.
- [42] J. Liesen and P. Tichy, “Convergence Analysis of Krylov Subspace Methods,” *GAMM-Mitteilungen*, vol. 27, no. 2, pp. 153–173, Dec. 2004.
- [43] T. Rappaport, *Wireless Communications: Principles and Practice*, 2nd ed. Prentice Hall PTR, 2001.
- [44] X. Chen, C. Gu, Z. Li, and Z. Niu, “Efficient Iterative Solution of Electromagnetic Scattering Using Adaptive Cross Approximation Enhanced Characteristic Basis Function Method,” *IET Microwaves, Antennas & Propagation*, vol. 9, no. 3, pp. 217–223, Feb. 2015.
- [45] X. Hu, Y. Xu, and R. Chen, “Fast Iterative Solution of Integral Equation with Matrix Decomposition Algorithm and Multilevel Simple Sparse Method,” *IET Microwaves, Antennas Propagation*, vol. 5, no. 13, pp. 1583–1588, Oct. 2011.
- [46] E. Bleszynski, M. Bleszynski, and T. Jaroszewicz, “AIM: Adaptive Integral Method for Solving Large-Scale Electromagnetic Scattering and Radiation Problems,” *Radio Science*, vol. 31, no. 5, pp. 1225–1251, Sep. 1996.
- [47] J. L. Guo, J. Y. Li, and Q. Z. Liu, “Analysis of Arbitrarily Shaped Dielectric Radomes using Adaptive Integral Method Based on Volume Integral Equation,” *IEEE Transactions on Antennas and Propagation*, vol. 54, no. 7, pp. 1910–1916, Jul. 2006.
- [48] O. Kim and P. Meincke, “Adaptive Integral Method for Higher Order Method of Moments,” *IEEE Transactions on Antennas and Propagation*, vol. 56, no. 8, pp. 2298–2305, Aug. 2008.
- [49] Z.-Q. Lu and X. An, “Fast Monostatic Radar Cross Section Computation for Perfectly Electric Conducting Targets using Low-Rank Compression and Adaptive Integral Method,” *IET Microwaves, Antennas Propagation*, vol. 8, no. 1, pp. 46–51, Jan. 2014.
- [50] C.-C. Liu and W. C. Chew, “Fast Far Field Approximation for Calculating the RCS of Large Objects,” in *Antennas and Propagation Society International Symposium, 1995. AP-S. Digest*, vol. 1, June 1995, pp. 22–25 vol.1.
- [51] C. Brennan and P. Cullen, “Application of the Fast Far Field Approximation to the Computation of UHF Pathloss over Irregular Terrain,” *IEEE Transactions on Antennas and Propagation*, vol. 46, no. 6, pp. 881–890, Jun. 1998.
- [52] C. C. Lu, J. M. Song, W. C. Chew, and E. Michielssen, “The Application of Far-Field Approximation to Accelerate the Fast Multipole Method,” in *The 1996 Antennas and Propagation Society International Symposium*, vol. 3, Jul. 1996, pp. 1738–1741.
- [53] T. J. Cui, W. C. Chew, G. Chen, and J. Song, “Efficient MLFMA, RPFMA, and FAFFA Algorithms for EM Scattering by Very Large Structures,” *IEEE Transactions on Antennas and Propagation*, vol. 52, no. 3, pp. 759–770, Mar. 2004.



- [54] R. Coifman, V. Rokhlin, and S. Wandzura, “The Fast Multipole Method for the Wave Equation: a Pedestrian Prescription,” *IEEE Antennas and Propagation Magazine*, vol. 35, no. 3, pp. 7–12, Jun. 1993.
- [55] N. Engheta, W. Murphy, V. Rokhlin, and M. Vassiliou, “The Fast Multipole Method (FMM) for Electromagnetic Scattering Problems,” *IEEE Transactions on Antennas and Propagation*, vol. 40, no. 6, pp. 634–641, Jun. 1992.
- [56] J. Song, C. C. Lu, and W. C. Chew, “Multilevel Fast Multipole Algorithm for Electromagnetic Scattering by Large Complex Objects,” *IEEE Transactions on Antennas and Propagation*, vol. 45, no. 10, pp. 1488–1493, Oct. 1997.
- [57] W. Chew, E. Michielssen, J. M. Song, and J. M. Jin, *Fast and Efficient Algorithms in Computational Electromagnetics*. Artech House, Inc., 2001.
- [58] C. C. Lu, “Indoor Radio-Wave Propagation Modeling by Multilevel Fast Multipole Algorithm,” *Microwave and Optical Technology Letters*, vol. 29, no. 3, pp. 168–175, May 2001.
- [59] W. B. Ewe, L. W. Li, Q. Wu, and M. S. Leong, “Preconditioners for Adaptive Integral Method Implementation,” *IEEE Transactions on Antennas and Propagation*, vol. 53, no. 7, pp. 2346–2350, Jul. 2005.
- [60] A. Heldring, J. Rius, and L. Ligthart, “New Block ILU Preconditioner Scheme for Numerical Analysis of Very Large Electromagnetic Problems,” *IEEE Transactions on Magnetics*, vol. 38, no. 2, pp. 337–340, Mar. 2002.
- [61] M. Bruning, P. Benner, A. Bunse-Gerstner, R. Bungler, J. Reiter, and J. Ritter, “A Sparse Approximate Inverse Preconditioner for the Method of Moments Accelerated with the Multilevel Fast Multipole Method,” in *The 2002 Antennas and Propagation Society International Symposium*, vol. 2, Jun. 2002, pp. 602–605.
- [62] M. Carr, M. Bleszynski, and J. Volakis, “A Near-Field Preconditioner and Its Performance in Conjunction with the BiCGstab(ell) Solver,” *IEEE Antennas and Propagation Magazine*, vol. 46, no. 2, pp. 23–30, Apr. 2004.
- [63] H. Chiba, T. Fukasawa, H. Miyashita, and Y. Konishi, “Convergence Property of Inner-Outer Flexible GMRES for Solving Electromagnetic Scattering Problems with Method of Moments,” in *The 2010 Antennas and Propagation Society International Symposium*, Jul. 2010, pp. 1–4.
- [64] D. Holliday, L. DeRaad, and G. St-Cyr, “Forward-Backward: a New Method for Computing Low-Grazing Angle Scattering,” *IEEE Transactions on Antennas and Propagation*, vol. 44, no. 5, pp. 722–729, May 1996.
- [65] M. Rodriguez Pino, L. Landesa, J. Rodriguez, F. Obelleiro, and R. Burkholder, “The Generalized Forward-Backward Method for Analyzing the Scattering from Targets on Ocean-Like Rough Surfaces,” *IEEE Transactions on Antennas and Propagation*, vol. 47, no. 6, pp. 961–969, Jun. 1999.
- [66] C. Brennan, P. Cullen, and M. Condon, “A Novel Iterative Solution of the Three Dimensional Electric Field Integral Equation,” *IEEE Transactions on Antennas and Propagation*, vol. 52, no. 10, pp. 2781–2785, Oct. 2004.

- [67] C. Brennan and D. Bogusevski, "Convergence Analysis for Buffered Block Forward-Backward (BBFB) Method Applied to EFIE," in *The 2006 Antennas and Propagation Society International Symposium*, Jul. 2006, pp. 4045–4048.
- [68] C. Brennan, D. Trinh-Xuan, M. Mullen, P. Bradley, and M. Condon, "Improved Forward Backward Method with Spectral Acceleration for Scattering from Randomly Rough Lossy Surfaces," *IEEE Transactions on Antennas and Propagation*, vol. 61, no. 7, pp. 3922–3926, Jul. 2013.
- [69] C. Brennan and D. Trinh-Xuan, "Improved Forward Backward Method with Spectral Acceleration for Scattering from Exponentially Correlated Rough Lossy Surfaces," in *The 2012 Loughborough Antennas and Propagation Conference*, Nov. 2012, pp. 1–4.
- [70] A. Motley and J. Keenan, "Personal Communication Radio Coverage in Buildings at 900 MHz and 1700 MHz," *Electronics Letters*, vol. 24, no. 12, pp. 763–764, Jun. 1988.
- [71] K. W. A. V. Dongen, C. Brennan, and W. M. D. Wright, "A Reduced Forward Operator for Electromagnetic Wave Scattering Problems," in *The 2006 6th International Conference on Computational Electromagnetics*, Apr. 2006, pp. 1–2.
- [72] C. Reddy, M. Deshpande, C. Cockrell, and F. Beck, "Fast RCS Computation over a Frequency Band using Method of Moments in Conjunction with Asymptotic Waveform Evaluation Technique," *IEEE Transactions on Antennas and Propagation*, vol. 46, no. 8, pp. 1229–1233, Aug. 1998.
- [73] J. Gong and J. Volakis, "AWE Implementation for Electromagnetic FEM Analysis," *Electronics Letters*, vol. 32, no. 24, pp. 2216–2217, Nov. 1996.
- [74] C. R. Cockrell and F. B. Beck, "Asymptotic Waveform Evaluation (AWE) Technique for Frequency Domain Electromagnetic Analysis," in *NASA Technical Memorandum 110292*, Nov. 1996.
- [75] C. A. Balanis, *Advanced Engineering Electromagnetics*, 2nd ed. John Wiley & Sons, 2012.
- [76] D. Dutta, *Textbook of Engineering Mathematics*. New Age International Limited, 2006.
- [77] R. Barrett, M. Berry, T. F. Chan, J. Demmel, J. Donato, J. Dongarra, V. Eijkhout, R. Pozo, C. Romine, and H. Van der Vorst, *Templates for the Solution of Linear Systems: Building Blocks for Iterative Methods*, 2nd ed. Society for Industrial and Applied Mathematics, 1994.
- [78] J. K. Reid, "A Method for Finding the Optimum Successive Over-Relaxation Parameter," *The Computer Journal*, vol. 9, no. 2, pp. 200–204, 1966.
- [79] M. Eiermann and R. S. Varga, "Is The Optimal w Best for the SOR Iteration Method?" *Linear Algebra and its Applications*, vol. 182, pp. 257 – 277, 1993.
- [80] D. Kapp and G. Brown, "A New Numerical Method for Rough-Surface Scattering Calculations," *IEEE Transactions on Antennas and Propagation*, vol. 44, no. 5, pp. 711–, May 1996.

- [81] C. Brennan, M. Condon, and V. Pham-Xuan, "Accelerated Buffered Block Forward Backward Method for Electrically Large Scattering Problems," in *The 2013 International Conference on Electromagnetics in Advanced Applications*, Sep. 2013, pp. 732–735.
- [82] D. Trinh-Xuan, C. Brennan, M. Mullen, and P. Bradley, "Extension of Fast Far Field Algorithm to Propagation over Lossy Dielectric Terrain and Buildings," in *The 2011 IEEE-APS Topical Conference on Antennas and Propagation in Wireless Communications*, Sep. 2011, pp. 1249–1252.
- [83] C. Brennan and D. Trinh-Xuan, "Fullwave Computation of Path Loss in Urban Areas," in *The 2014 8th European Conference on Antennas and Propagation*, Apr. 2014, pp. 1124–1127.
- [84] B. Babu, C. Brennan, and M. Condon, "Block Forward Backward Method for Computation of Electromagnetic Wave Scattering from a Collection of Inhomogeneous Bodies," in *The 2007 International Conference on Electromagnetics in Advanced Applications*, Sep. 2007, pp. 944–947.
- [85] C. Brennan and D. Bogusevski, "Buffered Block Forward Backward (BBFB) Method Applied to EM Wave Scattering from Homogeneous Dielectric Bodies," in *The 6th Scientific Computing in Electrical Engineering Conference*, Sep. 2007, pp. 301–308.
- [86] W.-D. Li, W. Hong, and H.-X. Zhou, "Integral Equation-Based Overlapped Domain Decomposition Method for the Analysis of Electromagnetic Scattering of 3D Conducting Objects," *Microwave and Optical Technology Letters*, vol. 49, no. 2, pp. 265–274, Feb. 2007.
- [87] W.-D. Li, H.-X. Zhou, and W. Hong, "A Cube-Based Scheme of IE-ODDM-MLFMA for Electromagnetic Scattering Problems," *IEEE Antennas and Wireless Propagation Letters*, vol. 8, pp. 630–633, May 2009.
- [88] C. Walshaw and M. Cross, "Mesh Partitioning: A Multilevel Balancing and Refinement Algorithm," *SIAM Journal on Scientific Computing*, vol. 22, no. 1, pp. 63–80, Jan. 2000.
- [89] S. Padmavathi and A. George, "Multilevel Hybrid Graph Partitioning Algorithm," in *The 2014 IEEE International Advance Computing Conference*, Feb. 2014, pp. 85–89.
- [90] D. Lasalle and G. Karypis, "Multi-Threaded Graph Partitioning," in *Proceedings of the 2013 IEEE 27th International Symposium on Parallel and Distributed Processing*. IEEE Computer Society, May 2013, pp. 225–236.
- [91] G. Karypis and V. Kumar, "A Fast and High Quality Multilevel Scheme for Partitioning Irregular Graphs," *SIAM Journal on Scientific Computing*, vol. 20, no. 1, pp. 359–392, Dec. 1998.
- [92] B. Hendrickson and R. Leland, "An Improved Spectral Graph Partitioning Algorithm for Mapping Parallel Computations," *SIAM Journal on Scientific Computing*, vol. 16, no. 2, pp. 452–469, Mar. 1995.

- [93] M. Benzi, “Preconditioning Techniques for Large Linear Systems: A Survey,” *Journal of Computational Physics*, vol. 182, no. 2, pp. 418 – 477, Nov. 2002.
- [94] O. Ergül and L. Gürel, “Efficient Solution of the Electric and Magnetic Current Combined-Field Integral Equation with the Multilevel Fast Multipole Algorithm and Block-Diagonal Preconditioning,” *Radio Science*, vol. 44, no. 6, Nov. 2009.
- [95] T. A. Davis, *Direct Methods for Sparse Linear Systems*. Society for Industrial and Applied Mathematics, 2006.
- [96] T. Malas and L. Gürel, “Incomplete LU Preconditioning with the Multilevel Fast Multipole Algorithm for Electromagnetic Scattering,” *SIAM Journal on Scientific Computing*, vol. 29, no. 4, pp. 1476–1494, Jun. 2007.
- [97] K. Sertel and J. L. Volakis, “Incomplete LU Preconditioner for FMM Implementation,” *Microwave and Optical Technology Letters*, vol. 26, no. 4, pp. 265–267, Aug. 2000.
- [98] O. Ergül and L. Gürel, *The Multilevel Fast Multipole Algorithm (MLFMA) for Solving Large-Scale Computational Electromagnetics*, 1st ed. Wiley-IEEE Press, 2014.
- [99] J. Lee, C. Zhang, and C.-C. Lu, “Sparse Inverse Preconditioning of Multilevel Fast Multipole Algorithm for Hybrid Integral Equations in Electromagnetics,” *IEEE Transactions on Antennas and Propagation*, vol. 52, no. 9, pp. 2277–2287, Sep. 2004.
- [100] E. Chow, “A Priori Sparsity Patterns for Parallel Sparse Approximate Inverse Preconditioners,” *SIAM Journal on Scientific Computing*, vol. 21, no. 5, pp. 1804–1822, Apr. 2000.
- [101] M. J. Grote and T. Huckle, “Parallel Preconditioning with Sparse Approximate Inverses,” *SIAM Journal on Scientific Computing*, vol. 18, no. 3, pp. 838–853, May 1997.
- [102] B. Carpentieri, I. S. Duff, and L. Giraud, “Sparse Pattern Selection Strategies for Robust Frobenius-Norm Minimization Preconditioners in Electromagnetism,” *Numerical Linear Algebra with Applications*, vol. 7, no. 7-8, pp. 667–685, 2000.
- [103] B. Carpentieri, I. S. Duff, L. Giraud, and G. Sylvand, “Combining Fast Multipole Techniques and an Approximate Inverse Preconditioner for Large Electromagnetism Calculations,” *SIAM Journal on Scientific Computing*, vol. 27, no. 3, pp. 774–792, 2005.
- [104] A. F. Peterson, “Mapped Vector Basis Functions for Electromagnetic Integral Equations,” *Synthesis Lectures on Computational Electromagnetics*, vol. 1, no. 1, pp. 1–124, 2006.
- [105] J. R. Mautz and R. F. Harrington, “H-Field, E-Field, and Combined-Field Solutions for Conducting Bodies of Revolution,” *Archiv fuer Elektronik und Uebertragungstechnik*, vol. 32, no. 11, pp. 157–164, Apr. 1978.
- [106] —, “A Combined-Source Solution for Radiation and Scattering from a Perfectly Conducting Body,” *IEEE Transactions on Antennas and Propagation*, vol. 27, no. 4, pp. 445–454, Jul. 1979.

- [107] A. F. Peterson, “The Interior Resonance Problem Associated with Surface Integral Equations of Electromagnetics: Numerical Consequences and a Survey of Remedies,” *Electromagnetics*, vol. 10, no. 3, pp. 293–312, 1990.
- [108] I. Hanninen, M. Taskinen, and J. Sarvas, “Singularity Subtraction Integral Formulae for Surface Integral Equations with RWG, Rooftop and Hybrid Basis Functions,” *Progress In Electromagnetics Research*, vol. 63, pp. 243–278, 2006.
- [109] P. Yla-Oijala and M. Taskinen, “Calculation of CFIE Impedance Matrix Elements with RWG and nxRWG Functions,” *IEEE Transactions on Antennas and Propagation*, vol. 51, no. 8, pp. 1837–1846, Aug. 2003.
- [110] M. Khayat and D. Wilton, “Numerical Evaluation of Singular and Near-Singular Potential Integrals,” *IEEE Transactions on Antennas and Propagation*, vol. 53, no. 10, pp. 3180–3190, Oct. 2005.
- [111] M. Abramowitz and I. Stegun, *Handbook of Mathematical Functions: with Formulas, Graphs, and Mathematical Tables*, ser. Applied mathematics. Dover Publications, 1964.
- [112] X. Sheng, J.-M. Jin, J. Song, W. C. Chew, and C.-C. Lu, “Solution of Combined-Field Integral Equation using Multilevel Fast Multipole Algorithm for Scattering by Homogeneous Bodies,” *IEEE Transactions on Antennas and Propagation*, vol. 46, no. 11, pp. 1718–1726, Nov. 1998.
- [113] J.-Y. Li and L.-W. Li, “Characterizing Scattering by 3D Arbitrarily Shaped Homogeneous Dielectric Objects using Fast Multipole Method,” *IEEE Antennas and Wireless Propagation Letters*, vol. 3, no. 1, pp. 1–4, Dec. 2004.
- [114] O. Ergul, I. van den Bosch, and L. Gurel, “Two-Step Lagrange Interpolation Method for the Multilevel Fast Multipole Algorithm,” *IEEE Antennas and Wireless Propagation Letters*, vol. 8, pp. 69–71, Apr. 2009.
- [115] I. van den Bosch, M. Acheroy, and J.-P. Marcel, “Design, Implementation, and Optimization of a Highly Efficient Multilevel Fast Multipole Algorithm,” in *The 2007 Computational Electromagnetics Workshop*, Aug. 2007, pp. 1–6.
- [116] I. V. d. Bosch. PUMA-EM Computational Electromagnetic Software. [Online]. Available: <http://puma-em.sourceforge.net/>
- [117] Linear Algebra Package (LAPACK). [Online]. Available: <http://www.netlib.org/lapack/>
- [118] P. Benner and L. Feng, “Recycling Krylov Subspaces for Solving Linear Systems with Successively Changing Right-Hand Sides Arising in Model Reduction,” in *Model Reduction for Circuit Simulation*, ser. Lecture Notes in Electrical Engineering. Springer Netherlands, 2011, vol. 74, pp. 125–140.
- [119] Z. Peng, M. B. Stephanson, and J.-F. Lee, “Fast Computation of Angular Responses of Large-Scale Three-Dimensional Electromagnetic Wave Scattering,” *IEEE Transactions on Antennas and Propagation*, vol. 58, no. 9, pp. 3004–3012, Sep. 2010.

- [120] E. K. Miller, “Model-Based Parameter Estimation in Electromagnetics. III. Applications to EM Integral Equations,” *IEEE Antennas and Propagation Magazine*, vol. 40, no. 3, pp. 49–66, Jun. 1998.
- [121] X. C. Wei, Y. J. Zhang, and E. P. Li, “The Hybridization of Fast Multipole Method with Asymptotic Waveform Evaluation for the Fast Monostatic RCS Computation,” *IEEE Transactions on Antennas and Propagation*, vol. 52, no. 2, pp. 605–607, Feb. 2004.
- [122] X. M. Pan and X. Q. Sheng, “Accurate and Efficient Evaluation of Spatial Electromagnetic Responses of Large Scale Targets,” *IEEE Transactions on Antennas and Propagation*, vol. 62, no. 9, pp. 4746–4753, Sep. 2014.
- [123] E. Liberty, F. Woolfe, P. Martinsson, V. Rokhlin, and M. Tygert, “Randomized Algorithms for the Low-Rank Approximation of Matrices,” in *Proceedings of the National Academy of Sciences*, Dec. 2007, pp. 20 167–20 172.
- [124] M. Mullen, C. Brennan, and T. Downes, “A Hybridized Forward Backward Method Applied to Electromagnetic Wave Scattering Problems,” *IEEE Transactions on Antennas and Propagation*, vol. 57, no. 6, pp. 1846–1850, Jun. 2009.
- [125] B. Liu, Z. Li, and Y. Du, “A Fast Numerical Method for Electromagnetic Scattering from Dielectric Rough Surfaces,” *IEEE Transactions on Antennas and Propagation*, vol. 59, no. 1, pp. 180–188, Jan. 2011.
- [126] D. Torrungrueng, H.-T. Chou, and J. T. Johnson, “A Novel Acceleration Algorithm for The Computation of Scattering from Two-Dimensional Large-Scale Perfectly Conducting Random Rough Surfaces with The Forward-Backward Method,” *IEEE Transactions on Geoscience and Remote Sensing*, vol. 38, no. 4, pp. 1656–1668, Jul. 2000.
- [127] H. Ye and Y.-Q. Jin, “Parameterization of the Tapered Incident Wave for Numerical Simulation of Electromagnetic Scattering from Rough Surface,” *IEEE Transactions on Antennas and Propagation*, vol. 53, no. 3, pp. 1234–1237, Mar. 2005.
- [128] D. Solimini, *Microwave Radiometry and Remote Sensing of The Environment*. Taylor & Francis, 1995.
- [129] D. Trinh-Xuan, “Accelerated Integral Equation Techniques for Solving EM Wave Propagation and Scattering Problems,” Ph.D. dissertation, Dublin City University, 2014.
- [130] L. Tsang, J. Kong, K. Ding, and C. Ao, *Scattering of Electromagnetic Waves: Numerical Simulations*, ser. Scattering of Electromagnetic Waves. Wiley, 2004.
- [131] R. W. Newton and J. W. Rouse, “Microwave Radiometer Measurements of Soil Moisture Content,” *IEEE Transactions on Antennas and Propagation*, vol. 28, no. 5, pp. 680–686, Sep. 1980.
- [132] L. Zhou, L. Tsang, V. Jandhyala, Q. Li, and C. Chan, “Emissivity Simulations in Passive Microwave Remote Sensing with 3-D Numerical Solutions of Maxwell Equations,” *IEEE Transactions on Geoscience and Remote Sensing*, vol. 42, no. 8, pp. 1739–1748, Aug. 2004.

- [133] Y. Oh, K. Sarabandi, and F. Ulaby, "An Empirical Model and an Inversion Technique for Radar Scattering from Bare Soil Surfaces," *IEEE Transactions on Geoscience and Remote Sensing*, vol. 30, no. 2, pp. 370–381, Mar. 1992.
- [134] P. Xu, K. Chen, and L. Tsang, "Analysis of Microwave Emission of Exponentially Correlated Rough Soil Surfaces from 1.4GHz to 36.5GHz," *Progress In Electromagnetics Research*, vol. 108, pp. 205–219, 2010.
- [135] S. R. Saunders and A. Aragon-Zavala, *Antennas and Propagation for Wireless Communication Systems*, 2nd ed. New York, NY, USA: John Wiley & Sons, Inc., 2007.
- [136] F. Alves, M. R. M. L. de Albuquerque, S. G. da Silva, and A. G. D'Assuncao, "Efficient Ray-Tracing Method for Indoor Propagation Prediction," in *The 2005 International Conference on Microwave and Optoelectronics*, Jul. 2005, pp. 435–438.
- [137] F. S. de Adana, O. G. Blanco, I. G. Diego, J. P. Arriaga, and M. F. Catedra, "Propagation Model Based on Ray Tracing for The Design of Personal Communication Systems in Indoor Environments," *IEEE Transactions on Vehicular Technology*, vol. 49, no. 6, pp. 2105–2112, Nov. 2000.
- [138] B. De Backer, F. Olyslager, and D. De Zutter, "An Integral Equation Approach to the Prediction of Indoor Wave Propagation," *Radio Science*, vol. 32, no. 5, pp. 1833–1850, 1997.
- [139] Y. Wang, S. Safavi-Naeini, and S. Chaudhuri, "A Hybrid Technique Based on Combining Ray Tracing and FDTD Methods for Site-Specific Modeling of Indoor Radio Wave Propagation," *IEEE Transactions on Antennas and Propagation*, vol. 48, no. 5, pp. 743–754, May 2000.
- [140] A. Hrovat, G. Kandus, and T. Javornik, "A Survey of Radio Propagation Modeling for Tunnels," *IEEE Communications Surveys Tutorials*, vol. 16, no. 2, pp. 658–669, Oct. 2014.
- [141] K. W. A. van Dongen, C. Brennan, and W. M. D. Wright, "Reduced Forward Operator for Electromagnetic Wave Scattering Problems," *IET Science, Measurement Technology*, vol. 1, no. 1, pp. 57–62, Jan. 2007.
- [142] Z. Q. Zhang, Q. H. Liu, C. Xiao, E. Ward, G. Ybarra, and W. T. Joines, "Microwave Breast Imaging: 3-D Forward Scattering Simulation," *IEEE Transactions on Biomedical Engineering*, vol. 50, no. 10, pp. 1180–1189, Oct. 2003.
- [143] T. Sarkar, E. Arvas, and S. Rao, "Application of FFT and the Conjugate Gradient Method for the Solution of Electromagnetic Radiation from Electrically Large and Small Conducting Bodies," *IEEE Transactions on Antennas and Propagation*, vol. 34, no. 5, pp. 635–640, May 1986.
- [144] P. Feldmann and R. Freund, "Efficient Linear Circuit Analysis by Pade Approximation via the Lanczos Process," *IEEE Transactions on Computer-Aided Design of Integrated Circuits and Systems*, vol. 14, no. 5, pp. 639–649, May 1995.
- [145] C. C. R. and B. F. B., "Asymptotic Waveform Evaluation (AWE) Technique for Frequency Domain Electromagnetic Analysis," Tech. Rep., 1996.

- [146] P. Zwamborn and P. Van den Berg, “The Three Dimensional Weak Form of The Conjugate Gradient FFT Method for Solving Scattering Problems,” *IEEE Transactions on Microwave Theory and Techniques*, vol. 40, no. 9, pp. 1757–1766, Sep. 1992.



# Publications

## Journals

V. Pham-Xuan, M. Condon and C. Brennan, "Modified Multilevel Fast Multipole Algorithm for Stationary Iterative Solvers," *IEEE Access*, vol. 3, pp. 774-786, 2015.

C. Brennan, D. Trinh-Xuan, V. Pham-Xuan, M. Condon and R. Mittra, "Full-Wave Analysis of Electromagnetic Wave Propagation over Terrain using the Improved Tabulated Interaction Method," *Radio Science*, vol. 50, no. 5, pp. 355-364, May 2015.

## Conferences

V. Pham-Xuan, D. Trinh-Xuan, M. Condon and C. Brennan, "Rapid Convergent Iterative Solver for Computing Two-Dimensional Random Rough Surface Scattering," in *The 2015 International Conference on Advanced Technologies for Communications (ATC)*, Oct. 2015, Ho Chi Minh, Vietnam.

V. Pham-Xuan, D. Trinh-Xuan, M. Condon and C. Brennan, "Fast Iterative Method for Computing Electromagnetic Scattering from Randomly Rough Surfaces," in *The 2015 International Conference on Electromagnetics in Advanced Applications (ICEAA)*, Sep. 2015, Turin, Italy.

V. Pham-Xuan, M. Condon and C. Brennan, "Efficient Full-Wave Computation of Radar Cross Section for Multiple Source Locations," in *The 9th European Conference on Antennas and Propagation (EuCAP)*, Apr. 2015, Lisbon, Portugal.

I. Kavanagh, V. Pham-Xuan, M. Condon and C. Brennan, "A Method of Moments Based Indoor Propagation Model," in *The 9th European Conference on Antennas and Propagation (EuCAP)*, Apr. 2015, Lisbon, Portugal.

V. Pham-Xuan, I. Kavanagh, M. Condon and C. Brennan, "On Comparison of Integral Approaches for Indoor Wave Propagation," in *The 2014 IEEE-APS Topical Conference on Antennas and Propagation in Wireless Communication (APWC)*, pp. 796-799, Aug. 2014, Aruba.

D. Trinh-Xuan, V. Pham-Xuan, S. Hussain and C. Brennan, "Integral Equation Based Path Loss Modelling for Propagation in Urban Environments," in *The 2014 International Conference on Electromagnetics in Advanced Applications (ICEAA)*, pp. 738-741, Aug. 2014, Aruba.

C. Brennan, M. Condon and V. Pham-Xuan, "On the Convergence Rate of the Accelerated Buffered Block Forward Backward Method," in *The 17th Research Colloquium on Communications and Radio Science into the 21st Century*, May 2014, Dublin, Ireland.

C. Brennan, M. Condon and V. Pham-Xuan, "Accelerated Buffered Block Forward Backward Method for Electrically Large Scattering Problems," in *The 2013 International Conference on Electromagnetics in Advanced Applications (ICEAA)*, pp. 732-735, Sep. 2013, Torino, Italy.

C. Brennan, M. Condon and V. Pham-Xuan, "Improved Buffered Block Forward Backward Method for Electrically Large Three-Dimensional Perfectly Conducting Bodies," in *The IET International Conference on Information and Communications Technologies (IETICT 2013)*, pp. 609-613, Apr. 2013, Beijing, China.

V. Pham-Xuan, D. Trinh-Xuan, I. de Koster, K. Van Dongen, M. Condon and C. Brennan, "Solution of Large-Scale Wideband EM Wave Scattering Problems using Fast Fourier Transform and the Asymptotic Waveform Evaluation Technique," in *The 2012 International Conference on Electromagnetics in Advanced Applications (ICEAA)*, pp. 1133-1136, Sep. 2012, Cape Town, South Africa.

# Acknowledgments

First and foremost, I would like express my deep gratitude to my supervisors, Dr. Conor Brennan and Dr. Marissa Condon. Dr. Conor Brennan inspired me in both scientific research and personal life. His constant enthusiasm for discovering different aspects of the electromagnetic world motivated me to overcome scientific challenges encountered during my 4 years at DCU. Our insightful discussions had great influence on my research. Careful and close supervision of Dr. Marissa Condon had significantly improved the quality of my work. Her dedication to helping is inspirational and is truly appreciated. Their patient guidance and enthusiastic encouragement made my Ph.D life more productive and stimulating. I also appreciate constructive comments and suggestions from Prof. Thomas Eibert and Dr. Yann Delauré on the improvement of my final work.

I greatly appreciate helps from technical staffs of the school of electronic engineering, especially Liam Meany and Robert Clare. Liam Meany and I had a very professional and enjoyable cooperation in the delivery of EE201 (Digital Circuits and Systems). Robert Clare was very kind and supportive in helping me with 3D printing stuffs. I also would like to thank my labmates: Dung Trinh-Xuan, Brendan Hayes, Sajjad Hussain and Ian Kavanagh. We had very interesting discussions about research and unforgettable memories about conference trips.

I wish to acknowledge all my friends in Ireland for their warm welcome, consistent encouragement in numerous ways and great activities such as football matches and BBQ parties. Special thanks to Tue Vu-Trong family, Linh Truong-Hong family, An Le-Khac family, An Phan, Vu Vo, Nhan Nguyen, Hung Cao and Loi Cao.

Last but not least, I am greatly indebted to my family for their unconditional love, patience and encouragement which enabled the completeness of my Ph.D project. My parents' understanding and encouragement gave me a strong confidence on myself to work hard and to continue pursuing a Ph.D program abroad.

Vinh Pham-Xuan

October 2015